QST-M-29

QST Takasaki Annual Report 2019

Takasaki Advanced Radiation Research Institute

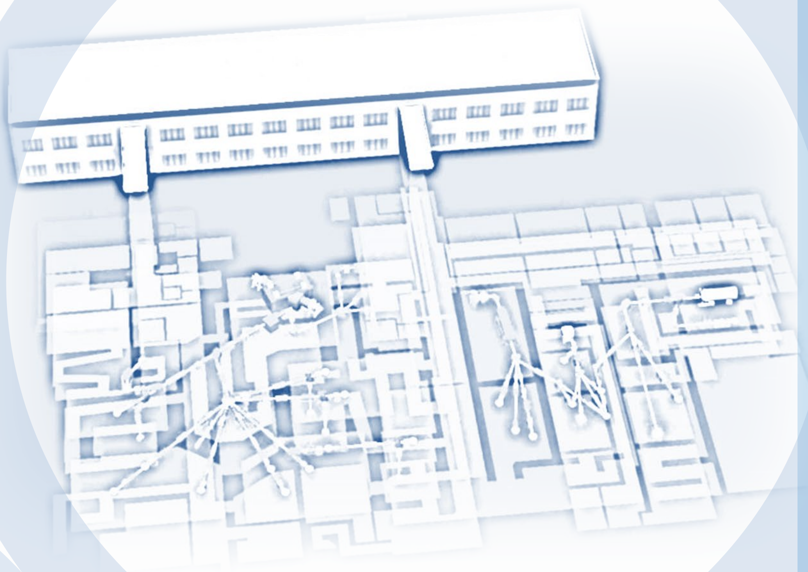

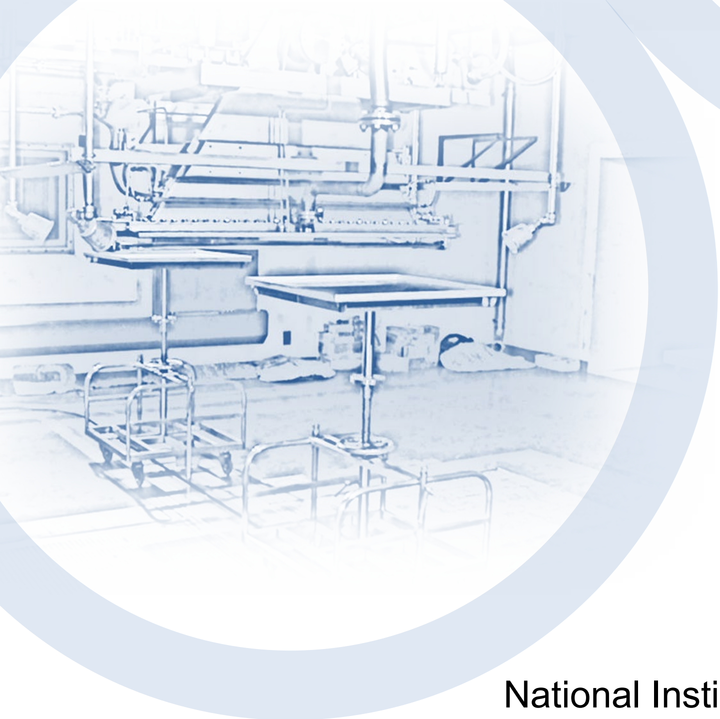

National Institutes for Quantum and
Radiological Science and Technology

Preface

Hisayoshi Itoh

Director General
Takasaki Advanced Radiation Research Institute
Quantum Beam Science Research Directorate
National Institutes for Quantum and Radiological Science and Technology

National Institutes for Quantum and Radiological Science and Technology (QST) was established in April 2016 by integrating the National Institute of Radiological Sciences (NIRS) and other institutes promoting quantum beam science research and nuclear fusion research in the Japan Atomic Energy Agency (JAEA). Currently, QST has three R&D directorates, *i.e.*, “Quantum Beam Science Research Directorate (QuBS),” “Quantum Medical Science Directorate,” and “Fusion Energy Directorate,” and one institute, *i.e.*, “Institute for Quantum Life Science.” QuBS consists of three research institutes, *i.e.*, “Takasaki Advanced Radiation Research Institute (TARRI),” “Kansai Photon Science Institute (KPSI),” and “Institute for Advanced Synchrotron Light Source (IASLS).” We are performing intensive fundamental and applied research in a wide range of fields, such as materials science, life science, and quantum beam technology, using advanced beam facilities. Both TARRI and KPSI have two research sites, *i.e.*, Takasaki and Tokai sites of TARRI and Kizu and Harima sites of KPSI. Typical beam facilities we use are the Takasaki Ion Accelerators for Advanced Radiation Application (TIARA) at the Takasaki site, Japan Proton Accelerator Research Complex (J-PARC) at the Tokai site, Japan-Kansai Advanced Relativistic Engineering Laser System (J-KAREN) at the Kizu site, and highly sophisticated beamlines of Super Photon Ring-8 GeV (SPring-8) at the Harima site. In IASLS, we are constructing a new advanced synchrotron light source for soft X-rays with ultrahigh intensity and coherence.

In TARRI, we have 15 research projects and two research groups conducting quantum beam science R&Ds with TIARA, 2-MeV electron accelerator, ^{60}Co gamma-ray irradiation facilities, etc., for contributing to the progress of science and technology as well as the promotion of industries Particularly to promote strong alliance with industries, the Advanced Functional Polymer Materials Research Group was launched in 2017 under the QST innovation hub program to develop next-generation graft-polymer materials with the combined use of quantum beam processing and analysis techniques as well as materials informatics. The Quantum Sensing and Information Materials Research Group was launched in August 2018 to conduct fundamental and applied research for realizing quantum devices, such as quantum sensors, quantum bits, and spin transistors, based on wide-bandgap semiconductors including diamonds and two-dimensional materials such as graphene. Moreover, we are performing R&D on advanced ion beam technology at the Beam Engineering Section of the Department of Advanced Radiation Technology. Additionally, our beam facilities are available to industries, academia, and governmental research institutes, and beam time is allocated to users based on the evaluation of their R&D programs.

This annual report covers the research activities at TARRI primarily for the fiscal year 2019 (FY 2019). This report comprises two parts—Part I and Part II. In Part I, the recent activities of all research projects and groups as well as the Beam Engineering Section are described. In Part II, the recent R&D results obtained using quantum beam facilities of TARRI are presented. This part is composed of 102 research papers in the fields of materials science, life science, and advanced quantum beam technology and eight status reports on the operation/maintenance of the quantum beam facilities. Note that as a typical topic in the materials science field, the novel heterostructure of graphene and Heusler alloy was successfully obtained for its application to next-generation spintronic memories. The heterostructure of high-quality single-layer graphene and half-metallic $Co_2Fe(Ge_{0.5}Ga_{0.5})$ (CFGG) Heusler alloy ferromagnet were synthesized by optimizing growth conditions using the chemical vapor deposition method. In the life science field, an imaging device of secondary electron bremsstrahlung (SEB) X-ray emitted during carbon-ion irradiation was developed for medical applications. Clear images of SEB X-ray were obtained from a 17-cm-diameter cylindrical phantom with a near-clinical dose of carbon ions. The developed camera is a promising device for SEB X-ray imaging during medical ion irradiation because the images agreed with the simulated results. For the advanced quantum beam technology, triple qubit comprising nitrogen-vacancy (NV) centers in diamonds has been created via molecular ion irradiation. Using nitrogen-rich $C_5N_4H_n$ ions, triple NVs were effectively created in diamonds. Obtained results indicated that the created triple NVs can act as a quantum register.

Concerning the status of quantum beam facilities, an azimuthally varying field (AVF) cyclotron and three electrostatic accelerators in TIARA have been steadily and safely operated as well as MeV electron and ^{60}Co gamma-ray irradiation facilities. We are planning to refresh the infrastructure in TIARA each year. In FY 2019, a centrifugal chiller system that chills and circulates water for water-cooled equipment, such as the main coil of the AVF cyclotron, was replaced with a new one. The operating performance and cost of the cooling system is expected to improve. The RI security system of the ^{60}Co gamma-ray irradiation facilities adapting the new regulations has been smoothly operated.

Finally, we extend our gratitude to both our domestic and foreign colleagues for cooperating, supporting, and encouraging our quantum beam science R&D as well as technological advance in the facilities of TARRI.

Facilities

Charged particle beams and RI facilities

Takasaki Ion Accelerators for Advanced Radiation Application (TIARA) consisting of four ion accelerators, an electron accelerator, and gamma irradiation facilities are available to researchers in QST and other organizations for R&D activities on new functional and environmentally friendly materials, biotechnology, radiation effects of materials, and quantum beam analysis. We are developing microbeams, single ion hits and uniform wide-area irradiation technique at the cyclotron. In addition, technical developments of three dimensional in-air PIXE analysis and production/acceleration of cluster ion beam such as C_{60} fullerene at the electrostatic accelerators are in progress.

Takasaki Ion Accelerators for Advanced Radiation Application: TIARA


TIARA facility


Cyclotron


Tandem accelerator


Single-ended accelerator

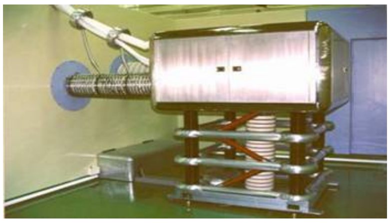
Ion implanter

Typical available ions

Accelerator	Ion	Energy (MeV)
AVF Cyclotron (K=110MeV)	H	10～ 80
	He	20～107
	C	75～320
	Ne	75～350
	Ar	150～520
	Fe	200～400
	Kr	210～520
	Xe	324～560
	Os	490
Tandem Accelerator (3 MV)	H	0.8～ 6.0
	C	0.8～18.0
	Ni	0.8～18.0
	Au	0.8～18.0
	C_{60}	0.8～9.0
Single-ended Accelerator (3 MV)	H	0.4～ 3.0
	D	0.4～ 3.0
	He	0.4～ 3.0
	e^-	0.4～ 3.0
Ion Implanter (400 kV)	H	0.02～0.38
	Ar	0.02～0.38
	Bi	0.02～0.37
	C_{60}	0.02～0.36

Energy-element range covered by the four accelerators

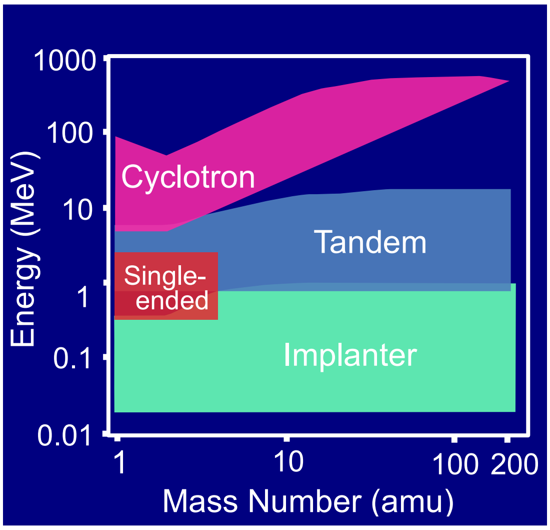

Cobalt-60 gamma-ray and electron beam irradiation facilities

Gamma-ray irradiation facility building

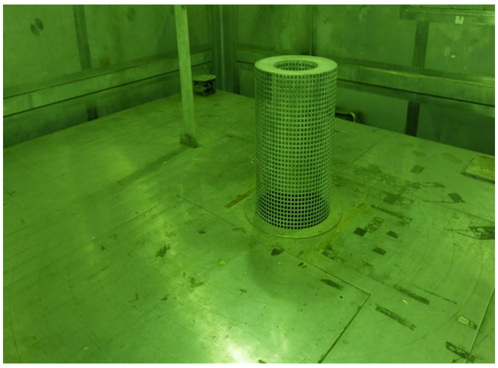

Gamma-ray irradiation room

Electron accelerator
（0.5～2.0 MeV, 0.1～30 mA)

Electron irradiation room with conveyor system

Specification

Apr. 2020

Name of facility	Cobalt-60 activity (PBq)	Number of rooms	Principal utilization
Co No.1 bld.	7.3	3	Radiation-resistance test Radiation effects on polymers
Co No.2 bld.	8.3	3	R & D on functional organic materials, inorganic materials and dosimetry
Food Irrad.	2.1	2	Radiation effects on biological substance and semiconductors

Dose-rate range

Unit：kGy/h

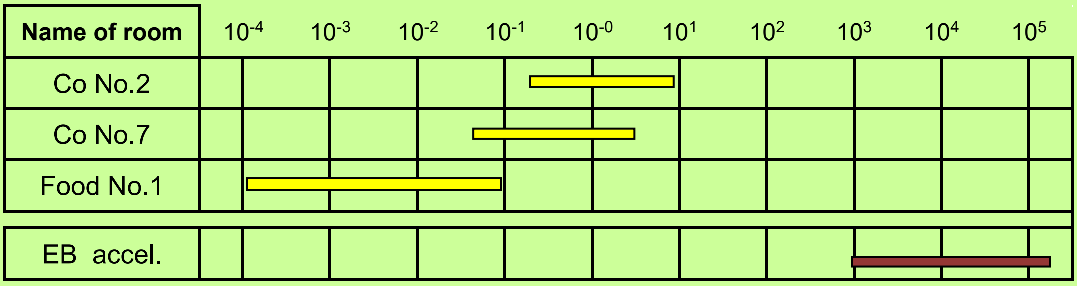

Contents

Part Ⅰ

Part Ⅱ

Part Ⅰ

Part Ⅰ

1. Materials Science

P1-1 Project “Functional Polymer”

Leader : Yasunari Maekawa

Project “Functional Polymer Research” has been developing the advanced functional polymer materials, such as polymer electrolyte materials and separation membranes for high performance fuel cells and hydrogen collection systems by using quantum beams. We have synthesized the proton- and anion-conducting electrolyte membranes (PEM and AEM) and the hydrogen permselective membranes using γ-rays and electron beams. We report herein two recent developments: poly(ether ether ketone) (PEEK)-based PEMs and poly(ethylene-co-tetrafluoroethylene) (ETFE)-based AEMs for hydrogen- and alkaline hydrated hydrazine-fuel cells. {1-01~03 in Part II}

Thermally stable graft-type polymer electrolyte membranes consisted in PEEK and crosslinked graft-polymers for fuel cell applications [1]

PEMs with higher proton conductivity at low relative humidity (RH) and superior mechanical properties under humid conditions have been required because these properties affect power generation efficiency and durability under extreme operating conditions in fuel cell systems. Since PEEK-based PEMs show well balanced properties of power generation and durability for PEM fuel cells at high temperature and dry conditions, the crosslinking structure were introduced in the graft polymers using a small amount of divinylbenzene (DVB) (up to 0.5 wt.%) for further improving the durability.

The ion exchange capacity of the DVB-crosslinked PEEK-PEMs with grafting degrees (GDs) of 100-114% was 2.2-2.7 mmol/g regardless of the amount of DVB. The increases in the DVB contents reduced the proton conductivity and water uptake from 0.18 to 0.10 S/cm and 67 to 43%, respectively. These confirm the successful incorporation of crosslinking structures on the graft polymers. The crosslinked PEEK-PEMs exhibited quite stable ion exchange capacities (IECs) even after 500 h in water at 120 ºC, as shown in Fig. 1. In contrast, the IECs of non-crosslinked PEEK-PEM decreased from 2.5 to 1.6 mmol/g for 500 h. The above results clearly showed that the thermal stability at high temperature increased with less compensation of the conductivity decreases by the incorporation of a small amount of DVB.

Imidazolium-based anion exchange membranes for alkaline anion fuel cells: Interplay between morphology and anion transport behavior [2]

We have previously reported that AEMs consisted of the ETFE base film and graft-copolymers of 2-metyl-N-methyl-4-vinylimidazole (Im) and styrene (St) with various ratios (Im/St = 6/4, 4/6, and 3/7) (AEM64, AEM46, and AEM37) exhibited both high ion conductivity and alkaline stability [3]. In this study, we investigated the correlation between the anion transport properties and microscopic structures of the AEMs analyzed using the small-angle X-ray scattering (SAXS) spectrometer (NANOPIX, Rigaku, Japan).

The anion transport properties were evaluated based on the transport efficiency defined as a ratio of anion diffusion coefficients in AEMs to dilution solutions (D/D_0). The D/D_0 for AEM46 and AEM37 was similar with AEM64 at low hydration levels, but clearly deviated down from it at high hydration levels. Figure 2 shows SAXS profiles of the AEMs at the high hydration level (80% RH). AEM46 and AEM37 exhibited peaks in a higher *q* range than that in AEM64. This is due to the morphological transition. The conducting phase in AEM64 were composed of graft polymers with homogeneously dispersed ions. In contrast, the conducting phase in AEM46 and AEM37 exhibited a heterogeneous structure with water puddles, resulting in the suppression of anion transport.

References

[1] S. Hasegawa *et al.*, Radiat. Phys. Chem. **171**, 108647 (2020).

[2] Y. Zhao *et al.*, J. Electrochem. Soc. **166**, F472 (2019).

[3] K. Yoshimura *et al.*, Soft Matter **12**, 1567 (2018).

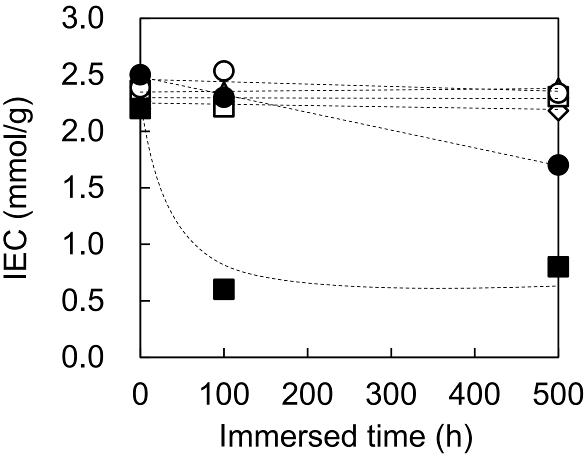

Fig. 1. Hydrothermal stabilities of PEEK-PEMs with various feed amounts of DVB (wt.%) in water at 120 ºC: 0 wt.% (●), 0.05 wt.% (○), 0.1 wt.% (□), 0.2 wt.% (△), and 0.5 wt.% (◇). Nafion 211 (■) were also plotted as a reference.

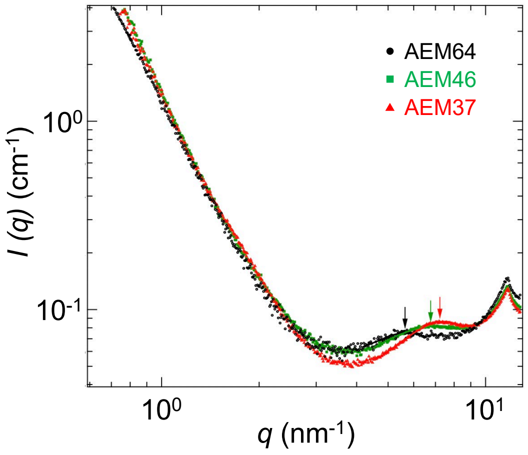

Fig. 2. SAXS profiles of the AEM64 (●), AEM46 (■), and AEM37 (▲) at 80% RH.

P1-2 Project “Advanced Catalyst”

Leader : Yasunari Maekawa

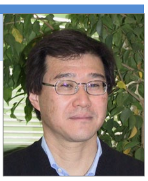

The main target of our project is development of catalytic materials for next-generation energy devices in future H_2 society by effective use of electron and ion beams. The advantage of our overarching strategy is that these quantum beams can lead to high-energy defect creation, active-site formation via non-equilibrium chemical reactions, and nano-to-micro fabrication. This report deals with R&D for component materials in proton exchange membrane fuel cells and H_2 production systems. {1-04~16 in Part II}

Non- and low-platinum electrocatalysts prepared by electron- and ion-beam irradiation [1-3] {1-04, 05, 07, 12, 14}

Non- or low-Pt oxygen reduction reaction (ORR) electrocatalysts are needed to decrease the device cost. Our advanced methods using electron and ion beams were pursued for the preparation of carbon-based catalysts and highly-active Pt nanoparticles (NPs).

There have been two approaches to developing carbon-based catalysts: (i) N doping in a graphitic structure; (ii) the formation of graphitic nanostructures such as shell-like and turbostratic graphite structures. We attempted ion implantation in a phenolic resin to prepare Fe NPs with a diameter of < 20 nm, which were used as a catalyst for the formation of the ORR-active turbostratic graphite [1].

We have recently found that the carbon support pre-irradiated with hundreds keV ions made the deposited Pt NP catalysts more active [2]. The extended X-ray absorption fine structure of the Pt L_3-edge indicated the shrinking of the Pt-Pt bond length in Pt NPs on the irradiated support. This result motivated us to investigate the overall picture of the interface between the Pt NPs and vacancies in irradiated carbon. Thus, X-ray absorption near-edge structure (XANES) measurements of C K-edge were performed to examine the interfacial structures [3].

Highly ordered pyrolytic graphite (HOPG) substrates were irradiated with 380 keV Ar^+ at a fluence of 1.0×10^{14} ions/cm^2. Pt NPs were deposited on the non-irradiated and irradiated HOPG supports by RF magnetron sputtering; the resulting samples are referred to as Pt/HOPG and Pt/irradiated HOPG, respectively. The C K-edge XANES spectra with a probing depth of approximately 0.6 nm (corresponding to a thickness of a few graphene layers) were measured at room temperature and below 2×10^{-8} Pa.

In the XANES spectra at an X-ray incident angle of 30º, six peaks corresponding to different chemical or electronic states were identified by curve fitting analysis. Interestingly, they involve a new state (peak F) due to the Pt-C bonding (~284 eV) in addition to the structures of the pristine and ion-irradiated HOPG such as the π* state (~285 eV; peak A). Table 1 shows the areal-intensity ratio of peak F to A. This was apparently higher for Pt/irradiated HOPG than for Pt/HOPG, suggesting that the introduction of vacancies in the graphite surface would modify the electronic structure caused by the Pt-C interaction.

New nano-sized materials prepared by swift-heavy-ion irradiation [4-6] {1-06, 08~11, 13, 15, 16}

An MeV-GeV heavy-ion beam gives one-dimensional polymer nanostructures through its high energy deposition within a limited cylindrical area along the path, *i.e.*, an ion track. Crosslinking reactions occur in the ion track, yielding a nanowire by subsequent development to remove the non-crosslinked parts, while degradation reactions occur to afford a straight nanopore after preferential dissolution of the ion track. We have recently developed a variety of new nanomaterials [4-6] such as cation-exchange membranes (CEMs), blackbody materials, and catalyst supports.

Nanostructure-controlled CEMs were prepared by ion-track grafting for applications to thermochemical water-splitting iodine-sulfur (IS) process for H_2 production. The IS process requires the electrochemical membrane Bunsen reaction at lower overpotentials. Most of the reactions have been carried out so far at room temperature using a commercially-available Nafion membrane and non-porous metallic-plate anode.

The CEM at an ion exchange capacity of 2.9 mmol/g was tested for the membrane Bunsen reaction under the conditions of various anode materials and temperatures. A testing electrolysis cell had an aqueous solution of SO_2 and H_2SO_4 as the anolyte and an aqueous solution of HI and I_2 as the catholyte. The cell voltage was recorded in the current-density range of 0 to 200 mA/cm^2 and theoretically analyzed by curve fitting. This enabled us to estimate the ohmic overpotential, V_{ohmic}, mainly associated with the proton transport in the CEM and activation overpotential of the anodic oxidation, V_{anodic}.

We found that the porous Au anode and a reaction temperature of 50 ºC gave the lowest overpotential. Figure 1 shows V_{ohmic} and V_{anodic} achieved in this study. Importantly, the V_{ohmic} value was about 1/4 that of the conventional membrane Bunsen reaction. This would be because our CEM possessed the lowest resistivity of 5.5 Ω cm, which corresponds to only 45% that of the conventional Nafion 212 membrane.

References

[1] A. Idesaki *et al.*, Quantum Beam Sci. **4**, 11 (2020).

[2] T. Kimata *et al.*, Radiat. Eff. Defects Solids **175**, 433 (2020).

[3] H. Okazaki *et al.*, J. Chem. Phys. **152**, 124708 (2020).

[4] S. Sawada *et al.*, Int. J. Hydrogen Energy **45**, 13814 (2020).

[5] A. Amemiya *et al.*, J. Mater. Chem. C **7**, 5418 (2019).

[6] S. Yamamoto *et al.*, Quantum Beam Sci. **4**, 8 (2020).

Table 1
The position, areal intensity of peaks A and F, and areal-intensity ratio (F/A).

	peak A		peak F		areal-intensity ratio (F/A)
	position (eV)	areal intensity	position (eV)	areal intensity	
Pt/HOPG	284.97	0.306	283.81	0.233	0.761
Pt/irradiated HOPG	285.00	0.212	283.93	0.254	1.20

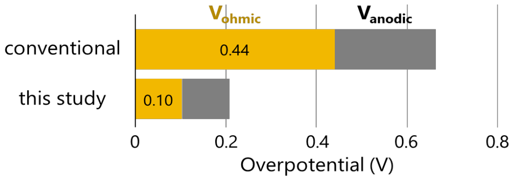

Fig. 1. V_{ohmic} and V_{anodic} for the membrane Bunsen reaction using the new CEM in this study, compared with those for the conventional reaction.

P1-3 Project “Positron Nanoscience”

Leader: Atsuo Kawasuso

The aim of this project is to reveal the novel phenomena related to “spin” in solids using our original spin-polarized positron beam technologies. So far, we have been constructing the spin-polarized surface positronium spectroscopy that is substantially useful for detecting spin-polarization at the first surface layer and the spin-polarized positron annihilation spectroscopy in strong magnetic field for detecting vacancy-induced magnetism. To establish the foundation of the above spectroscopies, deep understanding of positron and positronium elementary processes is also indispensable. We thus pursue such a basic aspect of positron physics, too. In this report, we pick up two achievements in the last fiscal year (2019); one is the magnetic insulation of graphene from substrate $Co_2FeGa_{0.5}Ge_{0.5}$ revealed by spin-polarized positronium spectroscopy and one is the vacancy spin polarization in Gd-implanted GaN studied by spin-polarized positron annihilation spectroscopy.

Magnetic insulation of graphene from CFGG studied by spin-polarized positronium spectroscopy [1]

Following previous work on graphene on Ni(111) and Co(0001) surfaces [Phys. Rev. B **97**, 195405 (2018)], the spin polarization of graphene on a $Co_2FeGa_{0.5}Ge_{0.5}$ (CFGG) (001) surface was examined using spin-polarized surface positronium spectroscopy. The graphene was found to be magnetically insulated from the CFGG(001) even after heat treatment, which increased the spin polarizations of graphene on Ni(111) and Co(0001). First-principles calculations indicated that graphene is weakly bound to the CFGG(001) surface mainly through the van der Waals interaction, and consequently the interlayer distance between graphene and the CFGG(001) surface is greater (~3 Å) than that between graphene and Ni(111) or Co(0001) (~2 Å). The weak hybridization between graphene and CFGG(001) sufficiently reduces the spin polarization in graphene, which enables the magnetic insulation of graphene from CFGG.

The extremely high carrier mobility and long spin diffusion length in graphene mean that graphene and ferromagnet heterostructures are receiving extensive research interest in the contexts of spintronic device applications and solid-state physics.

Spin-polarized carriers are induced into graphene in two ways. One is to magnetize the graphene itself through the magnetic proximity effect. Previous work has shown that graphene on Co(0001) and Ni(111) can be magnetized sufficiently because of the strong hybridization at the interfaces. The other way is to inject excess spins from a ferromagnet into graphene under an electric bias. In such a vertical spin valve configuration, the graphene middle layer should be magnetically insulated from the ferromagnet; that is, the hybridization between the graphene and the ferromagnet must be suppressed. As a candidate ferromagnet, the half-metallic Heusler alloy CFGG has been proposed recently. Confirming the magnetic insulation of graphene from CFGG requires the surface spin polarization of graphene-CFGG to be measured, which to the best of our knowledge has not been done until now.

In this work, we used spin-polarized surface positronium spectroscopy because it is guaranteed to detect the electron spin polarization of the first surface layer. The results show that the surface spin polarization of graphene-CFGG(001) is below the detection limit, and also that a relatively large interlayer spacing forms at the interface. First-principles calculations confirm that these results originate from the weak hybridization between graphene and the CFGG(001) surface.

Gadolinium-implanted GaN studied by spin-polarized positron annihilation spectroscopy [2]

Gd ion implantation and annealing were performed at 900 ºC for nominally undoped wurtzite GaN grown by metal-organic chemical vapor deposition. Spin-polarized positron annihilation measurements showed that vacancy clusters including at least 12 vacancies per cluster were the major positron-trapping centers and that the electrons in the vacancy clusters were spin-polarized. These observations could be explained by first-principles calculations. The previous speculation about the defect-assisted ferromagnetism of Gd-implanted GaN may be supported if vacancy clusters are considered.

The synthesis of dilute magnetic semiconductors is a key technology toward semiconductor spintronics. A successful dilute magnetic semiconductor is Mn-doped p-type GaAs and InAs with a Curie temperature of 180 K. It was predicted theoretically that doping Mn into GaN and ZnO will result in a high Curie temperature due to a high hole concentration of 10^{20} cm^{-3}. However, Mn-doping into GaN seems to be very problematic due to the formation of secondary phases. Meanwhile, the room-temperature ferromagnetism of Gd-doped GaN grown by molecular beam epitaxy was demonstrated. Several groups also reported colossal ferromagnetism in GaN:Gd. Here, “colossal” ferromagnetism means that the magnetization per an introduced Gd atom far exceeds $7\mu_B$, which is the intrinsic magnetization of a Gd atom.

However, the hard X-ray absorption spectroscopy studies showed that Gd atoms are only paramagnetic and the spin polarization of Ga atoms is almost null. Therefore, some defect species and oxygen impurities are thought to give rise to the magnetic order. Then, it has been proposed that single Ga vacancies and Ga vacancy-oxygen complexes are the source of ferromagnetism: an electrically neutral Ga vacancy has a magnetic moment of $3\mu_B$, and multiple moments can be coupled ferromagnetically with those of Gd atoms. So far, this hypothesis has not yet been confirmed.

In this study, we used spin-polarized positron annihilation spectroscopy to investigate Gd-implanted GaN. We found that instead of single Ga vacancies, vacancy clusters including at least 12 vacancies per cluster form during post-implantation annealing, and the electrons therein are spin-polarized.

References

[1] M. Miyashita *et al.*, Phys. Rev. B **102**, 045425(2020).
[2] M. Maekawa *et al.*, Phys. Rev. B **102**, 054427(2020).

P1-4 Project “Semiconductor Radiation Effects”

Leader : Takeshi Ohshima

Quantum technologies, such as quantum computation, quantum cryptography information and quantum sensing, are key technologies to change our life dramatically. Color centers of which optical and spin properties can be manipulated with high fidelity are expected to be applied to quantum bits (qubits) and quantum sensors. We create color centers in wide bandgap semiconductors such as diamond and silicon carbide (SiC) using ion and electron beams, and investigate their optical and spin properties. In addition, we are studying radiation response of semiconductor materials and devices since understanding these effects is important to develop radiation resistant technologies for space and nuclear applications. {1-20, 21, 22 in Part II}

Creation of triple qubit consisting of Nitrogen-Vacancy (NV) centers in diamond using molecular ions [1]

NV center in diamond is one of the most promising candidates for qubit and quantum sensor since its optical and spin properties can be manipulated at room temperature [2]. To realize quantum computer based on NV center, it is important to develop the creation methods of multiple NVs in which each NV can interact to create the entanglement state. However, for the current technologies, it is quite difficult to fabricate such multiple NVs because the distance between NVs for the entanglement should be tens nano meter or less. Here, we created triple NVs, in which each NV can entangle, using molecular ion beams. In this study, $C_5N_4H_n$ ions with an acceleration energy of 65 keV were implanted into a ^{12}C-enriched (99.95%) high purity diamond at room temperature. Thermal annealing at 1000 °C for 2 hours in forming gas (4% H_2 in Ar) was carried out after implantation to create NVs and reduce radiation damage. The creation of NVs was investigated using confocal fluorescence microscopy (CFM) with an excitation laser at a wavelength of 532 nm at room temperature. Figure 1 shows a schematic drawing triple NVs created by $C_5N_4H_n$ molecular ion implantation. As a result of double electron-electron resonance (DEER) measurements, we confirmed triple NVs with dipole-dipole interactions. This result indicates that the triple NVs can act as a quantum register. From the dipole coupling strength of each NV, the distance between NV_A - NV_B, NV_B - NV_C, and NV_C - NV_A is estimated to be 19.9, 11.5 and 8.8 nm, respectively.

High radiation resistant SiC junction field effect transistors (JFETs) [3]

SiC is expected to be applied to semiconductor devices with extremely high radiation resistance since its excellent physical properties [4]. In this study, we investigated gamma-ray radiation response of JFETs based on hexagonal (4H) SiC. Depletion mode n-channel SiC JFETs with a gate length of 18 or 36 μm were fabricated by National Institute of Advanced Industrial Science and Technology. The SiC JFETs were irradiated with gamma-rays up to 9 MGy at room temperature. The current (*I*) - voltage (*V*) characteristics of the JFETs were measured before and after irradiation. The values of threshold voltage, at which JFETs are turned on, were obtained from the *I* - *V* characteristics. Figure 2 shows threshold voltage shift as a function of gamma-ray dose. No significant change in the threshold voltage for the SiC JFETs is observed even after irradiation at 9 MGy although SiC Metal-Oxide-Semiconductor FETs show large threshold voltage shift (about 5 V at 2.5 MGy [5]). This result indicates that SiC JFETs are operated with high stability up to 9 MGy. Therefore, we can conclude that SiC JFETs are suitable for electronic device used in harsh radiation environments.

References

[1] M. Haruyama *et al.*, Nat. Commun. **10**, 2664 (2019).
[2] A. Gruber, *et al.*, Science **276**, 2012 (1997).
[3] A. Takeyama *et al.*, Mater. Sci. Forum **1004**, 1109 (2020).
[4] P. Friedrichs, *et al.*, Silicon Carbide (Wiley-VCH, Weinheim) Vol. **2** (2010).
[5] T. Ohshima *et al.*, Jpn. J. Appl. Phys. **55**, 01AD01 (2016).

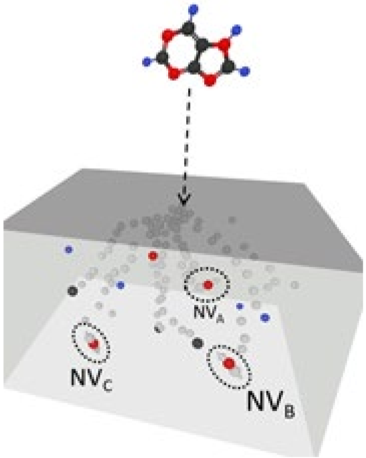

Fig. 1. Schematic drawing of triple NVs created by $C_5N_4H_n$ ions.

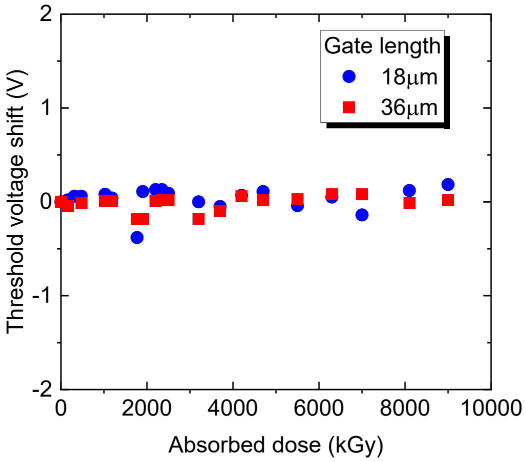

Fig. 2. Shift of threshold voltage for SiC JFETs due to gamma-ray irradiation. Circle and square symbols represent the results obtained from JFETs with gate length of 18 and 36 μm, respectively.

P1-5 Project “Environmental Polymer”

Leader : Noriaki Seko

Project “Environmental Polymer” has been developing the functional polymer fabrics for metal adsorbents by radiation induced graft polymerization technique using such as electron beams and γ-rays. The developed adsorbents can be expected for applications in removing and recovering trace metal ions from water. To development low cost, environmental-friendly and high-performance adsorbents, we started this research from both basic and applied science.

Synthesis of functional polymer fabrics for thorium removal in water [1,2]

A highly functional polymer fabrics for thorium (Th) removal in water were synthesized by ion-imprinting tecnologly and radiation grafting/crosslinking polymerization. As shown in Fig. 1, the phosphoric monomers composed of 2-hydroxyethyl methacrylic phosphoric acid di-ester and mono-ester were ligand exchanged with Th template before the radiaiton grafting. After grafting and crosslinking, a crosslinked Th ion-containing fabrics were obtained. The Th ions in the obtained fabrics were removed by acid. Thus, a novel Th-imprinted fabric adsorbent for Th removal was developed.

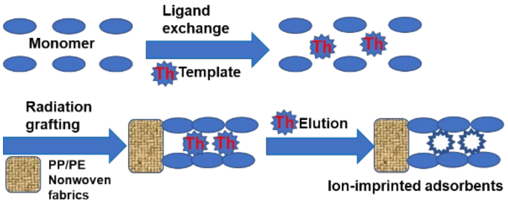

Fig. 1. Schematic iilustration for the preparation of the ion-imprinted adsorbets by the readiation grafting method.

The Th-imprinted adsorbents were tested using the batch adsorption method. It was found that the new adsorbents achieved a maximum distribution coefficient of 3.3 g/L and selectivity ratio (Th(IV)/U(VI)) of 9.5 after 90 min of contact time under acidic conditions. Furthermore, the adsorption kinetics of the adsorbents followed the pseudo-second-order kinetic model for both Th(IV) adsorption and U(VI) adsorption. Therefore, the synthesized fibrous surface Th-imprinted adsorbents is a promising candidate for the selective removal of Th ions from aqueous solution.

Table 1
Process factors for the Box-Behnken surface response modelling.

Factors	levels		
	low	medium	high
Dosage(g)	0.002	0.0035	0.005
Co (mg/L)	1.0	5.5	10
Time (h)	8.0	16	24

On the other hand, we also applied the Box-Begbken response surface modelling to optimize the adsorption conditions. For this purpose, a fibrous adsorbent was synthesized by radiation-induced graft polymerisation with 2-(dimethylamino) ethyl methacrylate (DMAEMA). The grafted substrate was used as an adsorbent to remove Th(IV) ions from water. As shown in Table 1, three factors, adsorbent dosage, initial concentration (Co) and adsorption time, were used for the surface response modelling. The optimization of the adsorption parameters of Th on the adsorbents were performed to ensure an efficient adsorption capacity over the experimental ranges applied. The conventional method of simultaneously investigating multiple factors by vary one factor while keeping others constant is time-consuming and prevents analysis of the interactive effects between factors. In this study, a total of 17 batch adsorption experiments were performed and the assumptions of the analysis of variance were applied to establish a prediction model for each response. The results indicated a good agreement between the model and experimental data. For example, the quadratic model for the prepared adsorbents showed an optimal adsorption capacity of 25.1 mg/g operating at an initial concentration of 5.5 ppm, reaction time of 24 h, and adsorbent dosage of 0.002 g (50 ml of solution) at a maximum desirability value of 1. Under these adsorption conditions, the experimental adsorption capacity of 24.9 mg/g was achieved, indicating that a good agreement with the predicted value. The results indicate that the response surface modelling is a good method for finding the optimized adsorption conditions and the prepared adsorbents are economically promising materials for the separation of Th(IV) ions.

Crown ether functionalized adsorbents prepared by combination of radiation grafting and the Kabachnik-Fields reaction [3]

We prepared a crown ether-functionalized adsorbent by radiation grafting and the subsequent Kabachnik-Fields reaction (Fig. 2). Due to the facile tethering of crown ethers on the surfaces, host–guest events occurred on the surface of ETFE films. It is expected that the proposed crown ether attachment protocol will result in the tethering of unique host molecules onto materials’ surfaces, and can capture not only ammonium guests, but also a wide range of metal cations selectively.

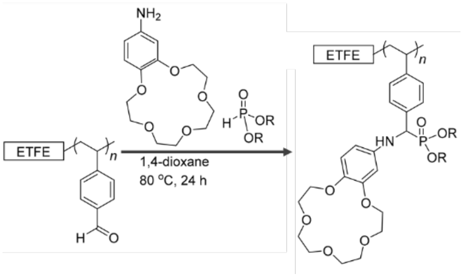

Fig. 2. Schematic illustration for the introduction of crown ether groups onto the vinylbenzaldehyde-grafted ETFE films by Kabachnik–Fields reaction.

References

[1] N.A.F. Othman *et al.*, Polym. Bull. **78**, 165 (2021).
[2] N.A.F. Othman *et al.*, Desalin. Water Treat. **179**, 172 (2020).
[3] M. Omichi *et al.*, Polymers **11**, 1337 (2019).

P1-6 Project “Biocompatible Materials”

Leader : Mitsumasa Taguchi

Project “Biocompatible Materials Research” has been developing the functional biocompatible materials based on the radiation-induced crosslinking technique. The obtained materials can be utilized for the bio-devices in diagnostic, treatment and regenerative medicine {1-28 in Part II}.

A simple method for production of multi-layer 3D integrated polydimethylsiloxane microfluidic chips [1]

Polydimethylsiloxane (PDMS) is most commonly used as a base material in microfluidic chips, particularly for proof-of-concept purposes in the academic community. PDMS has properties analogous to glass, such as biological inertness and optical transparency, while additionally enabling the quick and easy fabrication of devices at low cost. However, for mass production of the devices and for practical applications, particularly in diagnostics and drug development, it is necessary to overcome PDMS’s two major drawbacks: its hydrophobicity and the lack of a practical method for bonding PDMS layers.

Flat PDMS substrates were prepared by pouring a mixture of the respective precursor and curing agent (10:1 by weight) in a Si mold and heating on a hot plate at 150 °C in ambient air for 10 min. The cured substrates were then peeled from the molds. PDMS samples were irradiated by an electron beam (EB) or ^{60}Co γ-rays supplied from Irradiation Facilities of Takasaki Advanced Radiation Research Institute, QST. We put the samples in polyethylene terephthalate (PET)-based sterilization bags (KAPOLA γ, Meiwa Pax Co., Ltd.) or simply inserted PET films between the samples to prevent the bonding between the samples. The energy, beam current, and dose rate for the EB were 1 MeV, 1 mA, and 1.16 J/(g s) (J/g = kGy), respectively. The dose rate of γ-rays was 2.5×10^{-3} J/(g s). Both EB and γ-ray irradiations were conducted in ambient air at room temperature (~20 °C).

EB or γ-ray irradiation alone was apparently sufficient to cause the PDMS substrates to lose their original deformability in accordance with the irradiation dose and become rigid instead. The transmittance of PDMS substrate was almost unaffected in the range of visible light (wavelength: 400–900 nm) and remained above 90%, which is suitable for microfluidic devices. In addition to the hardening effect, hydrophilization of the PDMS was produced by both EB and γ-ray irradiation. The resultant water contact angles (WCAs) of the PDMS substrates decreased from the original values (> 110°) in accordance with the irradiation dose as shown in Fig. 1. Most importantly, the WCAs of EB- and γ-ray-irradiated PDMS substrates were unchanged even after storage for more than 80 days in ambient air at room temperature (~20 °C); this contrasts with hydrophilization using plasma, which suffers from the recovery of hydrophobicity in mere minutes. This result supports our perspective that the thickness of the hydrophilized layer is a key factor in prolonging hydrophilicity because it can hinder the reorientation of nonpolar groups from the bulk to the surface [2]. Both the EB and the γ-rays penetrate completely through the PDMS substrates and change the bulk into hydrophilic materials; thus, the hydrophobicity cannot be recovered.

Both EBs and γ-rays irreversibly bonded PDMS substrates when they are stacked before irradiation in addition to simultaneously inducing various modifications. Using these salient effects, we produced 3D integrated microfluidic chips (Fig. 2). For this, six PDMS layers (five microfluidic devices and a flat cover) were stacked and then irradiated by a 2 MeV EB. By the flow of blue and yellow food dyes introduced through the inlets, it was clearly shown that our method enabled leak-proof multi-layer bonding between the six layers. The blue and yellow solutions flowed individually from the first to the fourth layer via the various microchannels and chambers and then mixed in the fifth layer. The mixed solution (green) flowed from the fifth layer to the outlet in the first layer as planned. The multi-layer-bonded chip was functioned successfully as a 3D integrated chip.

References

[1] T. G. Oyama *et al.*, Lab Chip **20**, 2354 (2020).
[2] T. G. Oyama *et al.*, Appl. Phys. Lett. **112**, 213704 (2018).

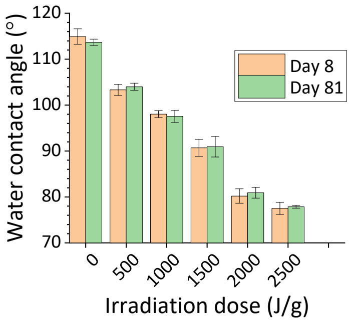

Fig. 1. Water contact angles of PDMS after irradiation by 1 MeV EB vs. those after storage for 81 days in ambient conditions.

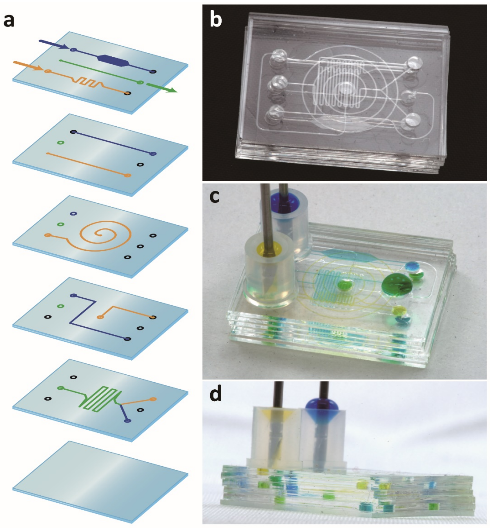

Fig. 2. 3D integrated microfluidic chip produced by 2 MeV EB irradiation. (a) Six stacked layers (five PDMS microfluidic devices and a cover) were (b) irreversibly bonded by EB irradiation, and (c, d) blue and yellow dyes flowed through them three-dimensionally as planned.

P1-7 Project “Spintronics in Two-dimensional Materials”

Leader : Seiji Sakai

Our project aims at developing novel quantum electronics and spintronics techniques for future information technology by taking advantages of the low dimensionality and quantum electronic properties of two-dimensional materials and related heterostructures. The advanced quantum beam techniques of QST and of our research group allow us to investigate and design the local atomic structures and spin-related electronic properties in low-dimensional material systems above the technological limits in nanomaterials science so far.

Novel heterostrucure of graphene and Heusler alloy for the next generation spintronic memories [1]

Graphene-based vertical spin-valves composed of a heterostructure of highly conductive graphene with a long spin life time and ferromagnets with high spin-polarization are expected to offer a large magnetoresistance effect without impairing the electrical conductivity, which could pave the way for next generation of memory technologies with extremely high recording density and low power consumption.

In this year, we demonstrated a key step in development of graphene/ferromagnet heterostructures [1]. A novel heterostructure consisting of graphene and a half-metallic Heusler alloy $Co_2Fe(Ge_{0.5}Ga_{0.5})$ (CFGG), ideally with 100% spin polarization, was successfully fabricated, and its promising properties for spintronic applications were revealed through the depth-resolved x-ray magnetic circular dichroism (XMCD) spectroscopy using synchrotron radiation.

The heterostructure of single-layer graphene (SLG) and half-metallic $Co_2Fe(Ge_{0.5}Ga_{0.5})$ (CFGG) Heusler alloy ferromagnet were synthesized by performing the CFGG deposition by magnetron sputtering and the graphene growth by chemical vapor deposition under *in situ* conditions. Figure 1 shows the optical microscopy images of graphene grown on the CFGG(001) thin film. High-quality SLG with complete coverage on the CFGG surface was obtained under the optimized growth condition.

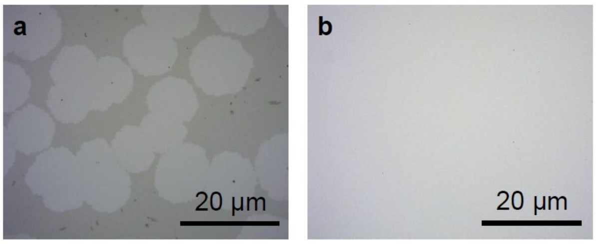

Fig. 1. Optical microscope images of the SLG/CFGG samples of (a) partial and (b) complete SLG coverage on the CFGG surface obtained without and with optimizing the growth condition, respectively. The areas of bright and dark contrast are the SLG covered and bare CFGG region, respectively.

Figure 2a shows the XAS and XMCD spectra of the SLG/CFGG(001) heterostructure at the Co $L_{2,3}$-edges. The spectra were obtained in the non-depth-resolved measurement mode with a large mean probing depth (λ_p) of $\lambda_p = \sim 50$ Å, which corresponds to the bulk region of the CFGG thin film away from the SLG/CFGG interface, and in the depth-resolved measurement mode at $\lambda_p = \sim 4$ Å, which corresponds to the region adjacent to the interface.

The spectroscopic features in the non-depth-resolved and depth-resolved XAS spectrum ($\lambda_p = \sim 50$ Å and ~4 Å, respectively) are compatible with each other, and no signs of degradation such as oxide and carbide formation are observed in each spectrum. The probing depth-dependent changes of the magnetic moments per Co atom; the total magnetic moment (m_{total}) and their spin and orbital components (m_{spin} and m_{orb}, respectively), evaluated from the depth-resolved XMCD spectra at different mean-probing depths are summarized in Fig. 2b, which demonstrates how the magnetic moments change with depth in the region near the interface. The consistent results were also obtained from the data at the Fe $L_{2,3}$-edges (not shown).

It was found that CFGG shows a small decrease in the spin magnetic moment m_{spin} by ~10% from that in the bulk region as the probed region approaches to the interface with decreasing λ_p. A noticeable increase in the orbital magnetic moments m_{orb} was also found at the smallest depth ($\lambda_p = \sim 4$ Å), corresponding to the interfacial region. The preservation of the large magnetic moment over the whole depth range is responsible for the fact that the high chemical ordering ($L2_1$ ordering) in the CFGG lattice is kept even in the vicinity of the interface due to the absence of strong chemical interactions between graphene and CFGG different from other SLG/ferromagnet (Fe, Ni) heterostructures. The m_{orb} increase just below the interface can be attributed to the orbital rearrangement in the atomic layer terminating CFGG at the interface. Theoretical calculations further demonstrated that the inherent two-dimensional electronic system of graphene and the half-metallic property of CFGG are well-preserved in the SLG/CFGG heterostructure and at its interface.

These results suggest that the SLG/CFGG heterostructure could show distinctive advantages over other graphene/ferromagnet heterostructures for realizing high-performance spintronic memory devices.

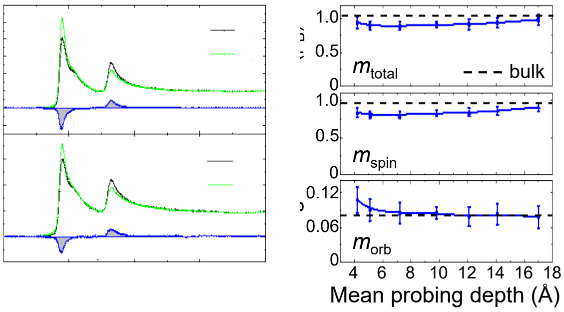

Fig. 2. (a) Co $L_{2,3}$-edge XAS and XMCD spectra in the non-depth-resolved mode ($\lambda_p = \sim 50$ Å) and depth-resolved mode ($\lambda_p = \sim 4$ Å). (b) Plots of the total magnetic moment (m_{total}) of Co and its spin and orbital components (m_{spin} and m_{orb}, respectively) vs. the mean probing depth (λ_p). In (a), the XAS data μ_+ and μ_- were obtained in remanence after applying a magnetic field parallelly and antiparallelly to the photon helicity vector, respectively. The dashed lines in (b) represent the magnetic moments in the bulk region obtained in the non-depth-resolved mode ($\lambda_p = \sim 50$ Å).

Reference

[1] S. Li *et al.*, Adv. Mater. **32**, 1905734 (2020).

P1-8 Project “EUV Ultra-fine Fabrication”

Chief : Hiroki Yamamoto

Project “EUV Ultra-fine Fabrication” has been developing the functional polymer materials such as high performance resist materials for extreme ultraviolet (EUV) and next generation EUV lithography. We have synthesized resist materials such as metal resist and block copolymer with chemical synthesis or by using quantum beams such as γ-rays and electron beam (EB). We aim to develop resist materials for EUV lithography and conduct fusion between top-down and bottom-up nanofabrication for next generation EUV lithography. We report herein two recent study: study on chemical reactions induced by the short pulse EUV in resist materials and study on fusion between top-down and bottom-up nanofabrication.

Elucidation of physical events and chemical reactions induced by the short-pulse EUV in resist materials [1]

Short-pulse EUV of a free-electron laser (FEL) is the most potential candidate as a next-generation EUV lithography light source. An X-ray laser (XRL) is suitable for the evaluation of resist materials in next-generation EUV lithography because of its short pulse width (7 ps) and high intensity (approximately 200 nJ/pulse at a maximum). However, reactions in the resist materials that are induced by the short-pulse EUV of FEL have not yet been elucidated.

In order to elucidate reactions in resist materials, that are induced by the short-pulse EUV of FEL, we investigated the morphological and chemical changes in poly(methyl methacrylate) (PMMA) induced by picosecond-pulsed EUV using XRL. To avoid ablation in PMMA, the XRL pulse energy should be attenuated less than 3–4 mJ cm^2 pulse.

Figure 1 represents residual film thickness as a function of exposure dose of PMMA sample developed after irradiation with XRL pulse. We clarified the sensitivity of PMMA measured for XRL irradiation requires a much smaller dose (2 mJ/cm^2). The obtained sensitivity for picosecond EUV irradiation was approximately 50 times higher than that for typical EUV irradiation. X-ray photoelectron spectroscopy (XPS) studies of PMMA revealed the unique main-chain and side chain decomposition after XRL irradiation. This decomposition-dominant reaction and the resultant high sensitivity of PMMA for XRL irradiation occur only for relatively high doses deposited by a picosecond EUV pulse. These result suggest the importance of a specific resist design policy for next generation EUV lithography.

Fusion between top-down and bottom-up nanofabrication for next generation lithography [2]

With further miniaturization of devices, sub-10 nm feature sizes are anticipated, which will not easily be obtained by EUV or EB lithography techniques in mass production, due to patterning limitations, tool costs, or low throughput and so on. Recently, directed self-assembly (DSA) of block copolymers has attracted significant attention as a promising nanolithography technique to surmount the fundamental limitations of conventional lithography. However, current methods for achieving DSA are generally complex, involving a large number of steps and a number of challenges remain with current approaches.

In order to simplify a number of processes in current DSA, we investigated lamellar orientation of polystyrene-*block*-poly(methyl methacrylate) (PS-*b*-PMMA) block copolymer by using a directly chemically patternable self-assemble monolayer (SAM). Figure 2 shows SEM image of PMMA etched lamellar PS-*b*-PMMA block copolymer on Au coated silicon substrates pre-coated with SAM. We demonstrated that lamellar orientation of PS-*b*-PMMA block copolymer could be performed using the change in the polarity of different regions of 6-(4-nitrophenoxy) hexane-1-thiol SAM, which is the conversion of the NO_2 group to an NH_2 group induced by EB. Also, we found that the vertical state persists only for appropriate irradiation dose and annealing temperature by examining the lamellar orientation of PS-*b*-PMMA. Our method has the potential to greatly simplify block copolymer directed self-assembly (DSA) processes as compared to the multi-step guiding layer fabrication procedures currently used.

References

[1] Y. Hosaka *et al.*, Appl. Phys. Lett. **115**, 073109 (2019).

[2] H. Yamamoto *et al.*, Quantum Beam Sci. **4**, 19 (2020).

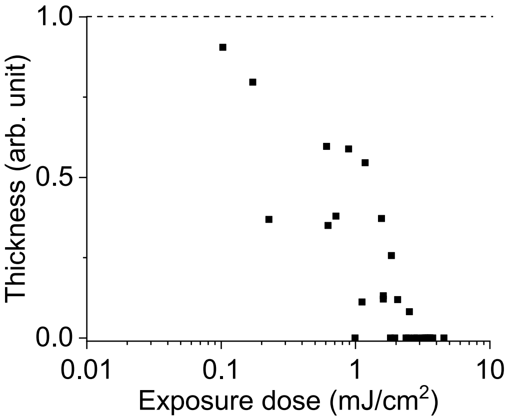

Fig. 1. Residual thickness as a function of exposure dose of 62 nm thick PMMA sample developed after irradiation with XRL pulse (pulse width: 7 ps, wavelength: 13.9 nm).

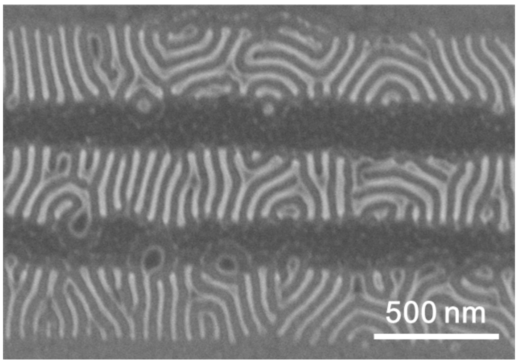

Fig. 2. SEM images of PMMA etched lamellar PS-*b*-PMMA block copolymer on Au deposited silicon substrates pre-coated with SAM. The widths of alternating stripes of SAM were 300 nm.

P1-9 Project “Element Separation and Analysis”

Leader: Hironori Ohba

Quantum beams are versatile sources for materials processing. Our project explores the basic process of the laser-matter interaction to separate elements from industrial waste liquid and performs synthesis of novel nanomaterials by ion or electron irradiation {1-31 in Part II}. Furthermore, we have been developed techniques for analyzing elements using laser-induced plasma spectroscopy under harsh environments {1-32 in Part II}. For the element separation research, we applied the separation using a laser-induced particle formation technique for the recovery of precious metals from a mixed solution. The recent result of metal recovery is introduced as follows.

Photoinduced gold recovery mediated by isopolymolybdate in strongly acidic HCl/NaCl solutions [1]

The separation using laser-induced particle formation is a novel technique to separate precious metals, PMs (PM=Au, Pt, Pd, and so on), from industrial wastewater [2]. In this technique, the separation is performed by irradiation of a pulsed ultraviolet (UV) laser to the wastewater, which leads to photo-reduction of the PM^{n+} ions into PM^0 neutrals, because the energy of the UV laser (> 3.5 eV) is well beyond reduction potential of PMs (for example, the standard electrode potential of the reduction $Pd^{2+} + 2e^- \rightarrow Pd(s)$ is +0.987 V). The PM^0 neutrals spontaneously form metal-particles, which is recovered by filtration. The energy of the UV laser that needs to reduce the PM^{n+} ions is correlated with the reduction potential of the PMs. Thus, by arranging the energy of the UV laser, we can select the PM species that is recovered by the laser-induced particle formation.

The laser-induced formation of gold nanoparticles (AuNPs) was studied in hydrochloric acid solutions containing isopolymolybdate. Aqueous solutions of $HAuCl_4$ (0.5 mM) in HCl (0.1–1.0 M)/NaCl media containing ethanol (0.5% v/v) were irradiated with 355 nm laser pulses (20 mJ/pulse energy, 10Hz repetition rate, 12 ns duration) in the absence or presence of molybdate. The reaction progress was probed by UV–vis spectroscopy.

Without molybdate, the formation of AuNPs is significantly hindered because a large excess of Cl renders the $AuCl_4$ precursor resistant to direct photoreduction with ethanol. When the aqueous ethanol (0.5% v/v) solution of $HAuCl_4$ (0.5 mM) that did not contain any additional acid or salt was irradiated with the laser, the formation of AuNPs was observed clearly by the emergence of an intense the surface plasmon resonance (SPR) photoabsorption at 530 nm (broken blue line in Fig. 1(a)), resulting in a solution color change from light yellow to dark red. In contrast, only a faint SPR band appeared upon irradiation of the aqueous ethanol (0.5% v/v) solution of $HAuCl_4$ in HCl (0.1 M)/ NaCl (0.9 M) (red line in Fig. 1(a)), which demonstrated the severe retardation of AuNP formation in the strongly acidic chloride medium.

The incorporation of molybdate into solution effectively mediates the photoinduced formation of AuNPs in 0.1–0.5 M HCl. For this range of acidity, photoirradiation generates the molybdenum blue (MB) species from the reaction of photoexcited $Mo_{36}O_{112}^{8-}$ (polyoxoanions) with ethanol, followed by the reduction of $AuCl_4$ with the MB species. Figure 1(b) shows the time evolution of the absorption spectra of the sample solution (0.1 M HCl) in which $AuCl_4^-$ and $Mo_{36}O_{112}^{8-}$ coexist. Upon photoirradiation, the MB band first emerged at 780 nm; then, the SPR band appeared at 540 nm. The growth of the SPR band is faster in the presence of molybdate (Fig. 1(b)) than in the absence (Fig. 1(a)), indicating that the addition of molybdate facilitates the AuNP formation. At a higher acidity, the formation of AuNPs is virtually undetectable because the MB species are no longer generated due to the absence of anionic molybdate precursors. Figure 2 shows the selected TEM image of AuNPs prepared in this study. The average diameters of the large NPs (> 10 nm) were determined as 154 ± 70 and 140 ± 61 nm for the solutions in 0.1 M HCl and 0.5 M HCl. The sizes of AuNPs were obtained with over 150 particles counted from the several TEM images.

References

[1] R. Nakanishi, *et al.*, J. Photochem. Photobiol. A **383**, 111994 (2019).

[2] M. Saeki *et al.*, J. Photochem. Photobiol. A **299**, 189 (2015)

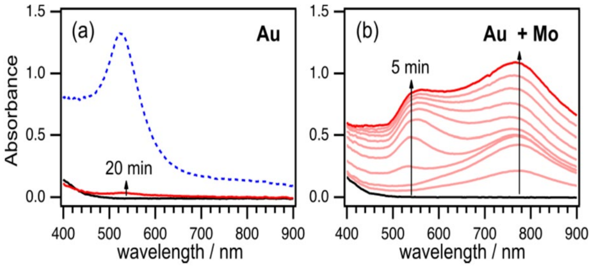

Fig. 1. Time evolutions of UV–vis spectra during photoirradiation with a 355 nm laser. (a) $HAuCl_4$ (0.5 mM) and (b) $HAuCl_4$ (0.5 mM)/Mo(VI) (20 mM) in HCl (0.1 M) /NaCl (0.9 M)/ethanol (0.5% v/v). The irradiation time is given in each panel. Black curves represent the spectra before irradiation. The broken blue curve in panel(a) shows the spectrum obtained after 20 min irradiation of $HAuCl_4$ in aqueous ethanol (0.5% v/v) solution without any other acid or salt added.

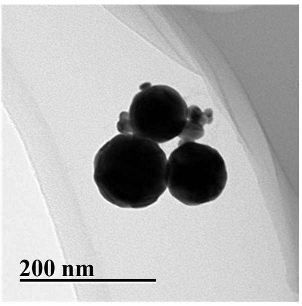

Fig. 2. TEM image of AuNPs formed by 5 min of photo irradiation of $HAuCl_4$ (0.5 mM)/Mo(VI) (20 mM) in HCl (0.5 M)/NaCl (0.5 M)/ ethanol (0.5% v/v) solution.

P1-10 Advanced Functional Polymer Materials Research Group

Leader : Yasunari Maekawa

The research of “Advanced Functional Polymer Materials Group” has been focused on efficient development technique for advanced functional polymer materials, which are widely used in advanced devices and construction materials. The technique includes materials informatics such as machine learning and neural network in addition to the established radiation techniques regarding to the radiation-induced graft polymerization and the X-ray/neutron structural analysis. This group has been conducting mainly the R&D for “Advanced functional polymer materials alliance” under QST innovation hub program in collaboration with participant companies [1].

Research results of “Advanced functional polymer materials alliance”

On the alliance project of the 3rd year, main achievements in four research subjects are as follows.

(1) Graft-polymerizability prediction: We are preparing functional polymer materials by the radiation-induced graft polymerization of 47 kinds of methacrylate monomers on polyethylene nonwoven fabric, and trying to construct the data-set composed of the various physical values with respect to the chemical structure and electronic state of the monomers as well as the obtained grafting degrees. As a result of linear multiple regression analysis with the grafting degree as the objective variable, it was found that the introduction of the explanatory variable related to the electronic state is an important factor in improving the prediction accuracy.

(2) Structural data accumulation: We analyzed the hierarchical structures of the proton- and anion-conducting electrolyte membranes (PEM and AEM) using quantum beam facilities such as small angle X-ray/neutron scattering. PEMs based on poly(ethylene-co-tetrafluoroethylene) (ETFE-PEM) were digitalized from the simulated structures obtained by dynamics simulation to estimate the size of the hydrophilic/hydrophobic phase and ion-channel as an ion transport region.

(3) Property prediction: We evaluated the properties of the PEMs, such as ion conductivity and water uptake, using machine learning. 12 physical and chemical values of the base polymers of PEMs were selected as an explanatory variable. By using a random forest method [2], the ion conductivity and water uptake of the PEMs could be estimated with favorable accuracy. The importance of each explanatory variable for the property prediction was clarified.

(4) Database preparation: To improve the database for materials informatics of the grafted polymers, a collection of the papers concerning the grafted polymers were continuously performed. The data for the database were efficiently extracted and collected using text mining tools as well as a developed data extractor.

Development of a simplified radiation-induced graft polymerization method [3]

We have reported the preparations of functional nonwoven fabrics by the radiation-induced emulsion graft polymerization and their properties. In general, the graft polymerization to the irradiated nonwoven fabrics is carried out under nitrogen atmosphere after nitrogen bubbling to eliminate the dissolved oxygen. However, the nitrogen bubbles that adhere to the surface of the nonwoven fabrics inhibit uniform graft polymerization. Moreover, with lower doses than 10 kGy, it the graft polymerization merely proceeded because of an insufficient elimination of the oxygen. The vacuum degassing to eliminate oxygen is a disadvantage in the emulsion graft polymerization using a surfactant because the monomer solutions foam and then overflow from the reaction vessel occasionally. In this work, we developed a simplified radiation-induced emulsion graft polymerization (SREG) method that involves a convenient and simple degassing process.

Scheme 1 shows a procedure of the SREG. The process is as follows: (1) The pre-irradiated PE/PP fabric was set in a glass jar and the monomer solution was poured. (2) A weight was placed on top of the sealed glass jar after the lid was closed and the jar was put in a vacuum desiccator for degassing. Dissolved oxygen in the monomer solution was eliminated through the small space between the lid and the jar. (3) The desiccator’s vacuum was released, and then the vacuum state was maintained automatically by the pressure difference between the internal and external pressure. (4) The sealed jar was held in a water bath at a constant temperature to perform the graft polymerization. 400 g weight on the lid of the glass jar was chosen based on the relationship between pressure in the vacuum desiccator and the vacuum degassing time. A period of vacuum degassing was enough for 15 min. As a result of the graft polymerization of glycidyl methacrylate to PE/PP fabrics irradiated with a dose range of 5-20 kGy, the grafting degrees increased with the increase of the reaction time as well as the dose. Even at the dose of 5 kGy, the grafting degree had highly reproducibility.

In order to perform a machine learning with favorable accuracy, the data-set composed of reliable experimental data is required. The SREG method would be useful for the efficient collection of the reliable data related to functional graft polymer materials.

References

[1] https://www.qst.go.jp/site/collaboration/1094.html.
[2] L. Breiman, Machine Learning **45**, 5 (2001).
[3] M. Omichi *et al.*, Polymers **11**, 1373 (2019).

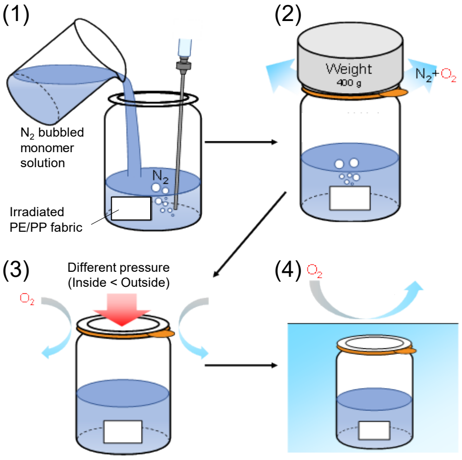

Scheme 1. Schematic image of a simplified radiation-induced emulsion graft polymerization.

P1-11 Quantum Sensing and Information Materials Research Group

Leader : Takeshi Ohshima

Quantum technologies such as quantum sensing, quantum information and quantum computing are indispensable technologies to realize “Society 5.0” and R&D for quantum technologies are intensively carried out all over the world now. We study quantum technologies together with domestic and international Universities and Research Institutes. Recent our research topics are spin defects which act as single photon emitters in wide bandgap semiconductors and a new technology combining spintronics with photonics “Spin-photonics”. In the former topic, we create negatively charged nitrogen-vacancy (NV) centers in diamond and silicon vacancy (V_{Si}) in silicon carbide (SiC) by energetic particle irradiation. We investigate the optical and spin properties of NV center and V_{Si}. We also fabricate electronic devices with such spin defects/single photon emitters to realize quantum devices. In addition, we explore new spin defects in wide bandgap semiconductors. In the later topic, we are proposing new devices in which the interaction between spins and photons is applied to realize extremely low energy consumption devices. The research results that link to this group are also shown in the results obtained by the research projects “semiconductor radiation effects” and “spintronics in 2D materials”

Creation of Nitrogen-Vacancy (NV) centers in SiC using irradiation [1]

Negatively charged nitrogen-vacancy (N_CV_{Si}) center in SiC is known as a single photon emitter at room temperature, and is expected to be applied to a spin qubit and a quantum sensor [2] (Fig. 1). However, the creation methods for N_CV_{Si} have not yet been developed. In this study, we create N_CV_{Si} in N-doped and high purity semi-insulating (HPSI) hexagonal (4H) SiC by ion irradiation and subsequent annealing. Figure 2 shows photoluminescence (PL) spectra obtained from HPSI 4H-SiC irradiated with N ions at 2x10^{14} /cm^2 and subsequently annealed at 1000 °C for 30 min in Ar. PL measurements were caried out at 80 K. For comparison, PL spectra obtained before irradiation (as-received) and after N irradiation but before annealing are also shown in the figure. Sharp PL peaks at wavelength between 1150 and 1250 nm which correspond to PL peaks for N_CV_{Si} (allows in the figure) are observed after annealing although no PL peaks originating from N_CV_{Si} are observed from as-received or irradiated samples, as shown in the figure. The same PL peaks are obtained from N-doped 4H-SiC after irradiation and subsequent annealing (not shown here). Also, it is worth noting that PL originating from N_CV_{Si} can be observed even at room temperature although a broad peak due to phonon side band is obtained without sharp peaks.

Figure 3 shows integrated PL intensity as a function of annealing temperature for N-doped 4H-SiC irradiated with N ions at 2x10^{14} /cm^2. Each annealing was done for 30 min in Ar. The PL measurements were carried out at 80 K, and the wavelength between 1215 and 1235 nm were integrated. The PL intensities are normalized by the value obtained from sample annealed at 1000 °C. The PL intensity increases with increasing annealing temperature up to 1000 °C although it decreases with increasing annealing temperature above 1000 °C. Thus, the highest PL intensity is found at an annealing temperature of 1000 °C. This suggests that N_CV_{Si} can be effectively created in SiC by annealing at 1000 °C.

References

[1] S. -i. Sato *et al.*, J. Appl. Phys. **126**, 083105 (2019).

[2] H. J. Bardeleben, *et al.*, Phys. Rev. B **92**, 064104 (2015).

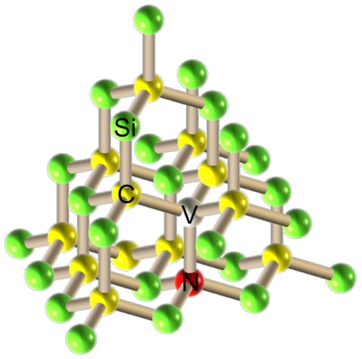

Fig. 1. Schematic diagram of N_CV_{Si} in SiC

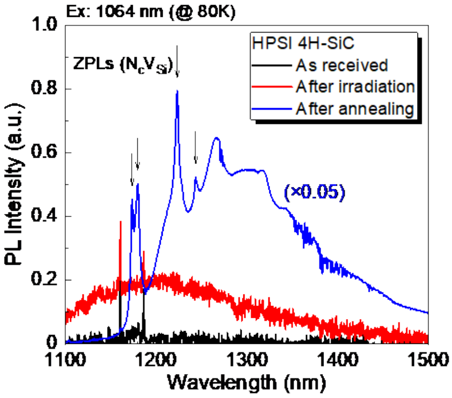

Fig. 2. PL spectra for HPSI 4H-SiC before and after N irradiation and after subsequent annealing. PL spectra was measured at 80 K. The wavelength of excited laser is 1064 nm.

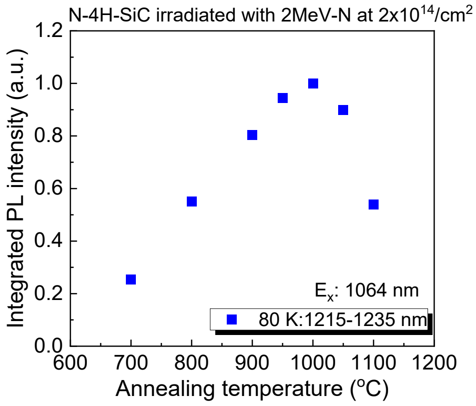

Fig. 3. PL spectra for HPSI 4H-SiC before and after N irradiation and after subsequent annealing. PL spectra was measured at 80 K. The wavelength of excited laser is 1064 nm.

Part Ⅰ

2. Life Science

P2-1 Project “Microbeam Radiation Biology”

Leader : Tomoo Funayama

The Project "Microbeam Radiation Biology" has been developing microbeam irradiation technologies for exploring the radiation response mechanisms of living organisms that has not been able to analyze by conventional irradiation methods.

Elucidating the effects of heavy ion irradiation at the molecular level is important for applying heavy ions to medical, agricultural and radiation safety field. However, heavy ions have a high LET, which results in microdosimetric non-uniform energy deposition in low fluence but biologically effective dose range. Organisms respond differently to radiation depending on their dose and deposited organs. The cellular response also varies with the intracellular structure being irradiated. Therefore, in order to elucidate the exact irradiation effect of heavy ions, it is necessary to obtain information of not only the dose, i.e., the number of irradiated ions, but also the exact location of the ion hitting at microdosimetric level.

The microbeam irradiation that enables target irradiation of a micron scale area of biological samples fulfills these requirements, thus it is a very useful to analyze radiation effects at the elemental dose level, where dose cannot be treated as a continuous value. Two microbeam devices were developed and has been improved at the TIARA cyclotron beamline. One is a collimated microbeam device and the other is a focused microbeam device (Fig. 1).

Updates of collimated microbeam device [1]

The collimated microbeam has been utilized for biological irradiation since 1994. The device can deliver a defined number of ions to the targeted region of biological sample. Size of beam spot ranges from 5 to 250 μm in diameter. Wide range of ion species from carbon to argon with LET from 70 to 1260 keV/μm can be provided for irradiation experiment. We have used this device to perform many irradiation experiments with wide range of biological samples. The samples irradiated have ranged from cultured cells to nematodes, medaka fish, and plant tissues.

In order to satisfy the demands of the various experiments, the device has been continuously improved, including improvements in the cell targeting and post-irradiation observation systems, and the expansion of available ion species. To improve targeting accuracy, a new cell targeting system was developed, which consisted of automatic stages with less than 0.1 μm positioning accuracy, and fully motorized microscope that is able to control all of its functions under PC control. In addition, an off-line observation system that acquires cellular response data by post-irradiation observation was updated with the same high positioning accuracy. The system was equipped with a high-sensitivity camera and dedicated software for live imaging experiment. These improvements have enabled us to efficiently perform experiments on the effects of heavy ion irradiation on various organisms from cells to individuals, and have greatly enriched the quantity and quality of data acquired per experiment.

Establishment of a method for irradiating biological target using focused microbeams [2]

The focused microbeam was developed to overcome the principle limitations of the collimated device to achieve more precise targeting. This device can focus the heavy ions with a diameter less than 1 μm in vacuum using a micro object slit and quadruple quadrupole lenses.

In order to irradiate the precise microbeam to specific intracellular organelle of cultured cells, a cell targeting system consisting of an inverted microscope and a set of high precision automatic stages was installed immediately below the vacuum window of the end station of the device. A CR-39 film was irradiated using the cell targeting system, and the size of the beam spots extracted to the atmosphere was measured. The measurement results confirmed that beam spot of neon ions is enough to target an intracellular region of cells, and a size of carbon-ion beam spot is enough small to irradiate a specific cell of an individual of small model animals such as nematode *C. elegans*.

Subsequently, we developed a sample preparation method to irradiate cultured cells and *C. elegans*, and tried to irradiate them by focused heavy-ion microbeams. The irradiated beams hit the targeted area of the sample, and the dose control was successfully carried out using an ion detector placed directly below the prepared sample. From these results, we concluded that we have established a method for irradiating biological target using focused beams to cells and small model organisms using this focused microbeam device.

To elucidate the biological effects of elemental dose level radiation where the dose cannot be treated as a continuous value, we will continue to develop and improve these microbeam devices.

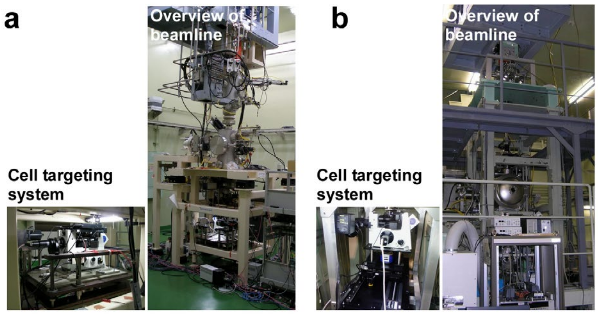

Fig. 1. Overview of heavy-ion microbeam devices of QST-Takasaki [modified figure from reference [1]
a) Collimated heavy-ion microbeam. It uses microaparture for generating microbeam spot. A minimum beam size is ~5 μm, wide range of ion spices (C~Ar), beam size(5~250μm), and LET (70~1260 keV/μm) available for irradiation, and utilized for biological experiment since 1994. b) Focused heavy-ion microbeam. It uses magnetic lens for generating microbeam spot. A minimum beam size is less than 1 μm in vacuum, and developed for rapid and precious targeting of biological samples precisely.

References

[1] T. Funayama, Quantum Beam Sci. **3**, 13 (2019).
[2] T. Funayama *et al.*, Nucl. Instrum. Meth. Phys. Res. B **465**, 101 (2020).

P2-2 Project "Ion Beam Mutagenesis"

Leader : Yutaka Oono

The ultimate goal of our project is to develop applications of quantum beam-based technologies in applied biological fields such as sustainable agriculture or environmental conservation. Ion beams are recognized as useful mutagens for plant and microbe breeding because they are thought to cause mutations via a mechanism distinct from those of chemical mutagens or gamma rays. We have investigated the detailed characteristics of the ion-beam-induced mutations by using specific gene markers or genome-wide sequencing {2-09, 11, and 13 in Part II}. In addition, under collaborations with academic or industrial research organizations, we are aiming to isolate valuable mutants in various organisms such as parasitic plants, plant growth-promoting rhizobacteria, oil-producing algae, sake yeasts, and other bacteria by ion-beam irradiation {2-10, 14, and 17~21}. Uncovering molecular basis of radioresistant organisms is another major business in our project {2-12, 15, and 16}.

Genome analysis of rice ion-beam mutants successfully tracked down candidate genes responsible for phenotypes of the mutants [1]

Rice is one of the most important crops for human beings and one of the major target plants for ion-beam mutagenesis. To understand the characteristics of the ion-beam-induced mutations in rice at the genomic level, we conducted whole-exome sequencing, which is a method analyzing only gene coding region, and analyzed induced mutations in selected rice mutants produced by carbon-ion beam irradiation. DNA libraries were constructed from five mutant rice lines (two dwarf and three early-heading-date mutants) by capturing DNA fragments covering exon region predicted in the genome. A total of 56 mutations were detected in the five mutant rice lines. The average mutation frequency in the M1 generation was calculated to be 2.7 × 10^{-7} per base. The breakdown of the 56 mutations was 24 single-base substitutions (SBSs), 23 deletions (DELs), five insertions (INSs), one inversion (INV), and three replacements. Six mutations were frame-shift or loss-of-exon mutations that are supposed to have high impact on gene function (Table 1). A gene functionally related to the phenotype of the mutant was disrupted by the high-impact mutation in four of the five lines examined, suggesting that whole-exome sequencing of ion-beam-irradiated mutants could facilitate the tracking down of candidate genes responsible for phenotypes of the mutants.

Characterizing genetic effect of different types of radiations, acute/chronic gamma-rays and carbon ions, in plants [2]

Recent availability of genome sequencing enables us to compare the effect of different types of radiations directly at the genomic level. We conducted whole-genome sequencing, characterized the mutations induced by acute and chronic gamma ray irradiation in Arabidopsis, and compared with those previously obtained by carbon ion beam irradiation. Dry seeds were used for irradiation by acute gamma rays and carbon ions, while growing plants of vegetative stage were used for chronic gamma ray-irradiation, which is performed for five successive generations. The result of dry seed irradiations showed that acute gamma irradiation induced a greater number of total mutation events (MEs) than carbon ion irradiation, while no difference was detected between the treatments in the number of MEs altering amino acid (AA) sequences. However, the number of genes with altered AAs in the acute gamma irradiation was smaller than that in the carbon ion irradiation (Fig. 1). This could be due to that the gamma rays predominantly induced SBSs, while carbon ion beam frequently induced DELs (≧2 bp in size). Chronic gamma irradiation (100 – 500 mGy/h) resulted in a higher number of MEs per dose as well as a higher frequency of large deletions than the acute gamma irradiation (Fig. 2). In the very low dose rate of chronic gamma irradiation (~1 mGy/h), the transition/transversion ratio decreased as the dose rate increased, although overall mutation frequency was the same as that in non-irradiated control, suggesting that plants actively respond to the very low dose rates of gamma rays and protect DNA by suppressing occurrence of mutations.

References

[1] Y. Oono *et al.*, Mutat. Res. Fund. Mol. Mech. Mutagen. **821**, 111691 (2020).
[2] Y. Hase *et al.*, Front. Plant Sci. **11**, 336 (2020).

Table 1
Phenotype, number and type of high impact mutation, and candidate gene of the five mutant rice lines.

Line	Phenotype	No. of high impact mutation	Type of high impact mutation	Candidate gene for the phenotype
A	Dwarf Small grains,	1	128-bp DEL	*GPA1*
B	Early heading date Wide leaves Broken flag leaf	3	1-bp DEL × 2 5-bp DEL	*PHYB*
C	Dwarf Culm bending	0		
D	Early heading date	1	33.6-kb DEL	*HD16*
E	Early heading date	1	535-kb INV	*HD1*

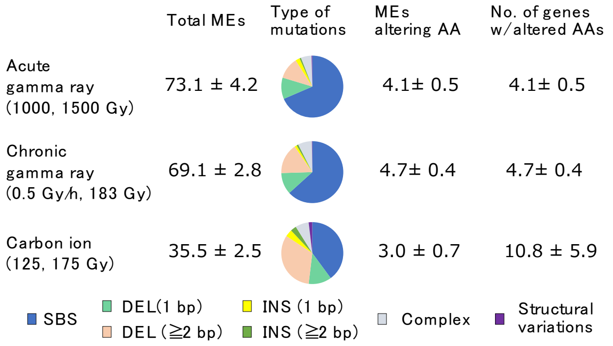

Fig. 1. Comparison of the MEs. The values (mean ± SD) are number of events or genes per plants.

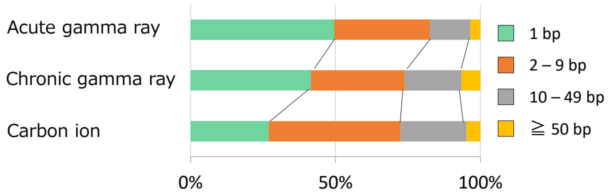

Fig. 2. Comparison of the size of deletions.

P2-3 Project “Medical Radioisotope Application”

Leader : Noriko S. Ishioka

The research objective of our project is to develop the radiopharmaceuticals labeled with useful radioisotopes (RI) for cancer theranostics. Our project focuses on the research of the RI drug delivery system (RI-DDS) using bioactive compounds such as antibodies and peptides in order to make the most of the ability of RI. To achieve our research objective, we also address effective RI production, the molecular mechanisms of radionuclide therapy, and dosimetry. {2-22～24 in Part II}

Novel ^{18}F-labeled α-methyl-phenylalanine derivative with high tumor accumulation and ideal pharmacokinetics for tumor-specific imaging [1]

Positron emission tomography (PET) with amino acid analogs has great impacts on the treatment of cancer by diagnosis, staging, and monitoring. Among them, 3-^{18}F-fluoro-α-methyl-L-tyrosine (^{18}F-FAMT) has been routinely used for tumor diagnosis in Gunma University Hospital. The specific accumulation of ^{18}F-FAMT in malignant tumors is exclusively promoted by L-type amino acid transporter 1 (LAT1), the expression of which is highly upregulated in many types of cancers. However, a major drawback of ^{18}F-FAMT PET is the relatively high frequency of false-negative results because of its low tumor accumulation level. These clinical findings have prompted the further development of ^{18}F-FAMT analogs with higher tumor accumulation and improved pharmacokinetics.

We previously designed and evaluated LAT1-specific ^{76}Br-labeled amino acid derivatives: 2- or 4-^{76}Br-α-methyl-L-phenylalanine (2-^{76}Br-BAMP and 4-^{76}Br-BAMP, respectively) [2]. In comparison with ^{18}F-FAMT, 2-^{76}Br-BAMP showed comparable tumor accumulation and markedly decreased renal accumulation. In contrast, 4-^{76}Br-BAMP showed higher tumor accumulation and extended blood half-life compared with those of ^{18}F-FAMT. These results suggest the potential of ^{18}F-labeled α-methyl-phenylalanine (^{18}F-FAMP) as tumor-specific amino acid tracers. In this study, we prepared ^{18}F-FAMP regioisomers (2-, 3-, or 4-^{18}F-FAMP) and stereoisomers (L- or D-form), and we comprehensively evaluated their potential as tumor-imaging agents (Fig. 1A).

The electrophilic radiofluorination reaction of L- or D-form α-methyl phenylalanine preferentially produced ortho-substituted ^{18}F-FAMP (2-^{18}F-FAMP) in decay-corrected radiochemical yield of 20–30%. The reversed-phase HPLC purification yielded each ^{18}F-FAMP with radiochemical purity >95%. The specific activity of each ^{18}F-FAMP was 2 – 3 MBq/μmol. Among the six ^{18}F-FAMP isomers, L-2-^{18}F-FAMP and the three D-^{18}F-FAMPs showed faster blood clearance and lower renal accumulation than L-3-^{18}F-FAMP or L-4-^{18}F-FAMP in biodistribution studies on normal mice (Fig. 1B). In LS180 human colorectal cancer cell line xenograft mice, L-2-^{18}F-FAMP exhibited significantly higher tumor accumulation than the D-^{18}F-FAMPs or ^{18}F-FAMT (Fig. 1C). The renal accumulation level of L-2-^{18}F-FAMP was significantly lower than that of ^{18}F-FAMT. Cellular uptake of L-2-^{18}F-FAMP was significantly inhibited by LAT1 substrates and LAT1-specific inhibitor, thus, L-2-^{18}F-FAMP would be taken up by tumor cells via LAT1. These results suggest that L-2-^{18}F-FAMP showed the most suitable pharmacokinetics and especially high tumor uptake via LAT1. The PET imaging with L-2-^{18}F-FAMP clearly visualized the tumor as early as 1 h after injection, and the high tumor accumulation level was retained for 3 h (Fig. 1D). These findings suggest the translational potential of L-2-^{18}F-FAMP as a new amino acid tracer. This promising PET tracer will eventually contribute to improvement in diagnostic accuracy for tumor.

References

[1] H. Hanaoka *et al.*, Mol. Pharm. **16**, 3609 (2019).
[2] H. Hanaoka *et al.*, J. Nucl. Med. **56**, 791 (2015).

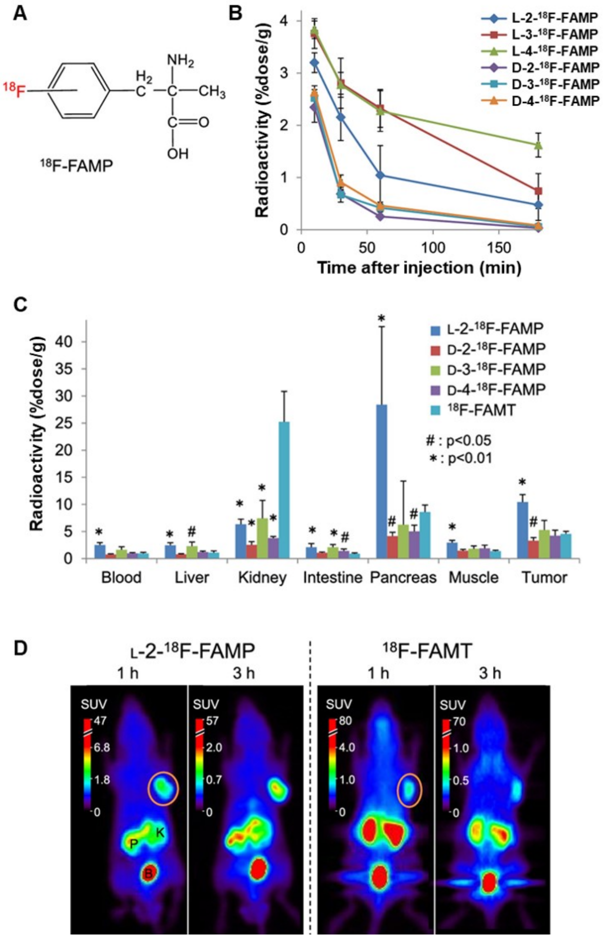

Fig. 1. *In vivo* evaluation of ^{18}F-FAMPs as tumor-imaging agents. (A) Chemical structure of ^{18}F-FAMP. (B) Blood clearance of ^{18}F-FAMPs in normal mice (mean ± SD, N = 4 - 5). (C) Biodistribution of ^{18}F-FAMPs and ^{18}F-FAMT in LS180-bearing mice at 1 h after injection (mean ± SD, N = 4 - 5). A statistically significant difference from ^{18}F-FAMT is indicated by # ($p < 0.05$) and * ($p < 0.01$). (D) PET images of LS180-bearing mice after injection of L-2-^{18}F-FAMP or ^{18}F-FAMT. PET imaging was carried out at indicated time points after injection. The standardized uptake value (SUV) was determined using an Inveon Research Workplace workstation (Siemens). The orange circles show the tumors. B, bladder; K, kidney; P, pancreas.

P2-4 Project “Radiotracer Imaging”

Leader : Naoki Kawachi

The aim of Radiotracer Imaging Research Project is to measure/visualize the radiation sources, and characterize the biological processes of organs, using radioisotopes (RI) and devices such as positron emitting tracer imaging system (PETIS). We will establish the most advanced techniques systematized for live-imaging using radiotracers and these production methods, nuclear imaging apparatus, and kinetic analytical methods for understanding the transport function related to agriculture and medicine within living systems. {2-25~30 in Part II}.

Development of an imaging device for secondary electron bremsstrahlung X-ray emitted during carbon-ion irradiation [1]

Imaging method of the therapeutic carbon-ion beams measuring secondary electron bremsstrahlung (SEB) emitted during beam irradiation is a promising method for range estimation. However, it is unclear whether the method can be used with clinical dose levels and whether the SEB X-rays from the deeper part of the body can be detected. To clarify these issues, we developed a new high resolution X-ray camera and perfomed an experiment of imaging of the beam trajectories in a rectangular-shaped water phantom measuring SEB X-rays during the irradiation of carbon-ions among different injection energies and intensities (Fig. 1(a)). In the experiment, we also tried to acquire the SEB X-ray images with an X-ray camera using a human-head-sized, 17 cm-diameter cylindrical phantom. We used 20×20×0.5 mm-thick cerium-doped yttrium aluminum perovskite, YA1O3 (YAP(Ce)) scintillator plate, which was optically coupled to a 25 mm square high quantum efficiency (HQE) type position sensitive photomultiplier tube (PSPMT) in order to realize a high resolution imaging detector for low-energy X-rays. The imaging detector was encased in a 2 cm thick tungsten container having a pinhole collimator on the front face of the camera. After measuring the performance of the camera, SEB X-ray imaging was taken during irradiation of the beams and compared the results with a Monte Carlo simulation. We imaged the beam trajectories by the SEB X-rays in real-time during the beam irradiation, and imaging and range estimation were succesfully conducted with near clinical dose level of 7.5×10^8 carbon ions. Clear images of SEB X-rays were obtained also for a 17 cm diameter cylindrical phantom. The images were good agreement with the Monte Carlo simulation using PHITS (Fig. 1(b)). It was confirmed that the developed YAP(Ce) camera is promising for imaging of SEB X-rays during irradiation of carbon-ions even with near clinical conditions.

Recent advances in radioisotope imaging technology for plant science [2]

As the plant body absorbs and accumulates various elements present in the soil and air, accurate monitoring of element kinetics is essential to understand their physiology. Accordingly, in the field of plant science, there is a significant need to investigate the physiological functions responsible for absorbing, transferring, and accumulating the essential and harmful elements present in environments of varying temperature, humidity, light intensity, and atmospheric composition. Autoradiography methods, despite a major limitation in terms of terminating the physiological activity of the test plant, have contributed immensely to the field of plant science. In recent years, various imaging technologies have been developed for investigating living systems. A very popular technique is radioisotope (RI) imaging, which utilizes images of the absorption of the RIs of a target element from roots to leaves to monitor the movements and distributions within the plant body.

Most of RI imaging systems employed in plant science research are based on the improvement of existing medical or preclinical RI imaging systems. However, in contrast to the medical field (which focuses on the distribution of drugs and compounds in the body), the understanding of element kinetics is the main concern in plant science research. In vivo tracking of the movement of various elements is of interest in plant sciences, and therefore, multiple images of the corresponding radioisotopes need to be simultaneously monitored. Furthermore, the radiation signals from RIs vary between beta rays, X-rays, and gamma rays due to their energy differences. Therefore, the investigations in plant sciences require an imaging system capable of covering a wide variety of elements. This is the central focus in the development of plant RI imaging technologies recently.

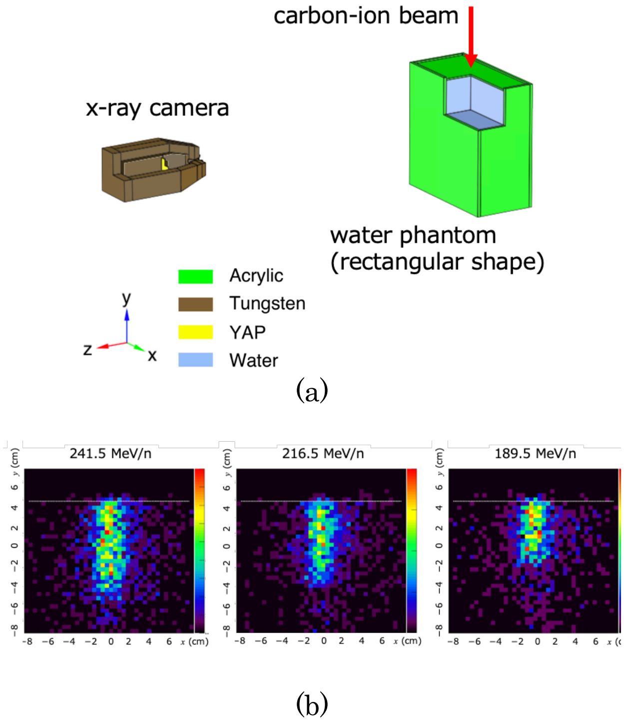

Fig. 1. (a) A three-dimensional view of the experimental setup and (b) SEB X-ray images simulated using PHITS.

References

[1] S. Yamamoto, M. Yamaguchi *et al.*, Phys. Med. Biol. **64**, 135019 (2018).

[2] N. Suzui *et al.*, Quantum Beam Science **3**, 18 (2019).

P2-5 Project “Generation of Radioisotopes with Accelerator Neutrons”

Leader : Kazuyuki Hashimoto

In our project, we have developed the production of medical radioisotopes (RI) for cancer diagnosis and therapy such as ^{99}Mo/^{99m}Tc, ^{90}Y, ^{47}Sc, ^{64}Cu, and ^{67}Cu using fast neutrons from a cyclotron accelerator. The neutrons were obtained by irradiating 40-50 MeV deuterons to beryllium or carbon. A separation and purification method of aimed radioisotope from the target materials and radioactive impurities has also been developed. We also investigate the production of medical RI such as ^{211}At and $^{95,\ 96}$Tc by the tandem accelerator in Tokai (Japan Atomic Energy Agency). Our final goal is to build a domestic production system of medical radioisotopes using accelerator driven neutrons.

Anomalous radioisotope production for ^{68}ZnO using polyethylene by accelerator neutrons [1]

In order to observe the production yields of ^{67}Cu ($T_{1/2}$= 61.9 h) which is known to have unique nuclear properties and chemical behavior for use in radionuclide therapy, we measured the yields of radionuclides after neutron irradiation on an enriched ^{68}ZnO sample covered with polyethylene blocks. The neutrons were generated from the ^{9}Be(d,n) reaction by 40 and 50 MeV deuterons. For 50 MeV deuterons we observed anomalously enhanced yields of ^{67}Ga, ^{66}Ga, ^{69m}Zn, and ^{64}Cu, more than 20-times larger than the yields for a ^{68}ZnO sample without the polyethylene blocks. At the same time, the yields of the same radioisotopes produced from an enriched metallic ^{68}Zn sample were almost insensitive to the presence of polyethylene. On the other hand, for 40 MeV deuterons the enhanced production was not observed.

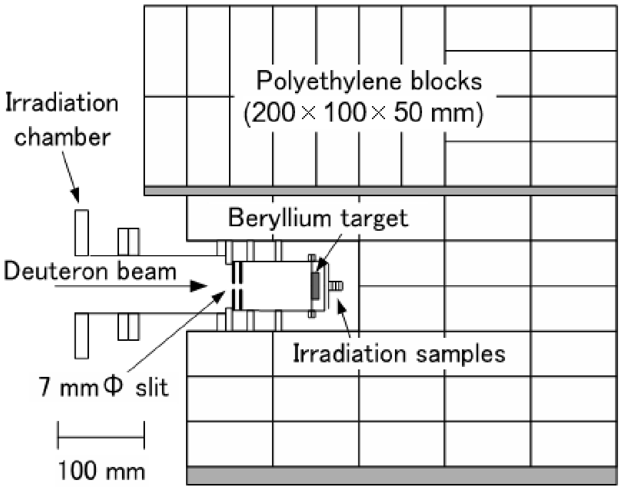

Fig. 1. Schematic view of the experimental setup at the position of the samples in polyethylene blocks [1].

This finding should be important for the production of radioisotopes in large quantity with accelerator neutrons. Especially, we could produce simultaneously several radioisotopes which are normally generated by proton-induced reaction from a single sample irradiated with the neutron beams. We found that the oxygen in the ^{68}ZnO sample plays a key role in the large production of those radioisotopes. To understand the large yield of radioisotopes, nuclear reactions occurring in the ^{68}ZnO sample should be more carefully studied, a subject of our future work. The experimental data are compared with the yields calculated by the simulation code Particle and Heavy Ion Transport code System (PHITS). Note that the calculated yields of these radioisotopes produced from the ^{68}ZnO sample covered with polyethylene blocks considerably disagree with the measured ones, while for the ^{68}ZnO sample without the polyethylene ones they are consistent with each other within a factor of 3.

Speciation of astatine reacted with oxidizing and reducing reagents by thin layer chromatography: formation of volatile astatine [2]

Alpha-emitting radionuclide ^{211}At ($T_{1/2}$ = 7.2 h) is one of the prospective candidates for utilization in target alpha therapy (TAT) of cancers. Astatine shows some different chemical behaviors compared with its homologue iodine. The understanding of basic chemical properties of astatine has been required to develop TAT agents for cancers.

In the previous study, three dissolved astatine species, astatide (At^-), astatate (AtO_3^-), and perastatate (AtO_4^-), were identified by thin layer chromatography (TLC) [3]. Further, the formation of volatile astatine was observed in the TLC analysis for solutions containing reducing agents.

In this study, to elucidate the relation between the production of the volatile astatine species and the redox behavior among At^-(−I), AtO_3^-(V), and AtO_4^-(VII), relative amounts of the dissolved and volatile astatine species were studied with TLC by varying concentrations of an oxidation agent of (KIO_4) and reducing agents (Na_2SO_3 and N_2H_4).

The astatine radionuclides were produced through the nuclear reaction of ^{nat}Pb(^{7}Li,xn)$^{nat-x}$At using the Japan Atomic Energy Agency (JAEA) tandem accelerator and were purified by dry distillation [4]. No-carrier-added astatine aqueous solution was used to prepare reaction mixtures; 6×10^{-6} – 6×10^{-3} M KIO_4, 1×10^{-4} – 1×10^{-1} M Na_2SO_3, and 9 – 29% $N_2H_4{\cdot}H_2O$. The mixtures were subjected to TLC on silica gel with an ethanol/water solution. Distributions of astatine radioactivity on the silica gel were measured with imaging plates. Chromatogram successfully separated the dissolved astatine species and provided their relative amounts as shown in Fig. 2.

The relative amounts of the dissolved astatine species were reasonably oxidized or reduced with an increase in concentration of KIO_4 and Na_2SO_3, respectively, without a remarkable loss of astatine activity. Whereas, in the case of N_2H_4 as a strong reducing agent (Fig. 2), the reduction of AtO_4^-(VII) enhanced the relative amounts of AtO_3^-(V) and At^-(−I). This facilitated the formation of the volatile species At(0) through the redox reaction between AtO_3^-(V) and At^-(−I) in dynamical equilibria due to both effects of the oxidation on silica gels and the reduction with N_2H_4, leading to the volatilization of At(0) from TLC plates. The At(0) volatilization subsequently leaded to a decrease in the amounts of AtO_3^-(V) and At^-(−I) on the TLC plates.

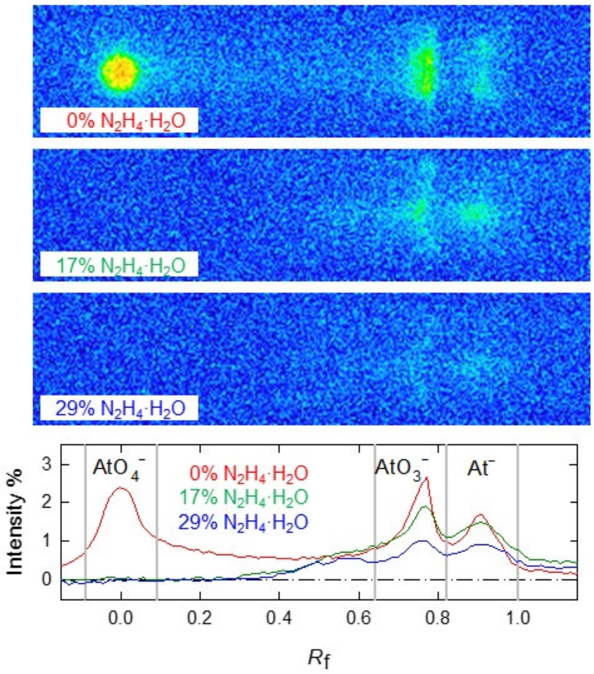

Fig. 2. Typical TLC images and chromatograms for N_2H_4 aqueous solution of astatine.

References

[1] K. Tsukada *et al.*, J. Phys. Soc. Jpn. **89**, 034201 (2020).
[2] I. Nishinaka *et al.*, J. Radioanal. Nucl. Chem. **322**, 2003 (2019).
[3] I. Nishinaka *et al.*, J. Radioanal. Nucl. Chem. **318**, 897 (2018).
[4] I. Nishinaka *et al.*, J. Radioanal. Nucl. Chem. **304**, 1077 (2015).

Part Ⅰ

3. Advanced Quantum-Beam Technology

P3-1 Project “LCS Gamma-ray”

Leader : Ryoichi Hajima

The research objective of LCS Gamma-ray Research Project is developing the technologies of high-brilliance γ-ray generation and exploring its scientific and industrial applications such as nuclear physics, nuclear astrophysics and non-destructive measurement of nuclear material. The γ-ray source is based on laser Compton scattering (LCS), which enables one to generate energy-tunable mono-energetic γ-rays. In the research project, we are developing critical components for electron accelerators to achieve small-emittance and high-average current beams, γ-ray optics and a Monte Carlo simulation code.

Compton scattering of γ-ray vortex with Laguerre Gaussian wave function [1]

Optical vortices with helical wave fronts carrying orbital angular momentum are interesting both for the fundamental research and for applications. For example, it is suggested that optical vortices could be created around rotating black holes. Furthermore, the concept of the vortex has been extended to various beams such as electrons and neutrons. In previous studies, X-ray vortex beams were generated by high-order harmonic radiations from helical undulators with high energy electrons, and the γ-ray vortex generation was suggested based on inverse Compton scattering with low energy vortex photons on high energy electrons, or with a highly intense circularly polarized laser for nonlinear scattering. Thus, it is expected to generate γ-ray vortices in the MeV energy region in the near future. However, there is a critical problem that optical devices such as holographic phase plates to measure light vortices at visible wavelengths cannot work in the MeV energy region.

In this research, we propose a method to identify photon vortices in the MeV energy in quantum level, the coincident measurement of the scattered photon and electron from each Compton scattering. We calculate the differential cross-section of Compton scattering of γ-ray vortices with a wave function of Laguerre Gaussian (LG) on an electron at rest in the framework of the relativistic quantum mechanics. Figure 1 shows the calculation results, the annulus structures, which reflect the distribution in the amplitude of the incident photon with the LG wave function. The momentum of the LG photon distributes out of the propagation axis to form the annulus. The size of the annulus depends on *L*, the projection of the orbital angular momentum for the photon propagation axis, and *p* is the number of nodes in the transverse direction. These results correspond to the shape of the photon wave function represented by the Laguerre function. These results indicate that when the energy of the scattered photon and both the momenta of the scattered photon and electrons are simultaneously measured, the amplitude distribution of the incident LG wave photon can be obtained.

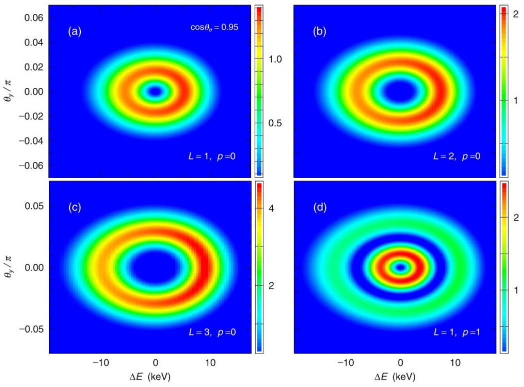

Fig. 1. The contour plots of the differential cross-section of Compton scattering integrated over the azimuthal angle ϕ_y at $\cos\theta_e = 0.95$ when $L=1$, $p=0$ (a), $L=2$, $p=0$ (b), $L=3$, $p=0$ (c), and $L=1$, $p=1$ (d).

The present results indicate that, with the coincidence measurement of the scattered photon and electron, one can identify the angular momentum and the node number of the LG wave function for the incident photon. Thus, the present proposed method is useful for the study of the nature of LG wave photons in addition to the verification of its generation.

Spin and parity determination of the 3.004-MeV level in ^{27}Al: Its low-lying multiplet structure [2]

The spin assignment of the 3.004-MeV level in ^{27}Al has an influence on the interpretation of the low-energy structure of ^{27}Al. Previous experiments have given spin $J=9/2$ to this level from inelastic neutron and proton scattering, and γ-ray angular correlations using a ^{26}Mg(p, γ) reaction. Despite the firm spin assignment of $J=9/2$, Angell et al. recently claimed a spin assignment of $J=7/2$ by measuring the integrated cross section of the 3.004-MeV transition in nuclear resonance fluorescence (NRF) experiments with a circularly polarized photon beam.

In the present work, NRF measurements using such a photon beam were performed to investigate low-lying states in ^{27}Al. The measured intensity asymmetry of the scattered γ rays with respect to the polarization of incident photons as well as the angular distribution ratio was used to determine spin and parity of levels in ^{27}Al in a model-independent fashion, as the NRF occurs only via electromagnetic interactions. The transition strength was also deduced from the measured scattering intensity. The present results are compared with those obtained via shell model calculations using the universal *sd* (USD) interaction. The intrinsic shapes of the low-energy levels of ^{27}Al are also investigated by using the “T-plot” of the Monte Carlo shell model (MCSM).

The results for the 3.004-MeV transition are shown in Fig. 2. From comparison with the calculations, the $J\pi=5/2+$ and 7/2+ assignments can be excluded at confidence levels of 87% (1.5σ) and 99.7% (3.0σ), respectively, but only the $J\pi=9/2+$ assignment is possible for the 3.004-MeV level. Here, we assume a pure E2 transition, i.e., $\delta=0$, for the 5/2+ → 9/2+ → 5/2+ spin sequence because a competing M3 transition is usually weak. The $J\pi=5/2+$ assignment can be further excluded by comparison of the measured and expected integrated cross sections.

From the theoretical analysis of the overlap probabilities, the 3.004-MeV level can be interpreted as the 9/2+ member of the multiplet resulting from the coupling of a d5/2 proton hole to the first exited 2+ level of ^{28}Si core. The analysis of the intrinsic shapes of the 2+ state in 28Si and the 9/2+

state in 27Al by using the Monte Carlo shell model calculations also supports this interpretation.

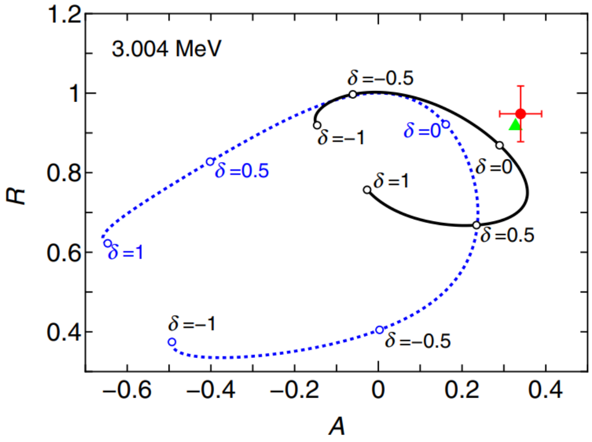

Fig. 2. Measured azimuthal asymmetry A and angular distribution ratio R for the 3.004-MeV transition. The values calculated for the spin sequence $5/2^+ \rightarrow 5/2^+ \rightarrow 5/2^+$ and $5/2^+ \rightarrow 7/2^+ \rightarrow 5/2^+$ with mixing ratios δ from −1 to +1 are plotted with solid and dotted lines, respectively. The value calculated for the spin sequence $5/2^+ \rightarrow 9/2^+ \rightarrow 5/2^+$ with $\delta = 0$ is also plotted with filled triangle.

Validating polarization effects in γ-rays elastic scattering by Monte Carlo simulation [3]

Elastic scattering of γ-rays by atoms comprises four sub-processes, namely, Rayleigh scattering, nuclear Thomson scattering, Delbrück scattering, and nuclear resonance scattering. Of these, Rayleigh scattering and nuclear Thomson scattering are associated with the scattering of a photon by electronic and nuclear charges of an atom, respectively. On the other hand, Delbrück scattering is an interaction between a photon and the strong Coulomb field in the proximity of a nucleus. Nuclear resonance scattering is associated with giant dipole resonance, and its contribution becomes appreciable when the energy of the incident photons exceeds approximately 5 MeV. All sub-processes contribute coherently to the scattering cross section via individual scattering amplitudes. The cross section of elastic scattering is proportional to the square of the resultant scattering amplitudes. Many experimental findings pertaining to the differential cross section have been accounted for based on superposition of the four sub-processes. However, validation of the theoretical calculations against experimental observations has focused on the scattering of unpolarized photons.

In the present study, we analyse the elastic scattering phenomenon by using a matrix representation of polarization based on Stokes parameters formalism. This analysis results in a set of direct expressions that highlight the general features of polarization effects in γ-ray elastic scattering. Then, we develop a Monte Carlo simulation based on our analysis by which arbitrary states of polarization of incoming or outgoing photons can be investigated.

We validated the proposed method by using available experimental data. One of the validations is the linear polarization resulting from the elastic scattering of initially unpolarized photons. The degree of linear polarization of the scattered photons is a function of the scattering angle. Usually, polarization of the scattered photons is determined experimentally by using a Compton polarimeter. As shown in Fig. 3(a), the results of a simulation of the elastic scattering of 1.33 MeV unpolarized photons by lead agree well with the experimental data. Similarly, the results of the simulation of 0.662 MeV photons agree well with the data as shown in Fig 3(b). Notably, an interference pattern is observed in the simulation at higher energies. This pattern originates from the interference of multipole amplitudes, which are summed with factors of varying sings at large angles when summed up to compose the total-atom Rayleigh scattering amplitudes. Also, the magnitudes of the amplitudes are very small compared to the small angle amplitudes. This gives rise to an increase in the error of the calculations.

The implemented simulation can be used to study interesting polarization effects of elastic scattering interaction, especially the circular dichroism associated with linear and circular polarization scenarios, as well as the potential use of elastic scattering as a polarization-diagnostic tool.

The developed code has been taken as a part of the official release of Geant4 (10.7 beta).

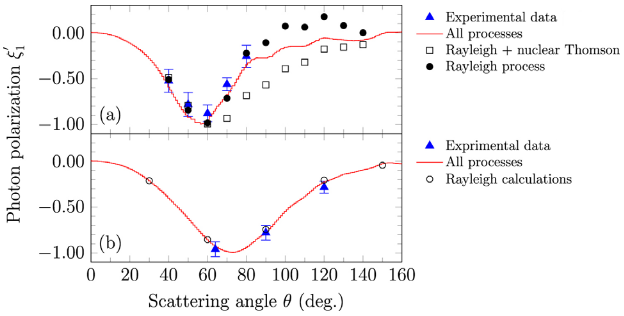

Fig. 3. Polarization of scattered photons simulated as a function of scattering angle. The triangles denote experimental measurements taken from the literature for (a) Pb at 1.33 MeV and (b) Pb at 0.662 MeV.

References

[1] T. Maruyama *et al.*, Sci. Rep. **9**, 51 (2019).
[2] T. Shizuma *et al.*, Phys. Rev. C **100**, 014307 (2019).
[3] M. Omer and R. Hajima, New J. Phys. **21** 113006T (2019).

P3-2 Beam Engineering Section

Section Manager : Yasuyuki Ishii

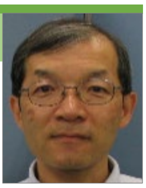

The research objectives in our section are development of various accelerator-related-techniques including ion-beam-irradiation-techniques and ion-beam-analyses. Each member has been engaged in individual researches more than one. Recent remarkable studies are shown as follows; the first article is lithium ion mapping in all-solid-state lithium batteries using Particle Induced X/γ-ray Emission (PIXE/PIGE) analyses, and the second one is High frequency plasma-pulse generation using a laser ion source. {2-31~33 and 3-01~08 in Part II}

Lithium ion mapping in all-solid-state lithium batteries using PIXE and PIGE analyses [1]

All-solid-state lithium batteries have vast potential as energy storage candidates beyond the conventional lithium battery. In recent years, sulfide-based solid lithium-ion conductors have attracted attention as solid electrolyte candidates for high-performance all-solid-state batteries. Particularly, Li10GeP2S12-type materials Li2S-P2S5 glass ceramic and argyrodite-type materials, which comprise a composite electrode of the battery, are highly preferred solid electrolytes because of their high ionic conductivities. Gaining insight into the reaction distribution in the composite electrode is key to understanding its structure and electrochemical properties. To analyze the lithium distribution in micrometer- or larger-scale areas that are typical of practical batteries, PIXE and PIGE techniques allow high-resolution quantitative determination of the concentration distribution of lithium and other elements in a sample by scanning with an ion beam.

Two types of circular pellet cells comprised the composite electrode were prepared as a sample in this study: an as-prepared cell (state of charge 0%, designated SOC-0) and a charged cell (state of charge 100%, designated SOC-100). The elemental distribution mappings at the cathode composite/separator interface of SOC-0 and SOC-100 with color tried to be visualized using PIGE. The experimental results are shown in Fig. 1. Left panels and right panels indicate SOC-0 and SOC-100, respectively. The elemental mapping area equals 100 × 100 μm^2. Since a comparison of the absolute value of gamma-ray intensity from lithium is difficult due to the use of different samples for the observation, the gamma-ray intensity of the lithium was normalized by the X-ray emission intensity of cobalt, because the amount of cobalt in the cathode composite is constant during the charging process. Therefore, the Fig. 1 shows the normalized lithium distribution mappings. The normalization processing reduced the lithium/cobalt intensity at the region where cobalt exists. As a result, the lithium distribution and its variation in the sulfide-based all-solid-state battery with the composite electrode were first observed using the PIXE and PIGE techniques.

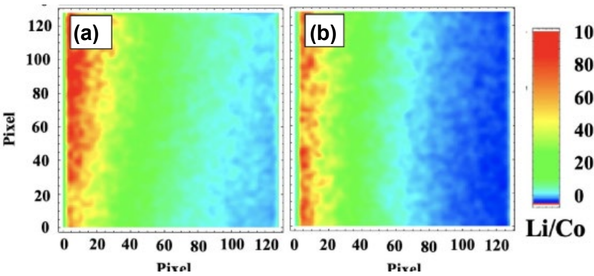

Fig. 1. Li ion distribution map of the ratio of Li/Co using PIGE and PIXE analysis.

High frequency plasma-pulse generation using a laser ion source [2]

A laser ion source (LIS) has been developed in exchange of the Freeman ion source equipped in the ion implanter at TIARA. Our objective of the development is to produce high intensity beams of any solid material ions, and to provide the beams switched in a short time. However, LISs generally produce pulsed ion beams. When a LIS is applied to the implanter, high repetition rate of the generation of plasma pulses is required to irradiate a sufficient number of ions on a target for experiments. In the experiments, two laser beams with the same energies and the same pulse-widths but different time intervals were irradiated on a graphite target at different time intervals. This experiments ended up determining the time interval of plasma pulses generated without the interaction.

The experimental results (Fig. 2) show that the total charge amount of two pulses are almost constant at the pulse interval down to 100 μs, but decreased rapidly below 100 μs. This indicates that the interaction between two pulses occurs below approximately 100 μs for the experimental condition. Therefore, the plasma pulses can be generated at a maximum of 10 kHz. In addition, it was estimated that an average current of 10 μA or more could be obtained by generating monovalent carbon ions at 100 μs intervals (10 kHz). It was found the LIS is a promising ion source for the TIARA ion implanter.

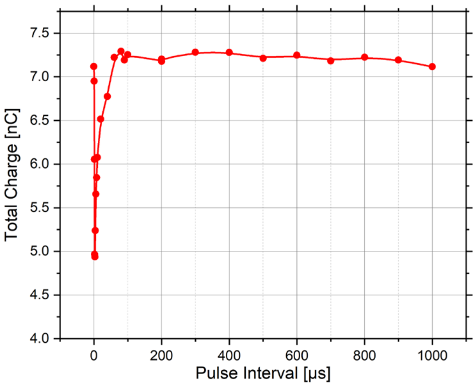

Fig. 2. Relationship between plasma pulse interval and generated charge.

References

[1] Y. Yamada *et al.*, The Electrochemical Society of Japan **88**(1), 45(2020)

[2] H. Kashiwagi *et al.*, Rev. Sci. Instrum. **91**, 033305 (2020)

Part Ⅱ

Part Ⅱ

1. Materials Science

1 - 01 A Long Side Chain Imidazolium-based Graft-type Anion-exchange Membrane: Novel Electrolyte and Alkaline-durable Properties and Structural Elucidation Using Small-angle Neutron Scattering Method

Y. Zhao[a], K. Yoshimura[a], A. Hiroki[a], H. Shishitani[b], Y. Maekawa[a]

[a]Department of Advanced Functional Materials Research, TARRI, QST,
[b]Daihatsu Motor Co., Ltd.

Anion-exchange membrane (AEM) fuel cells represent a new generation of potentially disruptive, low-temperature fuel cell technology with the potential to eliminate the high-cost barriers of mainstream proton exchange membrane (PEM) fuel cells. However, the performance of AEM fuel cells is not as good as that of PEM fuel cells, especially the membrane conductivity and long-term durability. The knowledge of AEM materials is still limited, including molecular design, hierarchical structures in the membrane, and structure/property relationships. Recently, we designed styrylimidazolium-based grafted AEMs (StIm-AEMs), in which imidazolium ionic groups are attached to styrene at the far side from the graft chains, prepared by radiation (60Co γ-ray source, Takasaki, QST) induced graft polymerization of p-(2-imidazoliumyl) styrene onto poly(ethylene-co-tetrafluoroethylene) (ETFE) films, followed by N-alkylation and ion-exchange reactions [1]. StIm-AEM with a grafting degree (GD) of 18% possesses a practical conductivity (>50 mS/cm) with a very low water uptake (WU) about 10% and high stability over 600 h in a 1M KOH solution at 80 °C. There exists a critical GD (GDc) of 20–25%, over which AEMs showed high WU and low alkaline durability. In this work, we correlate the conducting and durability properties of the membranes with the structures using small-angle neutron scattering (SANS) method to interpret their relationships [1].

Since the abovementioned unusual GD dependence of membrane properties cannot be explained by only chemical structures and their primary properties, the effect of higher-order structural transition may be profound in the membrane. To clarify the detailed AEM structures, three AEMs with GDs of 8, 11, and 14% and four AEMs with GDs of 30, 42, 56, and 86%, which are lower and higher GDs than GDc, were selected to perform SANS measurements. SANS profiles of these AEMs equilibrated in D2O were plotted in Fig. 1. According to the scattering features, we expediently separate these SANS profiles into two q-regions, where q is the scattering vector. Region I at q <1.3 nm^{-1} is related to the microphase separation between conducting and non-conducting phases, which has been characterized before [2]. Region II at q > 1.3 nm^{-1} is related to the local structures in the conducting phase. All AEMs showed a clear ionomer peak in Region II, indicating the formation of ionic clusters in the conducting phase. The further analysis of this ionomer peak using the hard sphere liquid model and Porod limit analysis reveals the detailed structures in the conducting phase. StIm-AEMs with GDs lower and higher than GDc show "reverse-micelle" structure with water domains dispersed in the polymer matrix and "micelle" structure with graft polymer aggregates dispersed in the water matrix, respectively, as illustrated in Fig. 2. AEMs with the "reverse-micelle" structure were more alkaline-durable owing to the lower number of water molecules around one ionic group, resulting in a slower hydrolysis degradation.

The results in this study indicated that the molecular design in this type of AEMs to prevent ionic structure inversion from "reverse-micelle" to "micelle" is crucial to suppress WU and maintain alkaline durability.

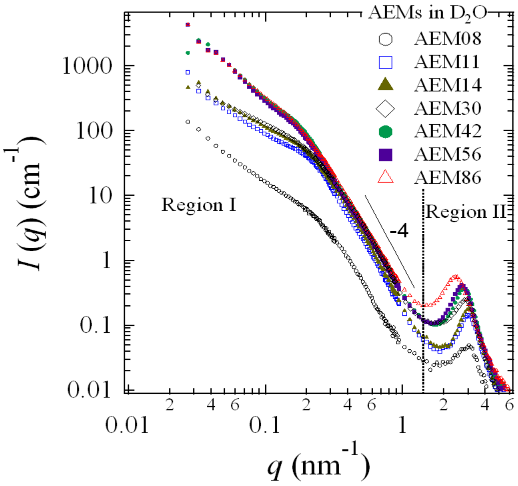

Fig. 1. SANS profiles measured for AEMs with different GDs equilibrated in D2O at room temperature.

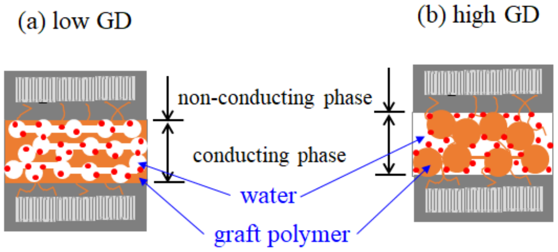

Fig. 2. Schematic illustration of the structures in AEMs.

Acknowledgments

This work was partially supported by Grant-in-Aid for Scientific Research (A) from Japan Society for the Promotion of Science (JSPS) (KAKENHI: 18H03850).

References

[1] Y. Zhao *et al.*, Soft Matter, submitted (2020).
[2] K. Yoshimura *et al.*, Soft Matter **12**, 1567 (2018).

1 - 02 Structural Analysis of Proton Exchange Membrane by Coarse-grained Molecular Dynamics Method

S. Okushima[a)], S. Hasegawa[a)], T. Kawakatsu[b)] and Y. Maekawa[a)]

[a)]Department of Advanced Functional Materials Research, TARRI, QST,
[b)]Department of Physics, Graduate School of Science, University of Tohoku

Materials informatics (MI) is a concept for the prediction of properties and efficient developments of many types of functional materials [1]. While MI applied to inorganic materials has already succeeded, it is challenging to apply MI to polymer materials because of the lack of the analytical data of the structures, which are strongly related to the properties. To solve this problem, we proposed the structural simulation method using coarse-grained molecular dynamics (CGMD) to expand the structural analysis and to digitalize the simulated structures for MI. We focused on a polyelectrolyte membrane (PEM) system which was composed of poly(ethylene-co-tetrafluoroethylene) (ETFE, a base polymer) grafted by poly(styrene sulfonic acid) (PSSA, a functional polymer) with a grafting degree (GD) of 35% and a water uptake (WU) of 41% (ETFE-PEM) [2].

Our proposed method is as follows: (1) The determination of the interface dots between the hydrophilic/hydrophobic region in the ETFE-PEM. (2) To fill out the hydrophilic region with the assembly of the spheres, which can be overlapped with each other. (3) A Markov clustering algorithm (MCL) method is applied for grouping the packed spheres by separating at the positions where the connection numbers to the neighboring spheres are small. Each group of separated spheres is determined as a cluster. The connection points should be the channel or branching points.

The result of the CGMD simulation is shown in Fig. 1(a). There is a phase-separated structure between the hydrophobic (ETFE) and the hydrophilic (PSSA/water) components. Such a structure is important for the ion transporting property of the ETFE-PEM. We applied our proposed structure analysis method to above calculated structure. In Fig. 1(b), the interface between the hydrophobic and hydrophilic regions can be visualized by a curvilinear surface composed of the calculated dots, in which the inner region of the interface corresponds to the hydrophobic components. Thus, the hydrophilic components seem to construct a wide and complicated ion channels in the ETFE-PEM, which possesses large amounts of graft-polymers and water molecules.

Figure 2(a) shows a cross section of the amorphous region, where the hydrophilic region is white, the hydrophobic region is gray and cross section of spheres is orange. Both narrow and wide paths of the hydrophilic regions can be filled out by spheres.

To extract the characteristic structure in the hydrophilic region with respect to the ion transport, the spheres consisting of different clusters, determined by an MCL method, are classified with different colors, as shown in Fig. 2(b). Each cluster is separated from other surrounding clusters at narrow points. We can digitize the important structure in the ion transport region by using the size of the clusters, i.e., the gyration radius, which can be estimated as the sum of distances between each center position of the spheres and the center of mass of the cluster..

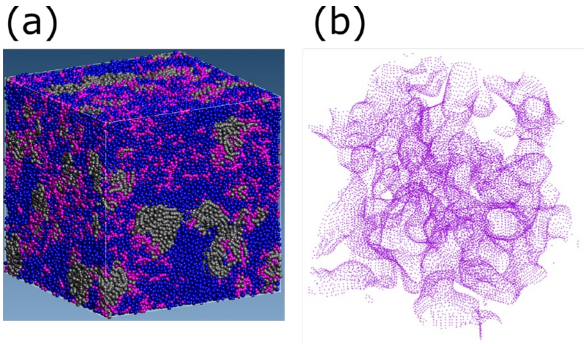

Fig. 1. (a) The structure from the CGMD simulation of ETFE-PEM. ETFE is gray, PSSA is purple, and water is blue. (b) The interface between the hydrophobic and hydrophilic regions in ETFE-PEM of Fig. 1(a).

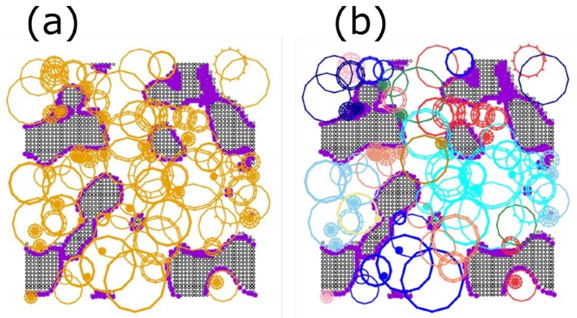

Fig. 2. (a) The result of sphere filling in the hydrophilic region in Fig. 1(a). The sphere is orange, the hydrophobic region is gray, and the interface is purple. (b) The result of applying a Markov clustering algorithm to the result in Fig. 2(a). The color is different by clusters.

Acknowledgments

This work was supported by JSPS KAKENHI Grant No. JP18H03850.

References

[1] C. C. Fischer *et al.*, Nat. Mater. **5**, 641 (2006).
[2] S. Okushima *et al.*, to be submitted.

1 - 03

Development of Gas Permselective Membranes by Radiation-Induced Graft Polymerization onto Ion-Beam Irradiated Polymer Films

S. Hasegawa, A. Hiroki, S. Sawada and Y. Maekawa

Department of Advanced Functional Material Research, TARRI, QST

Separation and purification of gas molecules with similar physical and chemical properties are an important matter in industry. In the present system for the gas separation and purification, however, it is accompanied by a large energy loss [1]. The permselective membranes are required to reduce the energy loss.

Radiation-induced graft polymerization is a useful technique for introducing new functions into polymer substrates. We previously reported that the hydrogen permselective membranes were prepared by the graft polymerization with γ-rays irradiated polyvinylidene fluoride films [2]. On the other hand, when polymer films are irradiated with heavy ion beam instead of γ-rays, radicals are produced in the latent track, which possess perpendicular cylindrical shape to the film surfaces within several hundred nm in diameter. The graft polymerization of vinyl monomers proceeds from the radicals, generated in the latent track to produce perpendicularly aligned cylindrical graft-polymer region with several hundred nm diameter. In this work, we propose a development of gas permselective membranes by the combination of the ion-beam irradiation and the graft polymerization (Fig. 1(a)).

Ethylene tetrafluoroethylene copolymer (ETFE) films (AGC Inc. 25 μm thickness) were irradiated with 560 MeV Xe ions ($^{129}Xe^{26+}$) at a fluence of 1×10^{8} ions/cm^2 at TIARA. The irradiated ETFE films were immersed into p-trimethoxysilyl styrene (TMSS) solution (TMSS/toluene = 50:50 vol%) at 60 °C to obtain TMSS-grafted ETFE (Fig. 1 (b)). The obtained TMSS-grafted ETFE showed grafting degrees (GDs) of 0.4 – 1.9%. The hydrogen (H_2) and methane gas (CH_4) permeabilities through the grafted membranes were conducted under several differential pressures.

The ion-beam irradiated (non-grafted) ETFE showed 1.0×10^{-11} and 0.1×10^{-11} mol/sec·m^2·Pa, which are comparable to those of original ETFE substrates 0.8×10^{-11} and 0.1×10^{-11} mol/sec·m^2·Pa), respectively. On the other hand, the H_2 and CH_4 gas permeabilities of the TMSS-grafted ETFE film with the GD of 1.9% showed 4.6×10^{-11} and 16×10^{-11} mol/sec·m^2·Pa, which were 5.8 and 160 time higher than that of ETFE substrate, respectively, resulting in the increase of CH_4/H_2 permeability ratio (3.5 times). Noted that the acceleration of gas permeability as well as gas permselectivity emerged by the TMSS-grafting on the ETFE films irradiated with Xe ions. Since the diameters of hydrogen and methane are 0.28 nm and 0.37 nm, respectively [3], it was suggested that the CH_4 gas permselectivity of TMSS-grafted ETFE films is induced by the interaction between the graft chains and the gas molecule but not by a molecular sieve effect.

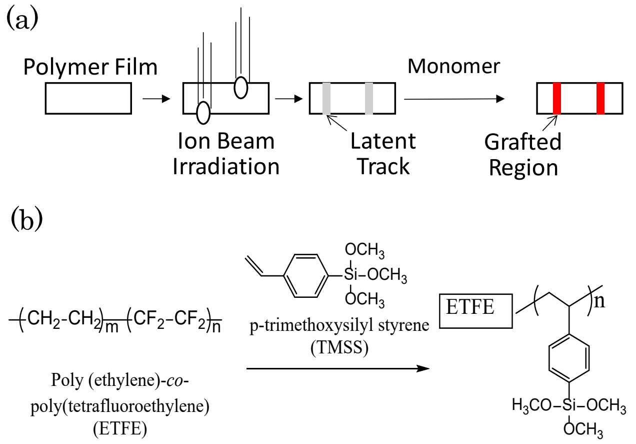

Fig. 1. Synthetic illustration (a) and chemical scheme (b) of gas permselective films prepared by the combination of ion beam irradiation and graft polymerization.

Table 1
Gas permeability and CH_4/H_2 permselectivity with TMSS-grafted ETFE films.

Sample No.	Ion Beam Irradiation	GD(%)	Gas permeability ($\times10^{-11}$ mol/sec·m^2·Pa)		CH_4/H_2
			H_2	CH_4	
1	-	-	0.8	0.1	0.1
2	○	-	1	0.09	0.1
3	○	1.9	4.6	16	3.5

Acknowledgments

This work was supported by the Japan Society for the Promotion of Science (JSPS) KAKENHI Grant Number JP16K06785.

References

[1] R.W. Baker *et al.*, Ind. Eng. Chem. Res. **41**, 1393 (2002).
[2] S. Hasegawa *et al.*, QuBS **4**, 23 (2020).
[3] H. Kuno *et al.*, The Piping Engineering **54**, 28 (2012).

1 - 04 Raman Spectroscopy of Ion-beam-irradiated HOPG Surface with Pt Nanoparticles

T. Kimata[a,b], S. Yamamoto[c], T. Yamaki[c], T. Terai[d] and K.G. Nakamura[a,b]

[a]Laboratory for Materials and Structures, Tokyo Institute of Technology,
[b]Department of Materials Science and Engineering, Tokyo Institute of Technology,
[c]Department of Advanced Functional Materials Research, TARRI, QST,
[d]The Institute of Engineering Innovation, The University of Tokyo

Platinum (Pt) nanoparticles with high oxygen reduction reaction (ORR) activity are required as cathode catalysts in proton exchange membrane fuel cells. Recently, Pt nanoparticles on the carbon substrate irradiated with argon ions (Ar^+) were found to show a higher ORR activity than those on the non-irradiated one. This result suggests that Pt nanoparticles would be influenced by ion-beam-induced lattice defects in the carbon substrate. In order to explore the origin of the activity enhancement, we investigated the interface structure between Pt nanoparticles and ion-beam irradiated highly oriented pyrolytic graphite (HOPG) surface by Raman spectroscopy.

The HOPG was irradiated with 380 keV Ar^+ at a fluence between 1.0×10^{12} and 1.0×10^{14} ions/cm^2 by the ion implanter at the Takasaki Ion Accelerators for Advances Radiation Application (TIARA) factory, TARRI, QST, Japan, and then deposited Pt nanoparticles using radio frequency (rf) magnetron sputtering. The mean particle size of the Pt nanoparticles on the non-irradiated HOPG and the HOPG irradiated at the fluences of 1.0×10^{12} and 5.0×10^{13} ions/cm^2 was observed using transmission electron microscope and obtained to be 2.85, 3.11, 6.02 nm, respectively [1]. Raman spectroscopic analysis of the pristine and pre-irradiated HOPG surfaces before and after the Pt deposition was performed. The Raman spectrum of HOPG has three peaks (D, G and D') between 500 and 2000 cm^{-1}. By using the D/D' and D/G intensity ratios and G-peak shift, we investigated the surface structure of irradiated HOPG, and discussed the structure of Pt-carbon support interface.

We investigated the surface structure of irradiated HOPG by the D/D' intensity ratio, and found that vacancy-like defects were formed on the HOPG surface by Ar^+-irradiation at the fluences between 1.0×10^{12} and 1.0×10^{13} ions/cm^2, and sp^3 defects were induced by irradiation more than 5.0×10^{13} ions/cm^2.

The Pt nanoparticles were deposited on these HOPG surface, then the G-peak position before and after Pt deposition was examined [2]. On the fluence of over 5.0×10^{13} ions/cm^2, the red Raman shifts were more obvious after the Pt deposition, as shown in Fig. 1 (a). This result indicated that the Pt deposition caused tensile stress to graphitic structure of the HOPG irradiated at higher fluences.

The phonon correlation length L_a was also investigated from the peak intensity ratio (R = D/G), such that $L_a = 4.4/R$ (nm). Pt deposition had lower effect on L_a with increasing Ar^+-irradiation on the substrate prior deposition of Pt, as shown in Fig. 1 (b). We also estimated by the L_a obtained from Raman spectrum that approximately 3 point defects were present at the interface structure between each 5 nm Pt nanoparticle and the HOPG irradiated with Ar^+ at the fluence of 1.0×10^{13} ions/cm^2.

In order to clarify the interface structure between Pt nanoparticles and ion-beam irradiated carbon support, we obtained the Raman spectra of irradiated HOPG with Pt nanoparticles, and then evaluated the number of defects at the Pt-carbon support interface.

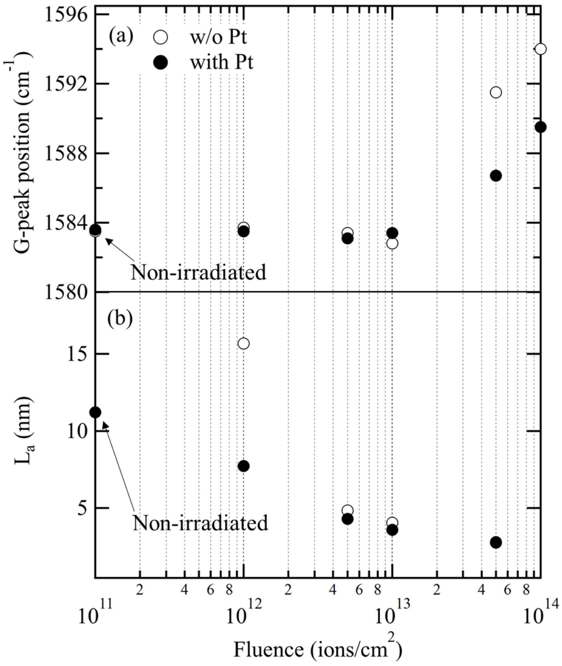

Fig. 1. (a) G-peak position and (b) L_a against the Ar^+ fluence.

Acknowledgments

This work was partly supported by the Collaborative Research Project of Laboratory for Materials and Structures (2018-No.51 and 2019-No.54), Institute of Innovative Research, Tokyo Institute of Technology.

References

[1] T. Kimata *et al.*, Radiat. Eff. Def. Sol. **175**, 433 (2020).
[2] T. Kimata *et al.*, Nucl. Instrum. Meth. Phys. Res. B **444**, 6 (2019).

1 - 05 Utilization of Ion Implantation Technique for Introduction of Fe Nanoparticles into a Carbon Precursor Polymer

A. Idesaki, S. Yamamoto, M. Sugimoto, T. Yamaki and Y. Maekawa

Department of Advanced Functional Materials Research, TARRI, QST

Nitrogen (N)-doped carbon materials, which exhibit a catalytic activity for an oxygen reduction reaction (ORR; $O_2 + 4H^+ + 4e^- \rightarrow 2H_2O$), recently have been extensively studied as platinum-alternative catalysts. The requirements of the catalytic activity for the ORR are as following: (1) the formation of turbostratic graphite nanostructure consisted of the hexagonal carbon layers piled up randomly or uniformly in a part, and (2) incorporation of nitrogen atoms into the graphitic structure as pyridinic nitrogen and/or quaternary nitrogen. The N-doped carbon catalysts are often synthesized from blends of various carbon precursor polymers and transition metal compounds of Fe, Co, and Ni. The added metal compounds produce metal nanoparticles (NPs) during the heat treatment, and the NPs play a role of a catalyst for the formation of the graphitic nanostructure. The texture of obtained graphitic nanostructure depends on the size of metal NPs: the turbostratic graphite structure is obtained in the case of the particle size of around 20 nm, and graphite structure, above several tens nm [1]. In most cases of previous studies, the particle size distribution after the carbonization is ranging from 20 to several tens nm. This suggests that the ORR-inactive graphite structure is preferred to form than the ORR-active turbostratic graphite structure. Thus, we propose metal ion implantation into a carbon precursor polymer as a method to introduce metal NPs with controlled the particle size below 20 nm in order to synthesize the turbostratic graphite structure. In this work, a phenolic resin (PhR) was implanted by 100 keV Fe^+ ions and heat-treated at 800°C in N_2 atmosphere.

The relationship between the ion fluence and mean particle size of formed Fe NPs is shown in Fig. 1. The mean particle size of Fe NPs increased almost linearly with the increasing ion fluence. This result suggests that the particle size is controllable in the range of 5-30 nm by the ion implantation technique. On the other hand, the mean particle size of Fe NPs obtained from the blend of PhR and $FeCl_3$, as a conventional method, hardly changed with the Fe concentration. This is caused by that the Fe NPs obtained from the $FeCl_3$-blended sample contain large particles with the size over 50 nm.

By the transmission electron microscopy (TEM) observation, it was found that the turbostratic graphite structure which is consisted of shell-like carbon layers and intricately distorted carbon layers was formed around the Fe NPs (Fig. 2). Furthermore, the peak analyses of Raman spectra of obtained carbon materials revealed that the carbon material obtained by the ion implantation (1×10^{15} ions/cm^2) contains more the turbostratic graphite structure than that of the carbon material obtained by the conventional method ($FeCl_3$-blending, 0.35 wt% Fe). This is caused by that the finer Fe NPs with mean particle size of 20 nm were introduced by the ion implantation technique (see Fig. 1).

As a summary, it was found that the ion implantation technique is useful to introduce the Fe NPs with controlling the particle size and that the formation of turbostratic graphite structure is promoted by the fine Fe NPs. It is expected that the N-doped carbon catalyst with high performance can be synthesized by controlling the graphitic nanostructure with introduction of the fine metal NPs.

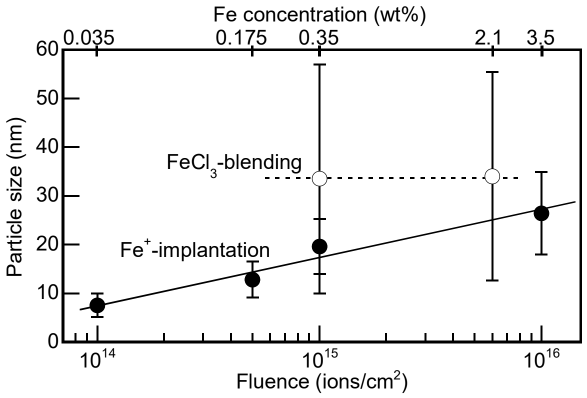

Fig. 1. Particle size of Fe NPs formed in the carbon materials with the ion implantation and the $FeCl_3$-blending.

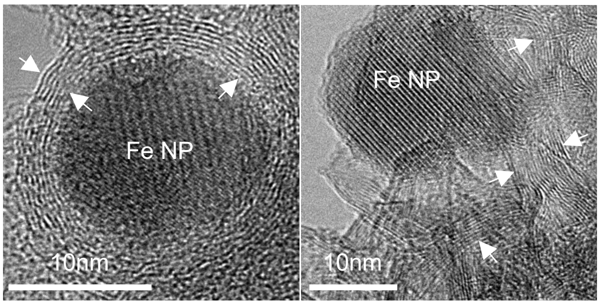

Fig. 2. Texture of obtained carbon material with the ion implantation (1×10^{15} ions/cm^2): shell-like carbon layers (left) and intricately distorted carbon layers (right).

Acknowledgments

This work was supported by JSPS KAKENHI Grant Number 18K11938.

References

[1] A. Oya and H. Marsh, J. Mater. Sci. **17**, 309 (1982).

1 - 06

Formation of Pt Nanoparticles Inside Ion-Track-Etched Capillaries

S. Yamamoto, T. Taguchi, H. Koshikawa, A. Idesaki, H. Okazaki and T. Yamaki

Department of Advanced Functional Materials Research, TARRI, QST

High-aspect-ratio capillaries (diameter: several hundreds of nm, length: several tens of µm) containing nanoparticles of precious metals (e.g., Pt, Au, and Ag) are expected to be applied to plasmonic absorbers materials. Plasmonic absorbers have the ability to convert light energy into heat energy. By adding catalytic qualities, it would be possible to apply plasmonic absorbers as gas-reforming materials**.** The ability to form highly dispersed precious metal nanoparticles into a narrow space is essential for the fabrication of the plasmonic absorbers. In this study, we demonstrated the preparation of ion-track-etched capillaries containing Pt nanoparticles in polyimide films. First, swift heavy ion beam irradiation and chemical etching were used to prepare capillaries in polyimide films. Then, Pt nanoparticles were formed inside the ion-track-etched capillaries by electron beam irradiation reduction method [1].

Polyimide films (Kapton, thickness: 25 µm) were irradiated with 350 MeV $^{129}Xe^{23+}$ ions at a fluence of 3 × 10^7 ions/cm^2. The irradiated films were etched in a sodium hypochlorite (NaClO) aqueous solution at 60 °C to create the capillaries. The electrical conductivity of the samples was enhanced for subsequent scanning electron microscope (SEM) and transmission electron microscope (TEM) observations by heating (i.e., carbonizing) them in the presence of N_2 for 3 h at 530 °C. The heat-treated polyimide films were immersed in an aqueous solution containing 0.5 mmol/L hexachloroplatinic acid hexahydrate (H_2PtCl_6) and 0.5 vol% ethanol (C_2H_5OH), and then irradiated with a 2 MeV electron beam of 500 kGy.

Figure 1 shows a cross-sectional SEM image of ion-track-etched capillaries created in heat-treated polyimide film after an etching time of 20 min, the capillaries presented a diameter of ~500 nm and were aligned perpendicularly to the film surface, suggesting that the capillaries were formed along the trajectory of a single Xe ion incident beam perpendicular to the film. Furthermore, the SEM observations revealed that the capillaries penetrated the films.

Figure 2 (a) shows two cross-sectional TEM images of precipitated Pt nanoparticles located on the wall of an ion-track-etched capillary, which was formed in a heat-treated polyimide film after an etching time of 20 min. The Pt nanoparticles with isolated aggregates were distributed homogeneously inside the ion-track-etched capillary. The size of the Pt nanoparticles (i.e., their diameter in the major axis direction) was measured based on high-magnification TEM images. The isolated aggregates were composed of Pt nanoparticles with sizes < 5 nm (Figure 4 (b)). The high-resolution TEM observations (i.e., lattice images) revealed that the Pt nanoparticles has crystalline structure. Overall, the TEM observations confirmed the formation of Pt nanoparticles with isolated aggregates inside ion-track-etched capillaries in heat-treated polyimide films. The results indicated the formation of homogeneous Pt nanoparticles and isolated aggregates inside the capillaries of polyimide film. Thus, it was demonstrated that a combination of ion and electron beam irradiation techniques can be applied to produce capillaries containing metal nanoparticles in flexible polymer films.

Acknowledgments

This research work was supported by JSPS KAKENHI Grant Number 18K04739.

References

[1] S. Yamamoto *et al.*, Quantum Beam Sci. **4**, 8 (2020).

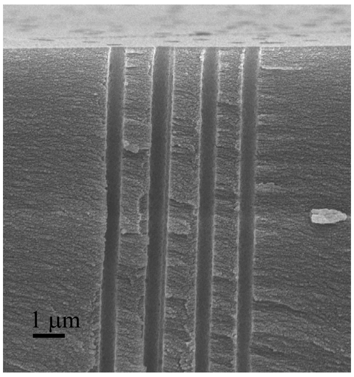

Fig. 1. Cross-sectional SEM image of ion-track-etched capillaries created in a heat-treated polyimide film after an etching time of 20 min.

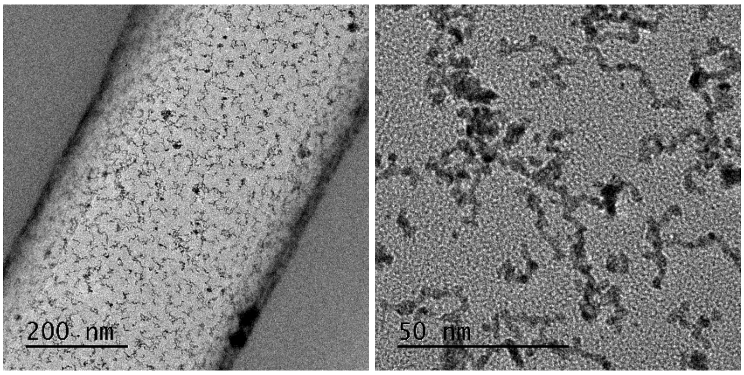

Fig. 2. (a) Low- and (b) high-magnification cross-sectional TEM images of Pt nanoparticles formed into an ion-track-etched capillary in a heat-treated polyimide film.

1 - 07 Improvement of Current Density for Vanadium Redox Flow Battery by Electron Beam Irradiation

H. Doki[a) c)], H. Ishitobi[b)], S. Yamamoto[c)], R. Obata[a) c)]
H. Okazaki[c)] and N. Nakagawa[b)]

[a)]Graduate School of Science and Technology, Gunma University,
[b)]Division of Environmental Engineering Science, Gunma University,
[c)]Department of Advanced Functional Materials Research, TARRI, QST

Introduction

The vanadium redox flow battery is expected to store renewable energy because it has the advantage that power and capacity can be designed independently. In contrast, there is a problem that the current density of the single cell is low due to the higher internal resistances such as kinetic resistance. Previously, in order to increase the current density by increasing the number of reaction site, heat treatment of the electrode materials in air have been conducted [1]. However, the conventional heat treatment takes time as long as 3 h. We focused on electron beam irradiation as an activation method that can form oxygen functional groups in a short time. When an electron beam is irradiated in air, it is considered that the surface oxygen groups can be added by the reaction between surface carbon and radicals and/or ozone from the water or the oxygen in air formed by the irradiation. In this study, we investigated effect of the electron beam fluence to the carbon material on the power density of the cell.

Experimental

Electron beam irradiation was performed on the carbon cloth (CC) (Nippon Carbon Co.), and then, characterization and electrochemical measurement were performed. The electron beam was irradiated with an acceleration voltage of 2.0 MV, 5 mA at from 1.39×10^{16} e cm^{-2} to 8.32×10^{16} e cm^{-2}, that takes 10 min to 60 min, to the CC under the air atmosphere at TAARI, QST. To evaluate the cell performance, current-voltage curves were obtained using a single cell with a pair of carbon block, which were current collectors, with an interdigitated flow channel. The Nafion 117 membrane was used as the separator. The 1 M vanadium species in a 3 M sulfuric acid aqueous solution was used as the electrolyte solution. The surface content of elements for the electrode materials was analyzed by X-ray photoelectron spectroscopy (XPS).

Results and discussion

The cell voltages with the irradiated electrode were higher than that of the pristine. The maximum power density of the cell using the irradiated electrode with the fluence of 1.39×10^{16} e cm^{-2} showed 1.6 times higher than that of the pristine electrode (Fig. 1). Therefore, it is considered that the oxygen functional groups would be added to the surface of the electrode material, and the relationship between the power output and the surface oxygen fraction at each irradiation fluence was investigated. When the electron beam was irradiated in air, the surface oxygen fraction increased. In particular, the fraction of C-O and C=O bonds increased significantly. There was a correlation between the fraction of the C-O and C=O bonds and the max power density (Fig. 2). Based on these results, when an oxygen functional group such as phenol or carbonyl is added to the surface of the electrode material, vanadium ions are adsorbed on the oxygen functional group, and the oxygen functional group behave as active sites that promote the charge transfer reaction. As a result, the kinetic resistance is reduced and the power output is improved. Therefore, the electron beam irradiation to the electrode material is considered to be effective as a treatment method for efficiently adding an oxygen functional groups as the active site in a short time.

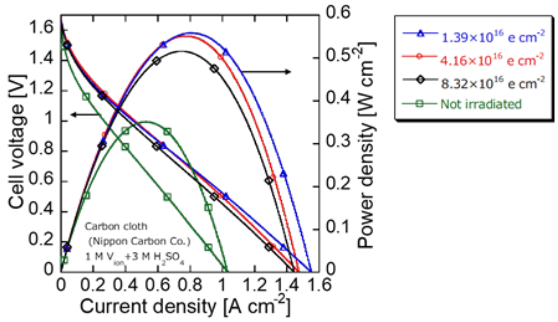

Fig. 1. Current-voltage curves of the irradiated electrodes.

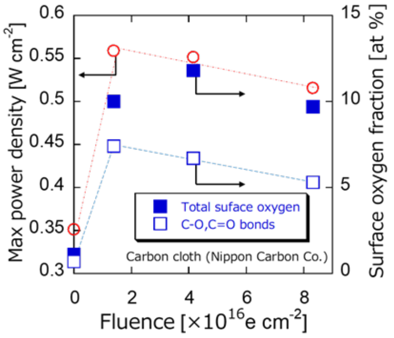

Fig. 2. Relation between fluence and max power density.

Acknowledgments

This research was supported by JSPS KAKENHI Grant Number JP18K14048, research grants from Gunma University (Super-Membrane Project & Element Science Project). We significantly thank these foundations.

Reference

[1] Alan M. Pezeshiki *et al.*, *J. Power Sources* **294**, 333 (2015).

1 - 08 Formation of Nanowires via Solid-State Polymerization of Ethynyl-Substituted 9,9'-spirobi[9H-fluorene]s Triggered by Swift Heavy Ion Irradiations

S. Sakaguchi[a)], T. Sakurai[a,b)], A. Idesaki[c)], H. Koshikawa[c)], M. Sugimoto[c)] and S. Seki[a)]

[a)]Department of Molecular Engineering, Graduate School of Engineering, Kyoto University,
[b)]Faculty of Molecular Chemistry, Kyoto Institute of Technology,
[c)]Department of Advanced Functional Materials Research, TARRI, QST

Acetylenes are the first monomer to polymerize by the energy deposited by ionizing radiations, where electric discharge in acetylene vapor atmosphere gave condensed materials on the wall of the discharge tube. Herein we report an efficient solid state polymerization of ethynyl-substituted 9,9'-spirobi[9*H*-fluorene]s (SBFs) *via* a unique nano-fabrication technique referred to as Single Particle Trigged Linear Polymerization (STLiP) initiated by high energy charged particles [1–3]. The resultant nanowires of polymerized/crosslinked SBFs show a gradual transformation from flexible to rigid rod-like structures with an increase in the reaction efficiency mediated by the ethynyl substitution. The estimated overall efficiency of initiation/propagation/crosslinking reactions is remarkably high, even in comparison with the primary yield of ionization events in the radiation chemical processes, marking up to $G > 80$ (100 eV)$^{-1}$ [3].

The STLiP method is the stepwise processes containing film fabrication, irradiation with swift heavy ions, and development with organic solvents (Fig. 1). All the SBF derivatives with/without bromo or ethynyl groups (Fig. 2) were purchased or synthesized, and transformed to thin films by spin-coating from $CHCl_3$ solutions. 450 MeV $^{129}Xe^{23+}$ was used as an ion species. The films after irradiation were isolated by development with toluene. The morphology of the nanowires was measured by using a Bruker Co. Multimode 8 atomic force microscopy (AFM).

Nanowire formation was clearly confirmed by AFM observation as shown in Fig. 2. The averaged cross-sectional radius (r), defined as $r = (r_x \cdot r_y)^{1/2}$ evaluated by AFM cross-sectional views, was found to be larger by substitution with Br or ethynyl groups (Fig. 2). The effect of Br substitution can be explained by high yield of free radicals via the dissociative electron attachment (DEA) reactions (Scheme 1a). For the impact of ethynyl groups, major two reaction mechanisms were proposed to illustrate the chain reaction in the polymerization: 1) initiating from excited state of an acetylene molecule formed by charge recombination followed by capturing neutral acetylene molecules; 2) terminal hydrogen dissociation from the excited state of acetylene leading to free radicals for subsequent chain reactions. Considering the restricted molecular motions in the solid phase, the former mechanism rarely occur in the STLiP process. Thus the formation of polymeric nanowire can be well explained by free-radical chain reactions proceed *via* the highly reactive vinyl radicals (Scheme 1b). The present results indicate the efficient chain reactions in the propagation steps by ethynyl modification of the starting materials, which is neither topochemical polymerization nor acid/base-catalyzed reactions.

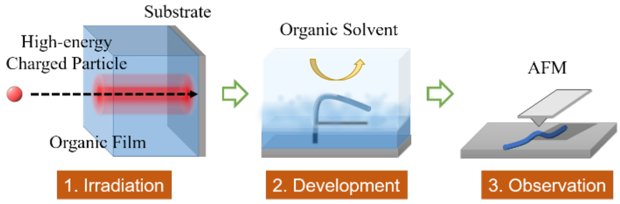

Fig. 1. Schematic illustration of nanowire fabrication processes by swift heavy ion irradiations and following isolation by development with organic solvents.

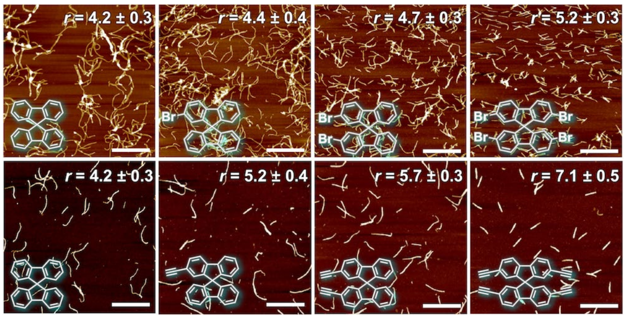

Fig. 2. AFM images of nanowires from spin-coated film of SBF derivatives. Irradiation was carried out with 450 MeV $^{129}Xe^{23+}$ at the fluence of 1.0 × 10^9 cm^{-2}. Scale bars represent 500 nm.

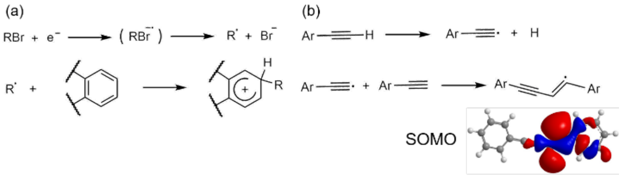

Scheme 1. Plausible primary reactions in (a) Br- and (b) ethynyl-substituted SBFs and structure of intermediates in the propagation steps of polymerization reactions. The optimized structures of a model compound of ethynyl-substituted SBFs were calculated by density functional theory with ROB3LYP/6-31G*.

References

[1] S. Sakaguchi *et al.*, Quantum Beam Sci. **4**, 7 (2020).
[2] T. Sakurai *et al.*, ACS Appl. Nano Mater. **3**, in press. (2020). DOI: 10.1021/acsanm.0c01242.
[3] S. Sakaguchi *et al.*, J. Photopolym. Sci. Technol. **33**, 91 (2019).

1 - 09

Water Permeation Performance of Cross-linked Radiation-Grafted Cation-Exchange Membranes for Efficient HI Concentration

N. Tanaka[a)], S. Sawada[b)] and T. Yamaki[b)]

[a)]HTGR Research and Development Center, JAEA,
[b)]Department of Advanced Functional Materials Research, TARRI, QST

A thermochemical water-splitting Iodine-Sulfur (IS) process [1] is expected as a promising method for hydrogen production. In the IS process, a new cation-exchange membrane (CEM) [2] prepared by the radiation-induced graft polymerization has been applied to the electro-electrodialysis (EED), which can enrich hydrogen iodide (HI) in an HI-I_2-H_2O mixture (HIx solution). Our previous studies to improve CEM performance presented the following two findings. First, the most important factors governing EED were the proton (H^+) and water selectivities [3]. Ideally, the former would be high, and the latter low. Second, the crosslinking structure in our grafted CEMs increased the H^+ selectivity because it inhibited the permeation of the other molecular and ionic components [4]. In this sense, it is of our great interest to investigate the effect of the crosslinking on the water selectivity, which is represented by a water permeation factor, β (corresponding to a ratio of permeated quantities of water to H^+) [3]. Therefore, we report the β values for the crosslinked CEMs with different ion exchange capacities (IECs) to understand and optimize all the crucial factors for EED.

The CEMs were prepared by pre-irradiation of the ETFE film with γ-rays, the graft polymerization of styrene (St) with and without 5 vol% DVB, and sulfonation. The resulting DVB-crosslinked and non-crosslinked CEMs exhibited the IECs of 1.4-3.1 mmol/g and 1.1-3.0 mmol/g, respectively. The β was measured using a filter-press type EED cell [2], to which a direct current of 200 mA/cm^2 was applied for 4 h at 313 K. The feeding HIx solution contained $HI = I_2 = 10$ mol/kg. The swelling ratio was measured by comparing the CEM volumes before and after immersion in the same solution.

Figure 1 shows the β values as a function of IEC. They were lower for the crosslinked CEMs than for the non-crosslinked ones at a given IEC. The non-crosslinked CEMs showed an increasing trend in β at higher IECs. In contrast, the crosslinked CEMs appeared to be independent of IEC. These results suggest that the introduction of DVB-based crosslinks led to the inhibition of water permeation.

Figure 2 shows the swelling ratio in the HIx solution as a function of IEC. The swelling ratio of the non-crosslinked CEMs increased as the IEC became higher, indicating that each of the ionic groups absorbed the HIx solution. Importantly, however, the crosslinked CEMs had the almost stable swelling ratio within the experimental errors. The crosslinking structure prevented the absorption of the HIx solution even if the ionic groups increased. We found the HIx absorbability of our non-crosslinked grafted CEMs to be independent of the temperature up to 373 K [3]. Thus, the present result would be true for the actual EED in the IS process.

The previous study [5] demonstrated that the DVB-based crosslinks reduced a size of ionic aggregates in the dried CEM. Considering the above result, we expect that the smaller-sized ionic domains of the crosslinked CEM would also be achieved in the HIx-solution environment. Therefore, the introduction of DVB as crosslinker was found to decrease the water selectivity due to the less swelling property of the CEM.

References

[1] H. Noguchi *et al.*, Int. J. Hydrog. Energy **44**, 12583 (2019).
[2] T. Yamaki *et al.*, Polymer **45**, 6569 (2004).
[3] N. Tanaka *et al.*, J. Membr. Sci. **411-412**, 99 (2012).
[4] N. Tanaka *et al.*, Proceedings of IMSTEC2020, 57.
[5] S. Balog *et al.*, Polymer **53**, 175 (2012).

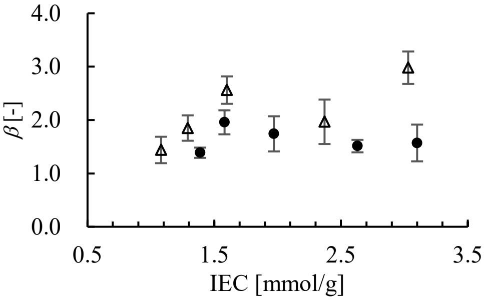

Fig. 1. IEC dependence of β for the crosslinked (●) and non-crosslinked CEMs (△).

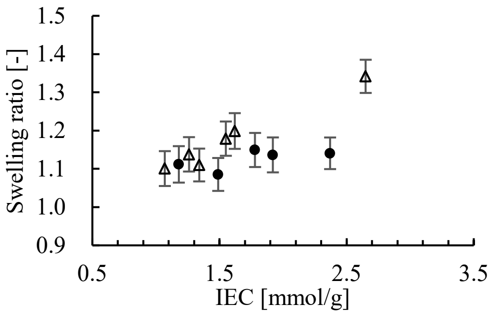

Fig. 2. IEC dependence of the swelling ratio for the crosslinked (●) and non-crosslinked CEMs (△).

1 - 10 Valence-selective Transport of Ions Across Charged Mosaic Membranes Prepared by Ion-track Graft Polymerization

R. Ueno[a)], K. Takeuchi[a)], T. Yamaki[b)], S. Sawada[b)], H. Koshikawa[b)],
Y. Kakihana[a,c)] and M. Higa[a,c)]

[a)]Graduate School of Sciences and Technology for Innovation, Yamaguchi University,
[b)]Department of Advanced Functional Materials Research, TARRI, QST,
[c)]Blue Energy center for SGE Technology (BEST), Yamaguchi University

A charged mosaic (CM) membrane consists of many cation- and anion-exchange regions, each of which is threading from one side of the membrane to the other. This special structure permits a selective permeation of electrolytes against non-electrolytes and importantly, has a potential to provide a high flux of electrolytes due to a presence of circulating current through the membrane. However, improvement of the mechanical strength for a pressure dialysis (piezodialysis) process has been a major challenge for a long time.

Thus, we have been working on the preparation of the CM membranes having both high mechanical strength and high electrolyte flux by using ion-track graft polymerization method [1]. Our preparation procedure involves the irradiation of anion exchange membrane (AEM) with heavy MeV-GeV ions and the grafting of anionic-group-containing monomers into each of the latent tracks. The resulting CM membrane has anionically-charged cylindrical nanochannels penetrated through the cationically-charged AEM; this structure is expected to improve the mechanical strength. We report here, as a preliminary result, an interesting finding that the valence-selective transport of ions was controlled by different charges of the CM membrane.

A commercially-available AEM, FAS-30 (fumasep®: FUMATECH) with a 30 μm thickness was used as a base film and irradiated with 560 MeV ^{129}Xe ions at a fluence of 3.0×10^8 ions/cm^2. After the irradiation, the grafting reaction was done by immersion in a 20 wt.% *p*-styrenesulfonate (SSS) monomer solution at 60 °C for 6 and 9 h, which gave CM membranes, CM-2 and CM-1, respectively. The membrane potential of the obtained CM membranes was measured using a KCl solution to investigate their charge density ratio (*CDR*):

$$CDR = CD_c / CD_a \quad (1)$$

where CD_c and CD_a are the charge densities of the cation- and the anion-exchange regions, respectively. Ion-permeation experiments were performed by using a diffusion dialysis system consisting of the CM membrane and either of aqueous KCl, NaCl and $CaCl_2$ solutions.

CM-1 and CM-2 exhibited membrane potentials of 22.3 and −21.1 mV, respectively. Thus, the *CDR* of CM-1 was larger than unity, while the *CDR* of CM-2 was smaller than unity. According to equation (1), the charge density of the cation-exchange region would be higher in CM-1 than that of the anion-exchange region, and vice versa in CM-2.

Figure 1 shows the concentration of ions in the low-concentration side of the dialysis system as a function of measurement time. The slope of the concentration variation was larger for CM-1 than for CM-2. This would be due to the fact that CM-1 had higher water content, which probably makes the ion transport faster. For both the CM membranes, the concentration change of KCl was quicker than that of NaCl. The hydrated ionic radius of K^+ is smaller than that of Na^+ ions, thereby leading to faster K^+ transport through CM-1 and CM-2.

The $CaCl_2$ salt in CM-2 exhibited the smallest slope among all the salts, while, in contrast, the $CaCl_2$ salt in CM-1 exhibited the largest slope. This difference would be rationalized by considering the following reasons. Ca^{2+} is a divalent ion, and therefore, its hydrated ion radius and ionic mobility is larger and lower, respectively, than those of monovalent Cl^- ions. Thus, the Ca^{2+} permeation will be a rate-limiting step in the diffusion of $CaCl_2$. CM-1 had the higher *CDR* than CM-2 did, meaning that CM-1 contained Ca^{2+} ions at higher concentrations. This is why the slope of $CaCl_2$ in CM-1 is much larger than that in CM-2.

In conclusion, the valence-selective transport of ions can be controlled using the CM membranes with different charges.

References

[1] M. Higa *et. al.*, Bull. Soc. Sea Water Sci., Jpn. **71**, 37 (2017).

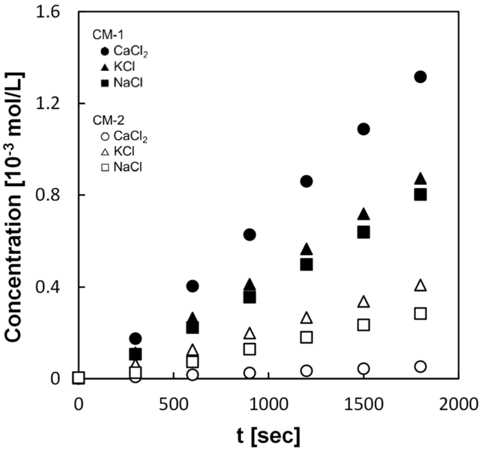

Fig. 1. Ionic concentration of a low-concentration side as a function of measurement time, t.

1 - 11

Fabrication of Planar Perfect Blackbody Materials Using Etched High-Energy-Ion Tracks

K. Amemiya[a], Y. Shimizu[a], H. Koshikawa[b], M. Imbe[a] and T. Yamaki[b]

[a]National Metrology Institute of Japan, AIST,
[b]Department of Advanced Functional Materials Research, TARRI, QST

Low reflectance black materials have various applications ranging from dark-level suppression to light energy harvesting. Carbon nanotube forests are known as the world's blackest materials [1,2]. Despite their excellent optical performance, they are too fragile to be used widely by the general public. Nickel-phosphorous (NiP) black surfaces, which have high-aspect-ratio conical micropores with oxide black layers, also show ultra-low reflectance of near 0.1% in the visible and near-infrared range [3,4]. For longer wavelengths, however, the reflectance of NiP black increases owing to its geometry and composition [4], which can be hardly customized for mid-infrared (MIR) use.

We are developing a novel planar perfect blackbody material [5,6] from etched ion tracks [7]. Poly allyl diglycol carbonate (CR-39 in trade name) plastic plates were irradiated with energetic heavy ion beam from AVF cyclotron of TIARA; then the samples were etched in NaOH solutions to fabricate randomly arrayed optical micro-cavities (etch pits) on their surface, followed by replica molding. The resultant blackbody sheet from poly dimethyl siloxane (PDMS) with carbon black fillers exhibited ultralow reflectance of $\lesssim$ 0.5% in UV–VIS-NIR-MIR, notably $\lesssim$ 0.1% in MIR while maintaining good mechanical durability [6].

Finite differential time domain (FDTD) simulation, which can calculate wave-domain optical propagation in materials of three-dimensional geometry, confirmed that the cavity aspect ratio should be > 3, and the cavity opening diameter of greater than the wavelength of interest is preferable when targeting < 0.1% total reflectance [4,6].

The ion track etching technique can easily manufacture such high-aspect-ratio micro-cavities of opening well above a few microns at will, by choosing ion species, energy, and exposure density with adequate etching time [7]. This means that the ion track etching technique can produce micro-cavity molds that are appropriate for the near-perfect MIR absorber. High absorptance is equivalent to high emissivity. Therefore, our PDMS blackbody sheet would be used as a planar standard infrared radiator, offering high-precision calibration of radiation thermometers including thermographic devices.

Such a thermal imager calibrator application requires a large-area planar blackbody. We tried the fabrication of a 100 mm x 80 mm PDMS blackbody sheet (Fig. 1). We successfully confirmed that the large-area blackbody sheet also exhibited ultralow reflectance of < 0.2% (near-unity emissivity of > 0.998) at thermal infrared wavelengths (8-15 μm). The reflectance values at two separate positions on the blackbody sheet agreed with each other (Fig. 2), which implied that the blackbody sheet would have high in-plane uniformity. This performance relies on the high uniformity of materials and processing techniques: a master mold and a replica material, and ion track etching techniques.

Acknowledgments

This work has been supported by the Inter-University Program for the Joint Use of JAEA/QST Facilities (proposal no. 19006) from Nuclear Professional School, School of Engineering, The University of Tokyo.

References

[1] Z.P. Yang *et al.*, Nano Lett. **8**, 446 (2008).
[2] K. Mizuno *et al.*, Proc. Natl. Acad. Sci. U.S.A. **106**, 6044 (2009).
[3] S. Kodama *et al.*, IEEE Trans. Instrum. Meas. **39**, 230 (1990).
[4] K. Amemiya *et al.*, Appl. Opt. **51**, 6917 (2012).
[5] K. Amemiya *et al.*, Nucl. Instrum. Meth. Phys. Res. B **356–357**, 154 (2015).
[6] K. Amemiya *et al.*, J. Mater. Chem. C **7**, 5418 (2019).
[7] S. Kodaira *et al.*, Radiat. Meas. **46**, 1782 (2011).

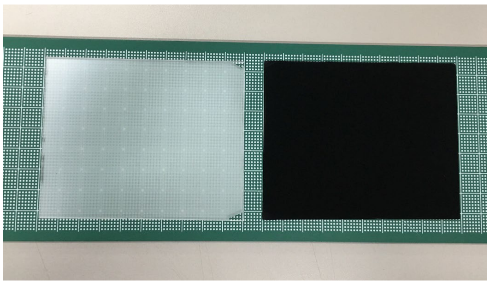

Fig. 1. (left) Microtextured mold via swift heavy ion manufacturing, and (right) its replica from PDMS with carbon black fillers.

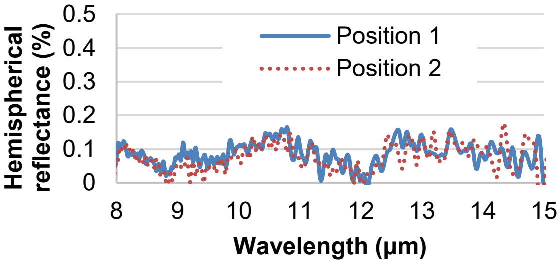

Fig. 2. Spectral hemispherical reflectance of the PDMS blackbody sheet.

1 - 12 Superconducting Properties of High-T_c $GdBa_2Cu_3O_y$ Films Irradiated with 10 MeV Au-ions

T. Ozaki[a)], H. Okazaki[c)], H. Koshikawa[c)], S. Yamamoto[c)] and T. Yamaki[c)]

[a)]Department of Nanotechnology for Sustainable Energy, Kwansei Gakuin University,
[c)]Department of Advanced Functional Materials Research, TARRI, QST

Superconductor's lossless current flow enables the design of highly dense and compact equipment, and hence offers powerful opportunities for increasing the capacity and the efficiency of power grids. The practical critical current density J_c, which is an important property of superconducting materials for energy applications, is governed by the vortex pinning strength. It is well-known that the vortex pinning is determined by the ability of defects in superconducting materials. Thus, there have been many papers about defect introduction by the irradiation with the particles of different masses and energies to increase J_c in magnetic fields. A low-energy ion irradiation has recently received a renewed interest as a practical method for improving pinning in $REBa_2Cu_3O_y$ (REBCO, RE = Y and rare earth) films [1-3]. In this work, we present superconducting properties in GdBCO films irradiated with 10 MeV Au-ions.

The samples were 0.5-μm thick GdBCO superconducting layers on clad-type textured metal substrates deposited by a pulsed laser deposition (PLD) process. A beam of 10 MeV Au-ions at fluences of 7.0×10^{10} to 4.0×10^{13} Au cm^{-2} was directed to the film surface at normal incidence. The superconducting properties were measured using a Quantum Design superconducting quantum interference device (SQUID) magnetometer.

Figure 1 shows a superconducting transition temperature, T_c, obtained by magnetization measurement as a function of fluence of 10 MeV Au-ions. In the inset of Fig. 1, we plot the calculated dpa (displacement per atom) as a function of fluence. The T_c of the GdBCO films significantly started to drop at around 8.0×10^{11} Au cm^{-2} (2.5×10^{-3} dpa) with Au-ion dose, and superconductivity disappeared at 4.0×10^{13} Au cm^{-2} (1.2×10^{-1} dpa). In the case of YBCO thin films irradiated with 200 keV He-ion, significant T_c degradation begins to occur at 3×10^{14} He cm^{-2}, corresponding to about 2×10^{-3} dpa [4], which is consistent with the result obtained from this experiment.

Figure 2 shows a critical current density, J_c, as a function of the magnetic field for pristine and the irradiated films at fluences of 4.0×10^{11} and 5.5×10^{11} Au cm^{-2}. The J_c enhancement as a function of magnetic field are displayed in the inset, where J_c enhancement is defined as the following equation:

(J_c of irradiated film – J_c of pristine film) / J_c of pristine film.

We found that the 10 MeV Au-ion irradiation yields up to more than 60% J_c enhancement in the magnetic field over 2 T. These results indicate that 10 MeV Au-ions irradiation is effective to provide strong pinning defects in the high-T_c GdBCO superconducting film.

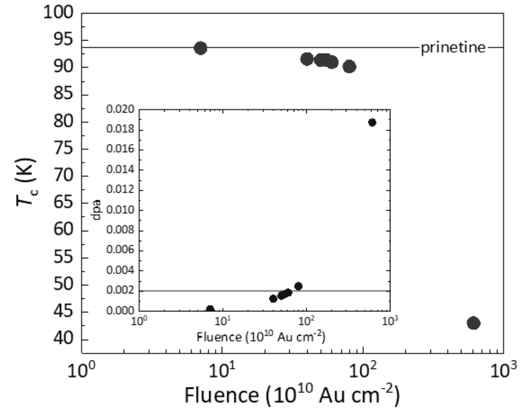

Fig. 1. Superconducting transition temperature T_c as a function of fluence for GdBCO films irradiated with 10 MeV Au-ions. The inset shows the calculated dpa (displacement per atom) as a function of fluence.

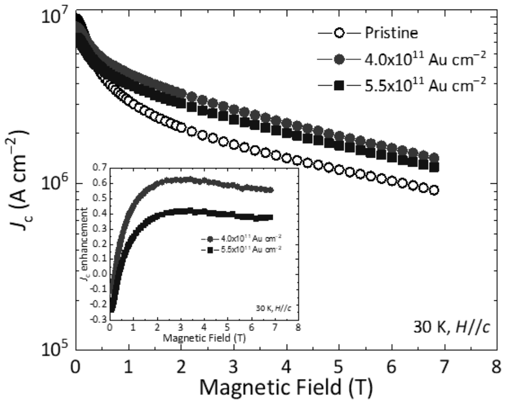

Fig. 2. Critical current density J_c as a function of magnetic field for a pristine (prior to irradiation) GdBCO film and films irradiated at 4.0×10^{11} and 5.5×10^{11} ion cm^{-2} of 10 MeV Au-ions at 30 K. The inset shows calculated J_c enhancement.

References

[1] H. Matsui *et al.*, Appl. Phys. Lett. **101**, 232601 (2012).
[2] Y. Jia *et al.*, Appl. Phys. Lett. **103**, 122601 (2013).
[3] M. W. Rupich *et al.*, IEEE Trans. Appl. Supercond. **21**, 6601904 (2016).
[4] S. Vadlamannati *et al.*, Phys. Rev. B **43**, 5290 (1991).

1 - 13

Preparation of Platinum-Nanocone Electrode Catalysts by Using Track-etched Membranes as Templates

H. Koshikawa[a], Y. Sato[b], S. Yamamoto[a], M. Sugimoto[a], S. Sawada[a] and T. Yamaki[a, b]

[a]Department of Advanced Functional Materials Research, TARRI, QST,
[b]Graduate School of Science and Technology, Gunma University

Metal nanocones directly integrated with a conducting substrate have the following structural advantages for electrocatalyst performance [1-3].

(i) the large surface areas accelerate the surface reaction

(ii) the open space among the nanostructures has efficient mass transfer

(iii) the nanocone shape, *i.e.*, a fine tip plus large base, enhances mechanical stability.

Our recent interest has been that the conical pores of the track-etched membranes can be used as a template for nanocone preparation. We report here the preparation of platinum nanocones by electrodeposition in the polycarbonate (PC) track-etched membrane [4] and their electrochemical characterization for applications to electrode catalysts.

A 50-μm thick PC film was irradiated with 150 MeV ^{40}Ar at fluences of 1.0×10^8 and 3.0×10^8 ions/cm^2 from the TIARA AVF cyclotron, QST-Takasaki. The experimental configurations for the irradiation were set so that the bombarding ions could stop inside the PC film. Etching of the irradiated film was then performed in a 2.0 M sodium hydroxide (NaOH) solution at 60 °C, leading to the formation of non-penetrating conical pores. A 50-nm thick platinum layer was deposited on the surface of the ion track-etched membranes by sputter deposition. This was used as a cathode for electroplating platinum with PRECIOUSFAB Pt3000 (Tanaka Kikinzoku Kogyo Co., Ltd.) at 60 °C by applying a voltage of 5.0 V for 3 min. The platinum nanocones were exposed by removing the PC film with an aqueous NaOH solution. The electrochemically active surface area (ECSA) were estimated by cyclic voltammetry (CV) in a nitrogen-saturated 0.5 M sulfuric acid solution between 0.02 and 1.17 V (vs. RHE). The electrocatalytic activity for the oxidation reaction of ethanol was evaluated by CV in an aqueous solution containing 0.5 M ethanol and 0.5 M sulfuric acid as the electrolyte.

Figure 1 shows scanning electron microscope (SEM) images of (a) the cross-section of the PC ion-track membrane obtained after the 40-min. etching and (b) the resulting platinum nanocones. The ion-track membrane appeared to have conical pores with a surface diameter of 550 nm and a depth of 2.4 μm. We confirmed that these pore dimensions roughly agreed with the base diameter and height of the nanocones, respectively.

The platinum nanocones of the same size were prepared at the areal density (corresponding, in principle, to the ion-beam fluence) of 1.0×10^8 /cm^2 and afforded to the electrochemical measurements. For comparison, a platinum film was electrodeposited on an as-purchased flat PC membrane. Figure 2 shows their CV curves of the ethanol oxidation reaction. Note that the current densities were standardized by ECSA and taken at 0.7 V vs. RHE on a forward scan. The current density was 3.2 times higher for the platinum nanocones than for the platinum film. During the voltammetry of the nanocones, the local high electric field was generated especially around each of their fine tips. This phenomenon might induce an attraction force on surrounding ethanol molecules to the electrode surface, thereby increasing an apparent reaction rate [2]. In conclusion, our platinum nanocones could be promising as an electrode catalyst material.

References

[1] S. M. Choi *et al.*, Electrochem. Acta **53**, 5804 (2008).
[2] M. Liu *et al.*, Nature **537**, 382 (2016).
[3] P. Serbun *et al.*, Eur. Phys. J. Appl. Phys. **58**, 10402 (2012).
[4] Y. Sato *et al.*, QST Takasaki Ann. Rep. 2017, **QST-M-16**, 40 (2019).

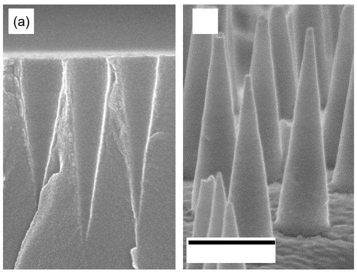

Fig. 1. SEM images of (a) the cross-section of the PC ion-track membrane and (b) the platinum nanocones.

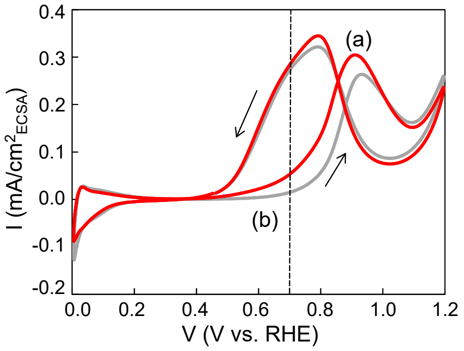

Fig. 2. CV curves of the ethanol oxidation reaction for the (a) platinum nanocones and (b) plate. The scan speed was 20 mV/s. The arrows indicate a scan direction.

1 - 14 Pt Nanoparticles on Ar$^+$-irradiated Carbon Support: Irradiation Defects Strengthen Pt-C Interaction for Higher Electrocatalytic Activity

H. Okazaki[a], A. Idesaki[a], H. Koshikawa[a], D. Matsumura[b],
S. Yamamoto[a] and T. Yamaki[a]

[a]Department of Advanced Functional Materials Research, TARRI, QST,
[b]Materials Sciences Research Center, JAEA

Pt nanoparticles on the Ar$^+$-irradiated glassy carbon (GC) substrate exhibited a higher oxygen reduction reaction (ORR) activity than those on the non-irradiated one [1,2]. This result suggests that the irradiation defects in GC would electronically affect the Pt nanoparticles; the extended X-ray absorption fine structure of the Pt L-edge actually indicated the shrinking of the Pt-Pt bond length in Pt nanoparticles on the irradiated GC [3]. Our DFT calculations also pointed out the lowering of the d-band center energy of the Pt nanoparticles due to vacancies at the graphite surface, which probably led to higher activity [4]. Thus, it is of great interest to understand the overall picture of the interface between the Pt nanoparticles and irradiated carbon. We examined the electronic structure near the interface in the carbon support by surface-sensitive X-ray absorption near-edge structure (XANES) measurements [5].

The HOPG supports were irradiated with 380 keV Ar$^+$ at a fluence of 1.0×10^{14} ions/cm^2 in a 400-kV ion implanter. In order to distinguish the C-C σ^* and π^* states in the XANES spectra, we used the HOPG as the carbon support and selected the E-vector direction of X-ray radiation. The Pt nanoparticles were deposited on the Ar$^+$-irradiated HOPG supports by RF magnetron sputtering. The XANES measurements of the C K-edge with a probing depth of approximately 0.6 nm (corresponding to a thickness of a few graphene layers) were performed at room temperature and below 2×10^{-8} Pa at BL-8, SR Center in Ritsumeikan University. We used linear polarized light with the E-vector and exposed the sample at 90° and 30° from the vertical direction of the sample plane. C K-edge spectra with C-C π^* intensities comparable to those of C-C σ^* can be observed at 30° while the spectra with only the C-C σ^* states can be acquired at an angle of 90°.

In order to estimate the quantitative change in the density of states (DOS), we fitted the spectra measured at 30° for the pristine HOPG, the irradiated HOPG, Pt/HOPG, and Pt/irradiated HOPG, as shown in Fig. 1. We can identify peaks (A) to (E) based on elaborate comparative analyses using our spectral results at 90° [5] and the assignments in ref. [6]; these correspond to (A) the π^* (~285 eV), (B) C-H* or C=O* (~288 eV), (C) π_2 (289.0 eV), (D) σ^* (~291.5 eV), and (E) σ_1 (292.5 eV) states. The Pt deposited samples additionally exhibited peak (F) at around 284 eV, which could be assigned to the Pt-C bonding state. The intensity ratio of peak (F) to peak (A) was higher for Pt/irradiated HOPG than for Pt/HOPG, indicating that the introduction of vacancies in the graphite surface would modify the electronic structure caused by the Pt-C interaction. If we assume such spectral modification to be relevant to the enhancement of the ORR activity, the Pt-C interaction should be one of the key factors for better electrocatalysts. In this sense, therefore, the modified Pt-C bonding state would be an origin of the observed structural and electronic changes in the Pt nanoparticles, *i.e.*, the lowering of the d-band center and the shrinking of the Pt-Pt bond length.

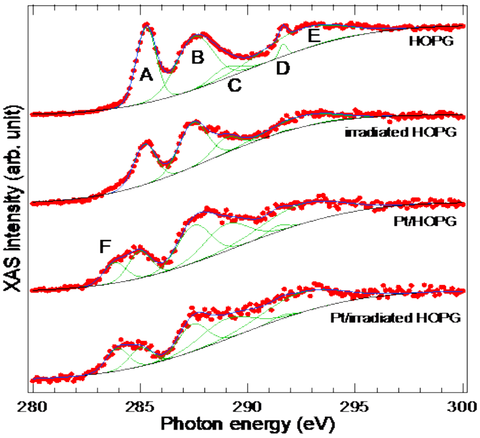

Fig. 1. All XANES spectra with the curve fitting result. The red dots, blue line, and green lines indicate the experimental data, the fitting results, and the fitting peak components, respectively.

The DFT calculations in ref. [7] suggested that vacancy introduction in the carbon support leads to strong hybridization between Pt and carbon, which would be a reason for increased ORR activity. In other words, the Ar$^+$-irradiation-induced vacancies probably make the Pt-C bonding stronger.

Acknowledgments

This work is partially supported by JSPS Grant-in-Aid for Scientific Research (KAKENHI) Grant Number 18H01923.

References

[1] T. Kimata *et al*., Surf. Coating. Tech. **306**, 123 (2016).
[2] T. Kimata *et al*., Nucl. Instrum. Meth. Phys. Res. B **444**, 6 (2019).
[3] K. Kakitani *et al*., Radiat. Phys. Chem. **153**, 152 (2018).
[4] K. Kakitani *et al*., Surf. Coating. Tech. **355**, 259 (2018).
[5] H. Okazaki *et al*., J. Chem. Phys. **152**, 124708 (2020).
[6] A. Nikitin *et al*., Surf. Sci. **602**, 2575 (2008).
[7] D.-H. Lim *et al*., J. Phys. Chem. C **115**, 22742 (2011).

1 - 15 Low-resistance Cation Exchange Membranes for HI Concentration Prepared by Ion-Track Graft Polymerization

T. Miyashita[a), b)], M. Nomura[a)], S. Sawada[b)], H. Koshikawa[b)] and T. Yamaki[b)]

[a)]Department of Applied Chemistry, Shibaura Institute of Technology,
[b)]Department of Advanced Functional Materials Research, TARRI, QST

The thermochemical Iodine-Sulfur (IS) process [1] for large-scale hydrogen production is composed of the following three reactions:

$SO_2 + I_2 + H_2O \rightarrow H_2SO_4 + 2HI$ (Bunsen reaction) (1)
$2HI \rightarrow H_2 + I_2$ (HI decomposition) (2)
$H_2SO_4 \rightarrow H_2O + SO_2 + 0.5O_2$ (H_2SO_4 decomposition) (3)

A distillation operation is necessary to extract concentrated HI between reactions (1) and (2). A key to achieving efficient distillation is to obtain the HI solution exceeding its azeotropic composition because the energy consumption can be minimized by restricting water vaporization.

For this purpose, electro-electrodialysis (EED) for HI concentration using a cation exchange membrane (CEM) was proposed [2]. We have so far been working on the preparation of the CEMs by a γ-ray grafting method and their EED testing [3]. Our key finding was that the voltage of an EED cell was reduced due to the low ohmic resistance of the CEM, but we still need further voltage reduction considering energy requirements for practical large-scale applications.

Therefore, we report here the preparation of new low-resistance CEMs by an ion-track grafting technique (Fig. 1). The base film was irradiated with high-energy ion beams to form cylindrical latent tracks, into which the graft chains were introduced. The resulting one-dimensional ion channels in the thickness direction are expected to efficiently transport protons for lower membrane resistances.

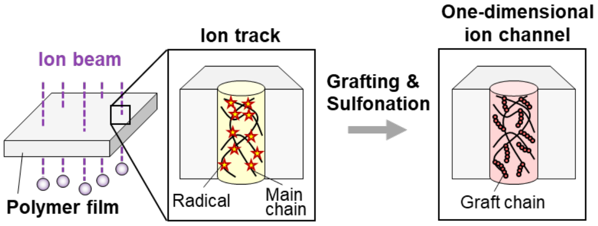

Fig. 1. Scheme for the preparation of a CEM by ion-track graft polymerization.

A 25 μm thick ethylene-co-tetrafluoroethylene (ETFE) film was irradiated with 560 MeV ^{129}Xe ion at a fluence of 3.0×10^8 ions/cm^2. An irradiated film was immersed in a toluene solution of styrene with volume concentrations of 50, 75, and 100%, and then kept at 60 °C for 1–24 h for graft polymerization. For sulfonation, the grafted film was immersed in a 1,2-dichloroethane solution of 0.2 mol/L chlorosulfonic acid at 50 °C for 8 h. The ion exchange capacity (IEC) was measured by an ion-exchange titration method. The resistance of the CEM was measured in an aqueous HI/I$_2$ solution ([HI] = [I$_2$] = 10 mol/kg) by a two-probe AC impedance technique.

The degree of styrene grafting was controlled by the reaction time and styrene concentration. The films with the grafting degree of 6.3-12% were sulfonated to prepare the CEMs with the IEC of 0.45-0.90 mmol/g. The sulfonation degree, the molar ratio of the sulfonic acid groups to the total grafted styrene units, was high enough for all the CEMs.

Figure 2 shows the relationship between the IEC and the membrane resistance for the ion-track grafted CEMs. The membrane resistance decreased with increasing the IEC. Importantly, this was lower than that of the conventional γ-ray grafted CEM at any IEC; for example, at the highest IEC of 0.9 mmol/g, it was 0.83 Ω cm^2, which represents a reduction of 45%. Accordingly, we can confirm efficient proton transport through one-dimensional ion channels of the ion-track grafted CEMs.

The preliminary, but promising result in the above spawns us to perform the EED tests using the low-resistance ion-track grafted CEMs. The cell voltage can be reduced compared to the case with the γ-ray grafted CEM. Further studies are now in progress.

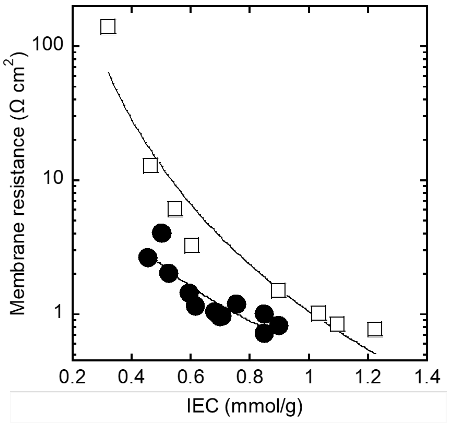

Fig. 2. Relationship between the IEC and membrane resistance for ion-track (●) and γ-ray grafted CEMs (□).

References

[1] S. Kasahara *et al.*, J. Chem. Eng. Jpn. **36**, 887 (2003).
[2] K. Onuki *et al.*, J. Membr. Sci. **192**, 193 (2001).
[3] N. Tanaka *et al.*, J. Membr. Sci. **346**, 136 (2010).

1 - 16 Overvoltage Reduction in Membrane Bunsen Reaction by Using Radiation-Grafted Cation Exchange Membranes

S. Sawada[a], N. Tanaka[b], S. Kubo[b], S. Imabayashi[c], M. Nomura[c] and T. Yamaki[a]

[a]Department of Advanced Functional Materials Research, TARRI, QST,
[b]Graduate School of Engineering and Science, Shibaura Institute of Technology,
[c]HTGR Research & Development Center, JAEA

The iodine-sulfur (IS) process is a promising technique for thermochemical water splitting to yield hydrogen [1] and consists of the following three reactions:

$2H_2O + SO_2 + I_2 \rightarrow H_2SO_4 + 2HI$ (~400 K) (1)
$H_2SO_4 \rightarrow 0.5O_2 + SO_2 + H_2O$ (700-1200 K) (2)
$2HI \rightarrow H_2 + I_2$ (500-800 K) (3)

The use of SO_2 and I_2 as recycling agents allows water to be decomposed at temperatures far lower than can be achieved for direct thermal decomposition (~4000 K).

Dokiya *et al*. proposed a new idea of the Bunsen reaction (Eq. (1)) by using a two-compartment electrolysis cell for energy consumption saving [2]. In this so-called membrane Bunsen reaction, the anode and cathode compartments are separated by a cation exchange membrane (CEM) and filled with aqueous solutions of SO_2 and I_2, respectively. During electrolysis, the following electrode reactions occur, and H^+ is simultaneously transported across a CEM from the anode to cathode side:

Anode: $SO_2 + 2H_2O \rightarrow H_2SO_4 + 2H^+ + 2e^-$ (4)
Cathode: $I_2 + 2H^+ + 2e^- \rightarrow 2HI$ (5)

To date, the commercial Nafion has been used as a CEM for the membrane Bunsen reaction. In this case, however, due to its high resistance for H^+ transport, the reaction overvoltage, V_{over}, was too high to be acceptable for industrial application. In order to reduce the V_{over}, the novel CEM with low resistance is needed.

In this study, we prepared the CEMs by a radiation-grafting method and applied them to the membrane Bunsen reaction [2]. A low-resistance grafted CEM was expected to reduce the V_{over}. In addition, the porous Au cathode with larger surface area was used instead of the conventional non-porous Pt cathode [2].

The CEMs were prepared by γ-ray irradiation of the base ethylene-*co*-tetrafluoroethylene (ETFE) film, grafting of styrene and subsequent sulfonation of the styrene units. The degree of styrene grafting increased with the reaction time and reached the maximum of 92%. The obtained CEMs exhibited the ion exchange capacity (IEC) in the range of 0.4–2.9 mmol/g. The CEM with the highest IEC of 2.9 mmol/g showed the resistivity of 5.5 Ω cm, which was less than half that of a Nafion 212 membrane (12 Ω cm).

Table 1 shows the conditions of the membrane Bunsen reaction tests. The anolyte was an aqueous solution of SO_2 (1.0 mol/kg) and H_2SO_4 (3.2 mol/kg), while the catholyte was an aqueous solution of HI (2.5 mol/kg) and I_2 (2.5 mol/kg). In the galvanostatic mode, the V_{over} was measured at the different current density, I, ranging from 0 to 200 mA/cm^2.

Figure 1 shows the V_{over} as a function of the I. In the low-I region (< 20 mA/cm^2), the V_{over} steeply increased for Run 2 due to the high activation potential for the cathode reaction. In contrast, Run 1 exhibited the far lower increase rate of V_{over} probably because the larger surface area of the porous cathode decreased the activation potential.

At the high-I region (> 50 mA/cm^2), the V_{over} linearly increased with increasing the I. The V_{over} at the maximum I of 200 mA/cm^2 for Run 1 was 0.21 V and was only one-third that for Run 2 (0.66 V). This result was mainly due to the difference in the CEM resistance corresponding to the slope of the line; the resistance values were estimated to be 0.52 and 2.1 Ω cm^2 for Run 1 and 2, respectively. It was concluded that the V_{over} was successfully reduced by using the low-resistance radiation-grafted CEM [2].

Table 1
Experimental conditions of the reaction tests.

Run	Membrane	Anode	Temp.
1	Grafted CEM (IEC=2.9 mmol/g)	Porous Au	50°C
2	Nafion 212 (IEC=0.90 mmol/g)	Non-porous Pt	20°C

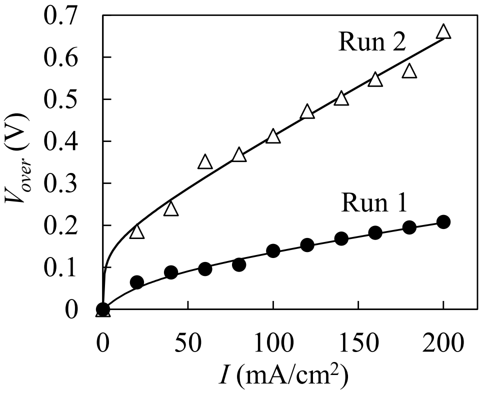

Fig. 1. The V_{over} as a function of the I for Runs 1 and 2.

Acknowledgments

This work was partially supported by the Council for Science, Technology and Innovation (CSTI), Cross-ministerial Strategic Innovation Promotion Program (SIP), "energy carrier" (Funding agency: JST).

References

[1] O. Myagmarjav *et al.*, Int. J. Hydrogen Energy **44**, 19141 (2019).
[2] S. Sawada *et al.*, Int. J. Hydrogen Energy **45**, 13814 (2020).

1 - 17 Vacancy-induced Magnetism in Gd-doped GaN Film Probed by Spin-polarized Positron Beam

M. Maekawa, S. Sakai, A. Miyashita and A. Kawasuso

Department of Advanced Functional Materials Research, TARRI, QST

Diluted magnetic semiconductors (DMSs) materials, such as Gadolinium-doped gallium nitride (GaGdN), have much attracted interest because the both of semiconducting and magnetic properties are emphasized at development of spintronics devices. Actually, it has been observed that Gd ion implanted GaGdN crystals exhibit room temperature ferromagnetism [1]. Although each Gd atom has a magnetic moment of 7 μB, the anomalous large magnetic moment as high as 4000 μB/Gd ('colossal' magnetization) has been reported [2]. The origin of such the anomalous magnetic moments is still unclear, however, some possible candidates are proposed, such as the vacancy-type defects [3]. In this study, the relationship between magnetism and vacancy-type defects in GaGdN is investigated employing the Magnetic Doppler broadening (MDB) method, which can detect magnetic moments localized at vacancy-type defects.

Samples used in this study were MBE-grown undoped GaN films with the thickness of 2 μm on sapphire substrates. Gd ions were implanted to these samples at 370 keV at a room temperature using a 400 keV ion implanter. Implantation doses are from 1×10^{12} cm^{-2} to 1×10^{15} cm^{-2}. After implantation, all the samples were annealed at 1173 K in air. The Doppler-broadening annihilation radiation (DBAR) spectra were obtained in the magnetic fields of ± 0.91 T at 300 K and characterized as the S parameter. The magnetic DBAR (MDB) intensities were also obtained as the difference between the S parameters for the positive and negative magnetic fields. Magnetization (M-H) measurements were carried out using a superconducting quantum interference device (SQUID) apparatus.

Figure 1 shows the M-H curves for the GaGdN samples. After the implantation and the subsequentially annealing, magnetizations are observed. Similar to the literature [3], the magnetization is confirmed. Figure 2 shows the incident positron energy dependence of S parameters and MDB intensities. After the Gd implantation and the annealing, S parameters are increased. Since positrons annihilate preferentially at the gallium vacancies [4], this result shows that the gallium vacancies are detected. In the case of the higher dose sample (> 1×10^{15} Gd/cm^2), the large increase of S parameter (~10%) are observed, indicating that the vacancy cluster might be formed. The MDB intensities also increased in the same region. This means that magnetic moments exist at the gallium vacancy clusters. On the other hand, in the low-dose sample with the small increase of S parameter (~4%), which is equivalent to single vacancies [4], MDB intensities show no significant increase. In addition, the magnetic response is very weak for the nitrogen ion implanted GaN sample, which only the gallium vacancies are introduced [5]. Some theoretical / experimental reports ever published propose that the Ga single vacancies relate with the magnetism, however from our MDB measurements, the ferromagnetism may be explained by electron spins associated with lager vacancy clusters.

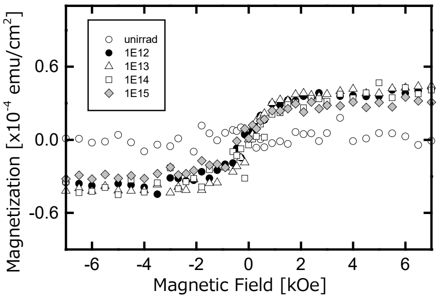

Fig. 1. Dose dependence for Gd-implanted GaN samples of M-H measurements.

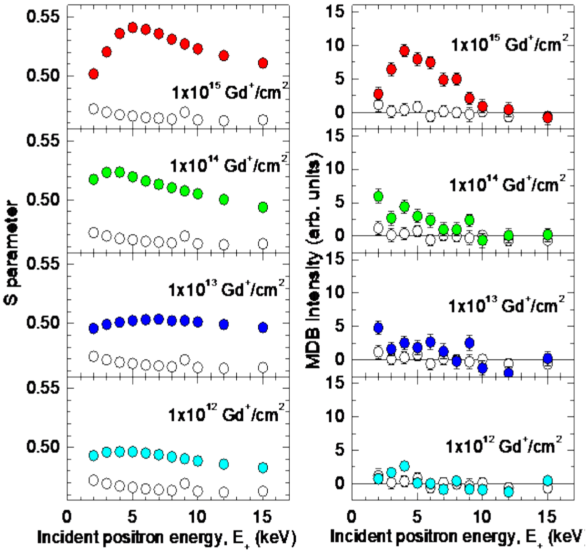

Fig. 2. Incident positron energy dependence for Gd-implanted GaN samples of S parameter and MDB intensity for various Gd implantation dose (filled circles) and for the unimplanted state (open circles).

References

[1] N. Teraguchi *et. al.*, Solid State Comm.**122,** 651 (2002).
[2] M. A. Khaderbad *et. al.*, Appl. Phys. Lett. **91,** 072514 (2007).
[3] S. Dhar *et. al.*, Phys. Rev. Lett. **94,** 037205 (2005).
[4] K. Saarinen *et. al.*, Phys. Rev. Lett. **79,** 3030 (1997).
[5] M. Maekawa *et. al.*, e-J. Surf. Sci. Nanotech. **16,** 347 (2018).

1 - 18

Ion Implantation of High Dense Bi in Si for Quantum Information Applications

K. Miki[a)], M. Maekawa[b)], J. Tang[a)], N. Miyamoto[a)], R. Shimazu[a)] and A. Kawasuso[b)]

[a)]Department of Electrical Material and Engineering, University of Hyogo,
[b)]Department of Advanced Functional Materials Research, TARRI, QST

Recently, it has been proposed and demonstrated that heavy elements are potentially suitable for new computing schemes using bound electrons for high temperature operation, e.g. quantum information processing [1]. However, in practice doping heavy elements into the Si crystal is difficult for a variety of reasons. These include, their low diffusion coefficient and solid solubility for thermal diffusion methods [2], their strong tendency towards surface segregation during molecular beam epitaxy (MBE) [3,4]. To overcome those problems, we used one solution to realize—Bi doping in Si crystal with a use of ion implantation. In this work, we fabricated the Bi doped Si sample with the dopant density of 1.1×10^{21} cm^{-3} (5.5×10^{15} cm^{-2}; 370 keV), 3.4×10^{20} cm^{-3} (1.7×10^{15} cm^{-2}; 370 keV), 1.1×10^{20} cm^{-3} (5.5×10^{14} cm^{-2}; 370 keV), 3.4×10^{19} cm^{-3} (1.7×10^{14} cm^{-2}; 370 keV), 1.1×10^{19} cm^{-3} (5.5×10^{13} cm^{-2}; 370 keV) , at TIARA facility, QST.

First, subsequent annealing (600 °C, 30 min) was applied to the dosed samples after chemical cleaning. Then, decrease of point defects was characterized by the S parameter analysis of positron annihilation measurement, at QST. Bi does not form any ally with Si, so anneal process is much easier rather than other material systems. We chose 600 °C for annealing to recover the ion implantation damages since the temperature is know as solid epitaxial temperature to change the amorphous part into crystal from the crystal region. As imagined, after the anneal at 600 °C, S parameters of samples with the Bi density under 1.1×10^{20} cm^{-3} (dose of 5.5×10^{14} cm^{-2}) decreased, while those over this critical Bi density increased.

Second, we tried ion implantation at elevated temperature of 600 °C. Since we thought accumulated strains could be released even for the samples over 1.1×10^{20} cm^{-3} at 600 °C. Unfortunately, contrary to expectations, S parameters of all the samples increased.

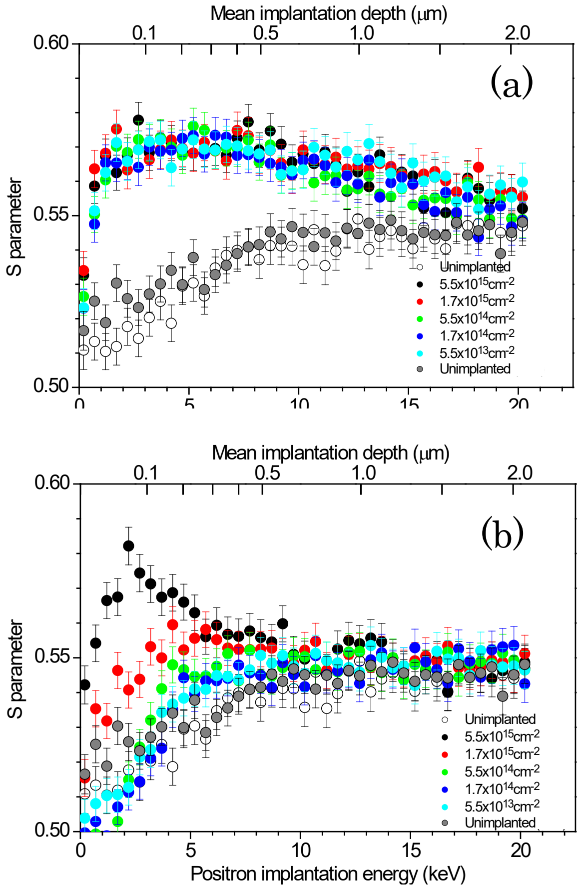

Fig. 1. S parameters of Bi:Si of various dose amounts of Bi dose, ranging of 1.7×10^{13} – 5.5×10^{15}, before (a) and after (b) the anneal at 600 °C for 30 min.

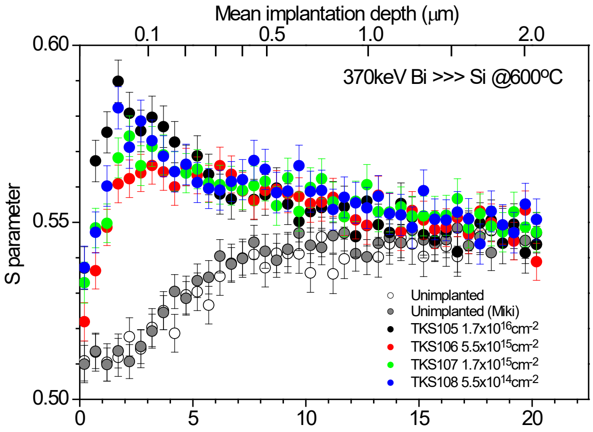

Fig. 2. S parameters of Bi:Si of various dose amounts of Bi dose, ranging of 1.7×10^{13} – 5.5×10^{15}, at elevated temperature of 600 °C.

Acknowledgments

A part of this work was supported by JSPS KAKENHI Grant Numbers JP17H05225, and 17H02777.

References

[1] A.M. Stoneham, *et al.*, J. Phys., Condens. Matter **15,** L447 (2003).
[2] F.A. Trumbore, Bell Syst. Tech. J. **39,** 205 (1960).
[3] K. Sakamoto *et al.*, Jpn. J. Appl. Phys. **32,** L204 (1993).
[4] K. Murata *et al.*, Appl. Phys. Lett. **111**, 152104 (2017).

1 - 19

Hydrogen Trapping Behavior of B2 Ordered Fe-Al Alloy with Irradiation

F. Hori[a], T. Yamada[a], N. Ogawa[a], A. Takano[a], A. Iwase[a],
M. Maekawa[b], A. Kawasuso[b], Q. Xu[c] and K. Ohsawa[d]

[a] Graduate school of Engineering, Osaka Prefecture University,
[b] Department of Advanced Functional Materials Research, TARRI, QST,
[c] Research Reactor Institute, Kyoto University,
[d] Research Institute for Applied Mechanics, Kyushu University

In general, compound alloys are expected for various type of new functional material because of their good properties such as specific strength to weight ratio, oxidation resistance and strength in elevated temperature. On the other hand, hydrogen embrittlement has reported for some compound alloys, such as a Fe-Al alloy. Considering of this hydrogen and defects interaction, we suggest that intermetallic alloys can be proposed as the hydrogen storage material by control of defects. However, the nature of basic defects in this alloy is not necessarily cleared yet. In addition, there is a few reports for defect control in intermetallic alloys by high energetic particles irradiation. We have been investigating defects behavior in many kinds of alloys for radiation damage and materials modification studies. Also, the nature of defects and their hydrogen trapping behavior in B2 ordered Fe-Al alloys with different energy of electron irradiations were examined. As a result, we have successfully controlled the vacancy type in B2 ordered Fe-Al alloy, and we found that hydrogen trapping behavior strongly depends on the vacancy type. In this study, we have performed proton irradiation for B2 ordered Fe-Al alloy in order to know the defects and hydrogen interaction. Fe-48at.% Al alloy sample was prepared by arc melting method in argon atmosphere. Sliced specimens with the thickness of 0.5 mm were annealed at 1073 K for 3 h followed by quenched into water. 1.5 MeV proton irradiation was carried out for these samples with the fluence of 1×10^{16} ions/cm^2 at TIARA in QST, Takasaki. Before and after irradiated samples were examined by X-ray diffraction (XRD) and positron annihilation measurements. Also, thermal desorption analysis (TDA) and micro Vickers hardness measurements have done with annealing isothermally up to 800 K.

Figure 1 shows the TDA spectra of H irradiated Fe-Al alloy. Clear peak appeared at 713 K showing that hydrogen released from radiation induced defects. Proton irradiation makes defects production and hydrogen atoms implantation simultaneously. It is considered that implanted hydrogen atoms are trapped at defects introduced by the irradiation immediately. In addition, desorption peak after proton irradiation did not match for 2 and 8 MeV electron irradiated one. This is probably due to the trapping hydrogen by other type of defects such as di-vacancy.

Figure 2 shows the annealing behavior of micro Vickers hardness with 1.5 MeV proton irradiated Fe-Al alloy. Before irradiation, the hardness is about 372 Hv for this sample. The hardness increased by the irradiation and decreased gradually with heating up to about 720 K. But it changed drastically at this temperature. This temperature corresponds to hydrogen desorption peak appeared in TDA. Then, mechanically hardening arises by the trapping of hydrogen in vacancy type defects. In other words, hydrogen desorption behavior can be deduced by hardness change. It found that the mechanical property recovers by desorption from defects in this alloy.

Acknowledgments

We would like to thank to the staff at QST for their kind support of irradiation experiments.

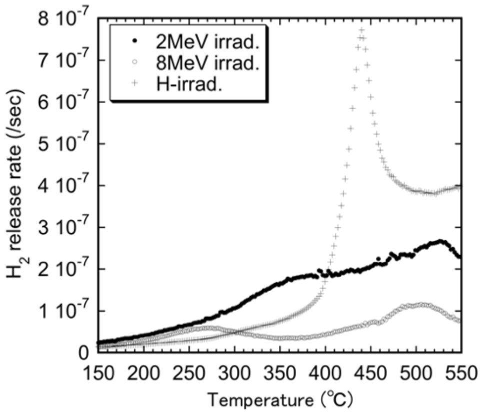

Fig. 1. TDA spectra of H irradiated Fe-Al alloy, as compared to H charged ones after 2 and 8 MeV electron irradiation.

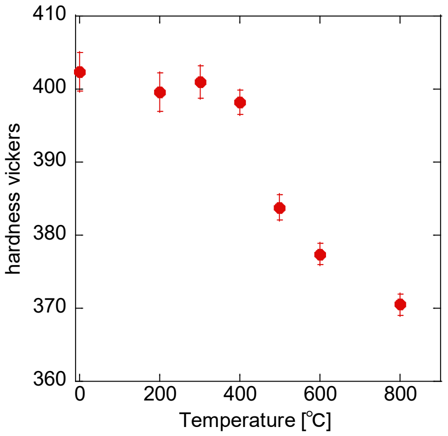

Fig. 2. Micro Vickers hardness change of proton irradiated Fe-Al alloy as a function of annealing temperature.

1 - 20

Single Event Effects Induced on FinFET Static Random-Access Memory

K. Takeuchi[a)], K. Yukumatsu[a)], T. Kato[b)], K. Sakamoto[a)], Y. Tsuchiya[a)], K. Watanabe[a)]
H. Matsuyama[b)], A. Takeyama[c)], T. Ohshima[c)], S. Kuboyama[a)] and H. Shindo[a)]

[a)]Research Unit I, Research and Development Directorate, JAXA,
[b)]Socionext Inc.,
[c)]Department of Advanced Functional Materials Research, TARRI, QST

Thanks to continuous down scaling of the semiconductor manufacturing process over the last 50 years based on the Moor's and Dennard's law, the Fin field effect transistors (FinFETs), which have three-dimentional gate structure (shown in Fig. 1), are currently adopted to the cutting edge semiconductor devices. While it is behind several technology generations compared with commercial processes, the manufacturing process for space parts also continues down scaling [1]. As technology advances, single event effects (SEEs) caused by heavy ion are getting worse. Even in the FinFET generation, it is still a major concern. It's important to evaluate SEEs on these devices for future space mission. The electronics used in the space must stand harsh environments such as heavy ion irradiation. This study investigates SEEs induced on FinFET static random-access memory (SRAM) irradiated with heavy ion.

The device under test (DUT) was fabricated in a commercial 14/16-nm bulk FinFET process. The single-port (1RW) six-transistor (6T) SRAM macros were implemented on a test chip to evaluate SEEs. The DUT contains 5.5 Mbit SRAM cells. The all logical "0", all logical "1" and checkerboard data patterns in the SRAM ("All0", "All1" and "CKB1", respectively) were used for SEE evaluation. For the CKB1, logical "0" and "1" were configured in a checkerboard pattern with "1" written in the first bit. The single event effects on the DUT were evaluated using the Takasaki Ion Accelerators for Advanced Radiation Application (TIARA) at the National Institutes for Quantum and Radiological Science and Technology (QST). A monoenergetic heavy ion beam was used for the evaluation. Table 1 lists ion used in this study and related information. Linear energy transfer (LET) and the ion travel range in Si were calculated by SRIM code [2]. The irradiations were performed at normal incidence and at room temperature.

The single bit upsets (SBUs) and multiple cell upsets (MCUs) were observed in all trials. No sudden current increases, single event latch-up (SEL) or single event functional interrupt (SEFI) were observed in any experiments. Figure 2 shows upset probability density of fail bit map (FBM) in case of Xe irradiation. It was plotted as normalized accumulation of each FBM, showing the average response of certain ion irradiation on certain data pattern. Figure 2 indicates the spacial response of FBMs against heavy ions and dependency on the patterns in SRAMs, which is one of the important parameter for making radiation-hardening-by-design (RHBD) circuits. By considering this spacial response of FBMs in addition to the SRAM bit cell size, the minimum critical length of the redundant transistors can be determined.

According to the further discussion on our previous study [3], characteristic charge collection mechanisms induced on FinFET transistors in SRAM are implied. Based on these results, JAXA is going to develop RHBD methodology, which is applicable on FinFET manufacturing process.

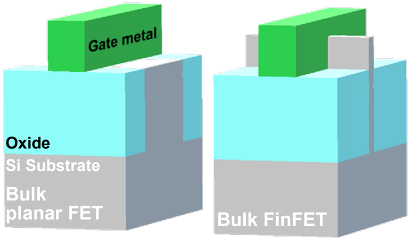

Fig. 1. Bulk planar FET (left) and bulk FinFET (right).

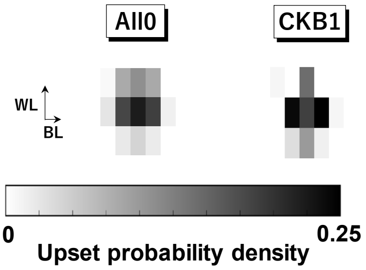

Fig. 2. Upset probability density of fail bit map (FBM) in case of Xe irradiation. WL and BL arrows indicate directions along word-line and bit-line, respectively.

Table 1
Test conditions.

Ion	Net Energy MeV	LET at Si surface MeV/(mg/cm^2)	Ion travel range in Si μm
^{129}Xe	454	68.9	35.0

Acknowledgments

The authors gratefully acknowledge the technical support of Ryoei Technica Corporation and members of the accelerator operation group at TIARA in the experiments.

References

[1] T. Hiramoto, "Prospects for a Data-Driven Society," 2019, Nikkei (in Japanese).
[2] J. F. Ziegler *et al.*, SRIM, the Stopping and Range Ions in Matter 2010 [Online]. Available: http://www.srim.org.
[3] K. Takeuchi *et al.*, "Characteristic Charge Collection Mechanism Observed in FinFET SRAM cells," 2020 (*in press*).

1 - 21 Radiation Damage on Carrier Lifetime of GaAs Subcells in Triple-Junction Solar Cells

T. Nakamura[a)], T. Sumita[a)], A. Ogura[a)], T. Okumura, M. Imaizumi[a)],
S.-I. Sato[b)] and T. Ohshima[b)]

[a)] Research and Development Directorate, JAXA,
[b)] Department of Advanced Functional Materials Research, TARRI, QST

InGaP/GaAs/Ge triple-junction (3J) solar cells are widely used as power sources for spacecraft owing to their high performance. Solar cells suffer damages by radiative particles such as high energy protons and electrons in an orbit. In particular, the degradation of open-circuit voltage (Voc) in the GaAs subcell dominates the damage of 3J solar cells (see Fig. 1). Therefore, the challenge is to understand the radiation effects on minority-carrier lifetime of GaAs subcells in 3J solar cells, which dominates the degradation of Voc in 3J solar cells. In this study, we investigate the radiation effects on the Shockley-Read-Hall (SRH) recombination lifetime in the depletion region of the GaAs subcell using the AB model [1]. In addition, by comparing the results with the characteristics of radiation-induced defects clarified in previous studies, the electrically activated defects behaving as recombination centers in this region is identified.

We employed an InGaP/GaAs/Ge 3J solar cell for space use as a sample. The 3J solar cell was irradiated with electrons at National Institutes for Quantum and Radiological Science and Technology (QST). The electron energy was 1 MeV and the fluence was 3×10^{14} cm^{-2} which is equivalent to the irradiation dose of solar panel in the geostationary orbit for approximately 5 years. Electroluminescence (EL) was measured before and after the electron irradiation. The average internal luminescence efficiency (η_{int}) was calculated using the EL intensity.

Figure 2 plots the dependence of η_{int} and forward-bias voltage on injected current of the GaAs subcell before and after the irradiation. The solid lines are the fitting curves using the 2-diode model. In the low-current regime, the current-voltage characteristics under the dark condition can be reproduced by diode with n=2. In this regime, the recombination current in the depletion region is significantly larger than that in the neutral region. Therefore, the broken lines, which are the calculated η_{int} of the depletion region from the AB model, should coincide with the experimentally obtained η_{int} (closed circles) particularly in the low-current regime. The SRH recombination lifetime in the depletion region was obtained as a parameter in the calculation. Using the obtained SRH recombination lifetimes of before and after irradiation, the damage coefficient for lifetime (K_τ) was estimated. Previous studies have revealed the K_τ for each of the radiation-induced defects in GaAs subcell by electron irradiation from deep level transient spectroscopy (DLTS) study [2]. By comparing the two K_τs obtained in this study and the previous studies, it is possible to estimate which radiation-induced defects are the most effective as recombination centers. The result suggests that H2-type defects [2] in the depletion region of GaAs subcell are the most effective.

In conclusion, minority-carrier lifetime degradation was analyzed and the most effective defects in the depletion region were identified. These results are important for developing high radiation-resistance of space solar cells.

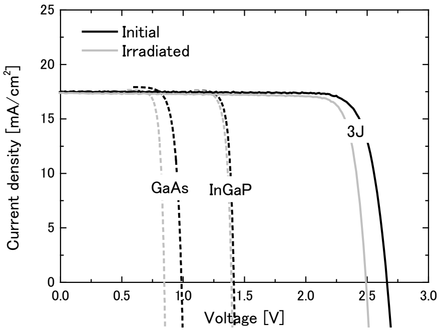

Fig. 1. Change in current-voltage characteristics due to 1-MeV electron irradiation.

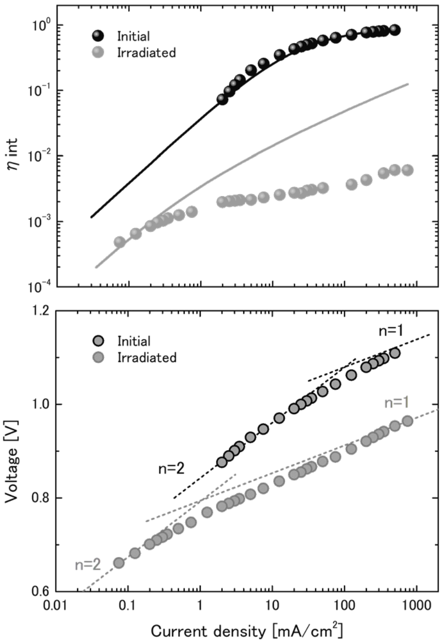

Fig. 2. The dependence of η_{int} and forward-bias voltage on injected current of GaAs subcell before and after the irradiation.

References

[1] T. Nakamura *et al.*, Prog. in Photovolt. **28**, 123109 (2020).
[2] D. Stievenard *et al.*, Phys. Rev. B **34**(6), 4048 (1986).

1 - 22

Fabrication of 3D Arrayed Silicon Vacancies in SiC PN Diodes by Particle Beam Writing

Y. Yamazaki [a], Y. Chiba [a,b], S. -i. Sato [a], T. Makino [a], N. Yamada [a], T. Satoh [a],
K. Kojima [c], Y. Hijikata [b], H. Tsuchida [d], N. Hoshino [d] and T. Ohshima [a]

[a] Department of Advanced Functional Materials Research, TARRI, QST,
[b] Graduate School of Science and Engineering, Saitama University,
[c] Advanced Power Electronics Research Center, AIST,
[d] Central Research Institute of Electric Power Industry

Quantum sensing by which temperature, magnetic and electrical fields can be measured is a promising application utilizing the principles of quantum mechanics. Silicon carbide (SiC) has a couple of spin defects available for a quantum sensor, silicon vacancy (V_{Si}), divacancy (V_CV_{Si}) and nitrogen-vacancy (N_CV_{Si}). A V_{Si}-based quantum sensor is the most appropriate to detect directly the internal state of a SiC power device because it can realize high sensitivity and high spatial resolution sensing at room temperature. Detailed data taken can help to improve device performance. To realize such the sensor with minimum degradation of the device performance, a three-dimensional (3D) grid manner V_{Si} array is required. In this study, we have fabricated 3D arrayed V_{Si} in a SiC pn diode by particle beam writing (PBW). Optical addressability of the V_{Si}s, the requirement for quantum sensing, were checked using optically detected magnetic resonance (ODMR) measurements.

The samples used in this study were in-plane pn (p^+nn^+) junction diodes with an opposite electrode fabricated in epitaxial 4H-SiC layers. A 3D arrayed V_{Si} was created at a vicinity of the electrode using the 3MV single-ended accelerator. To change the depth of the V_{Si}, ion species (H and He) and ion energy (0.5-3 MeV) were properly selected on the basis of a Monte Carlo simulation (SRIM). A laser-scanned confocal fluorescence microscopy (CFM) with a 671nm laser was utilized to confirm V_{Si}s and evaluate their optical properties at room temperature. For ODMR measurements, a loop coil was set just behind the sample for radio-frequency (RF) field exposure.

The CFM images of the sample are shown in Fig. 1(a) and (b). For the in-plane (XY) image, a dot array consisting of three different luminescent spots were clearly observed as designed. To confirm the depth of each spot, a cross-section (XZ) scan was carried out. As shown in Fig. 1(b), horizontally aligned three luminescent-spots-lines were observed. With correcting the influence of refractive index mismatch between air (=1) and SiC (=2.6), the depth was estimated to be ~5, 20 and 60 μm for the shallowest, middle and deepest spots, respectively. These were in good agreement with the values expected by the SRIM simulation.

Next, we performed ODMR measurements for three different-depth V_{Si}s. The ODMR spectra obtained from each spot were summarized in Fig. 2. The peak around 70 MHz, which was assigned as an ODMR peak from V_{Si} under a zero magnetic field [1], was observed for all spots. These results suggest that the 3D arrayed V_{Si} is capable of measuring the entire area of a SiC device from the fact that the thickness of a typical SiC device is on the order of 10 μm.

In conclusion, we successfully introduced a V_{Si}-based 3D quantum sensor into a SiC pn device. This is expected to be applied to practical SiC devices for improving their performance.

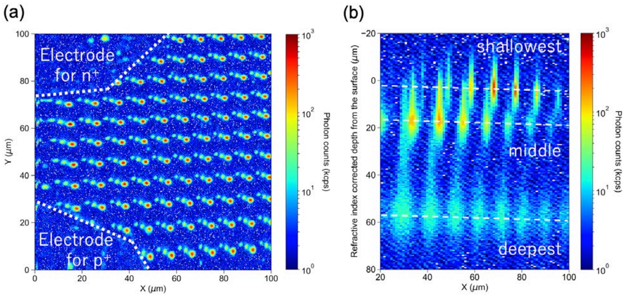

Fig. 1. (a) An in-plane (XY) and (b) a cross-section (XZ) PL mapping of a 3D arrayed V_{Si} in the pn diode.

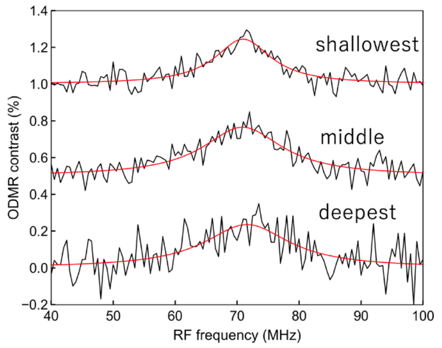

Fig. 2. ODMR spectra obtained from three different-depth luminescent spots under a zero magnetic field. Red lines show a Lorentzian fit of the data.

Acknowledgments

This work was supported by JSPS KAKENHI 17H01056 and 18H03770, MEXT Quantum Leap Flagship Program (MEXT Q-LEAP) Grant Number JPMXS0118067395. This study was carried out within the framework of IAEA CRP F11020.

Reference

[1] D. Simin *et al.*, Phys. Rev. Appl. **4**, 014009 (2015).

1 - 23

Hydrogen Storage Properties of Surface-Modified Palladium by Ion Irradiation

H. Abe[a], R. Morimoto[b] and H. Uchida[b]

[a]Department of Advanced Functional Materials Research, TARRI, QST,
[b]Course of Applied Science, Graduate School of Engineering, Tokai University

The effect of surface modification on the hydrogen absorption behavior in hydrogen-metal systems is an important topic from a scientific and industrial perspective. Palladium (Pd) can absorb large amounts of hydrogen; therefore, many studies have focused on the Pd-H system of ultrafine structure Pd [1]. A surface phenomenon is the formation of the Pd-H system due to the interaction of the H2 molecule with Pd. The introduction of vacancy-type defects in the Pd surface layer effectively improved the hydrogen absorption rate [2]. Regarding hydrogen absorption in materials, the absorption concentration of hydrogen atoms and the hydrogen absorption rate strongly depends on the metal's surface state. These results suggest that Pd's hydrogen storage characteristics may be improved by surface modification using ion irradiation. In this study, following last year's report [3], defect introduction was followed by further high-energy ion irradiation, and the initial hydrogen absorption reaction rate (initial reaction rate) was investigated. The initial reaction rate is equivalent to the recharging speed of the storage battery.

The samples used in this study were Pd sheets (99.99% purity, $7.5 \times 7.5 \times 0.1$ mm^3). The Pd samples were irradiated with 7 and 13 MeV N ions at room temperature using a 3 MV tandem accelerator at doses of 1×10^{14} cm^{-2}. The hydrogen absorption rates of irradiated Pd samples were investigated using an electrochemical method together with the previously reported energies (30, 100, 350 keV and 5 MeV). The initial reaction rate was measured by the change of current density mA(*g-alloy*)$^{-1}$ at a constant voltage -0.93 V and room temperature, and the hydrogen concentration absorbed by the negative electrode was calculated. The details of the electrochemical measurements have been reported elsewhere [4].

Figure 1 shows the correlation between the initial reaction rate and the ion irradiation energy, derived from the hydrogen storage curve of Pd irradiated with N$^+$. The horizontal axis shows the irradiation energy and ion implantation depth in Pd, and the vertical axis shows the initial reaction rate of hydrogen storage in Pd. The initial reaction rate of Pd become about 8 times faster as the irradiation energy was increased to 30, 100 and 350 keV in the case of N$^+$ irradiation. On the other hand, the initial reaction rate of Pd became slower as the irradiation energy was increased to 5, 7 and 13 MeV.

Since the initial reaction mainly occurred on the Pd surface layer, ion irradiation on the Pd surface layer is critical in the initial reaction rate. The upward convexity of the initial reaction rate depending on irradiation energy is due to the interaction of ion irradiation. The SRIM simulations [5] show that Pd's amount of defect formation is higher at the deeper implantation depth than at the surface layer for high energy MeV irradiation than for keV irradiation. On the other hand, the maximum defects formation in the Pd surface layer has a peak at more than 1000 nm above 5 MeV, while defects are continuously formed from the Pd surface layer to about 200 nm at 350 keV.

Therefore, the irradiation in the keV region, where a large number of defects are formed on the surface, has a significant effect on the initial reaction rate because the amount of the formation of defects is larger than that in the deep region. From the above, it was found that the introduction of defects into the surface layer by low-energy ion irradiation is more efficient for surface modification to increase the initial reaction rate.

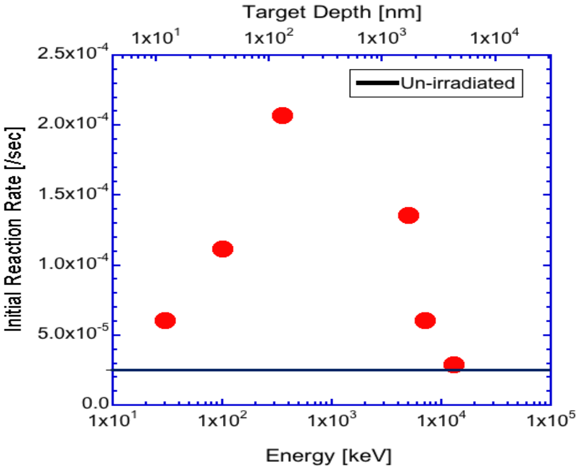

Fig. 1. Correlation between the ion irradiation energy (in the direction of the target defect depth) and the initial reaction rate.

References

[1] H. Uchida *et. al.*, J. Alloys Comp. **253-254**, 547 (1997).
[2] H. Abe *et. al.*, Nucl. Instrum. Meth. Phys. Res. B **206**, 224 (2003).
[3] H. Abe *et. al.*, QST Takasaki Ann. Rep. 2018, **QST-M-23** 60 (2019).
[4] H. -H. Uchida *et. al.*, J. Alloys Comp. **253-254**, 525 (1997).
[5] J. F. Ziegler, *Handbook of Ion Implantation Technology*, 1 (Elsevier, Amsterdam 1992).

1 - 24

Cu^{2+} Adsorption Capacity of Fibrous Grafted Metal Adsorbent Under Highly Alkaline Condition at pH 15

Y. Ueki and N. Seko

Department of Advanced Functional Materials Research, TARRI, QST

Along with the ultra-high integration of semiconductor devices, it is necessary to remove a trace amount of copper ions (Cu^{2+}) contaminated in surface etching solutions for Si wafers, in order to improve the manufacturing yield. The surface etching solutions are composed of high concentration alkaline aqueous solutions, such as 48wt% NaOH or 48wt% KOH solutions with pH > 15. The objective of this study was to evaluate the Cu^{2+} adsorption capacity of a fibrous grafted metal adsorbent under a highly alkaline condition.

In this study, six types of the fibrous grafted metal adsorbents with different functional groups were compared. The six functional groups were diol (Diol), sulfonic acid (SA), iminodiacetic acid (IDA), ethylene diamine (EDA), iminodiethanol (IDE) and piperazinyl-dithiocarbamate (PZ-DTC) groups. The PZ-DTC-type metal adsorbent was synthesized by radiation-induced emulsion grafting and subsequent three-step chemical modifications consisting of amination, deprotection, and dithiocarbamation, as previously reported [1]. The Cu^{2+} adsorption capacities of the metal adsorbents under a highly alkaline condition were examined through the batchwise adsorption tests. In this study, a 100 ppm Cu^{2+} aqueous solution adjusted to pH~15 using 10 M NaOH solution. The molar concentration ratio of Na^{+} and Cu^{2+} in the solution was 10 M and 1.573 mM. Therefore, the Na^{+} concentration was approximately 6400 times higher than that of Cu^{2+}, and the metal adsorbents were compelled to selectively adsorb a marginal amount of Cu^{2+} from the solution with the high concentration of Na^{+}. As shown in Table 1, the Diol-type adsorbent could not adsorb Cu^{2+}. This was expected because the diol group is hydrophilic having no metal ion adsorption capability. Similarly, the SA-type adsorbent could hardly adsorb Cu^{2+} from a high-concentration Na^{+} aqueous solution with pH~15. The Cu^{2+} adsorption capacity was 0.005 mmol-Cu^{2+}/g-adsorbent. This exceptionally low Cu^{2+} adsorption capacity was considered to be due to low metal ion selectivity of the SA group via electrostatic interaction.

In the case of the metal adsorbents with chelating functional groups such as IDA, EDA, IDE, and PZ-DTC groups, although each chelate-type adsorbent could selectively adsorb Cu^{2+} even from a high-concentration Na^{+} aqueous solution with pH~15, the Cu^{2+} adsorption capacities varied substantially. The IDA- and EDA-type adsorbents could selectively remove a trace amount of Cu^{2+}, which was dissolved in a high-concentration Na^{+} aqueous solution at pH 15. The Cu^{2+} adsorption capacities of the IDA- and EDA-type adsorbents were 0.082 and 0.128 mmol-Cu^{2+}/g-adsorbent, respectively. In addition, the Cu^{2+} adsorption capacity of the IDE-type adsorbent, which was used to clean the high alkaline etching aqueous solution of Si wafer and exhibited the highest performance in a previous study [2], was approximately 0.314 mmol-Cu^{2+}/g-adsorbent. The reason for these lower Cu^{2+} adsorption capacities is that the constituent atoms of IDA, EDA, and IDE groups contained oxygen and nitrogen atoms, which exhibit a high affinity for Na^{+}. Therefore, it is considered that various chelate groups such as IDA, EDA, and IDE groups could adsorb Cu^{2+} and Na^{+} simultaneously.

Meanwhile, in the case of the PZ-DTC-type adsorbent, the Cu^{2+} adsorption capacity at pH~15 was improved dramatically up to 0.754 mmol-Cu^{2+}/g-adsorbent. It was approximately 2.4 times higher than that of the IDE-type adsorbent, which is the highest level thus far [2]. The reason for the higher Cu^{2+} adsorption capacity is that the constituent atom of the PZ-DTC group does not contain an oxygen atom (which exhibits a high affinity for Na^{+}) but a sulfur atom (which exhibits a low affinity for Na^{+}). Therefore, the PZ-DTC groups could preferentially adsorb Cu^{2+} while excluding Na^{+}. The above results revealed that the fibrous grafted metal adsorbent with the PZ-DTC group does not lose its metal adsorption function even under a high alkaline condition with pH~15. In addition, it was observed that the PZ-DTC-type adsorbent could recover Cu^{2+} efficiently and selectively from a high-concentration Na^{+} aqueous solution with pH~15.

Table 1
Cu^{2+} adsorption capacity of fibrous grafted metal adsorbents under highly alkaline condition (pH 15).

Adsorbent type	Functional group density [mmol/g-adsorbent]	Cu^{2+} adsorption capacity [mmol-Cu^{2+}/g-adsorbent]
Diol-type	4.496	0.000
SA-type	2.768	0.005
IDA-type	2.172	0.082
EDA-type	3.005	0.128
IDE-type	3.015	0.314
PZ-DTC-type	2.112	0.754

References

[1] Y. Ueki *et al.*, QST Takasaki Annu. Rep. 2018, **QST-M-23**, 46 (2019).

[2] M. Tamada *et al.*, Radiat. Phys. Chem. **81**, 971 (2012).

1 - 25 Synthesis and Facile Surface Modification of Fully Biomass-Derived Fabrics

R. Kakuchi[a)], S. Yamashita[a, b)], T. Hamada[b)], M. Omichi[b)], K. Yoshimura[b)],
Y. Ueki[b)] and N. Seko[b)]

[a)]Division of Molecular Science, Graduate School of Science and Technology, Gunma University,
[b)]Department of Advanced Functional Materials Research, TARRI, QST

Chemical utilization of biomass materials has been desired because of the global petroleum shortage. In this respect, cellulose and lignin, well known wood biomass materials, have been gaining increasing attentions. When considering the wood-biomass structure, biomass is known to be composed of cellulose core and lignin as an outer layer. With taking above points into account, we aimed to artificially mimic the biomass structure based on the biomass-derived materials. Here, cellulose will be used as a facile matrix and lignin sourced polymers will be used as an outer layer. As such, we performed the recombination of cellulose fabrics and lignin-derived vinyl monomers by radiation-induced polymerizations to artificially mimic the wood structure starting from biomass components.

Before we prepared the hybrids from cellulose fabrics, we started our work with polyethylene (PE) fabrics as model substrates to ignore possible side reactions. The schematic procedure is shown in Scheme 1. First, the radiation-induced graft polymerization of pre-irradiated PE fabrics (50 kGy) and methacrylated vanillin (MV) was conducted in 1,4-dioxane at 60 ºC for 5 h to give poly(methacrylated vanillin)-grafted PE (PE-*g*-PMV). A grafting degree (GD) was 136%. The ATR-FTIR spectrum of PE-*g*-PMV showed the anchored surface aldehyde groups. To note here, PMV was revealed to show high reactivity for a wide range of multi-component reactions (MCRs) including the Kabachnik-Fields reaction (KFR) [1], which guarantees the efficient surface modification to afford MCR-ready biomass-sourced hybrids. Therefore, KFR of PE-*g*-PMV (GD = 136%), *p*-anisidine and diisopropyl phosphite was conducted in 1,4-dioxane at 80 ºC for 24 h to obtain polymeric *α*-amino phosphonate-grafted PE (PE-*g*-PAP). The results of IR, solid-state ^{31}P NMR and SEM-EDX indicated the high conversion of the surface aldehyde groups. Additionally, the SEM micrographs of PE-*g*-PAP showed no damage to the fiber structures. These results demonstrated that the PMV segment was successfully anchored on the PE surfaces and revealed to show high compatibility with the KFR process even on the surface.

Since the model reactions with PE fabrics proceeded smoothly, we next prepared hybrids from cellulose fabrics, which is the main concept of this work. The used procedure was following that of PE, except for a dose of 20 kGy instead of 50 kGy and methanol of graft polymerization solvent instead of 1,4-dioxane. The radiation-induced polymerizations and KFR gave PMV-grafted cellulose (Cell-*g*-PMV) (GD = 57%) and PAP-grafted cellulose (Cell-*g*-PAP), respectively. Figure 1 shows ATR-FTIR spectra of cellulose fabrics, Cell-*g*-PMV and Cell-*g*-PAP. The peak of aldehyde groups was observed at 1692 cm^{-1} in the spectrum of Cell-*g*-PMV, and then this aldehyde peak disappeared in the spectrum of Cell-*g*-PAP. Instead, the peak of phosphonate ester units appeared at 979 cm^{-1} in the spectrum of Cell-*g*-PAP. In addition to these IR results, the results of solid-state ^{31}P NMR and SEM-EDX indicated a successful synthesis of Cell-*g*-PAP. Moreover, the SEM micrographs of Cell-*g*-PAP showed no damage to the fiber structures as well as PE-*g*-PAP. All in all, these results chemically proved the recombination of cellulose fabrics and MV by radiation-induced polymerizations and the efficient surface KFR to control surface properties.

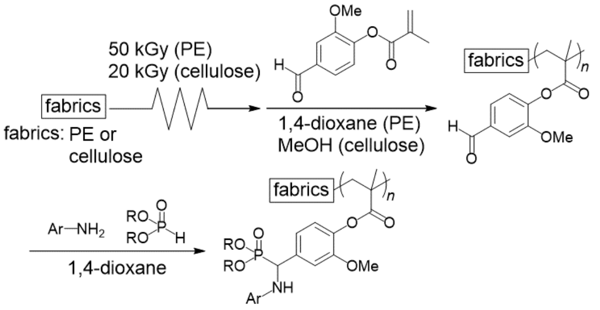

Scheme 1. Schematic procedure of the radiation-induced graft polymerization of MV and the surface KFR.

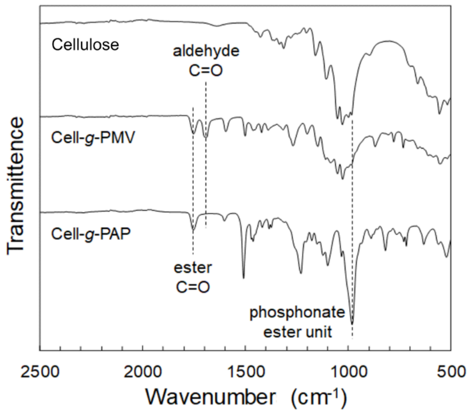

Fig. 1. ATR-FTIR spectra of the cellulose fabrics, Cell-*g*-PMV with a GD = 57% and Cell-*g*-PAP.

Reference

[1] R. Kakuchi *et al.*, Polym. Chem. **9**, 16 (2018).

1 - 26

Synthesis of Graft Polymerization-type Porous Silica Adsorbent with IDA Group and Evaluation of Adsorption Performance Using Micro-PIXE Analysis

Y. Arai[a),b)], S. Watanabe[a)], S. Ohno[a)], M. Nakamura[a)], A. Shibata[a)], F. Nakamura[c)],
T. Arai[c)], N. Seko[d)], H. Hoshina[d)], H. Fukumoto[b)], T. Agou[b)] and T. Kubota[b)]

[a)]Nuclear Fuel Cycle Laboratories, JAEA,
[b)]College of Engineering, Ibaraki University,
[c)]College of Engineering, Shibaura Institute of Technology,
[d)]Department of Advanced Functional Materials Research, TARRI, QST

The spent Plutonium Uranium Redox Extraction (PUREX) solvent containing uranium (U) and plutonium (Pu) is generated from the reprocessing process of spent nuclear fuel. The removal of nuclear materials is an important task for safety storage or disposal of the spent solvent. From our previous studies, the adsorptivity of Zr(IV) to simulate Pu(IV) has shown that the iminodiacetic acid (IDA)-type functional group is effective adsorption in a simulated spent PUREX solvent which is including high concentration of radiolysis product of solvent (dibutyl phosphate) [1]. However, to adapt the actual spent PUREX solvent, additional adsorption performance is required for the adsorbent. In this study, porous silica particles with a high specific surface area were used as a support of the adsorbent, and a new IDA-type adsorbent was synthesized to achieve the high adsorption rate. To introduce the IDA function onto the porous silica particles, the surface of the porous particles was pre-coated with a stylene-divinylbenzen copolymer as the supporting material. The new IDA-type adsorbent was synthesized by graft polymerization of glycidyl methacrylate (GMA) onto the pre-coated porous silica particles. 10 w/v% of GMA was emulsified with 1.0 w/v% of Tween 20 in the pure water. The porous silica and the GMA emulsion solution were put into a polyethylene bag and irradiated with 100 kGy by electron beams (2 MeV and 3 mA) simultaneously. The graft ratio of GMA was 49%. The obtained GMA-grafted silica particle was reacted in a 0.5 mol/L IDA solution (water:ethanol = 1:1 w/v%) at 343 K for 12 h to introduce the IDA functions. The amount of IDA was calculated by the weight increment of before and after IDA reaction and was approximately 2 mmol/g.

To investigate the performance of the new IDA-type adsorbent, the distribution of the surface of the adsorbent and the amount of adsorbed Zr(IV) were measured by micro Particle Induced X-ray Emission (PIXE) analysis. The Micro-PIXE analysis was carried out at the light-ion microbeam line connected to the 3 MeV single-ended accelerator at TIARA. A beam spot size and an irradiation area were 1×1 μm^2 and 100×100 μm^2, respectively. Energy resolution of a detector used for the Micro-PIXE was 110-220 eV at X-ray of 2.3 - 10.5 keV.

Figure 1 depicts the distribution of adsorbed Zr(IV) in the vertical direction of the new IDA adsorbent. In order to compare the change of Zr distribution with time (1~300 min), the intensity of the Zr-Kα line was normalized with the irradiated beam charge. Since the adsorbed Zr(IV) was distributed homogeneously on the adsorbent even in 1 min treatment, the introduced IDA was assumed to be efficiently complex with Zr (IV).

The amount of adsorbed material is known to be proportionally correlated with the total Zr-Kα intensity normalized with ion beam charge [2]. The amount of Zr(IV) was calculated as follows;

$$W_{Zr} = C_{Zr} / 14.59 \qquad (1)$$

W_{Zr}: amount of adsorbed Zr [mg-Zr/g]
C_{Zr}: normalized Zr-Kα intensity [nC^{-1}]

Figure 2 shows the amount of adsorbed Zr estimated by Eq. (1). Although the amount of adsorbed Zr(IV) from the simulated spent solvent with the IDA-silica adsorbent was approximately 1/10 of that from the 1M HNO$_3$ solution, the amount of adsorbed Zr(IV) reached an adsorption equilibrium in 1 to 30 min. The adsorption equilibrium of the commercial chelate resin was approximately 60 min [2]; thus, the adsorption kinetics was improved by this study.

References

[1] F. Nakamura *et al.*, Proc. DEM 2018, 195 (2018).
[2] Y. Arai *et al.*, Nucl. Instrum. Meth. Phys. Res. B **477**, 54 (2020).

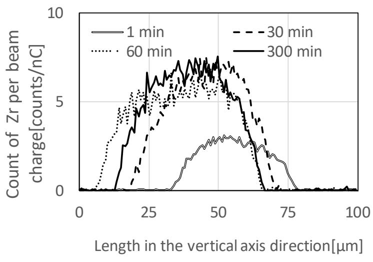

Fig. 1. Distribution diagram of Zr(IV) in the vertical direction recovered from the 1M HNO$_3$ solution.

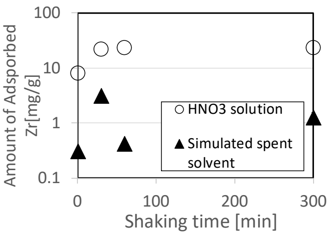

Fig. 2. Amount of adsorbed Zr(IV) onto the IDA-silica adsorbent estimated by micro-PIXE.

1 - 27

Fabrication of a Heavy Metal Adsorbent by a Simplified Radiation-Induced Emulsion Graft Polymerization Method

M. Omichi, Y. Ueki, N. Seko and Y. Maekawa

Department of Advanced Functional Materials Research, TARRI, QST

Contamination of water by heavy metals is a serious threat to human health and heavy metal adsorbents having a high enough quantity of a chelate structure on the surface are, therefore, in great demand. We developed a simplified radiation-induced emulsion graft polymerization (SREG) method without using gas/vacuum manifold [1]. The method involves a convenient and easy degassing process of a monomer solution using a commercially available sealed glass jar. A loaded weight on the lid of the jar was used to control the jar's internal pressure as the degassing of the monomer solution took place using a vacuum pump. The SREG method satisfies the grafting degree due to the easier irradiation at low absorbed doses that is expected to be applicable to the fabrication of heavy metal adsorbents. Its viability in synthesizing an appropriate heavy metal adsorbent was examined.

After gamma-ray irradiation of the polyethylene/polypropylene (PE/PP) fabric at a dose of 5 kGy, glycidyl methacrylate (GMA) was grafted onto the PE/PP fabric to produce PE/PP-*g*-GMA fabric using the SREG method (Dg = 72%). After the graft polymerization, the epoxy group of the GMA graft side-chain of the PE/PP fabric was converted to a disodium iminodiacetate (IDA) group to form PE/PP-g-GMA-IDA fabric. The IDA functional group is known to remove various kinds of heavy metals including Co(II) from wastewaters, and has been widely used as a commercial adsorbent. To introduce the groups onto PE/PP-g-GMA, the PE/PP-g-GMA fabrics were treated with 0.5 M IDA in a 1:1 v/v ethanol/water solution at 70 °C for 24 h. To confirm introducing the IDA group, PE/PP-g-GMA and PE/PP-g-GMA-IDA fabrics were characterized using FTIR-ATR (Fig. 1). The IDA group density and conversion were 1.6 mmol/g and 74%, respectively. In previous studies, the IDA group density of the adsorbent was mainly between 0.7 and 3.2 mmol/g, depending on the grafting degree and conversion. The SREG method at low absorbed doses was expected to be useful to fabricate heavy metal adsorbent. The adsorption ability of the PE/PP-*g*-GMA-IDA fabric was evaluated using the batch adsorption test. The Cobalt (II) ion was chosen as a model of a harmful heavy metal ion. Once Cobalt (II) was adsorbed by the PE/PP-g-GMA-IDA fabric, the remaining concentration of Cobalt (II) ion was determined using an inductivity coupled plasma optical emission spectrometer (Fig. 2). The initial concentration of the Cobalt (II) ion was 50 ppm, and the color of the solution was light pink. Over time, the color of the light pink solution became gradually lighter, and the Cobalt (II) concentration reached the limit of detection within 6 h. This result indicates that the PE/PP-*g*-GMA-IDA fabric had enough adsorption ability to essentially remove Cobalt (II) from a highly concentrated Cobalt (II) solution.

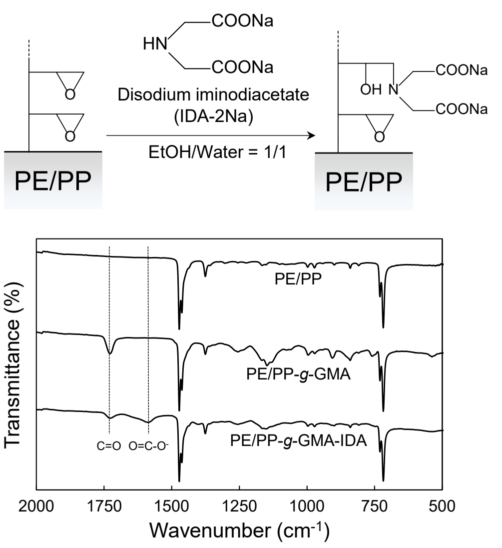

Fig. 1. FTIR-ATR spectra of the PE/PP, GMA-g-PE/PP, and IDA-GMA-g-PE/PP fabric.

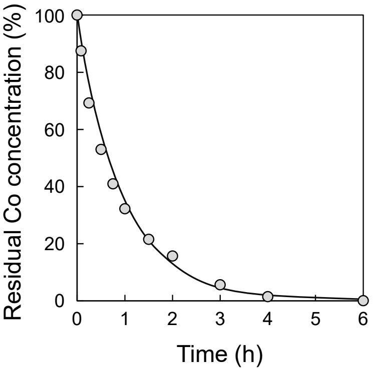

Fig. 2. Cobalt concentration (10 ppm) decay in water during adsorption of Cobalt (II) on IDA-GMA-g-PE/PP non-woven fabric.

Recently, several studies about the grafting of functional molecules on natural fibers have been reported, especially in developing countries. The natural fibers need low radiation doses because degradation of the cellulose, the main component of natural fibers, can remain limited in this range of radiation dose. The SREG method at a low dose is expected to be useful in the developing countries, which do not have high-dose-rate gamma-ray radiation or expensive experimental equipment.

References

[1] M. Omichi *et al.*, Polymers **11**, 1373 (2019).

1 - 28 Fabrication of Gd Coordinated Gelatin Nanoparticles for MRI Contrast Agent by Radiation Crosslinking

A. Kimura[a)], F. Yoshida[b)], M. Ueno[b)] and M. Taguchi[a,b)]

[a)]Department of Advanced Functional Materials Research, TARRI, QST,
[b)]School of Science and Technology, Gunma University

Gadolinium (Gd) based contrast agents with low molecular weight have been used for magnetic resonance imaging (MRI) diagnosis but invade the patient brain leaky blood-brain-barrier (BBB) partially [1]. Gd ions have toxicity and are released from Gd based MRI contrast agent in the patient brain due to biodegradation. U.S. Food and Drug Administration has placed a warning on all of them [2]. To ensure rapid renal excretion without invading the brain, the use of nanoparticles having 1 to 20 nm diameter is proposed as a safe MRI contrast agent [3-4]. This study proposes the use of the radiation crosslinking method for the production of nanoparticles made of natural polymers for MRI contrast agents. Gelatin which is biocompatible, non-toxic, and biodegradable was selected as a base material for the nanoparticle. The superiority of the radiation crosslinking method was investigated by comparing the number of Gd labeling reaction sites of radiation- and chemically- crosslinked gel.

A type of high molecular weight gelatin ($M_w = 1.5 \times 10^5$) was dissolved at 0.1 wt.% in Millipore Milli-Q water under nitrogen, oxygen, and air saturated conditions. The sample solutions were irradiated with γ-rays from ^{60}Co γ-sources at 0-50 °C in the dose range of 5–20 kGy (Gy = J kg^{-1}) at the dose rate ranging between 0.5-10 kGy h^{-1} at TARRI, QST. Chemically-crosslinked gelatin was synthesized using glutaraldehyde as a reference in chemical analysis. Particle size and zeta potential of the gelatin nanoparticles collected with an ultrafiltration unit were measured by a dynamic light scattering system. Radiation- and chemically- crosslinked gelatin gels were washed and vacuum-dried at 30 °C for 24 h. The dried samples were hydrolyzed in 6 mol dm^{-3} hydrochloric acid at 110 °C for 21 h with Pico-tag workstation. The hydrolysates of the gelatin gels were labeled with a fluorescent agent (4-fluoro-7-nitrobenzo-furazan) to enhance detection sensitivity. HPLC with a fluorescence detector was used to analyze labeled samples.

Gelatin nanoparticle was produced by γ-ray irradiation under controlled conditions of dose, dose rate, dissolved oxygen concentration, initial concentration, and temperature. The gelatin solution was irradiated with 5 kGy γ-rays (dose rate: 10 kGy/h) under the aerated condition at 25 °C to produce gelatin nanoparticles with an average particle size of 20 nm, which is a suitable size for safe MRI contrast agents. The nanoparticle has positive surface potential at 7.8 mV comparable to the zeta potential of the standard polystyrene nanoparticle at 1.8 mV, preventing aggregation of the nanoparticles during the long-term storage of 30 days.

Radiation- and chemically-crosslinked gelatin gels with a similar elastic modulus at around 5 × 10^5 Pa were synthesized and analyzed for their amino acid compositions. Tyrosine and phenylalanine which have higher reactivity with hydroxyl radicals from water molecules decreased by the irradiation though other amino acids showed less degradation. The consumption rate of lysine which has an amino group by the radiation was just 5 %, while that in the chemically crosslinking method was 18 %. This result indicates that radiation-crosslinked gelatin gel can combine more efficiently with ligand derivatives using an amino group which is a great advantage of the radiation crosslinking method for highly sensitive MRI contrast agent production. 1,4,7,10-Tetraazacyclododecane-1,4,7,10-tetraacetic acid (DOTA) mono-*N*-hydroxysuccinimide ester and DOTA-butylamine which have high reactivities with amino and carboxyl groups were used as a Gd ligand derivative to produce Gd coordinated gelatin nanoparticle (GdGN). GdGN in water was directly observed by a 200 keV transmission electron microscope with a liquid microscopy cell and the particle diameter of GdGN was found to be 20 nm or less as shown in Fig. 1, which was similar to that obtained by the dynamic light scattering system. The average particle size of GdGN remained almost the same as that before labeling with Gd complex, and GdGN has the potential of practical use of MRI contrast agents.

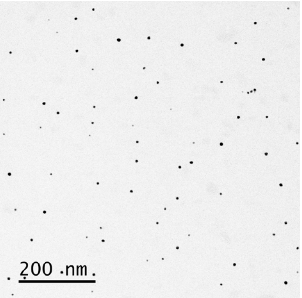

Fig. 1. TEM photographs of Gd coordinated gelatin nanoparticles produced by radiation crosslinking method.

References

[1] T. Kanda *et al*., Radiology **270,** 834 (2014).
[2] U. S. Food and drug administration. Available from URL:https://www.fda.gov/drugs/drug-safety-and-availability/fda-drug-safety-communication-fda-warns-gadolinium-based-contrast-agents-gbcas-are-retained-body.
[3] L. Jiang, *et al*., Biomaterials **34**, 7418 (2013).
[4] D. Furtado *et al*., Adv. Mater. **30**, 1801362 (2018).

1 - 29

Radiation-synthesized Starch/Polyacrylate Hydrogel as Super Water Absorbent

L. S. Relleve[a),]C. T. Aranilla[a)], B. J. D. Barba[a)], A. K. R. Gallardo[a)], V. R. C. Cruz[a)],
C. R. M. Ledesma[a)], N. Nagasawa[b)], L. V. Abad[a)] and M. Taguchi[b)]

[a)]Atomic Research Division, Philippine Nuclear Research Institute,
[b)]Department of Advanced Functional Materials Research, TARRI, QST

Super water absorbents (SWA) can absorb a very large amount of water (many hundred times their dry weight) and retain it even under pressure. They are synthesized by crosslinking highly hydrophilic macromolecules. SWA are used in a wide variety of applications such as disposable absorbents, in agriculture, and other fields where water absorption is needed. As soil water retainers or soil conditioners, SWA have been developed to improve the physical properties of soil in view of (a) increasing water-holding capacity, (b) increasing water use efficiency, and (c) increasing plant performance [1].

Formulation and preparation of starch/polyacrylate (PAAc) hydrogel were adapted from the “FNCA Guideline on development of hydrogel and oligosaccharides by radiation” [2]. Cassava starch (10% w/w) was gelatinized in hot water (heat gelatinization) or in alkali solution at room temperature (alkali gelatinization). In the heat gelatinization, acrylate (AAc, 20% w/w) was partially neutralized with potassium hydroxide (38% degree of neutralization, DN) before adding to the starch. In the alkali gelatinization, starch was first dispersed in potassium hydroxide solution (equivalent to 38% DN) at room temperature until it became viscous. AAc (20% w/w) was then added to the mixture and stirred for 30 min. Additional gels were prepared using the heat gelatinization with 20% AAc (50% DN using sodium hydroxide) and 3% starch, and with 15% AAc (75% DN using sodium hydroxide) and 0–15% starch.

Hydrogel formulations were poured into plastic pouches, sealed, and gamma-irradiated at the irradiation facility doses of 15–45 kGy at a dose rate of 0.5 kGy/h in Philippine Nuclear Research Institute. The gamma-irradiated polysaccharides were prepared at the cobalt-60 gamma-irradiation facility of TARRI, QST. The resultant gels were cut into cubes, air-dried, and oven-dried at 50 °C for 24 h. Samples were further ground to granules (1–3 mm) for evaluations of swelling kinetics, biodegradation, and soil-water retention.

Gel fraction, degree of swelling, and gel strength were all significantly higher in the alkali gelatinization, especially at doses of 20–25 kGy. The heat gelatinization involves the thermal disordering of crystalline structures in native starch granules. Once heated over its gelatinization temperature, typically between 57-65 °C, hydrogen bonding of starch molecules is disrupted, and water molecules become attached to their hydroxyl groups which leads to greater swelling and dissolution. On the other hand, in alkali treatment, the base ions disrupt the hydrogen bonding by deprotonation accompanied by some physico-chemical changes on the starch structure. Because of ionic interactions and transformations, alkali treatment seemed to be more effective in the gelatinization process and yielded better results than the simple heat gelatinization.

Biodegradability, which is a desired characteristic of SWA, is the ability of a material to be converted into carbon dioxide through the action of microorganisms such as bacteria, fungi, and algae. Despite the impressive characteristics of polyacrylate SWA, its low biodegradability, typically less than 1% rate of degradation in soil per six months, has been a significant setback in its utilization. Among the SWA tested, the starch/PAAc hydrogel had the highest biodegradability with a rate of 42% in 85 days.

Based on these data, the starch/PAAc hydrogel appears to be an ideal SWA material for agriculture due to its biodegradability. The soil water retention properties of the starch/PAAc hydrogel were also characterized at different application rates (applied as dried granules) in sandy soil. As expected, the water holding capacity of soil was found to increase with the concentration of the hydrogel. The starch/PAAc hydrogel can increase the water content to 48, 61, 76 and 92% with the addition of 0.25, 0.50, 0.75 and 1.0% hydrogel, respectively. The water content of the control (without hydrogel) was 38%. In the soil with 1.0% hydrogel, the amount of water was 50% even after 16 days while soil with 0.75% and 0.5% hydrogel had only 25% and 18% retention, respectively. For the soil without hydrogel and with 0.25% hydrogel, almost no water was present in soil after 16 days. Thus, the application rate of the hydrogel in the range of 0.5–1.0% could be effective for the soil water retention [3].

Starch/PAAc hydrogel appears to be a promising SWA material for agriculture due to its biodegradability and water retention performance as the soil water retainers.

References

[1] D. Jhurry, 1997. Food and Agricultural Research Council, Réduit, Mauritius, Agricultural Polymers. AMAS, University of Mauritius Réduit.

[2] FNCA Guideline on Development of Hydrogel and Oligosaccharides by Radiation Processing (2017).

[3] L. S. Relleve *et al.*, Radiat. Phys. Chem. **170**, 108618 (2020).

1 - 30

Preparation of Radiation and Heat Resistant Elastomer and Construction of System for Evaluation of Heat Resistance

C. Matsuda[a], N. Nagasawa[b], M. Ito[c], M. Sugimoto[b],
Y. Takeuchi[a], M. Taguchi[b], M. Washio[c] and S. Nakamura[a]

[a]Bridges Co. Ltd.,
[b]Department of Advanced Functional Materials Research, TARRI, QST,
[c]Faculty of Science and Engineering, Waseda University

Since the Fukushima Daiichi Nuclear Power Station accident, the prevention of containment damage as one of the measures against severe accidents has been enhanced among the new regulatory requirements for light water reactors in power generation in Japan. Especially, static sealing elastomer material of top head flange and equipment hatch is required to have radiation-resistance of 0.8 MGy and heat-resistance at 250 °C. Therefore, we developed new elastomer having heat and radiation resistance applied for static sealing material and also metrology of heat and radiation resistances with steam for evaluation.

The fluorine containing elastomers are used as a base material. The three types of samples were prepared by compounding with predetermined concentrations of various additives as a crosslinker, inorganic substances, plasticizer, using mixing roll at 50 ~ 60 °C. Then each sample was pressed in a hot press at 160 °C to form a sheet (100 mm × 120 mm, 0.5 mm thickness) and then irradiated with electron beams (EB) at doses of 120 - 200 kGy using a Cockcroft-Walton type 2 MeV electron accelerator at TARRI, QST. After EB-irradiation, the crosslinked sample sheets were cut into a dumbbell shape (ISO / ASTMD-1822-L standards). To evaluate crosslinking behavior of the sample, gel contents of the crosslinked samples were estimated by weighting the insoluble part of the crosslinked sheets after immersion in tetrahydrofuran for 8 hours at boiling temperature.

The evaluation was conducted by a sequential method combining gamma irradiation and a heat treatment. Irradiation was performed by Co-60 gamma-ray up to about 1 MGy at room temperature (RT) in air. And then the samples were aged in a vessel through continuous steam in an air oven which was kept at 250 °C ± 1.5 °C using the equipment constructed as shown in Figure 1. In the vessel, test pieces not only for a tensile test but also for compression set test can be installed as shown in Figure 2. After aging, the tensile test was performed using Strograph VE5D (Toyo Seiki Seisaku-sho, Ltd., Japan) with a crosshead speed of 200 mm/min at RT.

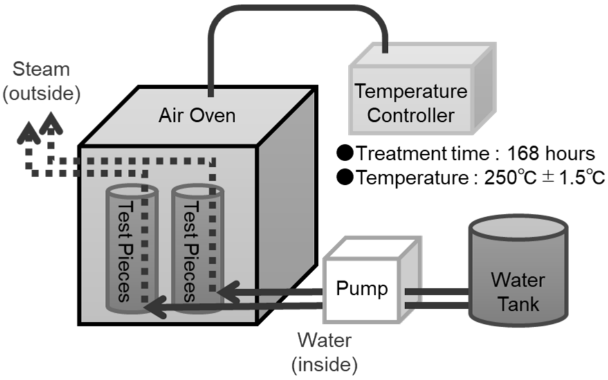

Fig. 1. Continuous steaming system for evaluation of heat resistance.

Fluorine containing elastomer as a base material has excellent heat resistant property at 200 °C among elastomers[1,2]. Even after the sequential treatment both gamma irradiation of 1 MGy and steaming at 250 °C for 168 hours, the produced sample did not change in appearance or shape, and retained elasticity. The gel fraction of the elastomer did not change before and after the sequential treatment. In the results of the tensile test, there was almost no change in mechanical properties (breaking strength, elongation at break, elastic modulus) due to the steam treatment. However, when combined with gamma-ray irradiation, the elongation at break reduced to 1/5 of that of the untreated sample, and the breaking strength was about 1.8 times larger. This research is in progress to the molding of o-ring with the produced compounds and the evaluation of them for application to static sealing materials.

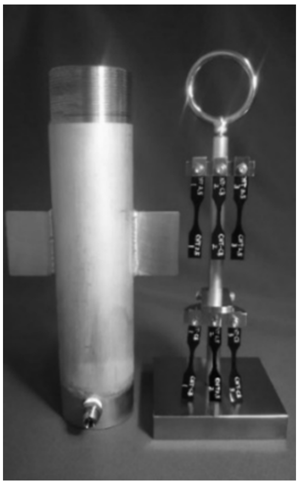

Fig. 2. Vessel (left) and electron beam crosslinked elastomers (right) for the tensile test.

References

[1] M. Ito, Radiat. Phys. Chem. **47**(4), 607 (1996).
[2] M. Ito, Nucl. Instrum. Meth. Phys. Res. B **265**, 227 (2007).

1 - 31 Gamma Ray Irradiation Effects to the Laser Beam Profile of Nd:YAG/Cr:YAG Ceramic Composite

K. Tamura[a)], R. Nakanishi[a)], H. Ohba[a)], M. Saeki[a)], T. Taguchi[a)], H. Lim[b)], T. Taira[b, c)]
and I. Wakaida[d)]

[a)]Tokai Quantum Beam Science Center, TARRI, QST,
[b)] Institute for Molecular Science, National Institutes of Natural Sciences,
[c)]Riken Spring-8 Center,
[d)] Collaborative Laboratories for Advanced Decommissioning Science, JAEA

Decommissioning of TEPCO Fukushima Daiichi nuclear power plant (F1-NPP) is needed, where molten fuel debris might be submerged in water. To obtain information inside the reactor core, remote inspection technique in narrow space is required. A fiber-optic probe laser-induced breakdown spectroscopy (LIBS) is considered one of the promising methods for remote inspection [1]. Giant-pulse microchip laser (MCL) is compact with high peak power of MW level, and since the feature is suitable for LIBS application, it was applied to remote LIBS system, where MCL is set close to the target and bright plasma is generated by direct laser irradiation. Based on the developed system, effective remote inspection is expected [2]. However, radiation effects to the system needs to be investigated considering its operation in the radiation environment. In the previous annual report, we reported that the laser output decreased by the increase of radiation dose rate of gamma ray. This time, the laser beam profiles of the developed system were measured, and the influences of high dose irradiation were investigated with gamma ray up to 10^4 Gy/h.

Radiation effects were measured for a monolithic Nd:YAG/Cr:YAG composite ceramics (Konoshima Chemical Inc.), where Nd:YAG is a gain medium and Cr:YAG is a saturable absorber. The YAG composite was set in a holder in an irradiation area at the gamma irradiation facility number-1. The composite was irradiated with gamma ray using ^{60}Co source. In this experiment, dose rate was increased step by step from 0 to 104 Gy/h by approaching the composite to the radiation source. Laser beam profile was measured with a beam profiler (Beamage-4M; sensor size - 11.3 × 11.3 mm^2; Gentec-EO, Canada). The profiler was set inside of the radiation area at approximately 110 cm from the composite exit, where the profiler was surrounded by walls of lead blocks for radiation shield except a hole left for laser beam introduction.

The far field beam quality was evaluated using the profiler. Figure 1(a) shows the 3D profile before irradiation (0 kGy/h) for the pump diode laser (LD) current of 70 A and LD duration of 100 μs, showing well approximated Gaussian beam profile. Figure 1 (b) shows a profile during irradiation (10 kG/h) for the LD current of 70 A and LD duration of 170 μs. The intensity of the profile reduced considerably due to the reduced laser intensity. Figure 1 (c) compares the corresponding lateral intensity plots before (0; 0 kGy/h) and during irradiation (10; 10 kGy/h), where intensity of the plots was normalized. Before irradiation, profile exhibits a close approximation to TEM00 Gaussian profile. By the irradiation, although the profile became noisy, it was still well approximated by the Gaussian profile. The relative FWHM width of the beam profile was estimated from the fitted curve as a ratio to that without radiation as a function of the dose rate. The beam width increased at high dose rate as shown in Fig. 1(d). The result provides an important information for laser applications in harsh environments.

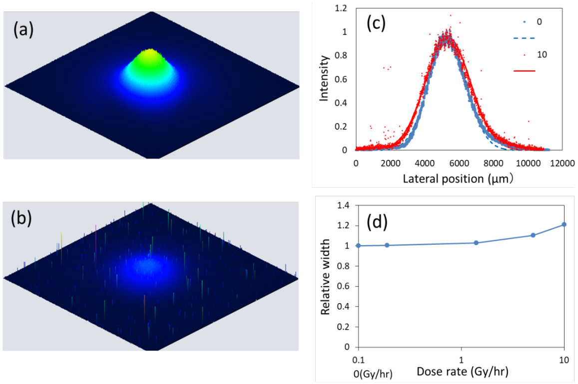

Fig. 1. The 3D beam profile for the dose rate of 0 (a) and 10 kGy/h (b) for 11.3 mm square area; (c) experimental and fitted lateral intensity distributions; (d) estimated FWHM width as a function of the dose rate.

Acknowledgments

This work includes a part of the results of “Advanced study on remote and in-situ elemental analysis of molten fuel debris in damaged core by innovative optical spectroscopy”, the Center of World Intelligence Project for Nuclear S&T and Human Resource Development, the Ministry of Education, Culture, Sports, Science and Technology (MEXT), Japan.

References

[1] M. Saeki *et al.*, J. Nucl. Sci. Technol. **51**, 930 (2014).
[2] K. Tamura *et al.*, J. Nucl. Sci. Technol., in press.

1 - 32 Ion Irradiation-Induced Novel Carbon Nanomaterials in Silicon Carbide Nanotubes

T. Taguchi[a], S. Yamamoto[b] and H. Ohba[c]

[a]Tokai Quantum Beam Center, TARRI, QST,
[b]Department of Advanced Functional Materials Research, TARRI, QST

Silicon carbide (SiC) has been reported to be wide-band-gap semiconducting materials for high temperature and high power use and high temperature structural materials. On the other hand, it is well known that one-dimensional nanomaterials, such as nanowires, nanorods and nanotubes possess new properties different from those of bulk materials. So far, we have succeeded in synthesizing polycrystalline single-phase SiC nanotubes and C-SiC coaxial nanotubes, in which multi-walled carbon nanotubes (MWCNTs) were sheathed with a SiC layer [1, 2]. We have also reported that in-situ transmission electron microscopy (TEM) was used to observe the microstructural developments of single-phase SiC nanotubes under ion irradiation, and the results are significantly different from those of bulk SiC [3]. Therefore, the novel microstructural change of C-SiC coaxial nanotubes by ion irradiation is expected. In this study, we reported the novel microstructural development of C-SiC coaxial nanotubes under the ion irradiation using in-situ TEM observation technique.

Carbon nanotubes (GSI Creos Corporation, Tokyo, Japan) were used as the template. The C-SiC coaxial nanotubes were synthesized by heating MWCNTs with Si powder (The Nilaco Corporation, Tokyo, Japan) at 1,200 °C for 100 h in a vacuum. The samples heated at the above conditions included many unreacted MWCNTs besides the C-SiC coaxial nanotubes. Therefore, the samples were then heated at 700 °C for 2 h in air in order to remove unreacted MWCNTs. The molybdenum grid holder, which deposited the C-SiC coaxial nanotubes, were irradiated with 200 keV Si^+ ions from 400 kV ion implanter at room temperature in TEM (Model JEM-4000FX, JEOL Ltd., Japan). In-situ TEM observation of C-SiC coaxial nanotube under Si^+ ions irradiation was carried out. The ion fluence was up to 9.1×10^{20} ions/m^2, and the corresponding irradiation damages for the SiC and carbon layer in C-SiC coaxial nanotubes were calculated by SRIM 2008 to be 23.8 and 22.3 dpa respectively.

Figure 1 shows the typical TEM images and selected area electron diffraction (SAED) pattern of the C-SiC coaxial nanotube after the irradiation with 200 keV Si^+ ions at room temperature. The results of TEM observation indicate that the carbon layer in the C-SiC coaxial nanotube was confirmed to have remained crystalline after the irradiation despite the complete amorphization of SiC crystals. Therefore, the carbon layer possessed better resistance against amorphization after ion irradiation, compared with the SiC layer in the C-SiC coaxial nanotube. Such an outcome is however not consistent with many previous works. In addition, new graphitic shells perpendicular to the nanotube length direction suddenly emerged after ion irradiation in the C-SiC coaxial nanotube. The TEM images and SAED pattern reveal that a successful synthesis of a new structured hybrid carbon nanomaterial was achieved for the first time, which consisted of one-dimensionally stacked graphene nano-disks with diameter less than 50 nm, and cylindrical MWCNTs, inside an amorphous SiC nanotube. Ion irradiation of C-SiC coaxial nanotubes therefore constitutes one of the new synthetic processes for making new structured carbon nanomaterials [4].

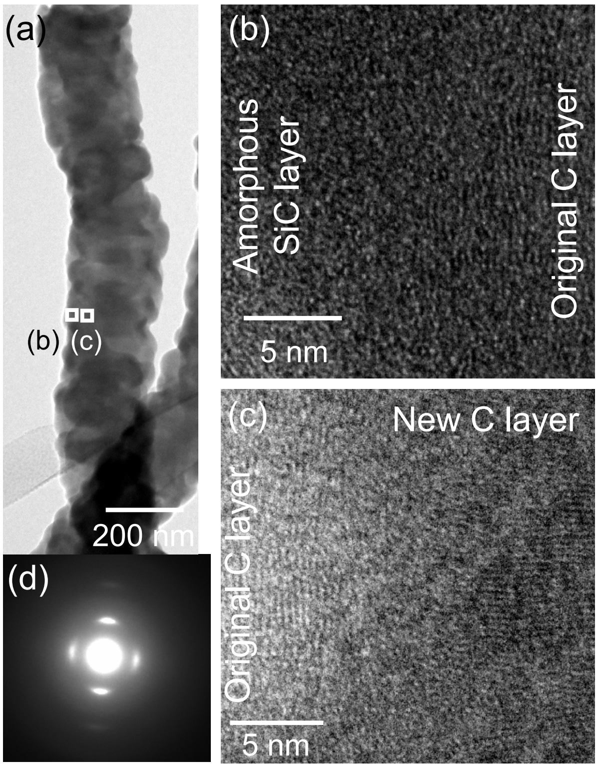

Fig. 1. Typical TEM images and SAED pattern of the C-SiC coaxial nanotube after irradiation with 200 keV Si^+ ions. (a) A low magnification TEM image, (b) high resolution TEM images of the nanotube's outer part, (c) middle part and (d) SAED pattern.

References

[1] T. Taguchi *et al.*, J. Am. Ceram. Soc. **88**, 459 (2005).
[2] T. Taguchi *et al.*, Physica E **28**, 431 (2005).
[3] T. Taguchi *et al.*, Acta Mater. **154**, 90 (2018).
[4] T. Taguchi *et al.*, Acta Mater. **173**, 153 (2019).

1 - 33

Prediction of Proton Conductivity of the Graft-type Polymer Electrolyte Membranes by Machine Learning Methods

S. Sawada[a], Y. Sakamoto[b], K. Tanaka[c], K. Funatsu[c] and Y. Maekawa[a]

[a]Department of Advanced Functional Materials Research, TARRI, QST,
[b]Graduate School of Engineering and Science, Gunma University,
[c]Graduate School of Engineering, University of Tokyo

Polymer electrolyte membrane (PEM) fuel cell is a promising clean energy conversion system to generate electricity from hydrogen. The critical component of the fuel cell is a PEM that transports H^+ from the anode to the cathode. The higher the proton conductivity of the PEM is, the higher the output power of the fuel cell is. In general, however, highly-conductive PEMs tend to excessively absorb water under a highly-humid condition, which sometimes deteriorates mechanical strength. Accordingly, much effort has been globally devoted to create the novel PEMs with high conductivity and low water uptake, which seem to be a tradeoff relationship.

QST has developed the fuel cell PEMs by a radiation-induced grafting method. This method involves the grafting of styrene or other monomers to irradiated base polymer films, and consecutive chemical reactions to introduce sulfonic acid groups. The obtained graft-type PEMs are composed of the base polymer and poly(styrene sulfonic acid) graft chains. Various types of base polymers can be selected, and the amount of sulfonic acid groups can be varied in a wide range.

Quite recently, we launched a new project to predict the properties of the graft-type functional polymer materials by machine learning methods. We paid attention to the above-mentioned tradeoff relationship between the proton conductivity and water uptake, and thus defined the following F parameter as a target property:

$$F(\mathrm{mS/cm}) = \text{proton conductivity} / \lambda,$$

where λ is the number of water molecules per one sulfonic acid group. A high F value means the overcome of the tradeoff relationship to increase proton conductivity even in a water-poor condition. Figure 1 shows the F of the graft-type PEMs as a function of the ion exchange density (IED), the amount of sulfonic acid groups per volume of a dried PEM. As a general trend, the F increased with increasing IED. However, the F values varied largely even at the same IED, probably depending on the types of base polymers, which cannot be explained so far.

In this study, we tried to predict the F by using a random forest (RF) method, one of the major machine learning techniques. For the RF prediction, the following 12 variables were used: 1 IED; 2 Density; 3 Permittivity; 4 Young's modulus; 5 Crystallinity; 6 Dipole moment; 7 Polar surface area ratio; 8 Water/octanol partition coefficient; 9 Molecular weight; 10 Formation energy; 11 Energy of highest occupied molecular orbital (HOMO); and 12 Lowest unoccupied molecular orbital (LUMO) (2-12 are the physical and chemical properties of the base polymer films). Variables 2-4 were taken from the film catalogues, Variable 5 was measured by differential scanning calorimetry, and Variables 6-12 were calculated by an ab initio molecular orbital method (wB97X-D/6-31G*). The experimental data was randomly divided into training data (70%) and test data (30%) for RF modeling and prediction performance evaluation, respectively.

Figure 2 (Left) shows the relationship between the predicted and actual values of the F. The root mean square displacement (RMSD) was calculated to be 0.583 and 0.962 mS/cm for the training and test data, respectively. The prediction accuracy of the RF model was enough high. Figure 2 (Right) shows the variable importance, the degree of contribution to prediction accuracy, calculated by a permutation method. As expected, the IED exhibited the highest importance. The crystallinity was found to be the second important variable. The low-crystallinity base film may enhance the connectivity of the ion channels for proton transport, thereby increasing the proton conductivity.

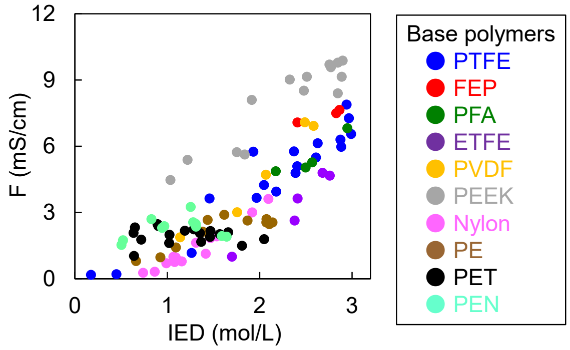

Fig. 1. The relationship between the F and IED for the graft-type PEMs prepared from various base polymers.

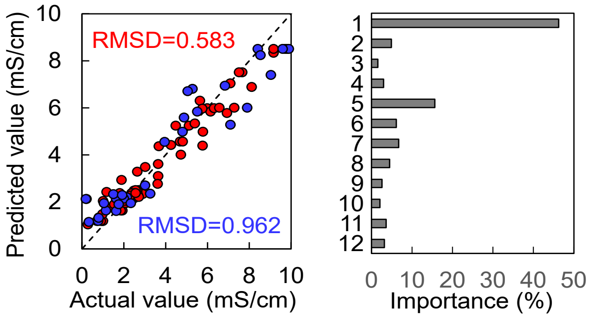

Fig. 2. (Left) Relationship between the predicted and actual F values for the training data (red) and test data (blue). (Right) Importance of all variables 1-12.

1 - 34

Industrial Mass Production Process of Pentadecafluorooctanoic-Acid-Free Polytetrafluoroethylene by γ-Irradiation

A. Oshima[a], T. Tanaka[b], R. Senba[b], K. Satoh[b], H. Seito[c] and N. Nagasawa[c]

[a]Graduate School of Engineering, Osaka University,
[b]Daikin Industries Ltd.,
[c]Department of Advanced Radiation Technology, TARRI, QST

The Registration, Evaluation, Authorisation and Restriction of Chemical (REACH) legislation in the European Union (EU) will apply to the manufacture and sales of pentadecafluorooctanoic acid ($C_7F_{15}COOH$, PFOA)-containing products in the EU from July 4, 2020; hence it is necessary to reduce PFOA contamination to less than 25 ppb and that of PFOA-related compounds to less than 1000 ppb [1]. Low molecular weight PTFE micro-powder is produced industrially by the chain scission of its polymerized powder or molded scraps induced by ionized radiation in air. There is a problem that PFOA is generated in this molecular weight reduction process and the content is 25 ppb or more [2]. Up to now, as a method of removing PFOA in a product, it is known that a method of volatilizing and removing PFOA generated by irradiation. Since the REACH regulation does not allow PFOA to be produced intentionally or unintentionally, such heat removal is not possible in the industry. In this study, we investigated the mass production method of low molecular weight PTFE that suppresses PFOA generation in the irradiation process below the detection limit.

Homopolymerized PTFE fine powder was used in the experiments. PTFE powder was sealed in a 18 mm-diameter glass ampoule for product analysis (10.0 ± 1.0 g) after evacuation to less than 4.0×10^{-3} Pa for 24 h and γ-rays irradiation was carried out at room temperature under vacuum and atmospheric conditions in 6 cell at TARRI. After irradiation, the melt viscosity was evaluated with a capillary rheometer. Furthermore, the emitted PFOA from irradiated PTFE was evaluated by LC-MS.

Table 1 shows the oxygen concentration in the system during γ-rays irradiation, the absorbed dose, and the PFOA content and melt viscosity of the obtained low molecular weight PTFE. It can be seen that production of PFOA by irradiation can be suppressed below the detection limit by reducing the oxygen concentration during irradiation. However, at around 150 kGy, it is higher than the melt viscosity (15×10^3 Pa·s to 10×10^4 Pa·s) obtained by the conventional method, and more irradiation is required to obtain the same melt viscosity as the conventional product. When the dose was set to 400 kGy under oxygen-free, which was more than twice the conventional dose, the melt viscosity could be in the same range as conventional products. In the case of irradiation under oxgen-free, chain scission is suppressed more than in air, as reported previously [3]. Therfore, it was found that low molecular weight PTFE having a PFOA content of REACH regulation or less can be obtained by γ-rays irradiation and heat treatment in the absence of oxygen in lab-scale.

Table 1
Amount of emitted PFOA and melt viscosity. γ-rays irradiation was carried out at 297 K under vacuum. Thermal treatment was demonstrated at 297 K and 423 K under vacuum during 24 h.

O_2 concentration (vol%)	Dose (kGy)	Treated temperature (K)	Amount of PFOA per polymer (ppb)	Melt viscosity (Pa·s)
< 1.0	150	423	< 5	$>20 \times 10^4$
	400		< 5	18×10^3
21	150	297	28	11×10^4
	400	423	377	4×10^2

Based on the mention above experimental results, we examined the industrial mass production process. 11 kg of PTFE fine powder was placed in polymer bag and then evacuated. The sample was irradiated with a dose of 400 kGy by γ-rays at an oxygen concentration of 100 ppm or less, with subsequent heat treatment performed at 423 ± 5 K for 20 h in the same atmosphere. As a result of confirming the amount of residual PFOA at each site in 11 kg of PTFE after irradiation, PFOA at each site was below the detection limit value of 5 ppb or less. That is, we were able to establish an industrial mass production process that cleared the REACH regulation.

Acknowledgments

The authors would like to thank Mr. Y. Haruyama and Mr. M. Takagi (QST) for their advice and assistance concerning γ-rays irradiation and Mr. H. Matsukawa (Osaka University) for sample preparation.

References

[1] European Chemicals Agency (ECHA), https://echa.europa.eu.
[2] Larsen, B. S., *et al.*, Analyst. **130**, 59 (2005).
[3] A. Oshima *et al.*, Radiat. Phys. Chem. **49**, 279 (1997).

1 - 35

Irradiation Tests of Radiation Hard Components and Materials for ITER Blanket Remote Handling System

M. Saito, K. Nakata, Y. Noguchi and N. Takeda

Department of ITER Project, NFI, QST

Introduction

The ITER blanket remote handling system (BRHS) will replace the first wall panels in a radiation environment having a dose rate of 250 Gy/h to 500 Gy/h. The ITER requirement for radiation hardness is 1 MGy for all BRHS components, however, 5 MGy was set as the target value to increase the availability of the system. In this study, maraging steels for wrenches for FW/SB bolts and AC servo motors were investigated.

Results

Maraging steel (YAG300, with and without nitriding treatment) samples (30 mm × 30 mm × 5 mm,) were irradiated at 1850 Gy/h up to 0.4 MGy then 1 MGy. The atmosphere around the samples was kept at 40 °C and 31.6% relative humidity by thermostatic chamber and by $MgCl_2$ saturated salt solution. Photos of the samples before and after γ-ray irradiation are shown in Table 1. Corrosion was observed on all samples after irradiation. Hydroxide compounds detected on the corroded samples suggest that the corrosion was enhanced by a combination of moisture around the samples and γ rays, as was observed in previous tests [1], however, in this study, SEM-EDX analysis detected less chlorine than oxygen in all the irradiated samples (Table 2). Thus, although humidity is considered to be a dominant factor contributing to corrosion, the effects of the $MgCl_2$ used in the saturated salt method to control relative humidity cannot be dismissed.

The BRHS will be driven by AC servo motors, the failure of which would severely impact the maintenance plan of the blanket modules. These AC servo motors were made by replacing generic parts with radiation hard parts [2]. These modified motors have been irradiated at a gamma ray irradiation facility where a radiation hardness of 8 MGy was confirmed [2], however, the motors were irradiated in static conditions only. In this study, we actively operated servo motors in a radiation environment to simulate the actual conditions in the ITER vacuum vessel. In previous tests [2], conduction resistance increased at 1 MGy because rubber clamps degraded and became loose. The motor cables have since been directly connected to the body without using rubber, which is expected to improve the electrical characteristics of the system. Two types of improved motors having different rated output powers were tested (four motors total: 400W_1, 400W_2, 60W_1, and 60W_2). These motors were operated for alternating 30-minute intervals of operation and stoppage over the course of five days, under radiation of 410 Gy/h to 560 Gy/h (at night the motors were only irradiated and not operated). After five days, verification tests were performed to measure conduction resistance, insulation resistance, and withstand voltage, the acceptance criteria of which are 0.5 Ω or less, 10 MΩ or more, and 5 mA or less, respectively. The servo motors were actively operated and were irradiated up to 0.1 MGy, then 0.3 MGy, and 0.7 MGy. All motors operated without error, and all values of the verification tests satisfied the acceptance criteria .

Conclusion

Corrosion was observed on all maraging steel samples after irradiation up to 1 MGy in an environment having a relative humidity of 31.6%. Irradiation tests for maraging steel using non-chlorine (i.e., non-halogen) test reagents are planned to determine if chlorine from the $MgCl_2$ saturated solution is a contributing factor (humidity value cannot be the same as the tests using $MgCl_2$ because a different reagent will be used). The AC servo motors were confirmed to operate in a radiation environment of up to 0.7 MGy. We anticipate servo motor acceptance criteria being satisfied even above 1 MGy and are planning to continue these irradiation tests up to 5 MGy.

Acknowledgments

The authors would like to acknowledge Mr. T. Obokata and Mr. T. Komizo of Hitachi Power Solutions, Mr. M. Hiratsuka and Mr. T. Fukabori of Nanotec Corporation, Mr. K. Mizuhashi and Mr. K. Takeuchi of Beam Operation Co., Ltd. and Mr. H. Seito from the Takasaki Advanced Radiation Research Institute who supported the development of these radiation hard components.

References

[1] M. Saito *et al.*, QST Takasaki Annu. Rep. 2018, **QST-M-23**, 54 (2020).

[2] M. Saito *et al.*, QST Takasaki Annu. Rep. 2016, **QST-M-8**, 66 (2018).

Table 1

Maraging steel samples before and after irradiation.

Sample	Irradiated dose [MGy]				
	0	0.4		1	
		γ ray source side	anti-γ ray source side	γ ray source side	anti-γ ray source side
YAG300	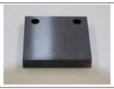	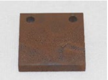			
YAG300 Nitriding Treatment					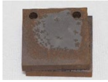

Table 2

Quantitative results from SEM-EDX analysis.

Sample	Dose [MGy]	Element mass concentration [wt%]										
		C	N	O	Al	Si	Cl	Ti	Fe	Co	Ni	Mo	Total
YAG300	0	4.26		0.55	0.13	0.12	-	0.89	62.49	9.87	17.03	4.66	100
	0.4	3.14		24.63	-	0.09	0.67	-	52.93	8.48	9.61	0.45	
	1	3.50		24.88	-	0.20	2.78	-	53.42	7.57	7.14	0.51	
YAG300 Nitriding treatment	0	5.36	1.67	3.85	3.67	0.18	-	0.73	58.35	8.24	14.48	3.48	100
	0.4	3.49		25.45	0.18	0.09	1.01	0.19	50.14	7.51	11.08	0.85	100
	1	3.69		21.63	0.13	0.10	1.85	0.12	55.50	7.82	8.85	0.32	100

1 - 36

Study on Fusion Neutron Irradiation Effects Using Multiple Ion-Beam Irradiation

D. Hamaguchi, M. Ando, H. Kurotaki, T. Nozawa

Department of Fusion Reactor Materials Research, RFI, QST

Reduced activation ferritic/martensitic steels (RAFMs) such as F82H and Eurofer97 are candidates for the blanket structural material for DEMO fusion reactors. Extensive work has shown the neutron irradiation effects in RAFMs but there still remains a lot of uncertainty on details of fusion neutron effects. One of the irradiation features for the blanket structure material is the high-dose and high-energy neutron irradiation that leads to an accumulation of displacement damage along with high levels of He and H production. One of the difficulties in predicting details of the development of this damage under fusion conditions is the lack of neutron irradiation facilities that produce irradiation conditions similar to the fusion reactor environment. Therefore, our approach is to develop information on particular events that are a specific part of the response under fusion neutron irradiation. We do this using existing irradiation facilities. Recently, we have conducted a series of ion irradiation experiments of RAFMs in the temperature ranged 300 to 500 ˚C for doses ranged from 20 to 80 dpa. These irradiations were mainly conducted at TIARA complex ion-beam irradiation facility using Fe^{3+} ions with or without He^{+} and H^{+} co-implantations. We have started post-irradiation examination (PIE) to collect information on dose and temperature dependence of void swelling along with irradiation hardening in this temperature and dose range.

The materials used in this study were F82H variants (IEA, Mod3, BA07, BA12 heats) and Eurofer97. The irradiations were carried out with 10.5 MeV Fe^{3+} ions plus 0.38 MeV H^{+} and/or 1.05 MeV He^{+} ions. In multiple ion-beam irradiation, He and H implantation rate were fixed to be 10 and 40 appm/dpa, respectively.

Figure 1 shows the irradiation matrix achieved so far during the series of irradiation campaign using TIARA facility up to 2019. Extensive irradiation experiments have been conducted in the temperature range 300 to 500 ˚C. The irradiation matrix is mostly fulfilled for single/dual/triple beam irradiation with the doses in 20 dpa incremental steps up to 80dpa. On the other hand, the data points within these matrixes will be achieved against only each one irradiation condition (n = 1) and therefore, the irradiation tests will be continued to acquire another set of data for same irradiation condition (n = 2···) to increase data accuracy. Also, the PIE campaign has been started and part of the irradiation hardening behavior and microstructure evaluation data has been obtained.

Figure 2a shows the hardness changes of F82H-IEA obtained by micro-indentation hardness tests in temperature range from 400 to 450 ˚C [1]. Here, clear hardenings by Fe-ion irradiation were seen only below 430 ˚C. On the other hand, although clear effect of He co-implantation was not seen at above 450 ˚C, there shows higher hardening below 430 ˚C and did not saturate with doses. This may be due to a formation of tiny He bubbles since the bubbles start to become larger above 450 ˚C, which was confirmed by microstructure observations.

Figure 2b shows examples of the maximum stress results obtained by micro-tensile testing for these conditions (single and dual-irradiation at 400 ˚C, up to 60 dpa). A little strength increase for dual-irradiated F82H was also detected in the micro-tensile testing. These results were almost in agreement with that of micro-indentation. However, it was shown that the effect of helium on irradiation hardening at 400 ˚C was also not strong in lath matrix of F82H, significantly.

Finally, Broader approach (BA) activities Phase II program, which is JA-EU international collaboration, started in 2020, and one of those tasks is the activity of predicting the effect of fusion neutron irradiation on F82H steel. The data obtained in this work will contribute greatly as simulated irradiation data by multiple ion-beam irradiation.

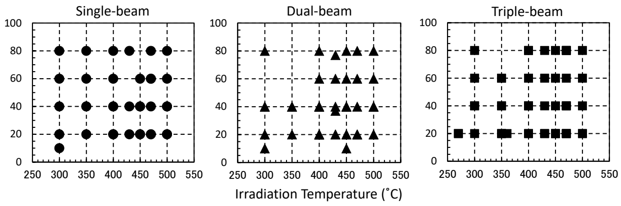

Fig. 1. Irradiation matrix achieved so far during the series of irradiation campaign using TIARA facility up to 2019.

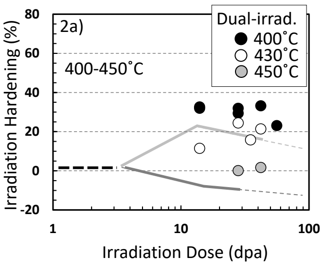

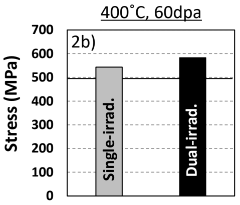

Fig. 2a. Hardness changes of F82H-IEA obtained by micro-indentation hardness results [1]. Lines indicate the irradiation hardening trend for Fe single-beam irradiation.

Fig. 2b. Examples of the maximum stress results obtained by micro-tensile testing for 400 ˚C, 60dpa.

Reference

[1] D. Hamaguchi *et al.*, QST Takasaki Annu.Rep. 2018, **QST-M-23**, 52 (2020).

1 - 37 Effects of Self-Ion Irradiation on Microstructure in Pure Tungsten

T. Miyazawa[a)], S. Nishimura[a)], Ju-Hyeon Yu[b)], M. Ando[b)], S. Nogami[a)], A. Hasegawa[a)],
T. Nozawa[b)] and H. Tanigawa[b)]

[a)]Department of Quantum Science and Energy Engineering, Tohoku University,
[b)]Department of Fusion Reactor Materials Research, RFI, QST

Considering the manufacturing capability, uniformity, and reproductivity, powder metallurgically (PM) processed hot rolled tungsten (W) is considered as divertor tile materials. The low temperature and grain boundary embrittlement caused by the recrystallization of the PM-W are important to maintain the soundness of the cooling performance and the structures of the divertor components. Fine grain structure as a result of hot-rolling and removal of elastic strain using stress-relieved (SR) heat treatment are beneficial in both improving low temperature embrittlement and strengthening [1]. Especially, SR-pure W with a lamella-like layered grain structure induced through the rolling process may enhance the resistance of embrittlement. Dislocation in a grain is also considered as the sink of point defects introduced by neutron irradiation. This study aims to investigate the effects of self-ion irradiation on pure W.

The original material was a PM processed pure W, which was hot-rolled and heat-treated with SR at 900 °C for 20 min. The pure W specimens examined in this work were carried out by final heat treatment at 1500 °C for 1 h for the recrystallization (hereafter R-pure W). The self-ion irradiation experiments were carried out at the irradiation temperature of 800 °C with 18 MeV W^{6+} ions by a tandem accelerator. The nominal displacement damages stand for the values at around 0.5 mm depth from the irradiated surface was 0.5 dpa. The nominal damage rate was 1.0×10^{-4} dpa/s. The microstructures of irradiated region were observed by TEM. Figure 1 shows bright and dark field of R-pure W after irradiation. Dislocation loops were existed, and no voids were observed. Figure 2 shows size histograms of dislocation loops in R-Pure W after irradiation. The mean size of the dislocation loops was approximately 5.2 nm. The number density of dislocation loops was 4.6×10^{21} /m^3. T. Hwang et al. [2] reported microstructure of SR-pure W after self-ion irradiation. Dislocation loops were also observed. However, the mean size of dislocation loops in SR-pure W was 1.5 nm, which was smaller than that in R-pure W. Further study is required in order to clarify the mechanism.

In parallel, the effect of irradiation on hardness was evaluated for three kinds of ITER-grade pure tungsten (IGW) with different manufacturing processes, i.e., original IGW, moderately cross-rolled CLW and highly cross-rolled CHW [3]. 18 MeV W^{6+} ions were irradiated to the maximum 8 dpa at 500 and 800 °C. Nano -indentation tests were conducted on irradiated surface of W. Figure 3 shows indentation hardness, indicating irradiation temperature dependence of saturation dose. For irradiation at 500 °C, saturation of irradiation hardening was observed in the early stage of irradiation (0.3 to 1.0 dpa). By contrast, for irradiation at 800 °C, irradiation hardening was saturated at 3.4 dpa. The key mechanism for such difference will be evaluated by following microstructural observation.

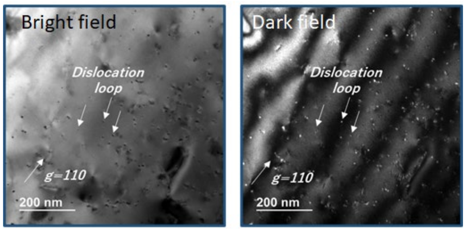

Fig. 1. TEM images of R-pure W to 0.5 dpa at 800 °C.

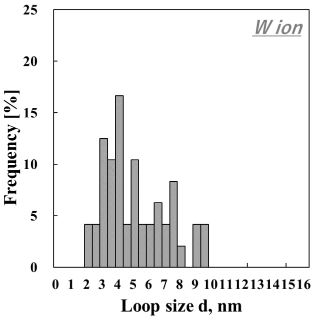

Fig. 2. Size histograms of dislocation loops in R-Pure W after irradiation.

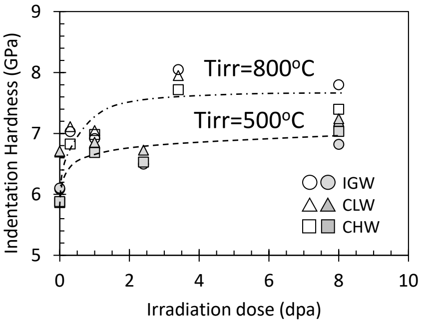

Fig. 3. Dose dependence of hardness of pure W.

References

[1] S. Nogami *et al.*, Fusion Eng. Des. **140**, 48 (2019).
[2] T. Hwang *et al.*, Nucl. Mater. Energy **9**, 430 (2016).
[3] J-H. Yu *et al.*, Fusion Eng. Des. **157**, 11679 (2020).

1 - 38

Effects of Irradiation on Surface Electrical Resistivity of High-Purity Silicon Carbide

T. Nozawa, M. Ando, D. Hamaguchi, H. Kurotaki and H. Tanigawa

Department of Fusion Reactor Materials Research, RFI, QST

Silicon carbide (SiC) is a candidate material of liquid metal breeding blanket for fusion, e.g., functional structure of flow channel inserts for the dual cool blanket system [1]. To realize the liquid metal system, electrical insulation is a key function of SiC. From the previous work by the authors in 2018, it was found that the surface electrical resistance was degraded by irradiation, i.e., radiation-induced electrical degradation (RIED)-like behavior. However, knowledge about the key mechanism of such electrical degradation is still insufficient. This study therefore aims to evaluate the effects of irradiation on surface electrical resistivity.

High-purity chemical vapor deposited (CVD) SiC disk (ϕ3 mm × 50 μm) was irradiated by single (6.0 MeV Si^{2+}, 1.0 × 10^{-3} dpa/s), dual (single + 1.0 MeV He^{+}, 130 appm/dpa) and triple (dual + 340 keV H^{+}, 40 appm/dpa) ion beams to evaluate the effect of transmutation He/H atoms to simulate fusion irradiation environment. The maximum dose was 31 dpa, which was the representative value calculated at the depth of 1.3 μm from the irradiation surface by the SRIM code, and irradiation temperature was ranged in about 600–1000 °C. Surface electrical resistivity was then measured at room temperature by the two-probe guard ring AC impedance method [2]. Besides, surface morphological change was evaluated by X-ray photoelectron spectroscopy (XPS).

Figure 1 shows the dose dependence of the surface resistivity. By irradiation with doses of 10–15 dpa, slight decrease of surface resistivity was identified, while, for the high-dose irradiation case (25–31 dpa), considerable reduction of the surface resistivity was marked by irradiation at comparably higher irradiation temperatures (> 750 °C). In contrast, the surface resistivity tended to decrease with increasing dose and irradiation temperature. For both cases, the impact of He/H co-irradiation was minor.

Figure 2 shows chemical composition profiles before and after self-ion (Si^{2+}) irradiation, indicating no remarkable change of silicon and carbon profiles by irradiation at ~800 °C. However, very slight increase of oxygen near the surface was probable. The surface modification may affect the surface resistivity of SiC.

References

[1] P. Norajitra *et al.*, Fusion Eng. Des. **69**, 669 (2003).

[2] N. Okubo *et al.*, Nucl. Instrum. Meth. Phys. Res. B **314**, 208 (2013).

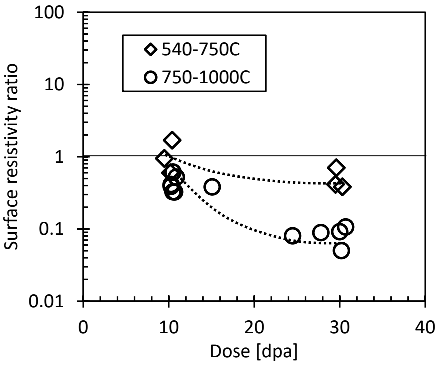

Fig. 1. Surface resistivity ratio (irrad./non-irrad.) vs. displacement damage dependence for CVD SiC.

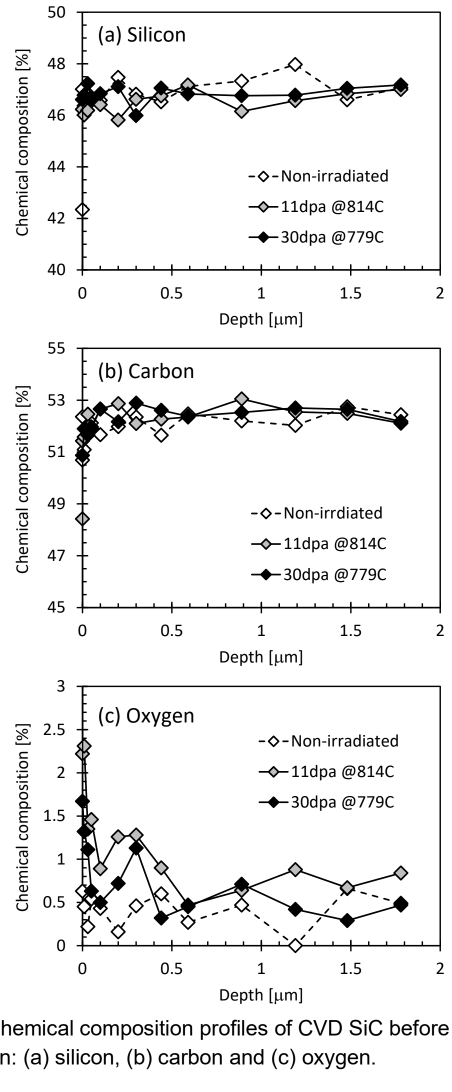

Fig. 2. Chemical composition profiles of CVD SiC before and after irradiation: (a) silicon, (b) carbon and (c) oxygen.

1 - 39 Gamma-ray Irradiation Experiment for ITER Diagnostic Systems in JADA II

S. Kitazawa, T. Hatae, M. Ishikawa, T. Oikawa, R. Imazawa, E. Yatsuka, H. Ogawa,
T. Maruyama, T. Ushiki, S. Tanaka, T. Sugie, H. Murakami, T. Kikuchi and T. Yokozuka

Department of ITER Project, NFI, QST

JADA (ITER Japan Domestic Agency) are developing to procure five diagnostic systems, microfission chamber (MFC), poloidal polarimeter (PoPola), Edge Thomson Scattering (ETS), divertor impurity monitor (DIM) and divertor infrared thermography (IRTh).

The reliability in the ITER radiation conditions of relevant equipment to be installed in the vacuum vessel, in the interspaces (IS) between the vacuum boundary and the biological shield and in the port cells (PC) outside the biological shields should be evaluated. In this study, we launched gamma-ray irradiation experiments in QST Takasaki Advanced Radiation Research Institute from 2018.

In the preliminary experiments, optical components on DIM, IRTh and ETS were irradiated up to 10 MGy for IS items or up to 200 kGy for PC items in 6th Cell at Co-60 2nd Building or 1st cell at Food irradiation Building and observed their optical properties. For DIM items, lens and some optical materials were verified [1], and then optical fibres for transmission of collected light from plasma and plasma faced metal mirrors are on-going to verify. For IRTh items, change of transmittance by gamma-ray irradiation for optical elements (CaF_2, ZnSe, ZnS, Si, Ge and K-GIR(Sumita Opt.)). For ETS items, laser-induced damage threshold (LIDT) was experimentally investigated for fused silica substrates with antireflection (AR) coatings for high-power lasers and dielectric mirrors (both compatible with two wavelengths of 1064 and 694 nm) irradiated with up to 10 MGy.

Several interesting results were obtained in the preliminary experiments. For DIM system, the designed observing optical range is in the range between 200 and 1000 nm. In the range, the irradiation effects on optical fibre transmittance are significant in the UV region of 200 – 400 nm. Several radiation resistant optical fibers have been selected in previous experiments [1] and further irradiation experiments are continuing to derive the optimum materials. Introduce moist air when breaking vacuum in ITER vacuum equipment, and then it is necessary to evaluate the deterioration of metal mirrors by gamma irradiation in humid environments. Molybdenum specimen were irradiated with gamma ray under various humidity environments to evaluate the reduce of reflectance and morphology.

In IRTh system, no significant change in transmittance was observed with gamma-ray irradiation up to 4.75 MGy to the optical components except CaF_2. However, a CaF_2 sample showed a degradation in the transmittance around the wavelength of 1.0 μm at 100 kGy. On the other hand, another sample showed no degradation in the transmittance even when 4.75 MGy gamma-ray was irradiated. Since impurity content in CaF_2 may have caused the variance.

In ETS system, so called N-on-1 test was applied to compare hardness of AR-coated fused silica sample against laser injection. Damage probability as a function of energy density obtained through N-on-1 test is shown in Fig. 1. LIDT of AR coating for 0° injections was more likely higher for the irradiated samples at a wavelength of 1064 nm [2]. Regarding the dielectric mirrors, the deterministic and fatal deterioration of the LIDT does not occur by gamma-ray irradiation of up to 10 MGy [2].

Acknowledgments

We would like to thank Naotsugu Nagasawa, Hajime Seito, Shunya Yamamoto and Hiroshi Koshikawa (QST Takasaki) and Masahiro Shimoyama and Sakiko Haruyama (RADA) for their cooperation in the irradiation and observation.

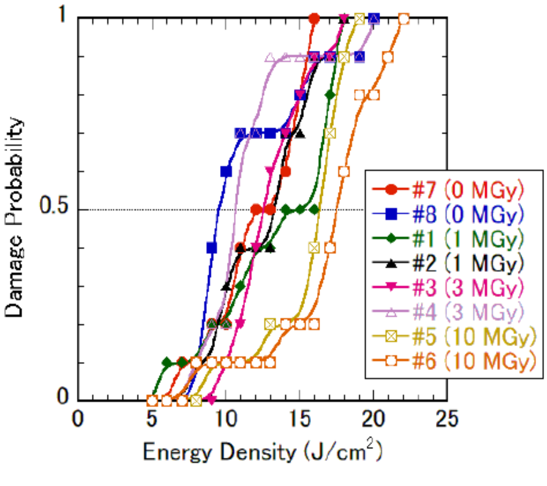

Fig. 1. Damage probability of laser windows as a function of incident beam.

References

[1] S. Kitazawa *et al.*, J. Plasma and Fusion Res. **14,** 3405089 (2019).

[2] E. Yatsuka *et al.*, Fusion Eng. Des. **160**, 111846 (2020).

1 - 40

Evaluation of Radiation Tolerance of COTS Device for Small Satellite

K. Tomita[a], K. Nakano[a], J. Harada[a], M. Sugai[a], K. Akashi[a],
T. Ohshima[b], S. Onoda[b] and T. Makino[b]

[a]Advanced Engineering Services Co., Ltd. (AES),
[b]Department of Advanced Functional Materials Research, TARRI, QST

In small satellite development, COTS (commercial off-the-shelf) devices are needed to be used due to some severe restrictions of the resource for installed components. For this reason, it is important to keep reliability for using COTS devices in small satellite development. Therefore, in order to ensure reliability for the small satellite, our company has evaluated COTS devices mainly for tolerance of the single event at Takasaki Advanced Radiation Research Institute (TARRI) since fiscal year 2008.

近年、小型人工衛星の開発が盛んになり、衛星搭載機器の低コスト化、小型化及び高機能化が要求されている。これらの要求を満たすため、民生電子部品の使用が望まれている。しかしながら、一般的に民生電子部品は宇宙環境下での使用を考慮して設計されておらず、耐放射線性は不明である。そこで民生電子部品の宇宙環境における動作状況、劣化状況を放射線試験により確認し、宇宙への適合性を把握することが必要となる。

放射線の電子部品への影響は、トータルドーズ(TID: Total Ionization Dose)とシングルイベント効果(SEE: Single Event Effect)の大きく 2 パターンに分けられる。TID はβ線、γ線、陽子線により発生する電子部品の性能劣化である。SEE は重粒子の入射により引き起こされる機能障害である。本研究において、民生電子部品の使用を想定している小型人工衛星は、低軌道かつ運用期間が 1 年と短いため、TID による影響は少ないと考える。一方、SEE は一度の発生で電子部品そのものや周辺回路を破壊する可能性がある。本研究は、様々な民生電子部品の試験を行い、SEE の発生を観測することで宇宙環境における耐放射線性の評価を行うことを目的としている。

本研究では量子科学技術研究開発機構施設共用制度を利用し、高崎量子応用研究所 TIARA 第 4 重イオン室の散乱ビーム照射試験装置を用い、AVF サイクロトロンからのカクテルビーム(N、Ne、Ar、Kr の 4 線種、または N、Ne、Ar の 3 線種)で試験した。SEE 発生頻度は、試験により得られた反転断面積、LET(Linear Energy Transfer) 閾値と CREME96 [Cosmic Ray Effects on Micro-Electronics(1996 Revision)] を用いて計算した軌道上放射線分布より算出した。

本研究で民生電子部品の使用を想定している小型人工衛星の軌道条件は、高度 700 km、軌道傾斜角 98 度、衛星構体は 2 mm 厚アルミニウム、運用期間 1 年である。算出した SEE 発生頻度と想定運用期間を比較し、民生電子部品の耐放射線性を評価した。

2019 年度は、民生のロードスイッチとバッファ IC(A、B の 2 種)を試料とした。ロードスイッチは小型人工衛星内で電源の ON/OFF やリセット回路用スイッチとして、バッファ IC は 3.3V 系から 5V 系へのレベル変換に使用できる。

2019 年度に試験を実施した試料、評価項目、試験結果及び想定軌道条件における SEE 発生頻度の算出結果を Table 1 に示す。

本試験では以下を評価項目とした。

- SEL (Single Event Latch-up)
- SEFI (Single Event Functional Interrupt)

SEL に関しては、試料の消費電流が SEL 判定閾値(通常動作時消費電流の 2 倍)以上に増加した場合に、SEL と判断し発生回数をカウントすることとした。また、SEE 発生後の試料の動作を正常復帰させる方法の確認として、電源リセットを行うこととした。SEFI に関しては、試料の誤動作を検知した場合に発生回数をカウントすることとした。

試験の結果、ロードスイッチは照射した 4 線種全てにおいて、SEL 及び SEFI は発生しなかった。そのため、Kr で SEE が 1 回発生したと仮定して、SEE 発生頻度を算出した。バッファ IC は照射した 3 線種全てにおいて SEL 及び SEFI は発生しなかった。そのため、Ar で SEE が 1 回発生したと仮定して、SEE 発生頻度を算出した。前述 2 つの評価では、ワーストケースを想定しているため、照射した線種の中で LET が最大のもので SEE 発生頻度を算出した。

Table 1 に示す Single Event Probability の値より、SEL 及び SEFI の発生頻度は想定している 1 年という運用期間に対して低く、十分な耐放射線性を有することが確認できた。

最後に、試料である民生電子部品は、宇宙環境での使用を想定して製造されたものではないため、本試験の結果が部品自体の性能・機能の優劣を示すものではないということを付記しておく。

Table 1
Single event probability.

Device under test	Evaluation Item	LET Threshold ($MeV\text{-}cm^2/mg$)	Cross-sectional area (cm^2)	Single Event Probability (event/year)
Load Switch	SEL	> 34.0	8.33E-07	< 6.08E-09
	SEFI			
Octal Buffer IC (A, B)	SEL	> 14.0	8.21E-07	< 2.64E-05
	SEFI			

1 - 41 Study on Hydrogen Generation from Cement Solidified Samples Loading Low-level Radioactive Liquid Wastes at Tokai Reprocessing Plant

F. Sato, R. Matsushima and S. Kataoka

Nuclear Fuel Cycle Engineering Laboratories, JAEA

Cement solidification of Low-level radioactive Liquid Wastes (LLWs) generated from Tokai reprocessing plant is planned in Low-level radioactive Waste Treatment Facility (LWTF). There are two kinds of LLWs, concentrated liquid waste and phosphate liquid waste. In LWTF, the concentrated liquid waste is categorized into “sodium carbonate effluent” with low radioactivity and “slurry” with comparatively high radioactivity by radionuclide separation and nitric acid ion decomposition [1]. The sodium carbonate effluent is planned to solidify with cement mixture, which contain 70~90 wt% Blast Furnace Slag (BFS) and 10~30 wt% Ordinary Portland Cement (OPC). The slurry and phosphate liquid waste are also planned to solidify with ‘Super Cement’, which is a commercial product of JGC Holdings Corporation and is an alkali activated slag cement with various minor additives.

It is known that G(H2) value of a cement solidified product containing radionuclides varies with cement and effluent composition. In this study, to obtain the G(H2) used for safety design of LWTF, as in last year, we investigated hydrogen generation from cement solidified samples containing these effluents [2, 3].

Figure 1 shows an example of the irradiation samples. The samples were prepared by mixing simulated liquid waste and cement using the composition planned in LWTF, then filled into a container (ϕ13 mm × 50 mmH) at 20 °C for a month to 7 months. After curing, these samples were put into a vial container (50 mL) one by one and were sealed with rubber septum. These samples were irradiated by Co-60 gamma-rays at about 2.5 kGy/h for 20 hours (shown in Figure 2). After the gamma irradiation, concentration of hydrogen gas generated in the vial was measured by gas chromatography and G(H2) was calculated using blank data measured previously.

As a result, the followings were clarified:

When the sodium carbonate effluent [Nitric acid radical decomposition ratio 90%, (10% $NaNO_3$ remaining)] was solidified with cement mixture (BFS/OPC = 9/1 weight ratio, hereinafter referred to as 9/1-cement), it became clear that the $G(H_2)$ of the solidified product (water cement ratio (W/C): 0.75, salt packing ratio: 20 wt%) was about 0.02 to 0.03 n/100eV in each curing periods. From this result, it is thought that $G(H_2)$ value of solidified carbonate solution with the 9/1-cement becomes constant in about one month. It was reported that $G(H_2)$ value of solidified carbonate solution with BC cement (BFS/OPC = 7/3 weight ratio) became constant (0.03 - 0.04) in about one month [3]. So, it is considered that $G(H_2)$ is not affected by the cement composition;

When the slurry waste which contained $NaNO_3$, $NaNO_2$, $NaHCO_3$, etc. as main components and Mg, Ni, Al, B, Fe, Si, TBP, etc. as impurities was solidified with the Super Cement, it became clear that the $G(H_2)$ value of the solidified product (water cement ratio (W/C): 0.67, salt packing ratio: 50 wt%) was about 0.03 to 0.04 n/100eV which was as low as of the product of solidifying the sodium carbonate effluent. In literature [4], it was reported that $G(H_2)$ of high-level liquid waste containing a large amount of nitrate was lower than that of pure water. From this result it is considered that nitrate contained in the slurry waste and sodium carbonate effluent reduce $G(H_2)$;

And when the phosphate liquid waste was solidified with the Super Cement after insolubilizing of the phosphate (NaH_2PO_4) using calcium hydroxide ($Ca(OH)_2$), it was found that the $G(H_2)$ of the solidified product (W/C: 1.37, salt filling rate: 14 wt%) was relatively low at 0.05 to 0.06 n/100eV. It is thought that insolubilized phosphate ($Ca_3(PO_4)_2$) in the product reduces $G(H_2)$;

Sodium Carbonate Effluent Solidified with 9/1-cement

Vial Container (50 mL) Sealed with Rubber Septum

Fig. 1. Example of irradiation samples.

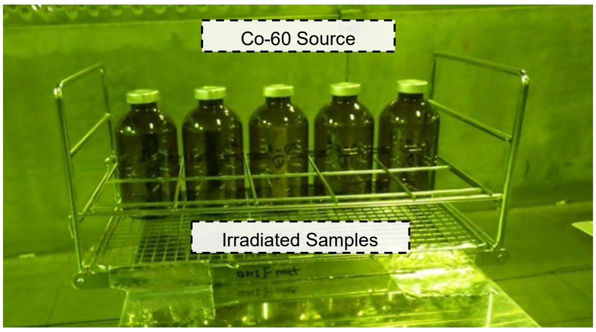

Fig. 2. Status of sample irradiation by Co-60.

References

[1] A. Sugaya *et al.*, WM2011 Conf. 11078 (2011).

[2] F. Sato *et al.*, Proc. of 2018 Fall Meeting of AESJ, 3J02 (2018).

[3] S. Kataoka *et al.*, Proc. of 2019 Fall Meeting of AESJ, 3I02 (2018).

[4] N. Nakagiri *et al.*, J of AESJ, Vol. **39**, No. 12 (1997).

1 - 42 Elemental Technology to Develop Radiation-resistant Sensor for Fuel Debris

M. Hagiwara[a], M. Sakaguchi[b], E. Hamada[b], M. Shoji[b], T. Kishishita[b], M. Miahara[b],
M. Tanaka[b], A. Takeyama[c], T. Makino[c] and T. Ohshima[c]

[a]Radiation Science Center, Applied Research Laboratory, KEK,
[b]Institute of Particle and Nuclear Studies, KEK,
[c]Department of Advanced Functional Materials Research, TARRI, QST

The state of fuel debris and the decommissioning method should be determined while estimating and reducing potential risks to accelerate the decommissioning of the Fukushima Daiichi Nuclear Power Plant, Tokyo Electric Power Company Holdings, Inc. Focusing on spontaneous fission neutrons emitted from submerged fuel debris, we are developing a boron-coated diamond neutron sensor readout system that operates in a high γ-ray environment, and underwater exploration device using a Remotely Operated Vehicle (ROV) with a multi-phased array sonar and a sub-bottom profiler (SBP) in interdisciplinary research and development (High Energy Accelerator Research Organization: KEK, National Maritime Research Institute: NMRI, and National Institute for Material Science: NIMS).

The irradiation evaluation of the key technologies (signal-processing integrated circuit for the diamond neutron sensor and acoustic exploration device mounted on ROV) establishes radiation-resistant basic technologies that support the decommissioning work by remote control. The purpose of the irradiation study is to investigate the total ionizing dose effect of γ-rays on circuits and acoustic exploration devices. As a wide range of applications can be expected for signal-processing integrated circuits, the absorbed dose targeted in the irradiation is set to be higher than 1 MGy, which provides us the operating limit of CMOS technologies.

Several transistors having normal structures and radiation-resistant structures were manufactured, and the static characteristics before and after γ-ray irradiation were investigated. The irradiation test was conducted at the γ-ray irradiation facility (Cobalt 1st Building, 2 cells) at TAARI, QST. The transistor samples were irradiated with ^{60}Co γ-rays until the absorbed dose reached 6 MGy, under the condition that could cause the largest damage to the transistor during irradiation (drain–source voltage V_{ds} = gate–source voltage V_{gs} = drain voltage V_{dd} (1.2 V)) and maintained current flow at room temperature.

Analog-to-digital conversion integrated circuits (ADCs) and high-speed amplifier circuits developed using the CMOS semiconductor process were also evaluated after the γ-ray irradiation. Typical operation conditions (bias voltages/currents and external digital signals for ADC) were maintained during the irradiation.

The irradiation effects on normal transistors with a long gate length (L) were not observed at several megagray in absorbed dose. We confirmed no performance deterioration below 1 MGy even for the minimum size transistors, but the static characteristics (I_{ds}–V_{gs}) varied depending on the transistor size beyond 1 MGy. The slope of the I_{ds}–V_{gs} curve decreased beyond 1 MGy for small transistors. It is caused by a decrease in the effective value of the gate width (W) due to the trap charges generated by γ-ray irradiation around the gate. As this phenomenon depends on the transistor structure near the gate, the effect heavily depends on the CMOS process; hence, a detailed evaluation is required in the future. Regarding the transistor with a structure enhancing radiation resistance, good static characteristics were observed even for a transistor with a short L that has been irradiated with an absorbed dose up to several megagray. It can be inferred that the effective change in W caused by the γ-ray irradiation is suppressed by changing the transistor shape as described above.

Regarding the irradiation test of the integrated circuit, the result of the successive approximation type 10 MHz ADC (SAR ADC) showed no performance degradation after γ-ray irradiation of several megagray. The current consumption of the power supply for the I/O circuit increased by 70 μA, but there was no change in the power consumption of the other circuit blocks. In addition, we determined the number of effective bits after irradiation to be 9.06 bits, which shows that the integrated circuit can be used as an ADC with 10 MHz 10-bit resolution. We also confirmed similar characteristics for a 100 MHz ADC.

To summarize, regarding the radiation resistance of the transistor, a transistor that can operate sufficiently up to 1 MGy can be manufactured via a commercial process by thinning the oxide film. It was also demonstrated that a transistor with a higher radiation resistance could be manufactured by further improving the transistor structure. We observed the deterioration of characteristics beyond 1 MGy for normal transistors with a short L and small W. Further experiments are required to develop high-radiation-resistive transistors. The proposed technology is considered valuable for monitoring and control in a high-radiation environment.

Acknowledgments

This study was conducted in the framework of “FY2018 Center of World Intelligence Project for Nuclear Science/Technology and Human Resource Development” of CLADS, JAEA, using the public utilization of the Co-60 irradiation facility at TAARI, QST.

1 - 43 Investigation of Dominant Factors Accelerating Corrosion Under Gamma-ray Irradiation

H. Ogawa and I. Ioka

Nuclear Science and Engineering Center, JAEA

Radiation field makes corrosion of the materials (Zr, SUS, etc.) accelerate. The number of ions generated by a radiolysis of the water or the steam becomes important as controlling factor of corrosion acceleration. In previous model, the number of ions formed by gamma-ray radiation, H^+, OH^-, O^- etc., are evaluated conventionally by a G value. In the radiation field, corrosion of the materials is promoted by these ions. However, the increase in corrosion rate at a radiation field can't be explained sufficiently by the evaluation from the G value. So, new corrosion model by the excitation effect of the material's surface was proposed as shown in Fig.1 [1]. When gamma-ray was applied to the material surface, a large number of electrons are formed by the photoelectric effect, Compton effect, pair production. The electrons released from the material surface ionizes the water or steam of the metal surface neighborhood. The water or the steam in the vicinity of material surface is irradiated by direct gamma-ray and the electrons emitted from the metal surface. Therefore, more ions (H^+, OH^-, O^- etc.) are produced at the surface in comparison with a distant place. It is considered that these ions make the corrosion in the material surface promote. The objective of our research is to clarify corrosion acceleration mechanism of materials under the gamma-ray radiation field.

The irradiation was performed at the gamma-ray irradiation facility of Takasaki Advanced Radiation Research Institute of QST. The ^{60}Co gamma-ray absorbed dose rate is 10 kGy/h. An irradiation time was set to 30 min. Commercial purified water was used in the experiment. The difference in dissociation ratio of the water by the radiolysis was checked using the pH method and the electric conductivity method. In order to clearly evaluate the influence of a radiolysis of the water, the glass beads were scattered in water to increase reaction surface area.

Figure 2 shows changes in pH and the electric conductivity of water which scattered glass beads by the gamma-ray irradiation. During the gamma-ray irradiation, pH decreases, and the electric conductivity showed a tendency to increase. After the gamma-ray irradiation, pH and the electric conductivity have not returned to the value before irradiation. It is considered that the hydrogen peroxide and the ozone generated by the radiolysis of the water is one of these causes. The concentration of hydrogen peroxide in water was measured after irradiation. The concentration of hydrogen peroxide was about 3.5 x 10^{-4} wt%. When the concentration of the hydrogen peroxide in water is less than 10 wt%, the pH value of the hydrogen peroxide water decreases with increase of the concentration of the hydrogen peroxide. The data of pH of 3.5 x 10^{-4} wt% hydrogen peroxide water was 5.58. This was the same as pH (5.56) of the purified water mostly. It seems that the decrease of pH after irradiation is not able to explain by the production of hydrogen peroxide.

In the future, we are going to check the effect of the ozone on pH of the gamma-ray irradiated water.

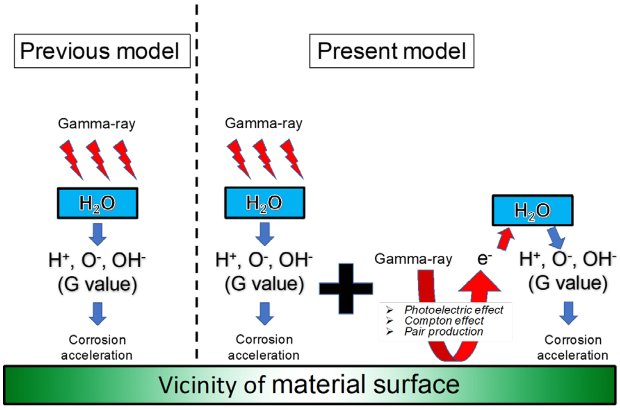

Fig. 1. Proposed new corrosion model by the excitation effect of the material's surface.

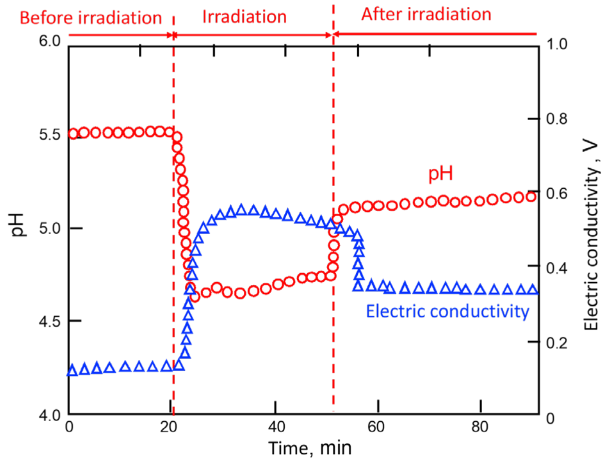

Fig. 2. Changes in pH and the electric conductivity of purified water which scattered glass beads by the gamma-ray irradiation.

Acknowledgments

This work was supported by JSPS KAKENHI Grant Number JP18K05003.

Reference

[1] H.Ogawa *et al.*, Nucl. Sci. Eng. **152**, 204 (2006).

1 - 44

Study on Gamma-ray-degradation of Adsorbent for Low Pressure-loss Extraction Chromatography

Y. Miyazaki[a)], Y. Sano[a)], N. Okamura[a)], M. Watanabe[a)] and M. Koka[b)]

[a)]Nuclear Fuel Cycle Engineering Laboratories, JAEA,
[b)]Beam Operation Co., Ltd.

Introduction

The partitioning and transmutation technology of long-lived and/or heat-generated minor actinide (MA; Am, Cm) is one of the strategies for reducing the volume and radiotoxicity of radioactive waste. JAEA has developed N,N,N’,N’,N”,N”-hexaoctylnitrilotri-acetamide (HONTA) as a MA-selective extractant and verified >99.9% Am recovery from high-level liquid waste [1 – 2]. Figure 1 shows the structure of HONTA.

The extraction chromatography has been paid attention to resolve issues of waste solvent, operation cost and radiolytic degradation of the current solvent extraction method [3]. For the past two years, granulation of porous silica particle with a diameter of 2 mm was established for low pressure-loss column partitioning system. HONTA was selected for the impregnating reagent and its extraction ability was evaluated by the batch-wise experiment. In this study, gamma-ray radiolysis of HONTA-impregnated silica type adsorbent was investigated by GC/MS analysis.

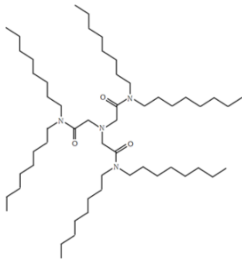

Fig. 1. Structure of HONTA.

Experimental

HONTA (purity >98%) was made by Chemicrea Inc. HONTA-impregnated silica type adsorbent (0.5 g) in 0.01 M nitric acid (10 mL) was exposed to gamma-ray irradiation at the Co-60 gamma-ray irradiation facility in TARRI, QST. After filtration, the irradiated adsorbent was washed with acetone and the obtained organic mixture was analyzed by using GC-MS instrument (GC-17A and GCMS-QP5050, Shimadzu Corp.).

Results and Discussion

Figure 2 shows the GC/MS chromatograms of the irradiated HONTA-impregnated silica type adsorbent at absorbed dose of (a) 0.51 MGy, (b) 0.91 MGy and (c) 2.09 MGy. Here, asterisk (*) is dioctyl phthalate, which is the remained organic solvent after adsorbent preparation, so it is excluded from radiolysis. There are total 5 products from HONTA and their generations are strongly correlated to absorbed dose. For example, irradiation at >1 MGy increases the number of radiolysis products.

Table 1 shows the proposed radiolysis structures of HONTA. The C-N bond and C-C bond around the carbonyl group are likely cleaved while the octyl side chain is little affected by gamma-ray irradiation. No. 4 and 5 are the unique products found for extraction chromatography.

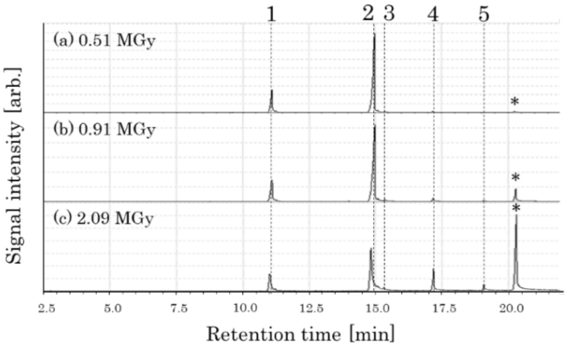

Fig. 2. GC/MS chromatograms of the irradiated HONTA-impregnated silica type adsorbent at absorbed dose of (a) 0.51 MGy, (b) 0.91 MGy and (c) 2.09 MGy.

Table 1
Radiolysis products of HONTA.

No.	1	2	3	4	5
Proposed chemical structure	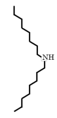 NH	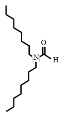 N O H	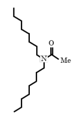 N O Me	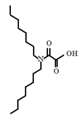 N O O OH	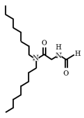 N O H N H O
Molecular formula	$C_{16}H_{35}N$	$C_{17}H_{35}NO$	$C_{18}H_{37}NO$	$C_{18}H_{35}NO_3$	$C_{19}H_{38}N_2O_2$
Molecular weight	241	269	283	313	326

Summary

The radiolysis of HONTA-impregnated silica type adsorbent was investigated and its products were identified from the GC/MS analysis. Further studies are required to understand radiolysis mechanism.

Acknowledgments

A part of this work is supported by the Innovative Nuclear Research and Development Program from the Ministry of Education, Culture, Sports, Science and Technology of Japan.

References

[1] Y. Sasaki *et al.*, Solv. Extra. Ion Exchange **32**, 179 (2014).
[2] Y. Ban *et al.*, Solv. Extra. Ion Exchange **37**, 489 (2019).
[3] Y. Wei *et al.*, Nucl. Tech. **132**, 413 (2000).

1 - 45 Irradiation Behavior of ODS Steels for Fuel Cladding Tube of Fast Reactor

T. Tanno, Y. Yano, S. Ohtsuka and T. Kaito

Oarai Research and Development Institute, JAEA

Background

JAEA is developing oxide dispersion strengthened (ODS) ferritic/martensitic steels with excellent high temperature creep strength properties as a fast reactor fuel cladding tube material [1]. One of the challenges in fast reactor fuel cladding tube is suppression of void swelling which is the dimensional change of materials due to neutron irradiation. ODS steel has nano-sized oxide particles finely dispersed in the matrix, which contributes to the excellent high-temperature strength of ODS steel. The large number of particle/matrix interfaces is thought to act as a sink for irradiation induced point defects and suppress void swelling, but the void swelling data of ODS steel at high doses (>200 dpa) are not necessarily abundant at present. Therefore, in this study, in order to evaluate the void swelling resistance of ODS steel, Fe^{3+} and He^{+} simultaneous irradiation simulating displacement damage and transmutation gas atom was carried out. The specimens tested in this study were multiple types of ODS steels with different matrix phases and non-ODS steels for comparison. The purpose of this study was to clarify the effect of nano-sized particles on the void swelling resistance.

Experimental

The specimens were variety of steels including 9Cr- and 12Cr-ODS, ferritic/martensitic steel (PNC-FMS) and austenitic stainless steel (PNC316). Different final heat treatments were applied depending on the steel type and shape of the specimens, resulting in different microstructures of matrix. 10.5 MeV Fe^{3+} and 1.2 MeV He^{+} ions were simultaneously irradiated using the tandem accelerator and single-ended accelerator in TIARA. The irradiation condition was set to accelerating void swelling in ferritic steel in order to emphasize the microstructure difference on swelling resistance. Helium concentration set to 1 appmHe/dpa which is 5 times the fast reactor core condition. An energy degrader was used to flatten the depth profile of He^{+} ions. The irradiation temperature was 470 °C which is peak swelling temperature of ferritic steels by ion irradiation [2]. The total irradiation dose was 94.5 dpa. The cross-sectional specimens for transmission electron microscope (TEM) were prepared by the lift-out method using a focused ion beam system, and the microstructure of irradiated region was observed by using TEM.

Results

TEM observation revealed that voids larger than 30 nm were found in non-ODS steels (PNC-FMS and PNC316) and 12Cr-ODS recrystallized ferritic steel but not in 9Cr-ODS and 12Cr-ODS ferritic steel, as shown in Fig. 1. The number density of voids was smaller in 12Cr-ODS than in non-ODS steels, although no quantitative analysis has been performed yet. Void swelling is the product of number density and size of voids. Thus, the observation result indicates that the ODS steel has a superior void swelling resistance. The interface between nano-particle and matrix may act as a sink site for vacancies and He-V complexes introduced by irradiation, resulting in the suppression of vacancy accumulation and void growth. On the other hand, there are no particle/matrix interface in non-ODS steels, resulting in the growth of voids. The difference in void formation behavior between 12Cr-ODS rod and cladding is discussed. The rod specimen is as bent-corrected condition after hot extrusion and has a relatively high dislocation density. On the other hand, the cladding specimen was cold-rolled and then subjected to recrystallization heat treatment. It has significantly larger grain size and lower dislocation density than the rod specimen. The larger dislocation density and longer grain boundary length in rod specimen effectively absorb point defects, leading to the suppression of void formation.

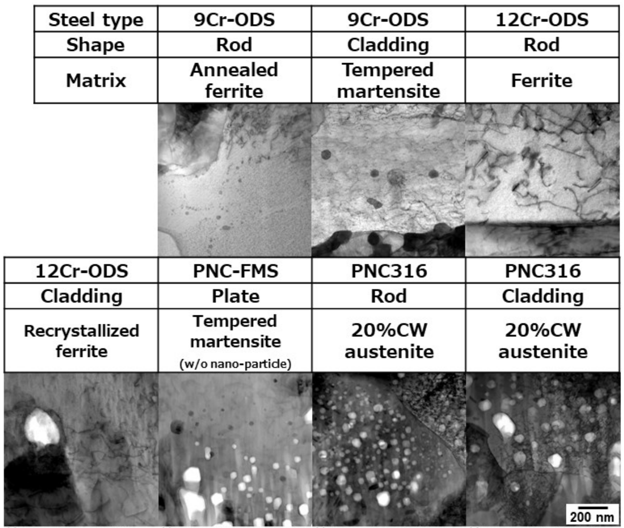

Fig. 1. Microstructure evolution in ODS and non-ODS steels (martensitic steel and austenitic stainless steels) after Fe^{3+} and He^{+} simultaneous irradiation up to 94.5 dpa at 470 °C.

Acknowledgments

The present work was supported by the Shared Use Program of QST Facilities.

References

[1] T. Tanno *et al.*, J. Nucl. Mater. **455**, 480 (2014).
[2] A. Kimura *et al.*, J. Nucl. Mater. **367-370**, 60 (2007).

1 - 46 Characterization of Growth Control in $Ti_{1-x}Al_xN$ Thin Films on Monocrystalline AlN by Reactive CVD

Y. Kasukabe[a), b)], H. Shimoda[b)] and S. Yamamoto[c)]

[a)]Global Learning Center, Tohoku University,
[b)]Department of Metallurgy, Tohoku University,
[c)]Department of Advanced Functional Materials Research, TARRI, QST

Films of $Ti_{1-x}Al_xN$ have been known as the material which exhibits superior mechanical and thermal properties, and those are widely used as coatings for industrial applications such as cutting tools. Irrespective of those attracting performance, little is studied on the growth mechanism as well as the chemical process. In this work, $Ti_{1-x}Al_xN$ thin films have been prepared by reactive Chemical Vapor Deposition (CVD) and analyzed by Field Emission Gun Scanning Electron Microscopy (FEG-SEM), Transmitting Electron Microscope (TEM) [1], and X-ray Diffraction (XRD).

Recently, it has been reported that $Ti_{1-x}Al_xN$ films have been grown by use of the titanium tetra chloride, $TiCl_4$, and c-plane (0001) monocrystalline hexagonal aluminum nitride, AlN, precursors [2]. The AlN has been prepared at 1500 °C with the gas mixture of NH_3 and $AlCl_3$ on c-plane (0001) monocrystalline hexagonal sapphire. During the $Ti_{1-x}Al_xN$ growth, hydrogen (H_2) gas is supplied in order to promote the reactivity. The growth has been performed at various temperatures between 800 °C and 1200 °C on the 100-nm-thick monocrystalline AlN on sapphire.

The surface morphologies of $Ti_{1-x}Al_xN$ layers deposited at (a) 800 °C, (b) 900 °C, (c) 1000 °C and (d) 1200 °C on monocrystalline AlN substrates were characterized by FEG-SEM. At temperatures lower than 1000 °C, surface morphologies appeared to be smooth. As the temperature was raised, the grain size appeared to become larger, but there was almost no substantial change between 800 °C and 1000 °C. However, the surface morphology deposited at 1200 °C was quite different form the others. The grains of films deposited at 1200 °C were much smaller than those fabricated at less than 1000 °C, and some of them seemed to grow in a columnar shape. Generally, as temperature is raised, reaction rate increases. If the reaction rate increases in this system, it can be expected that $TiCl_4$ and AlN react as soon as $TiCl_4$ reaches the AlN surface, leading to grow in a columnar shape. At temperature lower than 1000 °C, reaction rate is not as high compared to the system at 1200 °C, therefore, sufficient time to diffuse on the surface exists, leading to an increase of surface flatness. Furthermore, the chemical composition analysis of EDX equipped with TEM clarified that the average of 25-30 % Al, 35-40 % Al and 75-80 % Al were contained in the layers deposited at 1200 °C, 1000 °C and 900, respectively. This indicates that Al content in the grown $Ti_{1-x}Al_xN$ film can be decreased by raising the substrate temperature, which means that Al content in the grown film can be controlled by changing substrate temperature.

In order to characterize the effect of H_2 carrier gas flux on the $Ti_{1-x}Al_xN$ film morphology, the surface morphologies of the $Ti_{1-x}Al_xN$ layers deposited at 1200 °C for 15 minutes with H_2 carrier gas flux fixed (a) at 100 sccm (Standard Cubic Centimeter per Minute), (b) at 1000 sccm and (c) 2000 sccm on monocrystalline AlN substrates, were observed as shown in Fig. 1. Figure 1 (a) indicates there are many grains grown in a columnar shape. These columnar grains grow randomly. However, the surfaces of the layers fabricated with H_2 gas flux at more than 1000 sccm (shown in Fig. 1 (b) and (c)) are much flatter than that of the layer with 100 sccm. It can be considered that this phenomenon results from the transportation of $TiCl_4$ by H_2 gas flux and the reaction between $TiCl_4$ and AlN. If fewer H_2 carrier gas flux exists in the reactor, because of the high reactivity between $TiCl_4$ and AlN, these react to each other as soon as $TiCl_4$ reaches the AlN surface. Therefore, the surface tends to be rough in this condition. However, if enough amounts of H_2 gas flux exist, $TiCl_4$ can be carried effectively and easily diffuse on the surface, leading to the flatter surface. This indicates that surface morphologies of the grown $Ti_{1-x}Al_xN$ films can be controlled by changing the H_2 carrier gas flux.

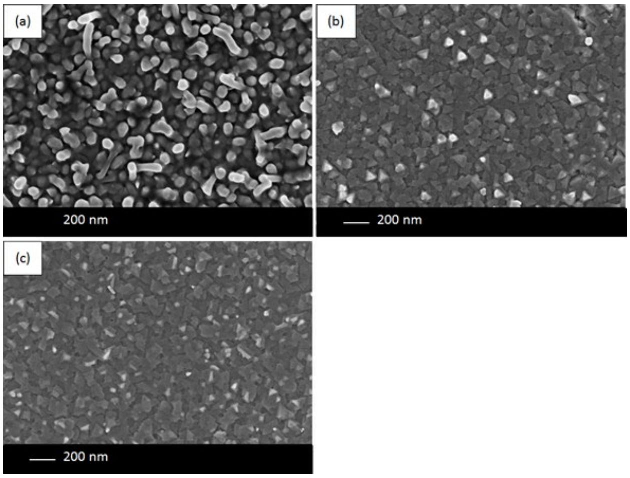

Fig. 1. Surface morphologies of the layers fabricated on monocrystalline AlN at 1200 °C with H_2 gas flux fixed at (a) 100 sccm, (b) 1000 sccm, (c) 2000 sccm observed by FEG-SEM.

References

[1] H. Abe *et al.*, JAERI-Research **96-047**, 1 (1996).
[2] R. Boichot *et al.*, Surf. Coat. Technol. **205**, 1294 (2010).

1 - 47

Evaluation of Bulk Irradiation Defect Distribution Simulating Neutron Irradiation on Tritium Retention in Damaged Tungsten

Y. Oya[a)], M. Nakata[b)], S. Yamazaki[b)], T. Wada[b)], A. Koike[b)],
M. Zhao[c)], F. Sun[a)] and T. Miyazawa[d)]

[a)]Faculty of Science, Shizuoka University,
[b)]Graduate School of Integrated Science and Technology, Shizuoka University,
[c)]Graduate School of Science and Technology, Shizuoka University,
[d)]Division of Technical Service, Shizuoka University

Tungsten (W) has been considered as a promising candidate for plasma facing materials (PFMs) in future D-T fusion reactors. During the operation of fusion reactors, W will be exposed to energetic particles, such as 14 MeV neutron produced by D-T fusion reaction, and energetic particles including hydrogen isotope ion, helium ion and charge-exchanged particles. It is well known that the damages introduced by both energetic particles and neutrons will enhance the hydrogen isotope retention by the formation of stable trapping sites [1, 2]. In addition, the distribution of damages introduced by charge-exchanged particles is concentrated near the surface region, while that by neutrons is uniformly extended throughout the bulk [2]. In this study, irradiation damages were introduced by both of neutron and 6 MeV Fe ion irradiations with various damage distributions, and the D retention behaviors were evaluated by thermal desorption spectroscopy (TDS).

A disk-type polycrystalline W (6 mm$^{\varphi}$ × 0.5 mm^{t}) purchased from A.L.M.T. Co. Ltd. was used. To remove impurities and damages introduced during the polishing processes, the samples were heat-treated at 1173 K under ultrahigh vacuum ($< 10^{-6}$ Pa). The irradiation damages were introduced by 6 MeV Fe^{2+} irradiations at room temperature with the damage concentrations of 0.01, 0.1 dpa (displacement per atom) by a 3 MV tandem accelerator in Takasaki Ion Accelerators for Advanced Radiation Application (TIARA) at National Institutes for Quantum and Radiological Science and Technology (QST). Thereafter, the samples were transferred to the neutron irradiation facilities. The fission neutron irradiation was performed at Kyoto University Research Reactor Institute (KUR) with the damage concentration up to 0.015 dpa.

After the damage introduction, the 1.0 keV deuterium ion (D_2^+) implantation was performed at Shizuoka University. The D ion fluence was set to be 1.0×10^{22} D^+ m^{-2} with the ion flux of 1.0×10^{18} D^+ m^{-2} s^{-1}. According to the calculation of SRIM code using displacement threshold energy of 50 eV, the implantation depth of 6 MeV Fe^{2+} was estimated to be about 1.5 μm [3]. In addition, that of 1.0 keV D_2^+ was also calculated to be up to 10 nm. The deuterium desorption behavior was evaluated by TDS at the temperature up to 1173 K with the heating rate of 0.5 K s^{-1}.

Figures 1 and 2 show the D_2 TDS spectra for neutron and/or Fe^{2+} irradiated W samples with various damage concentrations. In the multiple neutron - Fe^{2+} irradiated samples, the retentions of D at Peaks 3 and 4 were decreased as increasing the damage level by neutron irradiation . But, the desorption of D at Peak 2 was increased due to increasing of the trapping sites with lower D binding energy by neutron irradiation, as compared with the only Fe^{2+} irradiated samples. In addition, the total D retention was decreased by multiple neutron - Fe^{2+} irradiation compared to that by only Fe^{2+} irradiation, even though the damage level by neutron irradiation was increased. This may be caused by the formation of stables D trapping sites such as void clusters and voids were not formed by lower neutron fluence. It was considered that the hydrogen isotope recycling was enhanced due to damage introduction by neutron in the shallow region.

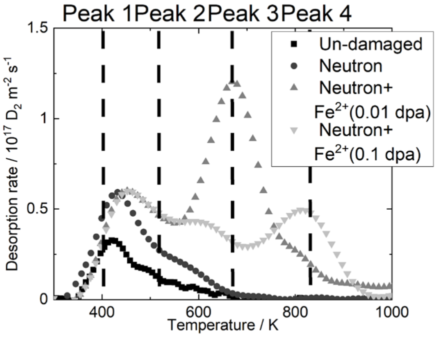

Fig. 1. D_2 TDS spectra for neutron and Fe^{2+} irradiated samples

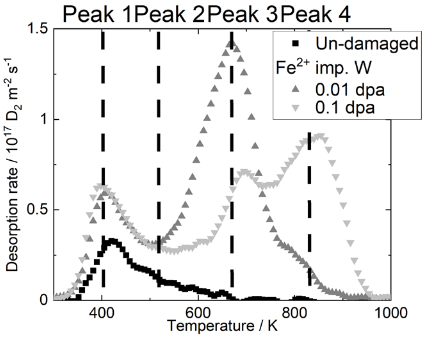

Fig. 2. D_2 TDS spectra for Fe^{2+} irradiated samples

References

[1] A. Hasegawa *et al.*, Fusion Eng. Des. **89**, 1568 (2014).
[2] H. Fujita *et al.*, Phys. Scr. **T167**, 014068 (2016).
[3] http://www.srim.org/.

1 - 48

Development and Application of Water Soluble Phenothiazine Type Color Former for Gamma Rays Detection System with Naked Eyes

T. Tachikawa and S. Ishibashi

Graduate School of Science and Engineering, Saitama University.

Gamma rays are used in various fields such as sterilization of medical instruments, prevention of germination of potatoes, sterilization of insects, and cancer treatment. However, since gamma rays are not sensed by five senses of human beings, special precautions are necessary for their leakage and they give people an ambiguous anxiety. In our laboratory, the color formers (CFs) have been investigated for the purpose of detecting low-dose gamma rays by visual observation [1 - 3].

In this study, the water - soluble phenothiazine type color former **1** which changes to the colored form by gamma ray in aqueous solution using divalent iron ion (Fe^{2+}) as an additive will be reported (Scheme 1).

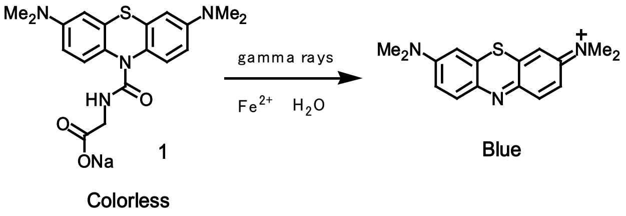

Scheme 1. Coloration of color former **1** by γ rays.

.

Color former **1** was prepared from methylene blue, cationic phenothiazine thiazine dye. Methylene blue was reduced with sodium dithionite under basic conditions and the amine derivatives were reacted with triphosgene to give the chloroformylated compound. And hypolization of the precursor obtained by the reaction of the chloroformylated compound with glycine methyl ester hydrochloride gave the phenothiazine type color former **1**.

The aqueous solution of color former **1** ($[\mathbf{1}]_0 = 0.13$ mM) was prepared and irradiated with γ rays derived from the ^{60}Co source at gamma-ray irradiation facility in Takasaki Advanced Radiation Research Institute (TARRI), with total doses of 10, 40, 70 Gy at a dose rate of 100 Gy/h at room temperature.

The color development of the solution could not be observed by visual inspection even at irradiation of 70 Gy. We considered that γ-irradiation to an aqueous solution of **1** is not enough to develop the color change. So, Fe^{2+} ($Fe_2SO_4 \cdot 7H_2O$) was added to the color former solution expecting that the more active hydroxyl radical would be generated in the solution by γ-irradiation. When 5 equivalents of Fe^{2+} was added to the solution, the increase in absorbance at 655 nm was the largest in the spectra measurement (Fig. 1), and the solution turned to blue. The color change was visually observed from the irradiation of 10 Gy (Fig.2).

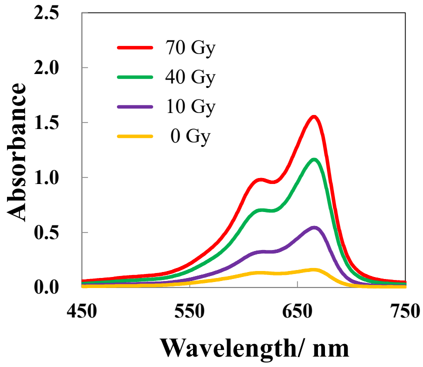

Fig. 1. Spectral changes of aqueous solution of **1** after γ- irradiation ($[\mathbf{1}]_0 = 0.13$ mM, $[Fe^{2+}]_0 = 0.65$ mM)

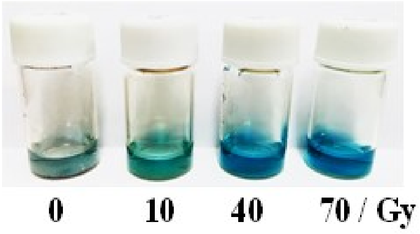

Fig. 2. Color changes of aqueous solution of **1** after γ-irradiation ($[\mathbf{1}]_0 = 0.13$ mM, $[Fe^{2+}]_0 = 0.65$ mM).

The aqueous solution of phenothiazine type color former 1 was not sensing to gamma rays but as Fe^{2+} converts the inactive species for **1** generated from water by gamma rays into active species for **1**, the addition of Fe^{2+} to the solution was revealed to sensitize the color development by γ-rays of the color former.

In conclusion, we reveal that the color change of the aqueous solution of the phenothiazine type color former **1** could be recognized by naked eyes after γ irradiation of 10 Gy by the addition of Fe^{2+} ion into the solution.

References

[1] H. Itoi *et. al.*, Chem. Lett. **38**, 1002 (2009).
[2] T. Tachikawa *et. al.*, Isotope News **731**, 7(2015).
[3] T. Tachikawa *et. al.*, Material Stage **14**(6), 1(2014).

1 - 49 Gamma-irradiation Effect on ESR Signals Derived from Hydrothermal Minerals and Its Application to Fault Dating

T. Fukuchi

Graduate Faculty of Interdisciplinary Research, University of Yamanashi

A new dating method is needed to evaluate the activity of faults in the regions without Quaternary overlying sediments. The ESR (electron spin resonance) dating technique is directly applicable to hydrothermal minerals generated in fault gouge, which is formed by fracturing and frictional heating in fault slip. ESR signals derived from such hydrothermal minerals give the age of fault slip.

Figure 1A shows ESR spectra obtained from the black indurated gouge (BM-1) and not indurated gouge (BG-2) in the Taiwan Chelungpu Fault Drilling Project (TCDP) Hole B 1194 m core [1]. ESR measurement conditions are as follows: Microwave frequency is 9.44 GHz, microwave power is 1 mW, measurement temperature is room temperature, modulation width is 100 kHz 0.05 mT, response is 0.3 s, scan speed is 8 min/scan., and computer accumulation is 3 times. Besides a paramagnetic Fe^{3+} ion signal ($g = 4.23$) and an organic radical ($g = 2.004$), a broad FMR (ferrimagnetic resonance) signal, which have been generated by hydrothermal reaction in recent fault slip, is detected.

To reproduce the hydrothermal reaction caused in fault gouge by fault slip, I carried out hydrothermal reaction experiments using the Nojima granite powder (Fig. 1B). The Nojima granite powder was put in a hydrothermal reactor with pure water and heated for 1-2 weeks at 240 °C. As a result, FMR signals similar to those detected from the black fault gouge samples in the TCDP Hole B 1194 m core are newly generated from the Nojima granite powder after hydrothermal reaction (Figs. 1C and 1D).

For detecting new ESR signals derived from hydrothermal minerals and investigating the gamma-irradiation effect on the FMR signals, I carried out artificial gamma-irradiation with a ^{60}Co source at 2 cell irradiation facility in the food irradiation building, Takasaki Advanced Radiation Research Institute, QST. The irradiation dose rate is 376.43 Gy/h. After gamma-irradiation, no new ESR signal derived from hydrothermal minerals is detected. The FMR signals increase with radiation dose although it is unclear whether or not they are applicable to fault dating.

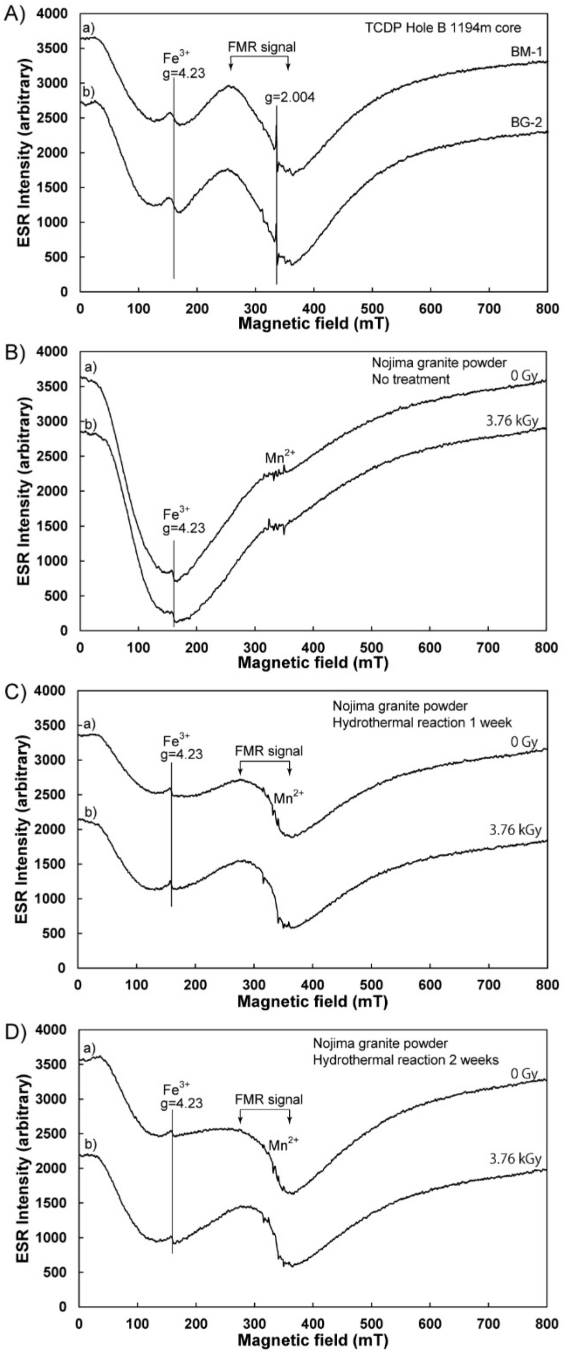

Fig. 1. A) Natural fault gouge samples BM-1 (a) and BG-2 (b) in the TCDP Hole B 1194m core, B) Nojima granite powder samples, C) Hydrothermal reaction samples heated for one week at 240 °C, D) Hydrothermal reaction samples heated for two weeks at 240°C. a) and b) in Fig.1B~1D are 0 Gy and 3.76 kGy, respectively. Mn^{2+} ion signals are derived from a manganese marker.

References

[1] T. Fukuchi, 2012, ESR techniques for the detection of seismic frictional heat. *In*: Earthquake Research and Analysis-Seismology, Seismotectonic and Earthquake Geology (ed. by D'Amico Sebastiano), Chap.16, p.285-308, InTech-Open Access Publisher.

Part Ⅱ

2. Life Science

2 - 01 Metabolomics in Carbon-ion-induced Bystander Effects on Normal Human Fibroblasts

M. Suzuki[a], T. Funayama[b], M. Suzuki[b], Y. Yokota[b] and Y. Kobayashi[b]

[a]Department of Basic Medical Sciences for Radiation Damages, NIRS, QST,
[b]Department of Radiation-Applied Biology Research, TARRI, QST

We have been studying the bystander effects in cellular radio-biological responses, such as chromosomal aberrations, cell death and gene mutation, in normal human fibroblasts or human tumor cell lines using the carbon-, neon- and argon-ion microbeams. So far the results obtained were summarized as follows;

(1) The observed bystander effects induced in normal human fibroblasts were clearly dependent on radiation quality, showing clear bystander effects induced by the lower-Linear-Energy-Transfer (LET) carbon ions but not the higher-LET neon and argon ions.
(2) Gap-junction mediated cell-cell communication was an important role for inducing the aforesaid effects.
(3) The bystander effect via secreted factor(s) at 24 h after irradiation was induced by argon ions but not carbon and neon ions in cell death, and by neon and argon ions not carbon ions in gene mutation.
(4) The secreted factor-induced bystander effects were suppressed by ascorbic acid but not dimethyl sulfoxide.
(5) In the case of communication between tumor and normal cells, the medium from the irradiated human tumor cells enable to induce damage in the neighboring non-irradiated normal cells via the secreted factor-induced bystander effects.

Thus heavy-ion induced bystander effects varied radiation quality (ion species and LET), biological endpoint and inducing pathway. Studies of bystander cellular responses induced by different radiation types can provide us an important information for evaluating human risk of the exposure for low-dose or low-dose-rate radiations, such as the accident of Fukushima Daiichi Nuclear Power Plants and developing tumor radio-therapy. However, there are a lot of unknown phenomena concerning cellular responses induced by low-fluence irradiations of heavy ions and still unclear their mechanism. For instance we want to know why the higher-LET argon ions never induce bystander cellular effects via gap-junction mediated cell-cell communication, what kinds of pathways in cell-cell communication bear the responsibility, what is the real substance(s) of the secreted factor(s).

We next target mechanism or mechanism(s) of pathways for heavy-ion induced bystander effects. We've just started the experiment forcing on metabolome level in order to identify metabolite concerning bystander effects using the metabolome analysis. This year we try to examine metabolome analysis against carbon-ion irradiated normal human fibroblasts, which showed the bystander cellular effects via gap-junction mediated cell-cell communication and report the preliminary data.

Normal human skin fibroblasts were irradiated with carbon-ion microbeams (103 keV/μm) generated at the HZ1 port of TIARA facility. Irradiations were carried out using the 256-cross-stripe method [1]. Briefly, the beam size of each irradiation point of the microbeam was 20 μm in diameter and the irradiations in each point were performed to deliver 8 ions. Immediately after irradiation, the medium was removed from the dish, methanol containing 2-isopropylmalic acid was added, the cells were scraping from the dish and collecting the cell suspension into the 15 mL polypropylene tube. The sample was washed twice in methanol, homogenized, centrifuged at 3000 rpm for 5 min and collected supernatant. After drying the solution containing methoxyamine hydrochloride and pyridine was added and shaking for 30 min. And then in the sample N-methyl-N-(trimethylsilyl)trifluoroacetamide was added, shaking for 30min, centrifuged at 16000 ×g for 1 min and collected supernatant. The sample was analyzed using the gas chromatography-mass spectrometry. The obtained data was calculated and analyzed using the SHIMAZU Smart Metabolites Database.

The preliminary result was summarized in Table 1. The data showed the candidate metabolites over 1.3 times higher in the ration of peak area in carbon-ion irradiated cells than that in unirradiated control cells using the database.

Table 1
The obtained candidate chemical compounds analyzed using the database.

Chemical compound	Peak ratio (irradiated/control)
Lactose	2.2
Histidine	1.9
Cystine	1.5
Pyruvic acid	1.3
3-Hydroxyisobutyric acid	1.3

We've just got the first result and are now analyzing each compound what kinds of roles they will bear the responsibility for induced bystander effects. We continue to study in order to understand mechanism or mechanisms for heavy-ion induced bystander effects.

Reference

[1] M. Suzuki *et al.*, JAEA Takasaki Annu. Rep. 2006, **JAEA-Review 2007-060**,107 (2008).

2 - 02 Carbon-ion and Proton Beams Revealed Hematopoietic Cell Responses Against Irradiation in Adult Medaka

S. Oda a), T. Yasuda a), D. Li a), T. Endo a), S. Mori a), E. Sha a), M. Suzuki b), T. Funayama b),
Y. Kobayashi b) and H. Mitani a)

a)Department of Integrated Biosciences, The University of Tokyo,
b)Department of Radiation-Applied Biology Research, TARRI, QST

Hematopoietic tissue is susceptible to irradiation, since hematopoietic stem cells are highly proliferative. In mammals including human, the main hematopoietic organ is bone marrow and located inside of bone and it is difficult to directly observe the dynamic responses of hematopoietic cells after irradiation. In contrast, the main hematopoietic organ in teleost is kidney and small fish like zebrafish and medaka have been excellent models to investigate hematopoietic cell dynamics. In this study, we conducted targeted irradiation of kidney in adult medaka, *Oryzias latipes*, with carbon and proton beams to investigate the responses of fish hematopoietic cells against irradiation.

When adult medaka were dorsally irradiated with carbon-ion ($^{12}C^{6+}$, 26.7 MeV/u) beam, peripheral blood cells decreased 7 days after irradiation and did not increase again within 28 days after irradiation. Histological examination showed that hematopoietic tissue in kidney was severely damaged and was not restored for 1 month after irradiation. The reduction of hematopoietic cells in the kidney was dose-dependent when fish were irradiated with 2 Gy, 5 Gy and 15 Gy of carbon ion beams.

Next, we put a 5.0 mm thick acrylic plate to shield the area other than the target area and conducted irradiation of only right kidney, both kidneys, and the whole body other than kidneys (Fig. 1). On the 7 day after the irradiation of carbon-ion beam, peripheral blood cells decreased in the fish of which kidneys were irradiated. We also found that at least one kidney was irradiated, peripheral blood cells decreased and that irradiation of the body other than kidneys did not induce the decease of peripheral blood cell numbers.

We also investigated the effects of proton (H^+, 15 MeV/u) beam on hematopoietic tissue in kidney of adult medaka. The dorsally irradiated fish and the fish irradiated with shield, which was expected to be irradiated only the kidneys on both sides, showed the decrease in the number of peripheral blood cell in the same manner as carbon-ion beam (Fig. 2). These results indicate that the irradiation with proton beam caused direct damages in hematopoietic cells in the kidney and the damages out of the kidney have little effects on the number of peripheral blood cells. It can be concluded that the number of peripheral blood cells can be used as a good indicator of the hematopoietic tissue damages in kidney. In contrast with the case of carbon-ion beam, hematopoietic cell in the kidney irradiated with proton beam (15 Gy) proliferated again and increased to the level of control 14 days after irradiation.

Fish are highly useful models to investigate the responses of hematopoietic cells against irradiation. Here, we reported that irradiation of adult medaka decreased peripheral blood cells and irradiation only of kidney resulted in the decrease of the peripheral blood cells.

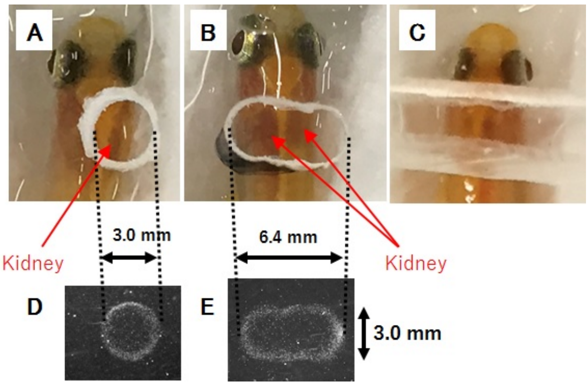

Fig. 1. Local irradiation of carbon ion and proton beams with shielding. (A, B) An acrylic plate (5.0 mm thick) with a circular opening (ϕ 3.0 mm) or an oval opening (major axis of 6.4 mm and minor axis of 3.0 mm) was put on fish to expose only right kidney or both kidneys and irradiation was conducted, respectively. The irradiated areas were confirmed by CR-39 exposure (D, E). (C) To expose the whole body other than the kidneys, an acrylic plate (5.0 mm thick) about 4.0 mm wide was put on the fish body to shield the kidneys and irradiation was conducted.

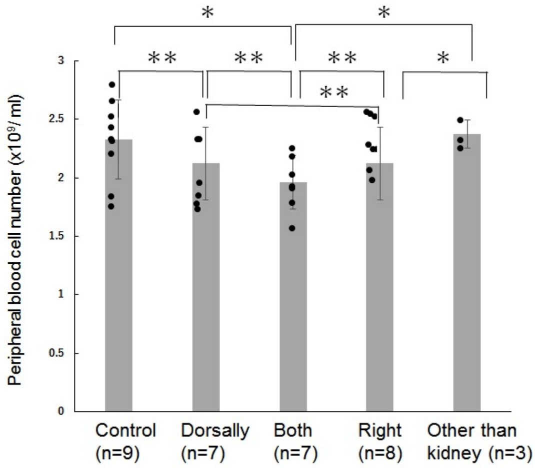

Fig. 2. Peripheral blood cells numbers in kidney-irradiated adult medaka. Blood was collected from the irradiated fish 7 days after the irradiation of proton beam and peripheral blood cells were counted under microscopy. When one or both of the kidneys of the fish were irradiated, peripheral blood cells decreased significantly.
* $p < 0.05$, ** $p>0.05$

2 - 03 A Trial to Improve Quantitative Analysis of the Area of Oxidative Damage in DNA Sheet Produced by Individual Carbon Ions with Different LETs

K. Urano[a,b], A. Ito[a], Y. Takano[a,c], S. Yoshida[a],
R. Hirayama[d], Y. Furusawa[e], Y. Yokota[f] and T. Funayama[f]

[a]School of Engineering, Tokai University,
[b]Nuclear Safety Research Center, JAEA,
[c]Graduate School of Med. Pharm. Sci., Chiba University,
[d]Department of Charged Particle Therapy Research, NIRS, QST,
[e]Department of Basic Medical Sciences for Radiation Damages, NIRS, QST,
[f]Department of Radiation-Applied Biology Research, TARRI, QST

Although the biological effects of heavy ions are generally thought to result mainly from direct action of radiation, we found that there still remains significant contribution of indirect action in the mammalian cell killing via OH radicals even at high LET with a few hundred keV/μm [1]. To confirm such observation, we have focused on the detection of the area of oxidative DNA damage induced by OH radicals that are probably produced in the penumbra region. In our preceding study, we developed a method to detect the location of 8-hydroxydeoxyguanosine (8-OHdG) by immunostaining method using fluorescence antibody against 8-OHdG generated in DNA-lipid complex sheet, hereafter referred to as DNA sheet, with water-insoluble nature, which enabled us to irradiate in water environment. Fluorescence dots that may result from incident individual ions could be observed using a standard fluorescence immunostaining protocol. However fluorescence dots probably due to background noise was hard to subtract from the fluorescence images. In the present study, we developed a possible way to eliminate the background dots, and compared the area size of dots produced by carbon ions with different LETs.

The irradiation of 220 MeV carbon ion with an LET of 108 keV/μm was carried out as follows: DNA sheet made on a coverglass was pretreated with Bouin fixative, and then set to an irradiation chamber perpendicular to the ion direction. During irradiation, the DNA sheet on which water was dropped was covered with mylar film to maintain water environment around the DNA sheet. In addition, carbon ions with an LET of 13 and 80 keV/μm from HIMAC facility at NIRS were used for comparison. The obtained images of fluorescence dots were analyzed using ImageJ image processing software.

First the image thresholding was conducted using the maximum entropy method. After setting ROI (Region of Interest) in the resultant image, the dot size was calculated by averaging over at least 400 dots per sample. The following elimination of background dots was developed: The distribution of maximum intensity in fluorescence dots is calculated for unirradiated DNA sheet. To obtain fluorescence intensity for dots that are certainly produced by irradiation, we used samples irradiated horizontally to incident beams. Since 8-OHdG generation is observed along a beam track, the intensity distribution on the fluorescence line is obtained as in the case of unirradiated samples. By comparing both intensity distribution profiles, the threshold level that properly discriminates between irradiated and unirradiated sample is determined. Following the above noise elimination procedure, the area size of fluorescence dots was estimated more precisely.

Figure 1a shows LET dependence of area size of the fluorescence dots. The size decreased with increasing LET, which was in contrast to our results reported last year [2]. To compare with penumbra size calculated by Chatterjee and Schaefer [3] more directly, the dot size was plotted against ion energy (Fig 1b). The tendency of size increase with increasing ion energy is consistent with their calculations. Our trial to eliminate background noise seems to work properly, resulting in the reproduction of the ion energy dependence of penumbra size by the calculations.

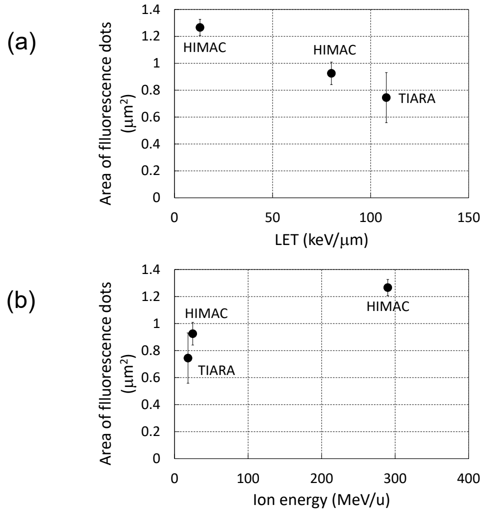

Fig. 1. Area size of fluorescence dots produced by carbon ion irradiation. (a) LET dependence, (b) Ion energy dependence.

References

[1] A. Ito *et al.*, Radiat. Res. **165**, 703-712 (2006).
[2] A. Ito *et al.*, QST Takasaki Annual Report 2018, **QST-M-23**, 66 (2020).
[3] A. Chatterjee and H. J. Schaefer, Radiat. Environ. Biophys. **13**, 215-227 (1976).

2 - 04

Heavy Ion Irradiation to Unfertilized Silkworm Egg Induces Developmental Arrest Immediately After Fertilization

T. Takahashi[a], R. Isoyama[a], Y. Souma[a], T. Funayama[b], M. Suzuki[b]
and K. Shirai[a]

[a]Faculty of Textile Science and Technology, Shinshu University,
[b]Department of Radiation Applied Biology, TARRI, QST

DNA damage checkpoints that detect DNA damage and arrest the cell cycle to gain time for repair play an important role in ensuring the accuracy of the genome. However, in the early embryo of the animal, it has been considered that there are no or incomplete checkpoint system. Because the early developing embryos have to repeat the rapid cell cycle (or nuclear cleavage).

We have observed a dose-dependent developmental delay in the silkworm embryos at early developmental stage irradiated with heavy ions. This suggests that the early developmental egg of the silkworm has a developmental arrest mechanism by the checkpoint. However, many mysteries remain in the response of the silkworm eggs to DNA damage, because the maternally derived components control early embryonic development.

We already confirmed that the silkworm egg in cleavage stage stopped developing immediately after heavy ion irradiation. In this study, we investigated the developmental arrest of the silkworm egg that irradiated the heavy ions at just before fertilization.

The silkworm strain used in the experiments was the pigmented non-diapause strain, *pnd pS.* The silkworm eggs at just before fertilization were corrected and irradiated with carbon ions (190 MeV) at 20 Gy. Then the irradiated eggs were incubated at 25 °C. Then the eggs were fixed by Carnoy's solution.

First, we irradiated pre-fertilized eggs (1.5 h after oviposition) with heavy ions and confirmed whether the development of the eggs was delayed. In the non-irradiated egg at 10.5 h after oviposition, the (cleavage) nucleus spread to the front of the posterior end of the egg, and the division cycle was cycle 9, whereas in the irradiated egg, the spread to the posterior end of the nucleus delay, and the developmental cycle was estimated to be cycle 6.

Then at 11 h 50 min after oviposition, the nuclei of the non-irradiated egg (control) reached the posterior end of the egg and the division cycle was cycle 11. On the other hand, the irradiated eggs also progressed their development. However, their development was delayed (The developmental cycle of the irradiated eggs was cycle 8). Therefore, it was confirmed that the irradiation (20 Gy of carbon ions) induced the unfertilized eggs to delay about 3 cleavage cycles.

Next, we investigated the effects of the heavy ion irradiation to the silkworm egg before fertilization (1.5 h after oviposition). As a result, at 2 h 50 min after oviposition (1 h 20 min after irradiation), one or two nuclei were observed in both irradiated and non-irradiated eggs. After then, the non-irradiated control eggs continued the development and reached stage 3 at 4.5 h after oviposition. On the other hand, there was one nucleus in most of irradiated eggs. Some eggs of the irradiated group were observed two nuclei. These results indicate the embryogenesis of the irradiated eggs stopped. Therefore, it was clarified that the unfertilized eggs of silkworm that were irradiated with heavy ions, stop their development.

Then we tried to identify whether the two nuclei observed in the irradiated egg are the two pronuclei (cycle 0), or the fertilized nuclei divided into two (cycle 2). We changed the irradiation timing to 1 hour after oviposition, then the effects to the cell cycle of the irradiation were observed.

As shown in Table 1, both irradiated and non-irradiated control eggs at one hour after irradiation have only one nucleus. At 2 h 20 min after irradiation, non-irradiated control eggs transferred to cycle 2, whereas most of irradiated eggs (8 of 9 eggs) have stopped their development at cycle 1. It didn't change even after 10 min (2 h 30 min after irradiation). Therefore, the irradiated eggs also fertilize at one hour after irradiation, and the two nuclei founded in the irradiated eggs were considered to be the fertilized nuclei of cycle 2.

In these studies, it was clarified that when the silkworm eggs before fertilization were irradiated with heavy ions, the development stopped just after fertilization or after first cleavage.

Table 1
The cell cycle arrest of the silkworm eggs just after fertilization by heavy ion irradiation.

	No. of nuclei	after irradiation (h)		
		1	2.33	2.5
non-irradiate control	1	7		
	2		6	7
20 Gy	1	5	8	11
	2		1	2

2 - 05

Foci Formation of Phosphorylated H2AX and 53BP1 After Mixed High-LET Radiation Exposure

S Yamabe[a], T Ohizumi[a], T. Funayama[b] and AJ. Nakamura[a]

[a]College of Science, Ibaraki University,
[b]Department of Radiation-Applied Biology Research, TARRI, QST

It is well known that organisms are exposed to various types of stresses in space. Especially, space radiation exposure is considered severe stress that affects organism health as the exposure dose is larger than the earth. These space radiations including high energy particles induce complex DNA damage. Furthermore, radiation exposure under the microgravity environment in space might induce different responses for radiation exposure from that on the ground. Since the failure of DNA damage repair may induce genomic instability and increase the risk of developing cancer, it is important to understand the difference of DNA damage response after space radiation exposure. Therefore, in this study, we evaluate the DNA damage responses after radiation exposure by immunostaining for phosphorylated H2AX (γ-H2AX) to assess the biological impact of those stresses in space.

Histone H2AX, which is a key protein in DNA repair, is rapidly phosphorylated at the site of DNA double-strand breaks (DSBs) following DNA damage induction [1-3]. Upon DNA DSB induction by ionizing radiation (IR), the accumulation of hundreds of molecules of various DNA repair proteins including γ-H2AX and 53BP1 can be visualized as a large focus at the DNA DSB site which is known as Ionizing Radiation-Induced Foci (IRIF) [4]. The γ-H2AX foci serve as sites of accumulation of DNA repair proteins and may also induce chromatin remodeling possibly to aid access of repair proteins to the DSB sites. Therefore, the formation of γ-H2AX foci is critical for efficient DNA repair and the maintenance of genome stability.

In this study, we analyzed the kinetics of γ-H2AX and 53BP1 foci formation and cell survival rate by colony formation assay after exposure of proton beam (20 MeV), helium ion beam (63 MeV) and carbon ion beam (190 MeV) that are considered as a component of cosmic rays (data not shown). Moreover, we investigated the foci formation after the combination of helium ion beam and carbon ion beam exposure.

TIG-3 (normal human diploid skin fibroblast) were plated on chamber slides and exposed to radiation. Cells were fixed by 2% paraformaldehyde and immunostained for γ-H2AX and/or 53BP1. Carbon ion beam, which causes more complex DNA damage than the helium ion, induced a larger size of γ-H2AX and 53BP1 foci than helium ion beam at one hour after exposure (data not shown). Interestingly, both large and small size of foci formation was observed in carbon and helium ion mixed beam irradiated cells (data not shown). These results indicate that the radiation-induced γ-H2AX and 53BP1 foci size depends on the energy of the radiation and large foci might be resulted by clustered DNA lesions. In fact, we observed a higher number of foci at 8 hours after irradiation, indicating the delayed kinetics of DNA repair for clustered DNA lesions (Fig. 1).

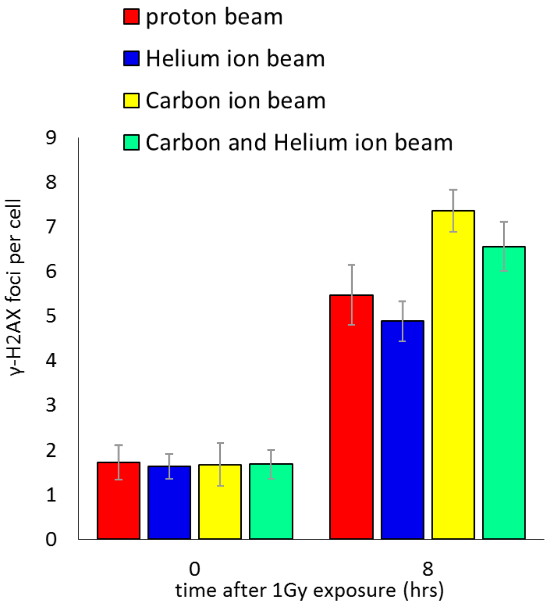

Fig. 1. Mean number of γ-H2AX foci per cell after radiation exposure.TIG-3 cells were exposed to either C-ion (1 Gy), He-ion (1 Gy), or both C-ion (0.5 Gy) and He-ion (0.5 Gy), and then fixed at 8 hr post irradiation.

In conclusion, our findings that show this heterogeneity of foci size which may affect DNA damage repair response, is unique and novel.

This study might provide new insights into DNA damage repair responses in space.

Acknowledgments

The present work was supported by JSPS KAKENHI, Grant-in-Aid for Scientific Research on Innovative Areas, Grant Number JP18H04964.

References

[1] W. M. Bonner *et al.*, Nat Rev Cancer. **12**, 957 (2008).
[2] E. Rogakou *et al.*, J Cell Biol. **146**, 905 (1999).
[3] E. Rogakou *et al.*, J Biol Chem. **273**, 5858 (1998).
[4] T. T. Paull *et al.*, Curr Biol. **10**, 886 (2000).

2 - 06

Analysis of Distance Limitation of Bystander Response Using Specially Designed Microbeam Irradiation Dish

T. Funayama, I. Nagafune and M. Suzuki

Department of Radiation-Applied Biology Research, TARRI, QST

High-LET heavy-ion beams have characteristic biological effects and thus have great industrial and medical value because it is applied in cancer treatment and radiation breeding. In addition, risk assessment of cosmic radiation that contains a heavy-ion radiation from galaxy is necessary for a manned space mission. Therefore, it has great importance to elucidate the biological properties of heavy ion radiation.

One of the main factors contributing to the characteristic biological effect of heavy-ion is considered to be non-uniform distribution of microdosimetrical energy deposition of heavy-ion radiation, which results in cells in a population irradiated not being hit with same number of ions. Such non-uniform dose distribution induces mixture of hit and non-hit cells within a cell population when irradiated with low dose of heavy-ion. On the other hand, heavy-ion radiation has a high elementary dose brought from its high-LET property, so that it derivers higher energy on cells even with single hit, resulting induction of cellular responses on hit cells. Therefore, radiation-induced bystander effect is considered to play an important role in low-dose high-LET radiation response.

To explore the mechanisms of the bystander effect of high-LET heavy-ion radiation, we developed a specially-designed cell irradiation dish for analyzing the distance limitation of intercellular communication in the bystander effect, which is difficult to carry out with the conventional general-purpose microbeam irradiation dish [1]. The dish was designed with a maze-like layout of grooves of 2 mm width to maximize the distance between cells. Maze-shaped wall component that was designed using three-dimensional CAD software was manufactured by desktop CNC milling machine. A cover glass to be a cell attach surface was adhered to a wall component, thereafter washed and sterilized for cell culture. To improve cell attachment efficiency on a glass surface, a treatment with vacuum plasma was carried out.

Human cervical cancer cells HeLa in exponential growth phase were inoculated in a maze dish, then the dish was placed in a CO_2 incubator for 6 hours to attach cells on a glass surface. The maze dish was placed on the sample stage of the collimated heavy-ion microbeam system of QST-Takasaki, and the cells at one end of the maze were irradiated with a carbon ion microbeam (15.8 MeV/u) of 250 µm in diameter with a dose equivalent to 5 Gy. After irradiation the sample was post-incubated for 6 hours, then the cells were fixed with 2% paraformaldehyde in PBS, and immunostained with anti-gamma-H2AX antibody to detect bystander response.

The results of preliminary analysis are shown in Fig. 1. Despite only irradiating an area of 0.04 mm^2 of the 4 mm^2 area at the edge of the maze (area A), the fluorescent intensity of gamma H2AX staining was increased in that area, indicating that the bystander effect was induced in the cells very near of the irradiated cells. The induction of bystander effects in more remote areas (area B-H) will require further analysis due to the large errors.

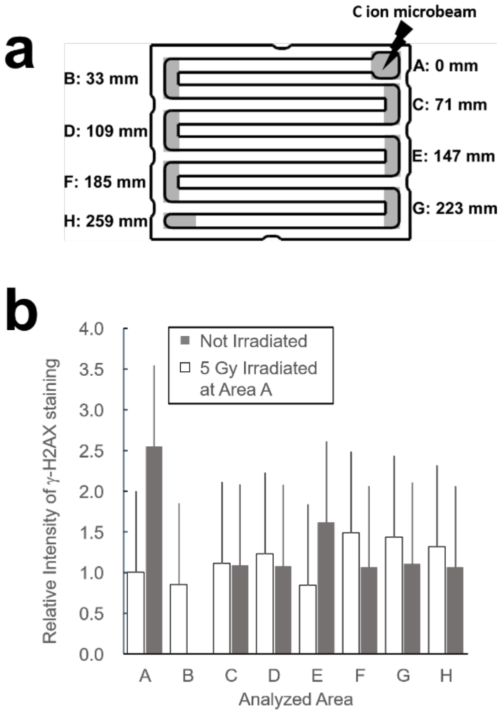

Fig. 1. Preliminary result of bystander analysis using maze-shaped irradiation dish. (a) Top view of maze dish. A maze-like arrangement of 2mm wide grooves can place cells up to 259 mm apart. A limited area (250 µm in diameter) of end of the maze (area A) were irradiated with a carbon ion microbeam, then bystander responses in eight different areas (area A-H) were analyzed. (b) Bystander responses in areas with different distance from irradiation point. Fixed cells were stained with anti-gamma-H2AX antibody, then the immunofluorescence signals were compared.

Acknowledgments

The present work was carried out in part with a JSPS KAKENHI (JP16K00552) and MEXT KAKENHI (JP18H04991).

References

[1] T. Funayama and M. Suzuki, QST Takasaki Annual Report 2018, **QST-M-23**, 64 (2019).

2 - 07

Analysis of the Effects of EGFR Signaling on Radiation Effects

T. Hara[a], T. Aoki[a], H. Sato[b], T. Funayama[c], Y. Nakagami[d], A. Okazaki[e],
T. Ohno[b] and Y. Suzuki[f]

[a]Department of Radiological Technology, Gunma Prefectural College of Health Sciences,
[b]Department of Radiation Oncology, Gunma University Graduate School of Medicine,
[c]Department of Radiation-Applied Biology Research, TARRI, QST,
[d]Department of Radiology, Dokkyo Medical University,
[e]Department of Radiation Oncology, Tsuboi Cancer Center Hospital,
[f]Department of Radiation Oncology, Fukushima Medical University School of Medicine

Purpose: Breast cancer, which has been incidence one million women annually worldwide, is one of the most common malignancies in women. There are five subtypes of breast cancer: Luminal A, Luminal B HER2 negative, Luminal B HER2 positive, HER2 positive non-luminal, and Triple negative, of which Triple negative has the worst prognosis [1]. However, no effective treatment has yet been established. So, focusing on the fact that triple negative type of breast cancer expresses a lot of epidermal growth factor receptor (EGFR) [2], we hypothesized that combination of EGFR inhibitors and radiotherapy on triple negative type of breast cancer (TNBC) would be an effective therapy.

Materials and Method: We used human breast cancer cell line which is triple negative type. Cytotoxicity was assessed by alamerblue or clonogenic assays in cell lines treated with EGFR inhibitor (Cetuximab) alone or in combinations. There were two protocols for combination of Cetuximab and irradiation. One was a pre-treat in which the drug was administrated before irradiation. The other is post-treat, in which the drug is administrated after irradiation. All irradiations were performed at the Takasaki Advanced Radiation Research Institute of QST.

Results: To determine an adequate concentration of Cetuximab for combination with γ-ray irradiation, the cytotoxicity of Cetuximab on TNBC cell was investigated with the alamerblue assay. In terms of drug dose, an ideal radiosensitizer has little or no cytotoxic effect by itself to minimize the damage to normal tissue and increase the therapeutic ratio. Therefore, the Cetuximab concentration that results in an approximately 20% inhibition of cell viability was used for experiments involving Cetuximab administration for 24 h combined with γ-ray. The protocol-specific effect of Cetuximab treatment on radiation was confirmed (Fig. 1). When TNBC cells were first subjected to radiation before Cetuximab, this treatment resulted in an enhancement of the radiation effect. However, administering Cetuximab after radiation did not enhance the effect of radiation. In the case of MDA231 cells, survival at 8 Gy of γ-ray alone was 0.006 and that by the pre-treat was 0.0003, respectively (P> 0.01). However, as shown in Fig. 2, in contrast to the effect on γ-ray irradiation, even this concentration of Cetuximab does not greatly increase the cytotoxic effect of carbon ion irradiation in MDA-MB-231 cells.

In summary, it was confirmed that there was the radiation enhancement effect of Cetuximab on γ-rays, but not with carbon rays. It was suggested that the pathway of the radiation effect depends on the type of radiation such as γ-ray and charged particle (carbon ion).

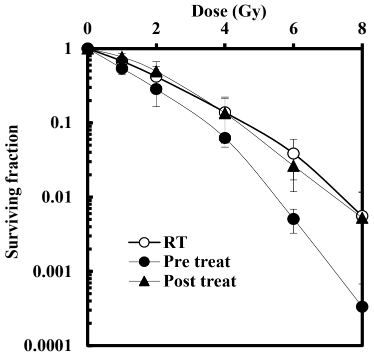

Fig. 1. Effect of Cetuximab on γ-ray irradiation in MDA-MB-231 cells. Cetuximab increased the cytotoxic effects of radiation.
RT: γ-ray irradiation only. Pre (Post) treat: Drug administration before (after) irradiation.

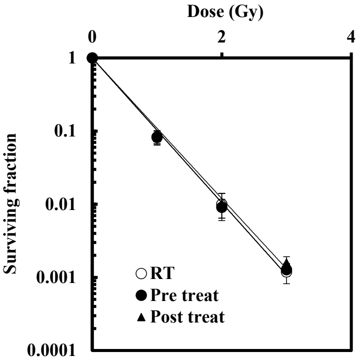

Fig. 2. Effect of Cetuximab on carbon ion irradiation in MDA-MB-231 cells. Cetuximab did not increased the cytotoxic effects of radiation. RT: Carbon ion irradiation only. Pre(Post) treat : Drug administration before(after) irradiation.

References

[1] F.M. Blows *et al.*, PLoS Med. **7**, e1000279 (2010).
[2] E.A. Rakha *et al.*, Clin Cancer Res **13**, 4429 (2007).

2 - 08

Development of a Novel Irradiation Method for Live *C. elegans* Individuals Using Focused Microbeams of Cyclotron-Accelerated Heavy Ions

M. Suzuki, T. Sakashita and T. Funayama

Department of Radiation-Applied Biology Research, TARRI, QST

We have previously developed a collimated microbeam device at a beamline of the AVF cyclotron of the TIARA, and established a method for targeted irradiation of localized parts of living organisms such as the nematode *Caenorhabditis elegans*, silkworm and medaka fish [1, 2]. A collimated microbeam generated with a 20 µm-diameter micro-collimator, that has a longer projectile range and can irradiate a thick target, has been used for irradiating model animals. However, this microbeam cannot target single specific cells of individuals. Since at least a 10-µm beam in air is required for targeting any single cells in individuals, we have recently developed a focused microbeam device with finer microbeam spots to carry out precise targeting [3].

In the present study, to irradiate *C. elegans* with a fine focused microbeam, we proposed a method for preparing samples that enable irradiation of single cells in live individuals. For immobilization of live *C. elegans* individuals during irradiation, we previously proposed an immobilization method where animals are enclosed in straight channels of a microfluidic chip with buffer solution and movements are inhibited without anesthesia [2]. Furthermore, for ion-beam irradiation, we developed ultra-thin, ion-penetrable, wettable polydimethylsiloxane microfluidic chips (Worm Sheets) [4, 5]. These Worm Sheets maintain moisture in the straight channels at least three hours. The total thickness of the sample including a Worm Sheet and upper and bottom cover films was sufficiently thin (~550 µm) to allow carbon ions to pass through. We employed a custom-made Worm Sheet and followed the immobilization method described previously [5].

To carry out microbeam irradiation to live *C. elegans* individuals, firstly we designed a sample frame that can hold Worm Sheets with enclosed animals and a CaF_2 scintillator for beam position detection (Fig. 1a). The frame has four square placeholders for a scintillator and for three Worm Sheets. By using this frame, it is possible to irradiate three Worm Sheets with animals in one irradiation batch. The upper surface of the scintillator coincides with the upper surface of the cover films sealing Worm Sheets to ensure that the whole upper surface of the sample is flat (Fig. 1b).

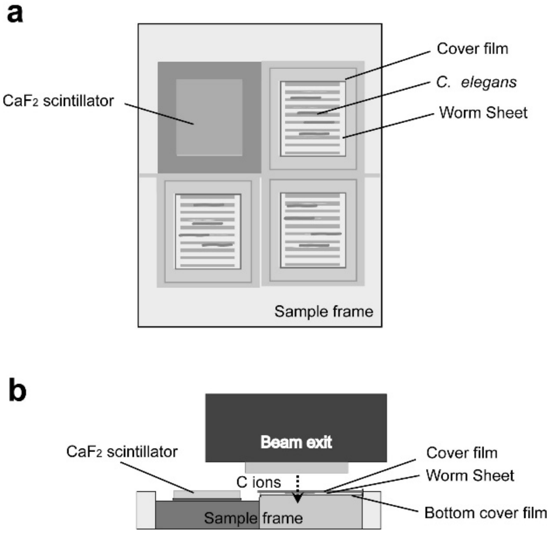

Fig. 1. Schematic diagram of the irradiation of live *C. elegans* with a focused carbon-ion microbeam. (a) Overhead view of immobilization of *C. elegans* individuals using Worm Sheets on a sample frame. The CaF_2 scintillator is placed on the sample frame. (b) Cross section view of the sample frame placed immediately under the beam exit.

A novel established method for immobilization of *C. elegans* individuals fulfills the requirements for focused microbeam irradiation. As shown in Fig. 1b, the top surfaces of the samples are flat and sufficiently thin to count ions, prevent sample dehydration and enable detection of the beam immediately before irradiation using a nearby installed CaF_2 scintillator. A beam size smaller than 10 µm was obtained for ^{12}C ions of 26.7 MeV/u at a distance of 2 mm from the beam exit. Targeted irradiation with a focused microbeam of an exact number of carbon ions to specific cells in live *C. elegans* individuals can be realized by the proposed method. The irradiation experiments using the focused microbeams, in which we target several neurons in a central nervous system, are in progress.

Acknowledgments

We thank the crew of the cyclotron of TIARA for their kind assistance; Drs. Y. Yokota, N. Miyawaki, H. Kashiwagi, T. Satoh and S. Kurashima for valuable discussions; and the Caenorhabditis Genetic Center for providing strains of *C. elegans.* This study was supported in part by JSPS/MEXT KAKENHI Grant Numbers JP16K00552, JP16710039, JP18K18839 and JP18H04991

References

[1] T. Funayama, Quantum Beam Sci. **3**, 13 (2019).
[2] M. Suzuki *et al.*, J. Radiat. Res. **58**, 881 (2017).
[3] T. Funayama *et al.*, Nucl. Instrum. Meth. Phys. Res. B **465**, 101 (2020).
[4] M. Suzuki *et al.*, J. Neurosci. Methods. **306**, 32 (2018).
[5] M. Suzuki *et al.*, J. Vis. Exp. **145**, e59008 (2019).

2 - 09

Detection of Somatic Mutations in Plant DNA by the Maximum-Depth Sequencing

Y. Oono[a], S. Kitamura[a], K. Satoh[a], S. Hirata[b] and I. Narumi[b]

[a]Department of Radiation-Applied Biology Research, TARRI, QST,
[b]Graduate School of Life Sciences, Toyo University

Radiation-induced mutagenesis is a powerful tool for generating mutants in plant biology. However, there is no quick and direct methods to evaluate radiation dose suitable for inducing mutations. In this work, we tried maximum-depth sequencing (MDS), a method that can detect extremely rare mutations in a population of cells through next generation sequencing (NGS) with error correction [1], to detect locus-specific somatic mutations in gamma-irradiated Arabidopsis plants.

Arabidopsis dry seeds were irradiated with or without 300 Gy gamma rays. Genomic DNA was extracted from 10-d-old seedlings. For detection of locus-specific somatic mutations, we chose 110-bp genomic region in the second exon of the Arabidopsis *TT8* gene as a model locus of target. The genome DNA was digested by a restriction enzyme that cuts the 3' side of the target, followed by attaching an adapter sequence for NGS and a random barcode to the target DNA by a polymerase reaction (Fig. 1(a)). Next, a primer that hybridizes outside of the barcode was used alone to amplify the target DNA linearly to generate complemental copies tagged with identical barcode from one original copy of the target (Fig. 1(b)). By this procedure, mutations derived from the original target should be appeared in all the reads tagged with the same barcode (● in Fig. 1), whereas mutations occurred by an erroneous reaction in PCR or NGS (▲ in Fig. 1) present independently in the reads within the same barcode (Fig. 1(c)).

DNA libraries prepared with 12 and 30 cycles of linear amplifications and PCR were processed by NGS (150-bp pair end) using Illumina NovaSeq6000. Approximately 59 million and 42 million sequence reads were obtained and grouped by 702,037 and 389,188 barcodes for the non-irradiated and irradiated samples, respectively (Table 1).

After examining the data, we decided to take a barcode for mutation analysis if number of reads tagged by the same barcodes (R) is ≧ 5 and to judge the barcode represents a mutant DNA if the ratio of the mutant reads (r) in the barcode is ≧ 60%. As the result, we detected 104 and 118 barcodes representing single base substitutions (SBSs) in the non-irradiated and irradiated samples, respectively (Table 1). Of these mutations, more than 85% was C→A transversions in both non-irradiated and irradiated samples (Fig. 2). The C→A transversions seem to originate from the target DNA but not to be derived from mutations occurred in plant cells because its complimentary transversions (G→T) account for only 0~1%. Most of the C→A transversions detected may be originated from DNA lesion or un-repaired mismatched nucleotides in the target DNA. Regarding insertion or deletion mutations, 1-bp deletions (DEL(−1)) were detected only in the irradiated sample (Table 1), suggesting that these deletion may be induced by the gamma irradiation.

In this work, we could confirm that the MDS reaction worked almost as we expected. Although the current result showed only a little difference between non-irradiated and irradiated samples, we hope further improvements of MDS reaction and bioinformatics will make this method available to determine radiation dose suitable for plant mutagenesis.

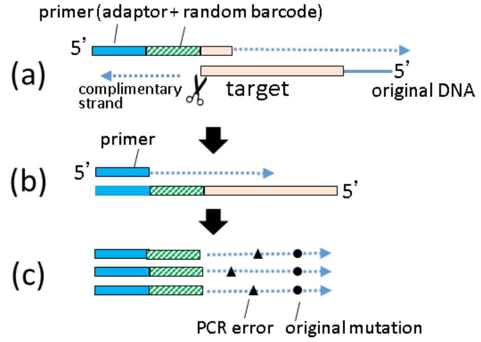

Fig. 1. Procedure of the MDS. After linear amplification, DNA library for NGS was generated by adding a reverse primer followed by PCR.

Table 1

Number of barcodes in the non-irradiated (0 Gy) and irradiated (300 Gy) samples.

	Number of barcodes	
	0 Gy	300 Gy
Total	702,037	389,188
R ≧ 5	88,242	79,582
r ≧ 60%	106	121
SBS	104	118
2 SBS*	2	0
DEL (−1)	0	3

*Two independent SBSs were detected in the reads.

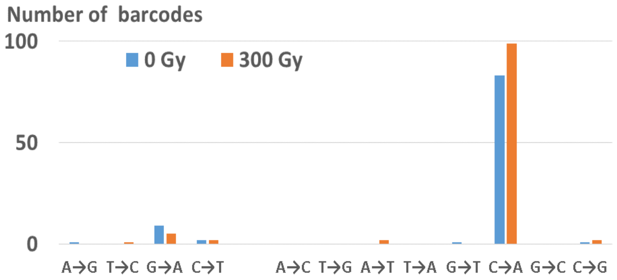

Fig. 2. Number of barcodes classified by types of SBS.

Reference

[1] J. Jee *et al.*, Nature **534**, 693 (2016).

2 - 10

Construction of Mutant Lines of the Parasitic Plant *Cuscuta campestris* Yuncker by Carbon Ion Irradiation, and Development of an *in vitro* System for Screening

R. Yokoyama[a)], K. Satoh[b)] and Y. Oono[b)]

[a)]Graduate School of Life Sciences, Tohoku University,
[b)]Department of Radiation-Applied Biology Research, TARRI, QST

This study of plant parasitism has begun with the economic impact of the parasites. *Cuscuta* species is one of the most widespread group of parasitic plants that subsists on various plant species, causing damages to important crops. *Cuscuta* species absorbs water and nutrients from host plants through an invasive organ called a haustorium [1]. Understanding the molecular basis of the invasive processes of *Cuscuta* species is of critical importance to crop production [2]. At present, however, several tools for molecular genetics in *Cuscuta* species have not been developed including mutant collections and screening technologies.

We chose *Cuscuta campestris* as a model system for molecular genetics in *Cuscuta* species because of its relatively small genome size (Fig.1). We established homozygous lines of *C. campestris* for identical genotype by self-pollination, and sequenced the genomes of the homozygous lines. Following the sequencing of *C. campestris* genome, we now promote to produce ion-beam irradiated *C. campestris* populations on a large scale for finding the various mutants in the same genetic background.

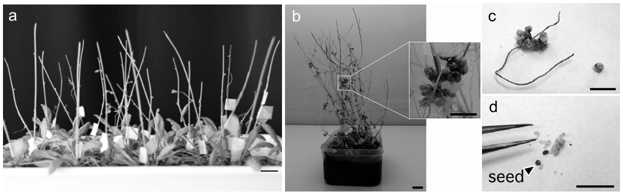

Fig. 1. *Cuscuta campestris* infecting a host plant. (a) *C. campestris* infecting *Arabidopsis thaliana* stem. (b) Fruiting of *C. campestris*. (c) and (d) Fruits and Seeds of *C. campestris*. Bar=1 cm.

To use high-throughput screening assays for parasitism mutants in *C. campestris*, we also developed an experimental system that *in vitro* regulates the haustorium development. Some studies reported that tactile stimuli induced the formation of haustoria, and far-red light or blue light irradiation promoted parasitism in *Cuscuta* seedlings. We investigated haustorial induction on *C. campestris* seedlings by tactile stimuli in combination with blue light irradiation according to the glass-plate method. For tactile stimuli, the *C. campestris* seedlings were held between two glass plates separated by pieces of plastic sheet. The glass plates were kept horizontal, and treated with irradiation of blue light (Fig.2). The results showed that both of tactile stimuli and blue light irradiation were simultaneously required for haustorial induction and formation, and subjected to haustorial induction for 24 h, and haustorial formation for 48 h (Fig.3).

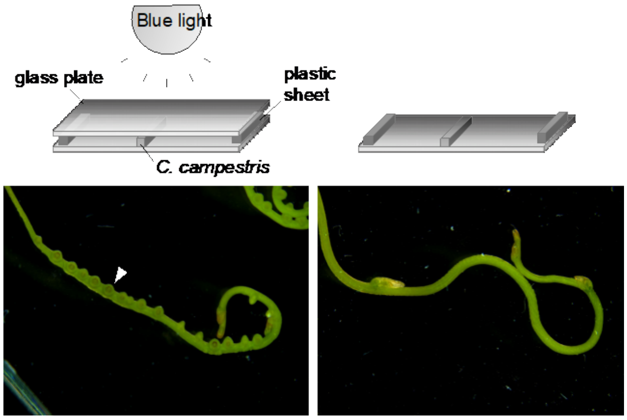

Fig. 2. Schematic images of the *in vitro* system for haustorium induction (Upper panel). Formation of haustoria in *C. campestris* that was pressed with a stack of glass slides under blue light irradiation for 48 h (left), compared with *C. campestris* observed without stimulation (right). Arrowhead indicates haustorium.

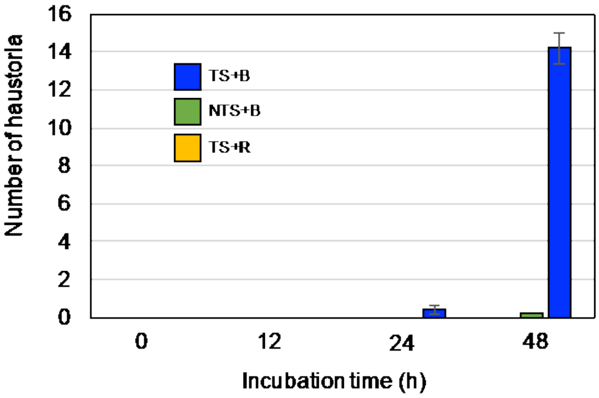

Fig.3. The number of haustoria per a *C. campestris* seedling. TS, tactile stimuli; NTS, no tactile stimuli; B, blue light irradiation; R, red light irradiation. Error bars represent SE (n=10).

The present system not only enabled us to monitor the processes of haustorial induction and formation, but also showed potential for the simple screening assay for haustorium mutants in *C. campestris*. Application of the *in vitro* system to a large-scale screening of haustorium mutants will provides opportunities to find mutants that are not encountered in typical phenotypic screenings.

References

[1] R. Yokoyama, Agri. Biotech. **3**, 57 (2019).
[2] Y. Kaga *et al*., Front. Plant Sci. **11**, 193 (2020).

2 - 11

Mutation Detection System for Three Flavonoid Biosynthetic Genes in Irradiated Arabidopsis Leaves

S. Kitamura[a], K. Satoh[a], Y. Hase[a], Y. Oono[a] and N. Shikazono[b]

[a]Department of Radiation-Applied Biology Research, TARRI, QST,
[b]Institute for Quantum Life Science, QST

Ionizing radiations can interact directly and/or indirectly with DNA molecules and induce a wide range of DNA lesions. All organisms have potential to repair those DNA lesions, but some of them could not be completely repaired, resulting in occurrence of mutations. Radiation-induced mutations are thought to occur in random. On the other hand, we previously constructed a mutation detection system using Arabidopsis seed colors as markers, and suggested that carbon ion irradiation onto young seedlings could induce mutations in *TT4* gene less frequently than those in another gene (*TT8*) [1]. Here, we tried to develop another mutation detect system using different vegetative tissues like leaves as markers in irradiated Arabidopsis.

Anthocyanins are one of the major pigments in plants, and known to control beautiful coloration in flowers and fruits. In Arabidopsis, anthocyanins provide reddish coloration in vegetative tissues such as leaves. *TT4*, *TT3* and *TT18* genes are prerequisite for synthesizing anthocyanins in Arabidopsis, and a homozygous mutant for one of those genes results in loss of red pigments. Therefore, preparation of heterozygous plants for those three genes followed by irradiation, makes it possible to induce mutations in either of their wild type allele, leading to anthocyanin (red pigment)-less tissues from reddish wild-type tissues.

Triple heterozygous plants (*TT4tt4 TT3tt3 TT18tt18*) were obtained by crossing of triple homozygous mutants for *tt4*, *tt3* and *tt18*, and their parental wild type. The heterozygous seeds were germinated in nutrient media, and 1-d-old seedlings were exposed to ^{60}Co gamma-rays at Food Irradiation Facility, TARRI, QST. Irradiated M1 plants were grown under standard conditions, and their vegetative tissues such as leaves were observed with respect to anthocyanin accumulation.

Before mutagenesis experiment, gamma-ray sensitivity in 1-d-old Arabidopsis seedlings was determined, based on the survival rate 3 weeks after irradiation. Survival curves were obtained for the triple heterozygous plants and the wild type. They were found to be similar to each other, having shoulder doses of 140 Gy. Then, half of the shoulder dose (70 Gy) was used for mutagenesis in triple heterozygous seedlings. As shown in Table 1, about 170~180 each of irradiated and unirradiated plants were investigated for anthocyanin accumulation in their vegetative tissues. Anthocyanin-less tissues were detected from gamma-ray irradiated plants but not from unirradiated plants. This suggests that anthocyanin-less tissues were induced by gamma-ray irradiation. Next, we tried to know whether anthocyanin-less phenotypes were derived from mutations in one of three heterozygous genes. We chose one of 10 anthocyanin-less tissues, extracted its genomic DNA, and investigated its heterozygosity at three loci (*TT4*, *TT3* and *TT18*) in this tissue. It was revealed that, whereas wild-type *TT3* and *TT18* alleles had no novel mutations and remained functional, wild-type *TT4* allele was deleted and new genomic composition without functional *TT4* was generated in this anthocyanin-less tissue (Fig. 1). Molecular investigations for other anthocyanin-less tissues as well as further mutation analysis using this system, will provide more in-depth knowledge on occurrence of radiation-induced mutations and their randomness in plants.

Table 1
Detection of anthocyanin-less tissues from triple heterozygous plants.

	No. plants analyzed	No. plants with anthocyanin-less tissues	
no irradiation	168	0	(0.0%)
gamma-rays 70 Gy	179	10	(5.6%)

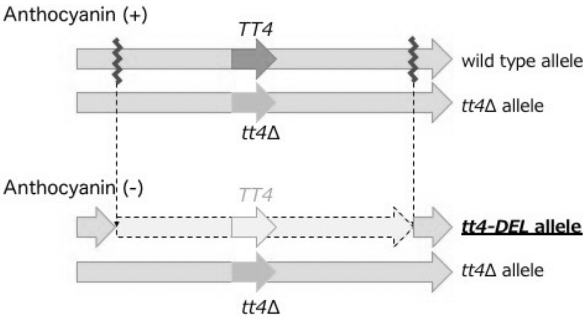

Fig. 1. Genomic composition in a new anthocyanin-less tissue. Wild type *TT4* allele was found to be deleted, resulting in absence of functional *TT4* gene in this tissue.

Acknowledgments

This work was partially supported by JSPS KAKENHI 19K12333.

Reference

[1] S. Kitamura *et al.*, QST Takasaki Annu. Rep. 2018, **QST-M-23**, 75 (2020).

2 - 12 Construction and Radioresistance Analysis of Knockout Strains of DNA Double-Strand Break Repair-related Genes in *Physcomitrella patens*

Y. Yokota and A. N. Sakamoto

Department of Radiation-Applied Biology Research, TARRI, QST

DNA double-strand breaks (DSBs) are the most lethal type of radiation-induced DNA damage. The main pathways for rejoining DSBs are error-free homologous recombination (HR), which uses intact sister chromatids as templates to accurately repair DSBs, and error-prone non-homologous end joining (NHEJ) and alternative end joining (a-EJ). *Rad51B*, *Lig4* and *PolQ* are the genes that play important roles in HR, NHEJ and a-EJ, respectively. We have reported that moss *Physcomitrella patens* cells are 200-folds more radioresistant than mammalian cells [1]. To elucidate its mechanism, we obtained knockout plants (*rad51b-1*, *lig4-1* and *polq-1* strains) of the *Rad51B*, *Lig4*, and *PolQ* from Dr. Nogué of INRA, France and found that only *Rad51B* is involved in radioresistance [2]. In the present study, to strengthed the findings, another knockout strain (*rad51b-2*, *lig4-2* and *polq-2* strains) targeting different sites of *Rad51B*, *Lig4* and *PolQ* was produced with CRISPR-CAS9 method and their radioresistance was measured.

A plasmid for expressing the gene of CAS9 protein, which cleaves genomic DNA in a guide RNA-dependent manner, was obtained from Dr. Nogué. Nucleotide sequences of *Rad51B*, *Lig4* and *PolQ* were obtained from public databases. The guide RNA for recruiting the CAS9 to the target site was selected from those recommended by the Chop Chop Harvard site [3] according to the following conditions: (1) it targets a site different from the already obtained knockout strain, (2) sequence that closely resembles the target sequence does not exist in the genome, (3) it targets the first or second exon, and (4) the cleavage efficiency of the target site is expected to be high. Selected *guide RNA* gene was synthesized and incorporated into a plasmid. The genes of CAS9, guide RNA and NPTII were transiently expressed in *P. patens* protoplasts, and geneticin-resistant colonies were picked up. The genomic DNA was extracted from the colonies and the target gene was sequenced. Then, a knockout strain was selected in which an immature stop codon occurred due to a deletion or insertion in the front of the open reading frame.

In all of the knockout strains, translation of mRNA to amino acid is stopped by occurrence of the immature stop codon and amino acid sequence was thus shortened (Fig. 1). To elucidate its influence on radioresistance, the wildtype and knockout strains were irradiated with γ-rays and their growth was compared. As a result, it was found that the resistance to γ-rays was almost same among wildtype, *lig4-1*, *lig4-2* and *polq-1* strains, but was significantly lost in the *rad51b-1* and *rad51b-2* strains (Fig. 2). This suggests that the radioresistance of *P. patens* is due to the accurate repair of DSBs with the HR pathway. We are now investigating the radioresistance of the *polq-2* strain. To elucidate the mechanisms of radioresistance, we will also measure the DSB repair kinetics of the knockout strains by pulse-field gel electrophoresis assay.

References

[1] Y. Yokota *et al.*, Genes **9**, 76 (2018).
[2] Y. Yokota *et al.*, QST Takasaki Annu. Rep. 2018 **QST-M-23**, 78 (2020).
[3] https://chopchop.cbu.uib.no/

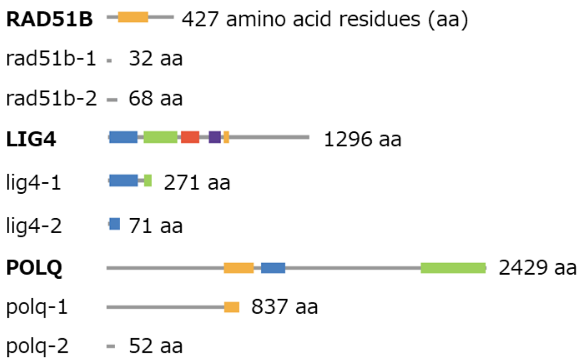

Fig. 1. Predicted open reading frames in wildtype (bold) and mutant strains. Each box means functional motifs.

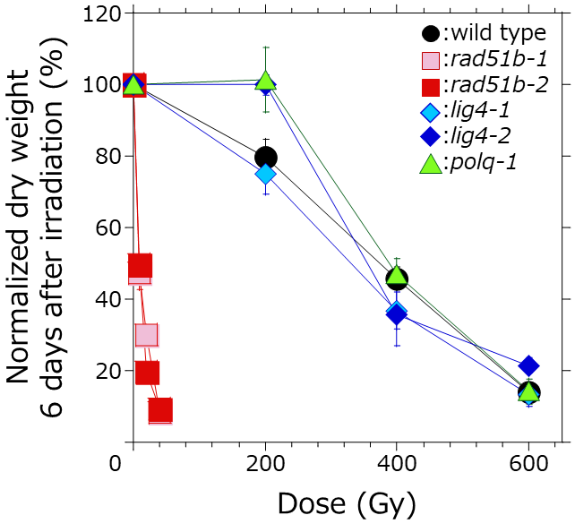

Fig. 2. Growth inhibition after γ-ray irradiation. Data represent the mean ± standard error of three or more independent tests.

2 - 13

A Comparative Study on Lethal Effect of Monomer and Cluster Proton Ion Beams in Bacterial Spores

Y. Hase[a], K. Satoh[a], A. Chiba[b], Y. Hirano[b] and K. Narumi[b]

[a]Department of Radiation-Applied Biology Research, TARRI, QST,
[b]Department of Advanced Radiation Technology, TARRI, QST

The cluster ion beams show specific irradiation effects compared to monomer ion beams due to their unique feature in energy deposition [1]. However, biological effects remained to be determined. The currently available cluster ion beams generated by linear electrostatic accelerators have a limited penetration depth and the samples have to be irradiated in a vacuum chamber. We used bacterial spores as a model organism and established the sample preparation and irradiation method for cluster ion beams [2]. In our previous study using carbon ions, the LET value was very high (1,141 keV/μm) and a single carbon atom deposited energy more than enough to kill the spore, and therefore, we failed to detect any “cluster effect”. Further analysis on the relationship between LET and lethal effects suggested that the LET range less than 150 keV/μm was suitable to investigate the cluster effect in our experimental system. Here, we compared the lethal effect of monomer and cluster beams using proton ions.

The spore samples were prepared as described previously [2]. In brief, 3 μl of spore suspension solution containing 2×10^5 spores was dropped onto a small piece of silicon wafer (10 × 10 mm). Spores were spread into almost monolayer by freeze drying followed by dew condensation treatment on ice. The samples were irradiated in a vacuum chamber with three kind of monomer ions (340 keV H^+ (LET 75.0 keV/μm), 500 keV H^+ (58.9) and 1 MeV H^+ (37.7)) and cluster ions (2 MeV H_2^+). The LET value of 2 MeV H_2^+ is 75.4 keV/μm, if we assume it is twice that of 1 MeV H^+. The spores on each silicon wafer were corrected in PBT buffer (10 mM sodium phosphate buffer containing 0.01% Tween20, pH 7.0), and the survival fraction was determined by the dilution plate method.

The survival fraction decreased with increased particle fluence on a semi-logarithmic scale (Fig. 1). The lethal effect of monomer ions depended on the LET. The 340 keV H^+ that has the highest LET value showed the highest lethal effect. In case that H_2^+ is regarded as a single particle, the LET value of 2 MeV H_2^+ is close to that of 340 keV H^+. However, the lethal effect of 340 keV H^+ is higher than that of 2 MeV H_2^+ per particle (Fig. 1A). This shows that the density of energy deposition in the ion track greatly affects the lethal effect of particle beams.

The 2 MeV H_2^+ and 1 MeV H^+ have the same incident energy per atom, however the lethal effect of 2 MeV H_2^+ seems slightly lower than that of 1 MeV H^+ per atom (Fig. 1B). This might be a negative cluster effect regarding the lethal effect. It could be interpreted that, in case of 2 MeV H_2^+, two proton atoms in a cluster had more chances to affect the same gene because the two atoms were in close proximity.

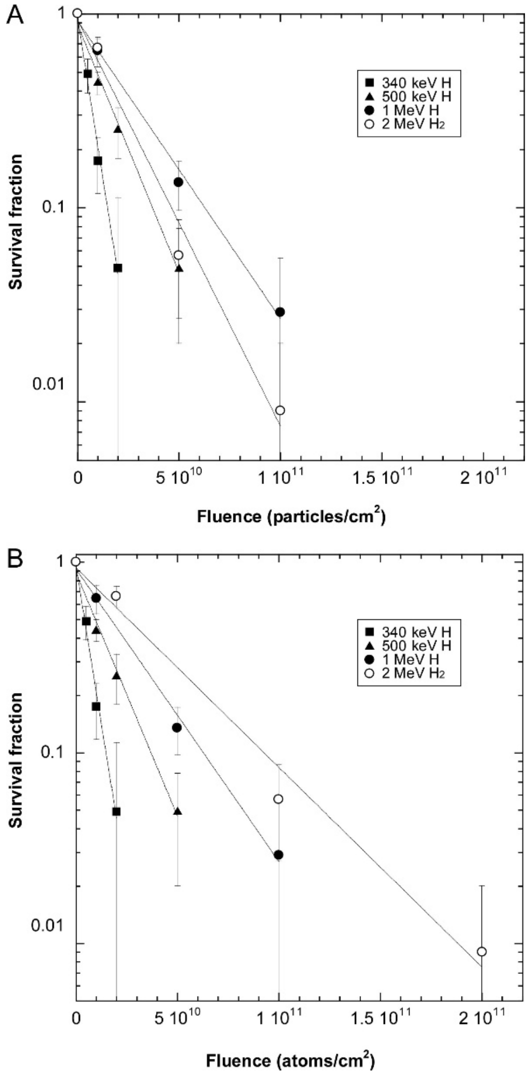

Fig. 1. Survival fraction of irradiated *B. subtilis* spores shown as a function of particles/cm^2 (A) and atoms/cm^2 (B).

Acknowledgments

This study was partially supported by JSPS KAKENHI JP17K05133.

References

[1] A. Chiba *et al.*, Nucl. Instrum. Meth. Phys. Res. B **315**, 81 (2013).

[2] Y. Hase *et al.*, Quantum Beam Sci. **3**, 8 (2019).

2 - 14

Mutagenesis of the Oil-producing Algae by Heavy Ion Irradiation

H. Araie[a], Y. Hase[b], Y. Iwata[c], Y. Oono[b] and I. Suzuki[d]

[a]Department of Biosciences, Kanto Gakuin University College of Science and Engineering,
[b]Department of Radiation-Applied Biology Research, TARRI, QST,
[c]Research Institute for Advanced Electronics and Photonics, AIST,
[d]Faculty of Life and Environmental Sciences, University of Tsukuba

For biofuel production by microalgae, three improvements are essential; the higher concentration of the algae biomass, higher productivity of oil contents, and a strain with unique oil property. In this study, we focused on very-long-alkyl ketones so-called alkenone (Fig. 1), which are thought to be good candidates for biofuels [1]. We selected one of the alkenone-producing haptophytes, *Tisochrysis lutea* (Strain T-Iso), because some molecular biotechnological methods and information are available [2, 3]. Here, we tried heavy ion irradiation which has an advantage to obtain useful mutants [4, 5]. In addition, the obtained mutants can be applicable to the open system as non-GMO.

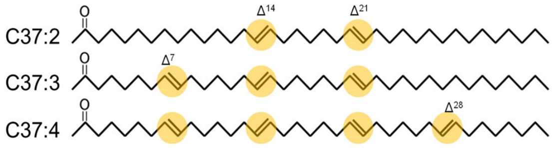

Fig. 1. Alkenone structures. The carbon number of these alkenones is 37 and they have two to four *trans*-type double bonds and a keto group at a C2 position.

So far, we have selected high oil-producing strains by monitoring fluorescence intensity of lipids stained with Nile red regent by using microplate reader (SYNERGY HTX, BioTek). It is considered that these high oil-producing strains had features such as high growth rate, high intracellular carbon ratio to lipid, or the suppression of lipid degradation.

Alkenone is known to be used as an energy source like polysaccharides under dark condition. [6]. Therefore, we cultured the selected high oil-producing strains with 96-well plate for 2 weeks and then put them in dark condition for 1 week. Finally, we obtained 9 strains that remained the highest fluorescence intensity in both Nile Red and Chlorophyll as the first candidates and following 22 strains as the second candidates (Fig. 2). Here, we checked these candidate strains whether the amount of alkenone was suppressed.

In analysis of the alkenone amounts by GC-FID, we cultured 24 of 31 candidate strains in plastic flask for 2 weeks and then put them in dark condition for 1 week. When we compared the alkenone amounts before and after dark conditions, we obtained 5 candidate strains (Fig. 3). Alkenone degradation of these candidates were more suppressed than the wild type under the dark conditions. One of 5 candidates was the first candidates that remained 88% of alkenone before the dark conditions. Four of 5 candidates were the second candidates.

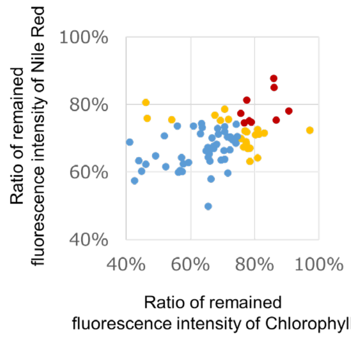

Fig. 2. Mutants that suppressed lipid degradation. Ratio of remained fluorescence intensity of Nile Red and Chlorophyll after the 1 week dark condition. Red circle: 9 strains that remained highest fluorescence intensity in both Nile Red and Chlorophyll, Orange circle: 22 strains that remained higher fluorescence intensity in both Nile Red and Chlorophyll, Blue circle: The other strains.

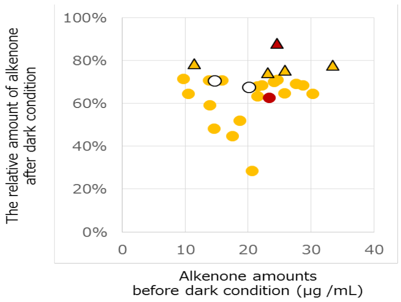

Fig. 3. Comparison of alkenone amount before and after dark condition. We cultured 24 of 72 strains in plastic flask for the comparison of the alkenone amounts before and after dark condition. Red: Frist candidates, Orange: Second candidates, Open circle: T-Iso (wild type), Triangle: Candidate strains in which alkenone degradation is suppressed under dark condition.

References

[1] O'Neil *et al.*, Energy Fuels **29**, 922 (2015).
[2] Endo *et al.,* Sci. Rep. **8**, 11230 (2018).
[3] Carrier *et al.*, Algal Res. **29**, 1 (2018).
[4] Ota *et al.*, Biotechnol. Biofuels **9**, 13 (2016).
[5] Yamada *et al.*, Sci. Rep. **6**, 26327 (2016).
[6] Tsuji *et al.*, Mar. Biotechnol. **17**, 428 (2015).

2 - 15

Construction of Luciferase Reporter Strains for Functional Analysis of DNA Damage Response Regulator PprI in *Deinococcus radiodurans*

K. Satoh[a)], T. Sanzen[a,b)], Y. Oono[a)] and I. Narumi[b)]

[a)]Department of Radiation-Applied Biology Research, TARRI, QST,
[b)]Graduate School of Life Sciences, Toyo University

Deinococcus radiodurans is a representative strain of radioresistant bacteria and has extremely high resistance to various DNA damage caused by gamma rays, ultraviolet rays, desiccation, free radical-generating substances, and DNA cross-linkers. The previous studies revealed that the expression of a unique DNA repair-related protein, PprA, was up-regulated by a DNA damage response regulator, PprI, following DNA damage in *D. radiodurans* [1]. Analysis of the genome sequences of *Deinococcus* spp. discovered the radiation/desiccation response (RDR) motif, existing upstream of the radiation-inducible genes (RDR regulons) such as *pprA* and *ddrA* genes [2]. The RDR motif serves as an operator sequence in the unique DNA repair response system [3]. Another regulatory protein DdrO binds the RDR motif and serves as a repressor. Following DNA damage, the metalloprotease activity of PprI cleaves DdrO, resulting in induction of the RDR regulon [4]. However, the detailed functional site of PprI protein is poorly understood. In an effort to gain an insight into the role of PprI in DNA damage response mechanism in *D. radiodurans*, we generated luciferase reporter strains that were regulated by *pprI* expression plasmids.

Firstly, we constructed a luciferase reporter DNA cassette consisted of an engineered firefly luciferase gene (FL) and an *Escherichia coli* spectinomycin resistance gene (Spc) as a genetic marker. The expression of FL was controlled by the *ddrA* promoter including the RDR motif. Next, this luciferase reporter DNA cassette was intergrated into the genome of the wild-type and the *pprI*-deleted mutant strains via homologous recombination, and the resulting FL reporter strains were designated DARP and SIRP, respectively. The *pprI* expression plasmid pEXpprI carrying an *E. coli* chloramphenicol (Cm) resistance gene was introduced into the strain SIRP. As controls, empty pRAD1 vector was introduced into strains DARP and SIRP. *D. radiodurans* cells carrying the plasmids were incubated at 30 °C for 24 h in TGY broth containing 350 μg/mL Spc and 3 μg/mL Cm. Cells were harvested, washed, and resuspended in 10 mM sodium phosphate buffer (pH 7.0). Aliquots (0.25 mL) of the cell suspension were dispensed into 15 mL-volume test tubes and irradiated at room temperature with 2 kGy of ^{60}Co gamma rays at Food Irradiation Facility, TARRI, QST. After irradiation, cells were resuspended in 2 mL TGY broth and incubated at 30 °C for different post-irradiation times (0 and 2 h) with agitation. FL activity in cell suspension (10 μL) were measured using the Bright-Glo Luciferase Assay System (Promega). Chemiluminescent signals were visualized using an Ez-CaptureMG chemiluminescence imaging system (Atto). The relative reporter activity was calculated as the ratio of the luminescence from FL to the optical density at 600 nm of the cell suspension.

We successfully generated luciferase reporter strains for functional analysis of PprI in *D. radiodurans*. As shown in Fig. 1, in strain DARP carrying pRAD1, FL reporter activity was enhanced following 2 kGy gamma irradiation at 2 h post-irradiation time. On the other hand, FL reporter activity in the *pprI*-deletion strain SIRP carrying pRAD1 was not observed following irradiation. Like strain DARP, the FL reporter activity in the strain SIRP carrying pEXpprI was enhanced following irradiation by functional complementation with the *pprI* expression plasmid. This result suggests that the *D. radiodurans* PprI is a key protein for DNA damage response regulator. Currently, we constructed several mutated *pprI*-expression plasmids. Further, the FL reporter assay with *pprI* mutation library will help to delineate the functional site of PprI in regard to the DNA damage response mechanism in *D. radiodurans*.

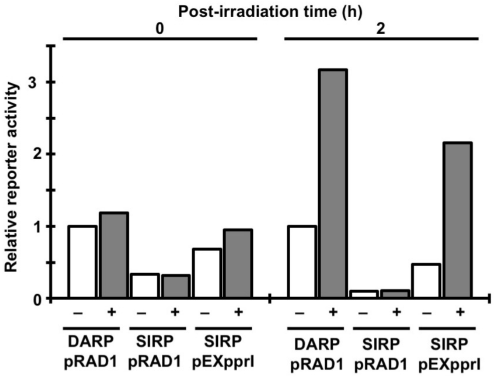

Fig. 1. Changes in FL reporter activity following irradiation. Cells were irradiated (+) or mock irradiated (–) with gamma rays at a dose of 2 kGy, incubated for 0 or 2 h and then subjected to the FL reporter assay. Values represent the relative reporter activity normalized in relation to the mock-irradiated DARP value of 1 for each post-irradiation time.

Acknowledgments

This work was supported by JSPS KAKENHI Grant Number JP18K05423 to K. Satoh.

References

[1] Y. Hua *et al.*, Biochem. Biophys. Res. Commun. **306**, 354 (2003).
[2] D. R. Haris *et al.,* PloS Biol. **2**, e304 (2004).
[3] M. Ludanyi *et al.*, Mol. Microbiol. **94**, 434 (2014).
[4] H. Lu *et al.*, DNA Repair **11**, 139 (2012).

2 - 16 Functional Analysis of Radiation-Inducible Protein DdrA and Its Paralog Protein DdrAP in *Deinococcus radiodurans*

Y. Futami a), K. Satoh b), N. Tomita a), T. Sanzen c), T. Shimosaka a), Y. Oono b)
and I. Narumi a,c)

a) Faculty of Life Sciences, Toyo University,
b) Department of Radiation-Applied Biology Research, TARRI, QST,
c) Graduate School of Life Sciences, Toyo University

Deinococcus radiodurans is a representative strain of the radioresistant bacteria characterized by extraordinary tolerance toward various DNA damaging agents such as ionizing radiation, ultraviolet rays and DNA cross-linkers [1]. Following exposure to such agents, a number of genes which lack readily identifiable homologues among known proteins are induced. Of these, DdrA (DNA damage response A) is one of the most highly induced genes [2]. This protein has an evolutionary relationship to eukaryotic Rad52, a protein that is important for DNA double-strand break repair and homologous recombination [3]. It has also been shown that DdrA binds to 3'-overhang DNA ends to protect them from degradation by nucleases [4]. However, the detailed function of DdrA in DNA repair mechanisms of *D. radiodurans* is not yet thoroughly understand. Sequence homology analysis revealed that *D. radiodurans* possesses a DdrA paralog, DdrAP, which is constitutively expressed in cells unlike DdrA. Although DdrAP is widely conserved in the member of genus *Deinococcus*, the function of DdrAP protein remains unclear.

In this study, we constructed knockout strains for the DdrA-encoding gene (*ddrA*) and DdrAP-encoding gene (*ddrAP*) of *D. radiodurans* and investigated sensitivities of these mutant strains to DNA damaging agents and DNA replication inhibitors in order to gain an insight into the role of these genes in DNA repair mechanisms.

A ddrA knockout stain was generated from *D. radiodurans* wild-type R_1 (WT) by the double crossover-mediated mutagenesis technique using the kanamycin phosphotransferase gene as a marker (designated Δ*ddrA*). *A ddrAP* knockout stain was generated by the double crossover-mediated mutagenesis technique using the hygromycin phosphotransferase gene as a marker (designated Δ*ddrAP*). Sensitivities of WT and the knockout strains to DNA damaging agents and DNA replication inhibitors were investigated by serial dilution spotting method [5].

Whereas Δ*ddrA* exhibited sensitivities to gamma rays, ultraviolet rays, and nalidixic acid, Δ*ddrAP* exhibited resistance to gamma rays, bleomycin, and novobiocin (Fig. 1). Among the strains tested, there was no difference in sensitivities to the DNA alkylating agent methyl methanesulfonate and the DNA oxidant hydrogen peroxide. Nalidixic acid and novobiocin are inhibitors of DNA gyrase subunit A (GyrA) and subunit B (GyrB), respectively. From the results of sensitivity test, it was suggested that DdrA and DdrAP are interacted with GyrA and GyrB, respectively, so that the effect of these inhibitors to the protein complex consisted of DdrA, DdrAP, GyrA and GyrB is altered by inducing conformational change.

Taking into consideration the result that Δ*ddrAP* exhibited a resistance to gamma rays and bleomycin, both of which produce DNA double strand breaks, and the fact that the DNA repair promoting protein PprA is interacted with DNA gyrase [6], DdrAP seems to involved in condensed nucleoid-dependent end joining (CNDEJ), the double strand breaks repair mechanism in which PprA plays a crucial role in *D. radiodurans* [1].

Acknowledgments

This work was supported by JSPS KAKENHI Grant Number JP17K07730 to I. Narumi.

References

[1] Y. Ishino *et al.*, Curr. Opin. Microbiol. **25**, 103 (2015).
[2] D. R. Haris *et al.,* PloS Biol. **2**, e304 (2004).
[3] I. Gutsche *et al.*, Biochim. Biophys. Acta **1784**, 1050 (2008).
[4] L. M. Iyer *et al.*, BMC Genomics **3**, 8 (2002).
[5] R. Thomas *et al.*, Biotechnol. Rep. **8**, 45 (2015).
[6] S. Kota *et al.*, Extremophiles **20**, 195 (2016).

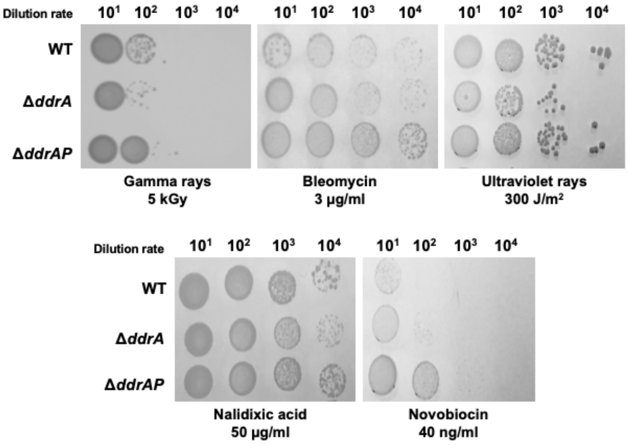

Fig. 1. Sensitivities to DNA damaging agents and DNA replication inhibitors.
For gamma and ultraviolet rays, 5 µl aliquots of serially diluted cells were dropped on TGY agar and subjected to irradiation. For remaining chemical treatments, 5 µl aliquots of serially diluted cells were dropped on TGY agar supplemented with each chemical. TGY agar was incubated at 30 ºC for 2 d.

2 - 17 Development of Sake Yeasts Preparation Method with Improved Viability for Ion-Beam Mutagenesis

T. Watanabe[a)], M. Yanagisawa[a)], K. Satoh[b)] and Y. Oono[b)]

[a)]Gunma Industrial Technology Center,
[b)]Department of Radiation-Applied Biology Research, TARRI, QST

Japanese sake, called as “koku-syu” is a traditional liquor of Japan. It is made from steamed-rice, koji-rice, and water. The various characters of Japanese sake such as sweetness/dryness, rich/light, acidity, and *ginjyo*-aroma vary depending on sake yeasts. Therefore, various sake yeasts are isolated and bred at each region of Japan. Our group have succeeded in breeding and practical utilization of sake yeast *Saccharomyces cerevisiae* No. 227 by ion-beam mutagenesis for the first time in the world [1]. Moreover, we also bred non-urea producing Gunma KAZE2 yeast (KAZE2-Arg) which is suitable for export by ion-beam irradiation [2]. However, the viabilities of sake yeasts prepared for ion-beam mutagenesis were under 0.1%. Thus, it was considered that some mutagenesis stress was provided for yeast cells before ion-beam irradiation. Therefore, some improvement trials are needed for evaluating superiority of ion-beam breeding methods.

Previous conditions were follows. Yeast cells were statically pre-incubated in YM5 medium (0.3% yeast extract, 0.3% malts extract, 0.5% peptone, and 5% glucose) at 30 °C for 4 d. Cells were harvested and washed with sterilized saline (0.9% NaCl) and adhered on cellulose acetate membrane (0.22 μm). These operations were done in the clean bench (Fig. 1). After freeze-dried treatment, 20 ml of YM medium (0.3% yeast extract, 0.3% malts extract, 0.5% peptone, and 1% glucose) was added on the membrane and incubated at room temperature for 1 h. Diluted with sterilized saline, yeast cells were spread on YM plate medium (consolidated with 2% agar) and incubated at 30 °C for 1 d. Viabilities of yeast were determined by calculating the number of single colonies (treatment) divided by the total number of colonies (mock treatment).

In this study, we investigated conditions to prepare yeast cells for ion-beam mutagenesis. Firstly, we changed growth condition of yeast cells from the stationary phase to the log phase that is usually used for ethylmetansulfonate mutagenesis and UV-irradiation [3, 4]. *S. cerevisiae* kyokai no. 701, type strain of sake yeast, was incubated in YM medium (0.3% yeast extract, 0.3% malts extract, 0.5% peptone, and 1% glucose) with shaking at 150 rpm, 30 °C for 24 h. After freeze-dried treatment, viability of yeast was improved to about 0.1%.

Next, we thought that osmotic stress condition might induce yeast cells to adapt drying stress condition. We added 1% of NaCl in YM medium to increase osmotic stress. However, viability of yeast was decreased under 0.1%. On the other hand, viability of yeast was increased to 0.6% by adding1 M Sorbitol in YM medium (YMS medium) which was utilized as a protective material for expansion stress [5]. This result gave us a hint to change YMS medium to YPDS medium (1% yeast extract, 2% peptone, 2% glucose, and 1 M sorbitol). This improvement increased yeast viability to 2%.

Freeze-dried treatment causes to yeast cells freeze stress and drying stress. Subsequently, we changed drying method. After filtration, membranes were air-dried on clean bench at room temperature for 10 min. Yeast viability was drastically improved to about 60%. However, membrane was recovery cultivated for 2 h, yeast viability drastically decrease to 2%. This trouble could be avoided by changing YM medium to YPD medium (1% yeast extract, 2% peptone, and 2% glucose).

Summary, improved conditions were follows. Yeast cells were cultivated in YPDS medium with shaking at 150 rpm, 30 °C for 24 h. Cells were harvested and washed with sterilized saline (0.9% NaCl) and adhered on cellulose acetate membrane (0.22 μm). After air-dried treatment, 20 ml YPD medium was added on the membrane and incubated at room temperature for 1-2 h. Yeast viabilities were reached at 90%. In the future study, we would like to evaluate superiority of ion-beam breeding methods comparing with UV-irradiation.

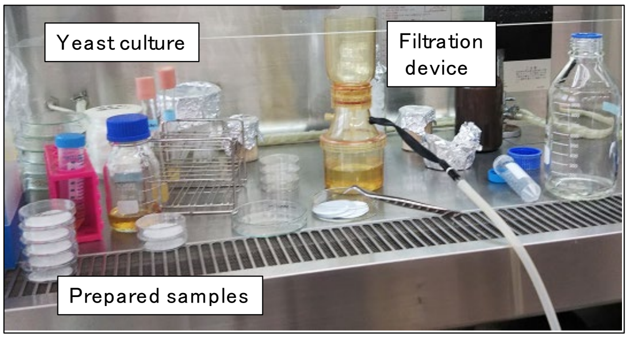

Fig. 1. Appearance of preparation of the yeast cell samples for ion-beam irradiation.

References

[1] T. Masubuchi *et al.*, JAEA Takasaki Annu. Rep. 2012, JAEA-Review **2013-059**, 117 (2014).
[2] T. Watanabe *et al.*, QST Takasaki Annu. Rep. 2018, **QST-M-23**, 81 (2020).
[3] T. Watanabe *et al.*, Appl. Microbiol. Biotechnol. **80**, 331 (2008).
[4] T. Watanabe *et al.*, Biosci. Biotechnol. Biochem. **77** 917 (2013).
[5] T. Watanabe *et al.*, J. Biosci. Bioeng. **103**, 225 (2009).

2 - 18

Nitrogen-Conditioned Screening of *Chlamydomonas* Mutants That Do Cell Growth and Lipid Accumulation Simultaneously Under Nitrate-Replete Condition

T. Oyama[a], Y. Kato[b], T. Hasunuma[a,b], C. Ogino[c], K. Satoh[d],
Y. Oono[d] and A. Kondo[a,b,c]

[a]Graduate School of Science, Technology and Innovation, Kobe University,
[b] Engineering Biology Research Center, Kobe University,
[c]Graduate School of Engineering, Kobe University,
[d]Department of Radiation-Applied Biology Research, TARRI, QST

Microalgae biofuel has attracted global attention as a new energy resource that replaces fossil fuels. Although there are valuable microalgal strains for biofuel production, complexity in cultivation process remains as the problem. Microalgae generally do cell growth by consuming nitrogen source, and accumulate lipids in the cells after completely consume nitrogen source. Thus, nitrogen deficiency is a common trigger for lipid accumulation in microalgae, however, it drastically inhibits cell growth [1]. To avoid this trade-off problem between cell growth and lipid accumulation, this study aimed to develop a breeding method of microalgae strains that can simultaneously perform cell growth and lipid accumulation under nitrate-replete conditions.

In this study, random mutagenesis by heavy ion beams [2] was combined with nitrate-conditioned and fluorescence-activated cell sorter (FACS)-based screening. To prepare a mutant population with high genetic diversity, marine microalga *Chlamydomonas* sp. KOR1 was irradiated with 50 Gy of the carbon ion beams ($^{12}C^{5+}$, 220 MeV) accelerated by an AVF cyclotron at TIARA, QST. Then, the mutants were cultured under the nitrate-replete conditions, stained with lipophilic fluorescence dye BODIPY, and subjected to FACS screening. After repeating the sequential procedures to sort cells with high-BODIPY fluorescence, KAC1710, which can accumulate lipid under the nitrate-replete conditions, was obtained (Fig. 1). The procedure was further repeated using KAC1710 as the parent. Consequently, KAC1801, which can accumulate more lipids than KAC1710 was obtained (Fig. 2).

KAC1710 and KAC1801 showed decreases in biomass production (Fig. 3A) and nitrate consumption (Fig. 3B), while lipid content and lipid productivity under the nitrate-replete conditions were significantly improved in these mutants compared (Fig. 3C and 3D). These results suggest that restricted nitrate intake triggered direction of carbon flux to lipid synthesis. KAC1710 and KAC1801 accumulated 19.1% and 26.6% lipid-dry cell weight at day 5, respectively (Fig. 3C). Lipid productivities of KAC1710 and KAC1801 were 112 mg/L/d and 162 mg/L/d, respectively (Fig. 3D).

The breeding method developed in this study is assumed to be available in other microalgae. In addition, development of a sustainable cultivation strategy for microalgae biofuel production is expected in the future based on the achievements in this study.

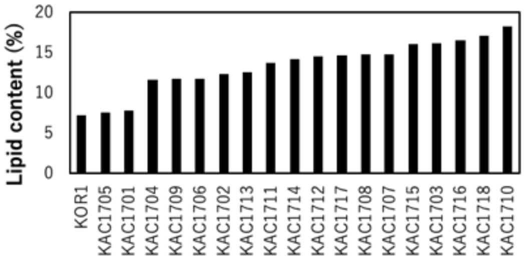

Fig. 1. Result of first-round screening.

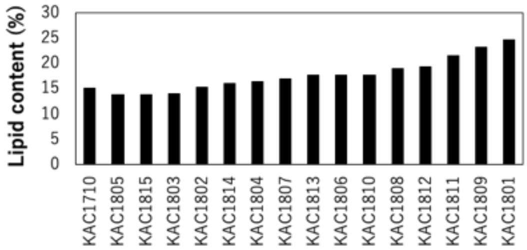

Fig. 2. Result of second-round screening.

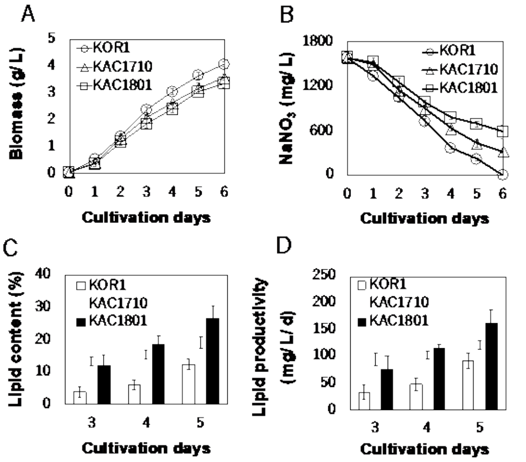

Fig. 3. Lipid productivity of KAC1710 and KAC1801.

Acknowledgments

This study was conducted by the financial support of ImPACT program, Cabinet Office, Government of Japan.

References

[1] K. Tan *et al.*, Biotechol. Biofuels **9**(1), 255 (2016).
[2] Y. Kato *et al.*, Bioresour. Technol. **245**, 1484 (2017).

2 - 19 Damage and Growth Inhibition of *Bacillus subtilis* Spores by Ion-beam, Gamma Irradiation and Heat Treatment

H. Den[a], A. Futenma[a], T. Sakai[a], N. Maeda[a], H. Sakamoto[b], T. Tsuchido[b],
M. Furuta[a], K. Satoh[b] and Y. Oono[b]

[a]Quantum Radiation Engineering, Graduate School of Osaka Prefecture University,
[b]Research Center of Microorganism Control, Organization for Research Promotion, Osaka Prefecture University,
[c]Department of Radiation-Applied Biology Research, TARRI, QST

Bacillus subtilis is known as Gram-positive, rod-shaped, aerobic, spore-forming bacterium that is naturally found in soil. *Bacillus* spores have a hard, layered structure depositing 2,6-Pyridinedicarboxylic acid (DPA) in their dehydrated core region containing genomic DNA protected by acid-soluble small proteins contributing the registance of the spores against various bactericidal stresses. such as heat, desiccation, chemical, and radiation [1]. The spores release DPA from their cores together with hydration during the germination process and vegetative cells are formed through subsequent outgrowth and moved to vegetative growth again. These processes can be monitored by tracking the turbidity changes of liquid culture because the refractive index of light scattering changes within the culture during spore germinaiton. Besides, Ionizing radiation induces DNA damages including single-strand breaks and double-strand breaks and generates reactive oxygen species which also induces DNA strand breaks. Ion beams have a high linear energy transfer (LET, keV/μm) and give DNA damage containing double-strand break locally (clustered damage) than gamma rays do [2].

In this work, we used *B. subtilis* 168 (*trpC2*) spores, and the germination and growth process of the spores was investigated by ^{60}Co gamma rays and ion beam irradiation in comparison with heat treatment.

The spores of *B. subtilis* 168 were prepared by inoculating the vegetative cells onto the Schaeffer's sporulation medium [3] at 37 ºC for 4 d, harvested and treated sequentially with 1 mg/ml lysozyme and 1% SDS. Aliquots (1 mL) of the spore suspensions at 10^9 CFU/ml were dropped onto the sterilized cellulose membrane and dried then irradiated four kinds of ion beams (^{4}He^{2+} [50 MeV; 19.4 keV/μm], ^{12}C^{6+} [190 MeV; 148.7 keV/μm]; and ^{20}Ne^{8+} [350 MeV; 440.8 keV/μm] accelerated by an AVF cyclotron at TIARA, TARRI, QST or with ^{60}Co gamma rays (0.2 keV/μm) at Osaka Prefecture University. The irradiation doses ranged from 0.6 to 6 kGy.

Irradiated spores were recovered from membranes, and cultivated in 96-well microplate containing LB broth (1 mL) with shaking by Multiscan GO Microplate Spectrophotometer. During the cultivation, OD_{650} of the culture was automatically measured. Viability of the spores was determined by colony counting. Heating was also conducted to the spore at 98 ˚C to compare the effect on the germination process [4].

The ^{12}C^{6+} ion beam-irradiated spores showed the most sensitivity among the ion beams used for irradiations. The lethal effect of spore was estimated to be in the order ^{12}C^{6+} > ^{20}Ne^{8+} > ^{4}He^{2+}.

The initial spore germination process ion–beam irradiated spores seemed to be similar with ^{60}Co gamma rays. Outgrowth phase after the germination became longer with their irradiation sensitivity increased according to different LET of each ion beam species (Fig. 1). These results suggest that damaged sites in spores are similar between gamma- and ion-beam irradiations.

As ion beams have higher LET values to potentially cause more intensive damage on the germination system and DNA damages including clustered damages on the *Bacillus* spores, more detailed study should be required.

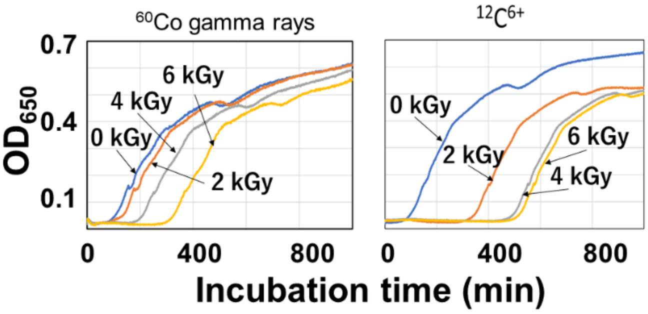

Fig. 1. Growth curve of ^{60}Co-gamma and ^{12}C^{6+}-irradiated *Bacillus subtilis* spores.

References

[1] F. Kunst *et al.*, Nature **390**, 249 (1997).
[2] C. F. Dunne, Br. J. Hosp Med. **74**, 166 (1999).
[3] P. Schaeffer *et al.*, Proc. Natl. Acad. Sci. USA, **54**, 704 (1965).
[4] Futenma *et al.*, Biomicroworld 2017, October 18-20, 2017 Madrid, Spain.

2 - 20 Characterization of TetR-type Repressor Which Cause the Delayed Contact-dependent RED Production in *Streptomyces coelicolor*

S. Asamizu[a,b], T. Ishizuka[a], M. Yanagisawa[a], K. Satoh[c], Y. Oono[c] and H. Onaka[a,b]

[a] Graduate School of Agricultural and Life Sciences, The University of Tokyo,
[b] Collaborative Research Institute for Innovative Microbiology, The University of Tokyo,
[c] Department of Radiation-Applied Biology Research, TARRI, QST

Actinomycetes, filamentous Gram-positive bacteria, are a major source of bioactive natural products which can be drug candidates. Genome analyses of actinomycetes have revealed the huge number of “cryptic” secondary metabolite biosynthetic gene clusters, indicating the potential of actinomycetes for the production of far more diverse secondary metabolites than previously thought. We have studied about the bacterial interaction induced production of secondary metabolites by actinomycetes. *Tsukamurella pulmonis* TP-B0596 (here after Tp) had been shown to possess ability to induce production of secondary metabolites by *Streptomyces* species, which are not detected or poorly produced in a mono-culture [1]. Until now, 7 classes, total 29 new compounds had been isolated from the co-culture with various actinomycetes and Tp (the method named combined-culture) [2]. Object of this study is to elucidate the gene(s) which are involved in the response for activation of secondary metabolism within actinomycetes. Elucidation of the mechanism can lead to the fundamental understanding of bacterial interaction and secondary metabolism, as well as application for genetic tools to discover novel bioactive natural products from untapped gene matters.

Streptomyces species respond to mycolic acid-containing bacteria by production of secondary metabolism in a contact dependent manner [1,3]. Here we employed forward-genetic study using mutagenesis by heavy ion beam to investigated the gene(s) responsible for the responsive production of secondary metabolism induced by Tp. Using *Streptomyces coelicolor* JCM4020 as a model strain, we employed carbon ion beam ($^{12}C^{5+}$, 220 MeV) induced mutagenesis to generate spore mutant library of *S. coelicolor*. Then we screened the undecylprodigiosin (RED) production deficient mutants of *S. coelicolor* by mixing them with Tp on agar plates using red / white phenotype of the colonies as indication. Through this screening, 118 mutants from around 152,000 tested spores were obtained. We further tested the phenotype of the 118 mutants by growth on minimum medium and formation of aerial mycelia, and finally selected 59 mutants. We first re-sequenced the genomes from 16 mutants and identified the 44 mutations [4,5,7]. We performed gene complementation and found that mutations in glutamate synthase (gltB), elongation factor G (fusA), and sarA (putative membrane protein) caused the RED deficient phenotypes [6,7]. We then re-sequenced the genome of 26 mutants and further gene complementation study revealed that molybdopterin biosynthetic enzyme (*moeA*), and tetR-like transcriptional regulator (*sco1718*) are also responsible for the phenotype differences. We generated a targeted gene disruptants of tetR-like transcriptional regulator in *S. coelicolor* A3(2) and confirmed the over 8-h delayed production of RED by contact of Tp, compared to the wild-type. (Fig. 1) We speculate that the TetR-like protein is a repressor for the expression of adjacent ABC transporter (*sco1719-20*), thus efflux of the unknown small molecule is prevented and accumulated in the cell, which caused stress to cell that can lead to the RED production.

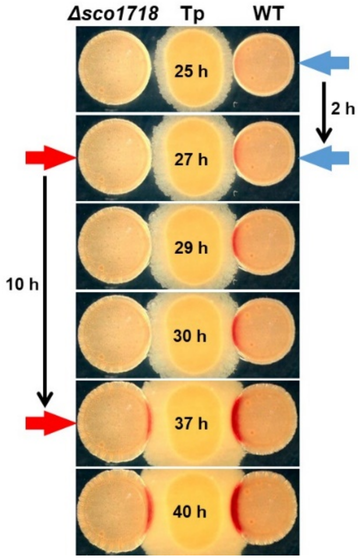

Fig. 1. Time lapse analysis of interaction between Tp and the disruptant (Δ*sco1718*) or wild-type (WT) strains.

References

[1] H. Onaka *et al.*, Appl. Environ. Microbiol. **77**, 400-6 (2011).
[2] H. Onaka *et al.*, Comprehensive Natural Products III, (2019). DOI: 10.1016/B978-0-12-409547-2.14692-X
[3] S. Asamizu *et al.*, PLoS One **10**, e0142372 (2015).
[4] M. Yanagisawa *et al.*, QST Takasaki Annu. Rep. 2016, **QST-M-8**, 97 (2018).
[5] S. Asamizu *et al.*, QST Takasaki Annu. Rep. 2017, **QST-M-16**, 106 (2019).
[6] S. Asamizu *et al.*, QST Takasaki Annu. Rep. 2018, **QST-M-23**, 88 (2020).
[7] S. Asamizu *et al.*, IFO Res. Commun. **32**, 95 (2018).

2 - 21

Generation and Screening of *Bacillus pumilus* Mutants with Improved Plant Growth-Promoting Effects Using Ion-beam

M. Yasuda[a], K. Satoh[b], Y. Oono[b], T. Yokoyama[a] and S. Okazaki[a]

[a] Graduate School of Agriculture, Tokyo University of Agricultural and Technology,
[b] Department of Radiation-Applied Biology Research, TARRI, QST

Bacillus pumilus strain TUAT-1 (hereafter referred to as TUAT-1) promotes the growth of several plants, including that of rice (*Oryza sativa* L.) and Brassica species [1–3]. An inoculant was developed using TUAT1 that has been commercialized in Japan since 2017. TUAT-1 has been shown to increase shoot and root growth in rice, mustard, radish, and komatsuna, mainly due to its effects to promote nutrient uptake by plant roots [4, 5]. Inoculation of plants with TUAT-1 biofertilizer at sowing and transplanting resulted in significant changes in plant biomass, nutrient uptake, tissue N content, tiller number, root length, and the number of roots in the forage rice [6].

Despite, the large body of experimental evidence on the growth-promoting effects of TUAT-1, our knowledge of the conditions required for consistent positive interaction between the bacteria and the plant in field conditions, is limited. Generally, bacterial inoculation improves plant growth and rice yield, but the effects often change by the soil physical or chemical properties, climate, and target crops. This makes it difficult for TUAT-1 biofertilizers to be utilized more efficiently and widely. Thus, the generation of the TUAT-1 mutants with stable and improved plant growth-promoting effects might be of great importance in biofertilizer development. Therefore, the specific objectives of this study were (i) to determine the best condition for ion beam irradiation to TUAT-1 and (ii) to screen the TUAT-1 mutants with stable and improved plant-growth-promoting effects.

The TUAT-1 was grown in LB medium at 37 °C for 16 h. Aliquots (0.1 ml) of bacterial suspension (5×10^7 cfu/ml) were dropped onto sterilized membranes in the petri dish (30 mm diameter) and these dishes were covered with a sterilized polyimide film. Cells were irradiated at different doses (0, 100, 150, 250, 500, 1000, 1500, and 2000 Gy) with helium ion beams ($^4He^{2+}$, 50 MeV) accelerated by an AVF cyclotron at TIARA, QST. Survival rates were determined by comparing the number of colonies per dish and the most appropriate doses to produce mutants were selected.

As expected, survival rates were decreased by radiation dose. We could not observe any colony formation in the cells exposed to 500 Gy or higher. The survival rates were 0.11% for 250 Gy, 1.96% for 150 Gy, and 4.6% for 100 Gy. We therefore decided to use irradiation dose of 150 Gy to generate mutants.

It has been reported that TUAT-1 showed higher plant-growth-promoting effects on rice plants when inoculated as spores [7]. Thus, the TUAT-1-based biofertilizer “Kikuichi” is produced using the spores of TUAT-1, however, the spore-formation of TUAT-1 remains difficult to induce and spore-forming rate is low. Therefore, screening of the high-spore forming TUAT-1 mutants is now ongoing. Besides, we recently obtained the series of evidence that the rice roots inoculated with TUAT-1 produced less nitric oxide than uninoculated roots (Yokoyama et al. unpublished). The nitric oxide is generally known as a signal which controls various events in plant development including cell division, meristem formation, and defense responses against pathogens. The reduction of nitric oxide by TUAT-1 suggests that the TUAT-1 scavenges nitric oxide to promote its infection and/or induce root development. We therefore aimed to isolate TUAT-1 mutants that possess higher nitric oxide scavenging activity. Our efforts are currently directed toward screening these mutants and we will analyze their plant-growth-promoting activities when we obtain the candidates.

In conclusion, we set up the condition of Ion-beam mutagenesis for *Bacillus pumilus* TUAT-1 as a plant growth-promoting rhizobacteria. Screening of the TUAT-1 mutants that possess improved spore-forming activity and nitric oxide scavenging activity is ongoing. The TUAT-1 mutants obtained by Ion-beam mutagenesis provide useful resources for screening of various beneficial strains that will be used for next-generation biofertilizers.

References

[1] S. Djedidi *et al.*, J. Plant Res. **127**, 585 (2014).
[2] S. Djedidi *et al.*, J. Plant Res. **128**, 147 (2015).
[3] S. Djedidi *et al.*, J. Environ. Radioact. **157**, 27 (2016).
[4] HP Aung *et al.*, Sci. Tot. Environ. **521–522**, 261 (2015).
[5] KT. Win *et al.*, Agronomy **8**, 216 (2018).
[6] KT. Win *et al.*, PLoS ONE **14**, e0220236 (2019).
[7] NP. Ngo *et al.*, Soil Sci. Plant Nutr. **65**, 598 (2019).

2 - 22 Basic Examination of Soft Agar Colony Formation Assay for PC12 Pheochromocytoma Cells

T. Sakashita, Y. Yokota, Y. Ohshima and N. S. Ishioka

Department of Radiation-Applied Biology Research, TARRI, QST

Introduction

Pheochromocytomas (PCCs) are rare neuroendocrine tumors with malignant progression. Clinical improvement of malignant PCCs with β-emitting *meta*-^{131}I-iodobenzylguanidine (^{131}I-MIBG) constitutes a stage of partial remission in metastatic PCC [1]. Recently, we reported strong anti-tumor effects of α-emitting *meta*-^{211}At-astatobenzylguanidine (^{211}At-MABG) in a PCC mouse model, suggesting a potential option for targeted α therapy (TAT) for patients with malignant PCC [2]. We also found that the gene expression profiles of cell cycle checkpoints displayed similar modes of cell death via the p53-p21 signaling pathway after ^{211}At-MABG treatment and γ-ray irradiation [3]. This p53-dependent pathway would induce reproductive cell death, *e.g.* cell cycle arrest. However, we have not yet checked for reproductive cell death in pheochromocytoma (PC12) cells by colony formation assays because PC12 cells showed strong aggregation. Here we employed the soft-agar colony formation assay of PC12 cells by modifying the previously reported method [4].

Materials and methods

Cell culture. PC12 cells were cultured in RPMI1640 medium (Wako, Osaka, Japan) supplemented with 5% v/v fetal bovine serum (FBS), 10% horse serum (HS), 100 U/ml penicillin and 100 μg/ml streptomycin in a humidified 5% CO_2, 37ºC incubator.

Cell irradiation. PC12 cell suspension was irradiated by ^{60}Co γ-rays at the absorbed dose of 10 Gy.

Cell detachment. Several ml volume of PC12 cell suspension was centrifuged at 200 rcf for 3 min, and supernatant was removed. Cell pellet was gently resuspended in 1 ml accutase (Nacalai tasque, Kyoto, Japan), and incubated for 30-40 minutes in a humidified 5% CO_2, 37ºC incubator.

Remove small aggregates. Detached cells were placed on 10 μm and 15 μm double-layered cell strainers to remove small aggregates fromsingle cells.

Cell count. Passed cells through cell strainer were manually counted under microscope with a Burker-Turke hemocytometer equivalent to 10^4 cells/ml.

Soft agar colony formation assay. Passed single cells through the cell strainers were diluted to obtain appropriate number of colonies after culture in a soft agarose. Cells were suspended in the RPMI1640 medium with 0.3% w/v agar and the cell suspension was overlaid onto the RPMI1640 medium with 0.7% bottom agar in 6-cm dishes. Cells were allowed to grow for 4-5 weeks at the 5% CO_2, 37ºC incubator. Finally, cells were stained with MTT (3-(4,5-dimethylthiazol-2-yl)-2,5-diphenyltetrazolium-bromide, Roche AB) for 1 hour and colonies were manually counted under the microscope.

Results

We carried out the basic examination of soft-agar colony formation assay for PC12 pheochromocytoma cells. First issue was the aggregation of PC12 cells. After 30-40 min incubation with accutase, we found over 80% detached PC12 cells and could count them by a microscope (Fig. 1 (a)). Next, we examined soft-agar colony formation of PC12 cells with or without γ irradiation (Figs. 1 (b) and (c)). 4-5 weeks after γ irradiation, we could observe a few PC12 colonies. Plating efficiency was about 0.25 at 0 Gy. A very dense and prominent morphology like corona virus was a characteristic of this colony. We will plan to apply this method to examine the cell-killing effect of ^{211}At-MABG treatment.

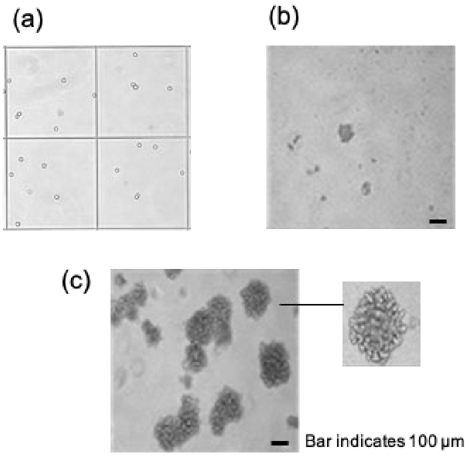

Fig. 1. Detached PC12 cells and colony formation. (a) Detached cells in a Burker-Turke hemocytometer. (b) Colonies of γ-rays irradiated PC12 cells. (c) Colonies without γ irradiation.

Acknowledgments

We would like to thank three students for their help, A.A.D.D. Castro, H. Mori and Y. Ohtsuka, who were students of 2019 summer school course at QST. We also would like to thank Prof. Y. Matsumoto of Tokyo Institute of Technology for his advice of soft-agar colony assay.

References

[1] J.A. Carrasquillo *et al.*, Semin. Nucl. Med. **46**, 203 (2016).
[2] Y. Ohshima *et al.*, Eur. J. Nucl. Med. Mol. Imaging **45**, 999 (2018).
[3] Y. Ohshima *et al.*, Theranostics **9**, 1538 (2019).
[4] J. Geli *et al.*, Endocrine-related Cancer **14**, 125 (2007).

2 - 23

Immuno-PET Imaging for Non-invasive Assessment of Cetuximab Accumulation in Non-small Cell Lung Cancer

A. Yamaguchi[a], A. Achmad[a], H. Hanaoka[a], A. Kanai[a],
Y. Sugo[b], N. S. Ishioka[b] and Y. Tsushima[a]

[a]Gunma University Graduate School of Medicine,
[b]Department of Radiation-Applied Biology Research, TARRI, QST

Introduction

Non-small cell lung cancer (NSCLC) remains a deadly cancer worldwide, even with advances in treatment strategies such as molecular targeted therapy and immunotherapy. Overexpression of epidermal growth factor receptor (EGFR) is one of the characteristics of NSCLC, which makes anti-EGFR drugs an attractive therapeutic option for this cancer. Molecular imaging with radiolabeled antibodies, including immuno-positron emission tomography (PET) imaging, can provide quantitative information about antibody uptake at a whole-body level in a non-invasive fashion.

In this study [1], we evaluated the usefulness of ^{64}Cu-DOTA-cetuximab for the selection of EGFR-overexpressing NSCLC tumors using xenograft mouse models with human NSCLC cell lines having various EGFR protein expression levels.

Experimental

Lung tumor xenografts were prepared by subcutaneous injection of 5×10^6 cells in 100 μL PBS suspension in the dorsal flank of the mice in awake. The EGFR expression levels of NSCLC tumors were determined by *ex vivo* immunoblotting according to the procedure previously described [2].

Copper-64 (150–300 MBq) was produced on a cyclotron *via* ^{64}Ni(*p,n*)^{64}Cu nuclear reaction. For ^{64}Cu-labeling, DOTA-cetuximab was dissolved in sodium acetate buffer and then added to the dried $^{64}CuCl_2$. The resulting mixture was incubated for 1 h at 40 °C. Purification of ^{64}Cu-DOTA-cetuximab was carried out using PD-10 desalting column.

To study PET usefulness for the assessment of EGFR expression level *in vivo*, xenografts of lung cancer cell lines were intravenously injected with 2–20 MBq ^{64}Cu-DOTA-cetuximab *via* the tail vein in awake. Considering the pharmacokinetics of monoclonal antibody and the physical half-life of ^{64}Cu (12.7 h), PET images were taken 48 h after injection.

Results and Discussion

The whole-body distribution and tumor-targeting efficiency of cetuximab was visualized non-invasively using small-animal PET imaging at 48 h after injection of ^{64}Cu-DOTA-cetuximab in mice with NSCLC xenografts. As shown in Fig. 1, PET imaging clearly depicted the high uptake of ^{64}Cu-DOTA-cetuximab in HCC827 xenografts, which highly overexpress EGFR.

Figure 2 shows the relationship between tumor ^{64}Cu-DOTA-cetuximab uptake and EGFR expression levels which were normalized over EGFR-null control H520. A strong correlation was found between tumor uptake of ^{64}Cu-DOTA-cetuximab and adjusted EGFR band density.

This study has demonstrated that cetuximab uptake in NSCLC tumors can be assessed by PET using ^{64}Cu-labeled cetuximab. Significantly high uptake of ^{64}Cu-DOTA-cetuximab was noted in NSCLC tumors with very high EGFR expression levels compared to tumors with medium or low EGFR expression levels.

These results suggest the potential usefulness of cetuximab immuno-PET for non-invasive prediction of cetuximab uptake in NSCLC.

References

[1] A. Yamaguchi *et al*., BMC Cancer **19**, 1000 (2019).
[2] A. Achmad *et al*., Canc. Sci. **103**, 600 (2011).

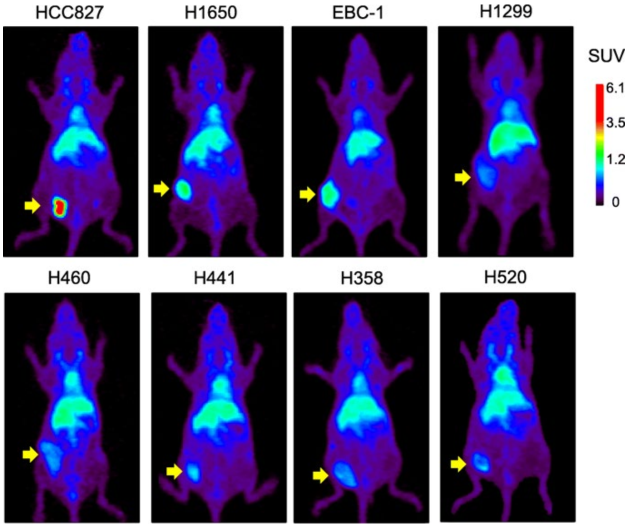

Fig. 1. Representative ^{64}Cu-DOTA-cetuximab PET images in mice xenograft models with NSCLC tumors with varying EGFR expression levels at 48 h. Arrows indicate the location of tumors.

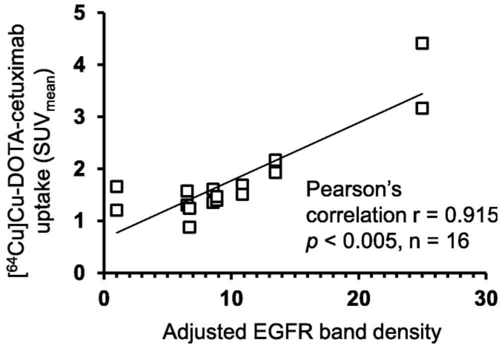

Fig. 2. Correlation between EGFR expression and tumor uptake of ^{64}Cu-DOTA-cetuximab.

2 - 24

Evaluation of the Cooling Effect by He Gas for the Production of ^{211}At with a Bi Plate

S. Watanabe[a], M. Koka[b], K. Enomoto[b], N. Miyawaki[a),c)], T. Sakashita[a],
I. Sasaki[a] and N. S. Ishioka[a]

[a] Department of Radiation-Applied Biology, TARRI, QST,
[b] Beam Operation Co., Ltd.,
[c] Department of Advanced Radiation Technology, TARRI, QST

Astatine-211 (^{211}At) with 7.21 hours of half-life is one of the promising alpha-emitting radionuclides for the targeted alpha therapy (TAT), internal radiotherapy using alpha emitting radioisotopes [1]. ^{211}At is basically produced by irradiating He beams with 28–29 MeV to a bismuth (Bi) target. Irradiations with high beam current (μA order) are necessary to produce ^{211}At for preclinical and clinical studies because they require radioactivity of ^{211}At on the order of subGBq to GBq. Low melting point of Bi (273.1°C) often causes melting of the Bi during irradiation with high beam current. We have produced ^{211}At by using a Bi plate as a target in TIARA. We used to irradiate the Bi plate with 3.5 μA of beam current without Bi melting. However, a Bi target was unfortunately melted by irradiation with 3.0 μA of beam current after updating the beam line for radioisotope production in 2019. As a result, long-time irradiation has to be needed to produce ^{211}At enough amounts for preclinical studies. The aim of this study is therefore to optimize irradiation condition without observing Bi melting.

A Bi target and its setup are illustrated in Figure 1. A Bi target (10 × 10 × 0.25 mmt) was used in this study. The Bi target (highlighted in red) and Al plate for degradation of incident energy (highlighted in blue) were set in a target holder. The incident energy was adjusted to 28–29 MeV. The target holder was cooled by He gas (front) and circulating water (back) during irradiations. He gas was passed through freezers (ice, ice/NaCl, and dry ice/ethanol). Irradiation time was 1 and 10 minutes. Produced radionuclides and their radioactivity were determined by high-purity germanium (HP-Ge) gamma-ray detector coupled with multi-channel analyzer.

In order to investigate cooling effect by He gas blowing to the front of the target holder, irradiations were performed by using He gas passed through three different freezers. Results of target condition after irradiation and production yield (defined as MBq/μA*h, radioactivity by irradiating with 1 μA of beam current for 1 hour) of ^{211}At are summarized in Table 1.

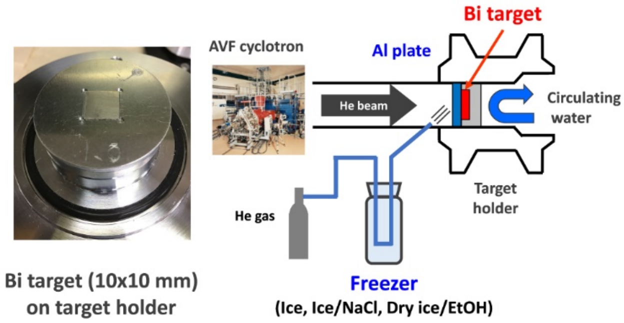

Fig. 1. Bi target (left) and target setup (right).

Table 1
Target conditions after irradiations and production yields (MBq/μA*h).

Freezer	None		Ice (- 0 °C)		Ice + NaCl (- 20 °C)		Dry ice + EtOH (-76.5 °C)	
Beam current	Melt	Production yield	Melt	Production yield	Melt	Production yield	Melt	Production yield
2.5 μA	No	14.6 ± 2.1	—		—		No	17.3 ± 4.9
3.0 μA	Yes	15.7 ± 3.0	Yes	14.2	Yes	14.3	No	18.4 ± 4.6
3.5 μA	Yes	17.6 ± 2.0	—		—		No	18.5 ± 2.6
4.0 μA	—		—		—		No	19.0 ± 0.45
4.5 μA	—		—		—		No	17.7 ± 2.3

The Bi target was melted by irradiation with 3.0 μA of beam current when He gas was not cooled and was passed through ice or ice/NaCl freezer. On the other hand, a Bi plate was not melted when He gas was passed through dry ice/ethanol under the same beam current. These results indicate that dry ice/ethanol are most effective to avoid melting the Bi target. Irradiations with higher beam current were performed by cooling the target with He gas passed through dry ice/ethanol. As a result, the target was not melted when irradiating with 4.5 μA of beam current. Production yield was 17.7 ± 2.3 MBq/μA*h in this case. Since the highest beam current was 2.5 μA in case of no freezer, 3 hours were required to produce over 100 MBq of ^{211}At. On the other hand, almost the same amount of ^{211}At as those with no freezer was successfully obtained by irradiation for 1.5 hours when He gas was passed through dry ice/ethanol. Improvement of He gas cooling allowed us to obtain enough amounts of ^{211}At for preclinical studies with shorter-time irradiation. We are continuing to make efforts for the further improvement of irradiation conditions such as the use of beam scanning.

Acknowledgments

We are grateful to Dr. Satoshi Watanabe, Mr. Koji Imai, and staff of TIARA for operating the AVF cyclotron.

References

[1] D.S. Wilbur, Nat. Chem. **5**, 246 (2013).

2 - 25 Application of OpenPET as 3-D Imaging Device of Carbon Distribution in Fruit

K. Kurita[a], Y. Miyoshi[b], Y. Nagao[b], M. Yamaguchi[b], N. Suzui[b], Y.-G. Yin[b], S. Ishii[b],
N. Kawachi[b], K. Hidaka[c], E. Yoshida[d], S. Takyu[d], H. Tashima[d] and T. Yamaya[d]

[a]Materials Sciences Research Center, JAEA,
[b]Department of Radiation-Applied Biology Research, TARRI, QST,
[c]Kyushu Okinawa Agricultural Research Center, NARO,
[d]Dept. of Advanced Nuclear Medicine Sciences, NIRS, QST

Research on the distribution and dynamics of photoassimilates in plants, especially those in fruits, is important for improving food production. Positron emission tomography (PET) and using carbon-11 (^{11}C) are valuable to obtain 3-D images of photoassimilates. For plant experiments, however, it is important to adjust a system to plant's growth environment. General PET devices, even small-animal PET devices, are not suitable for plant studies for the following reasons. First, the conventional PET devices are too large to be contained within a growth chamber. Second, even though it is often important to visualize the vertical movements of elements or molecules in plants, the general PET devices are operated horizontally. This can be solved by using a small OpenPET prototype which is a compact PET device that has an open space in its field of view (FOV) [1]. In this work, we upgraded the OpenPET system for the PET study of fruits and successfully realized the 3-D imaging of a photoassimilate labeled with $^{11}CO_2$ in a fruit of a strawberry plant. The small OpenPET prototype, which is shown as a schematic shown in Fig. 1(a), is a compact PET device that can visualize a variable open space between two detector rings [2-3]. The two black rings are detector rings covered with a thin metal cover, with an inner diameter of 110 mm. The axial imaging FOV is adjustable; 99 mm in case of no open space and 126 mm in case of the maximum open space.

For plant experiments, it is important to adjust the environment around a target plant because the physiological functions of plants are strongly influenced by environmental conditions. The OpenPET is compact (approximately 55 cm long, 35 cm wide and 40 cm tall), and can be set in a small-capacity growth chamber. Also, it has LGSO ($Lu_{0.4}Gd_{1.6}SiO_5$: Ce) as the scintillator, which is not a deliquescent material. Thus, the OpenPET can be used in plant growth environments with high temperature and high humidity. Meanwhile, vertical movements of elements or molecules in plants are often important in studies on physiological functions because many plants grow vertically. The original OpenPET was designed for the use in a horizontal setup, which is similar to a conventional PET device. Here, the OpenPET was technically upgraded for plant studies. Figure 1(b) shows an example of a fruit imaging setup using the upgraded OpenPET. It can be set up either vertically or horizontally by mounting it on a supporting base unit. This improvement facilitates setting a fruit into the FOV properly.

To examine the reliability of ^{11}C imaging in fruits, an imaging experiment was performed with an intact strawberry plant (*Fragaria* × *ananassa* Duch. cv. Fukuoka S6). The $^{11}CO_2$ gas produced with a compact cyclotron in the TIARA was fed to the fourth leaf of the strawberry plant. The secondary fruit was set up at the center of the FOV of the OpenPET through the hole of the detector rings, and PET data were measured for 2.5 h.

Figures 2(a, b) show slices of the 3-D PET image of the strawberry fruit for 165-190 min after the $^{11}CO_2$ feeding and a time-activity curve of the ^{11}C in the fruit, respectively. Figure 2(a) shows that the photoassimilates were accumulated in a part of the fruit. In addition, Fig. 2(b) indicates that the OpenPET images enable us to conduct kinetic analysis of the influx of the ^{11}C-labeled photoassimilate into the strawberry fruit. From these results, we confirmed that the OpenPET was a device suitable for research of the physiological functions of the photoassimilates in plants with fruits.

References

[1] K. Kurita *et al.*, Nucl. Instrum. Meth. Phys. Res. A **954**, 161843 (2020).
[2] T. Yamaya *et al.*, Phys. Med. Biol. **56**, 1123 (2011).
[3] E. Yoshida *et al.*, Radiol. Phys. Technol. **5**, 92 (2012).

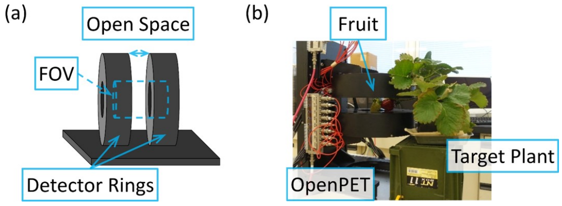

Fig. 1. (a) Schematic of the compact OpenPET prototype. (b) Example of a fruit imaging setup using the upgraded OpenPET.

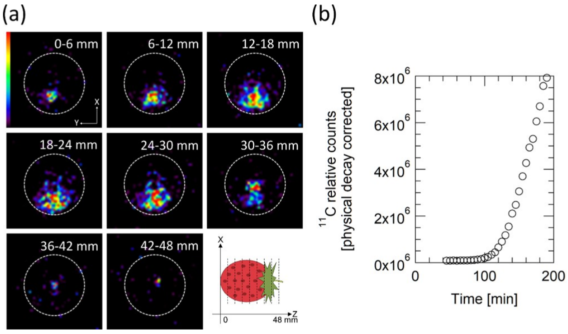

Fig. 2. (a) Tomograms of frames of the 3-D PET imaging of the strawberry fruit 165-190 min after feeding $^{11}CO_2$. (b) Time-activity curve of ^{11}C in the strawberry fruit.

2 - 26

Study on Aluminum Detoxification Mechanism of Tea Plants (*Camellia sinensis*) by Measuring Trace Element Distribution of Tea Leaves

K. Yasuda[a], K. Yasuda[a], M. Koka[b], N. Yamada[c], R. Yamagata[c] and N. Kawachi[d]

[a]Department of Informatics and Environmental Science, Kyoto Prefectural University,
[b]Beam Operation Co., Ltd.,
[c]Department of Advanced Radiation Technology, TARRI, QST,
[d]Department of Radiation-Applied Biology, TARRI, QST

Although aluminum is toxic to plants, tea accumulates aluminum in high concentrations. The mechanism for detoxifying aluminum has not yet been clarified, but it is presumed that it forms a compound with other elements to detoxify it. Research is progressing to elucidate the mechanism that makes aluminum harmless, and it has been pointed out that it is possible to make other elements and compounds harmless. Fluorine has been pointed out as one of the elements forming the compound. In this study, the micro-PIXE (particle-induced X-ray emission) / PIGE (particle-induced gamma-ray emission) method was used to measure the elemental distribution of aluminum and fluorine in tea leaves, and the possibility of aluminum and fluorine forming compounds was investigated.

Three types of tea leaves, Samidri, Asahi, and Yabukita, which were collected at Kyoto Prefectural Tea Research Institute and had a growth period of 1 year or more, were used as samples. The tea leaves were cut to a thickness of 120 μm in the vertical direction of the vein using a microtome (Plant Microtome MTH-1), and freeze-dried for 4 hours. Micro-PIXE/PIGE measurements were performed using a microbeam line at TIARA, QST. A 3-MeV proton microbeam was irradiated to the cross section of the tea leaf. Characteristic X-rays and γ-rays from a $^{19}\mathrm{F}(p,\alpha\,\gamma)^{16}\mathrm{O}$ reaction were detected with Si(Li) and NaI detectors, respectively. A beam size was about 1 μm x 1 μm, and beam current was 50 ~ 70 pA during the measurement.

Figure 1 shows the elemental distributions of Al and F in the surface epidermis obtained by measuring the Samidori sample. The area around 10 μm on the horizontal axis corresponds to the epidermis. It can be seen that Al is localized in the cell wall of epidermal cells. F is also distributed on the boundary of epidermal cells, but it seems to have a different distribution from Al. In order to investigate the difference in distribution in more detail, a line distribution was created by projecting these two-dimensional element distributions along the horizontal axis (Fig. 2). This figure shows that Al has a peak at 10 μm. On the other hand, F has a peak at 13 μm, which is different from the position of the Al peak. In the F line distribution, a peak is seen near 25 μm, however not in Al. This indicates that the distributions of Al and F are not perfectly aligned. The primary reason for the discrepancy in distribution is that the distribution of F in epidermal cells is different from that of Al, however X-ray attenuation may also be involved. The energy of Al K_αX-ray is 1.49 keV. Considering the thickness of the cell and the attenuation of the X-ray, the Al K_αX-ray from the cell located deeper than the sample surface cannot be measured. That is, for Al, only cells on the sample surface are observed. On the other hand, the energy of γ-rays from F is high at 6 to 7 MeV, and there is almost no attenuation inside the sample, so γ-rays emitted deeper than the sample surface can also be detected. The thickness of the sample used in this measurement is 120 μm, which corresponds to the thickness of several cells, and we cannot exclude the possibility that we are observing several cells on top of each other with respect to F. A more detailed discussion of F distribution in the cell would require measurements on thinner samples.

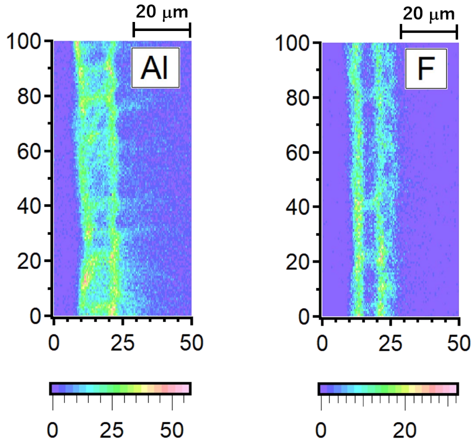

Fig. 1. Two-dimensional elemental distribution of Al (left), and F (right) near epidermal region obtained with a Samidori sample.

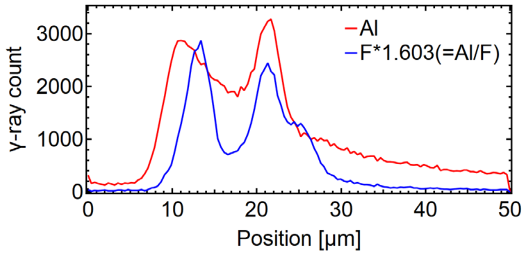

Fig. 2. Line distributions of Al (black) and F (blue) near epidermal region.

2 - 27 Identification of Multi-element Accumulation Mechanism in Legume

J. Furukawa[a)], N. Suzui[b)], Y.-G. Yin[b)], K. Kurita[b)], M. Koka[c)], N. Yamada[c)], R. Yamagata[c)],
N. Kawachi[b)] and T. Satoh[c)]

[a)] Life and Environmental Sciences, University of Tsukuba,
[b)] Department of Radiation-Applied Biology Research, TARRI, QST,
[c)] Department of Advanced Radiation Technology, TARRI, QST

Plants need various elements for its growth. Not only major elements, such as nitrogen, phosphorous and potassium, but many essential trace elements are needed for plant development. The analysis of trace element content and localization in the focused organ or tissue is important to identify its functions. Especially, under some stress conditions, information about the localization of trace elements in the tissue level is highly valuable for investigating where the deficiency or toxicity of elements is perceived and how to control the mechanisms for keeping homeostasis of plant body. Micro-PIXE (Particle Induced X-ray Emission) method can detect multi-element distributions in the same sample and visualize those localizatons with high-resolution images [1, 2, 3]. As for the element behavior induced by its deficiency or excess, the regulations of the activities in root mineral uptake and/or root to above ground part, shoot, translocation are well observed. Therefore, we combined the PETIS (Positron Emitting Tracer Imaging System) technique, which has a huge advantages in measureing element translocation in plants [4, 5], with Micro-PIXE. In this study, iron (Fe) localization in the roots and zinc (Zn) translocation activity of *Lotus japonicus* were focused. Because, Fe and Zn transfer is closely related in some uptake steps. *L. japonicus* is a model legume and its two experimental lines, MG-20 and B-129, have a diversity in some metal concentrations including Fe, Ni, Cu and Zn in seed [6].

In the comparison of two cultivars of *Lotus japonicus*, MG-20 and B-129, it was suggested that B-129 had a low activity of iron translocation from root to shoot. To clarify the difference of iron transport mechanism, atmospheric Micro-PIXE analysis was carried out using their root tissues. As for the preparation of PIXE imaging, root samples were embedded in the compound for a freeze sectioning and sliced to 20-100 µm sections by freezing microtome and then pasted on the polycarbonate film for 3 MeV H$^+$ beam exposure. The iron accumulation was well observed around the vascular bundle tissue in B-129 root. The vascular specific localization patterns suggested the iron transport was suppressed at the step of xylem loading of iron. To confirm the effect of this deficit of Fe homeostasis on the multi-element accumulation observed in B-129, Zn behavior was investigated under several Fe nutrition conditions using PETIS system. After 7 days cultivation of MG-20 and B-129 with hydroponics using 1/10 Hoagland's solution, plants were transplanted to Fe deficient (1/10 Fe) and Fe excess (10X Fe) solutions for 3 weeks and then subjected to PETIS measurements. In our previous experiments using four-day-treated samples, low Fe sample showed high Zn uptake and high Fe treatment induced the suppression of Zn uptake in B-129. However, in this three-week-treated samples experiment, high Fe concentration treatment showed active Zn translocation from root to shoot in B-129 (Fig. 1). These results suggest Fe condition in the plant body also regulates Zn uptake and translocation activities in *Lotus japonicus*, especially in B-129. For identifying responsible mechanisms in these different Zn behaviors, gene expression analysis involved in Zn uptake and translocation are under investigation.

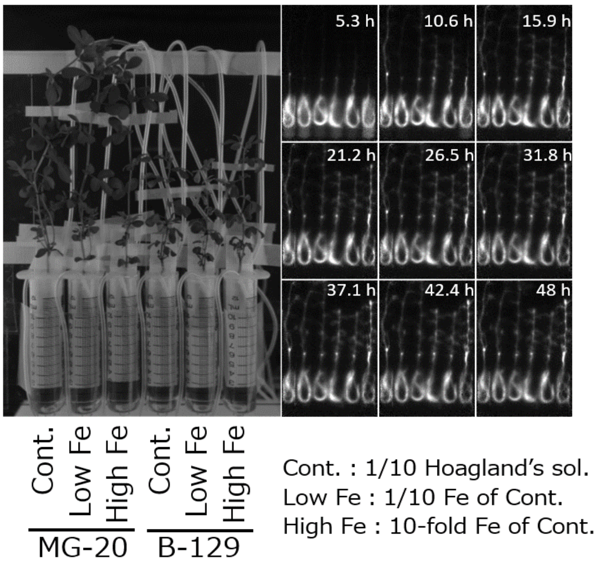

Fig. 1. Real-time ^{65}Zn localization images obtained by PETIS. Six plants and solution containers are observed in each frame and the samples are MG-20s (Control, 1/10 Fe, 10 × Fe) to B-129s (Control, 1/10 Fe, 10 × Fe) from left to right. Each plant was treated with indicated solution for 3 weeks before the PETIS measurement.

References

[1] T. Yamamoto *et al.*, JAEA Takasaki Annu. Rep. 2014, **JAEA-Review 2015-022**, 88 (2016).
[2] Y. Noda *et al.*, QST Takasaki Annu. Rep. 2015, **QST-M-2,** 151 (2017).
[3] N. Suzui *et al.,* RADIOISOTOPES **68**, 643 (2019)
[4] N. Suzui *et al.*, Plant Methods **13**, 40 (2017)
[5] N Suzui *et al.*, Quantum Beam Sci. **3**, 18 (2019)
[6] M.A. Klein and M.A. Grusak, Genome **52**, 677 (2009)

2 - 28

Elucidation of Cesium Transport Behavior in Soybean Root System

M. Igura[a], N. Suzui[b], Y.-G. Yin[b], Y. Miyoshi[b] K. Enomoto[b], T. Satoh[c] and N. Kawachi[b]

[a]Institute for Agro-Environmental Science, NARO,
[b]Department of Radiation-Applied Biology, TARRI, QST,
[c]Department of Advanced Radiation Technology, TARRI, QST

Soybean shows higher nutrient uptake compared to other crops, and it has been suggested that symbiotic bacteria such as rhizobia are involved in element uptake. Elucidation of mechanism of cesium- and coexisting element-uptake in soybean root system is indispensable for development of radiocesium reduction technology of soybean. The purpose of this study is to clarify the distribution of radiocesium in roots and nodules of soybean and to elucidate the transportation route from the root system to the above-ground parts.

The Japanese soybean cultivar Enrei infected with the rhizobia (*Bradyrhizobium japonicum*) was cultivated for about one month by hydroponic culture. It is known that the amount of cesium uptake in soybean is strongly influenced by the concentration of coexisting potassium. Therefore, the potassium concentration in the hydroponic solution was reduced to 1/100 of the normal composition to acclimate to the low potassium concentration condition before the positron emitting tracer imaging system (PETIS) analysis. In this experiment, pulse-chase experiment was conducted to evaluate cesium absorption in the root system and radiocesium transport behavior to the stem. Positron-emitting cesium-127(^{127}Cs) was produced and purified in the Takasaki Ion Accelerators for Advanced Radiation Application (TIARA), applied to the soybean root system for 16 hours (pulse experiment), and then the hydroponic solution was replaced with another solution without ^{127}Cs (chase experiment).

As a result of real-time imaging analysis by PETIS, accumulation of ^{127}Cs was confirmed in roots and nodules, and remarkable accumulation was observed in nodules (Fig. 1). The ^{127}Cs signal of roots showed a decreasing tendency with time, and it was considered that ^{127}Cs decreased by transportation to the stem. It was confirmed that ^{127}Cs signal showed a similar decreasing tendency in nodules as roots in the strains with low cesium absorption, and it was suggested that nodules are also involved in radiocesium transport to the stem. On the other hand, ^{127}Cs signal in the nodules gradually increased when the root system abundantly absorbed ^{127}Cs. The increase of cesium signal in the nodules was considered to be due to translocation from the roots, suggesting that cesium was transferred between root and nodules. In addition, the elemental distribution in soybean roots and nodules by micro particle induced X-ray emission (microPIXE) analysis showed a difference in the distribution of cesium and potassium in each root and nodule [1]. It is considered that these show different roles of root and nodule inabsorption and accumulation of cesium/potassium.

In these real-time image analysis and elemental distribution analysis, radiocesium was significantly accumulated in the nodule tissue, and radiocesium transport between the root and the nodule was confirmed. These suggested that the nodule tissue is also involved in radiocesium supply to the above-ground plant parts.

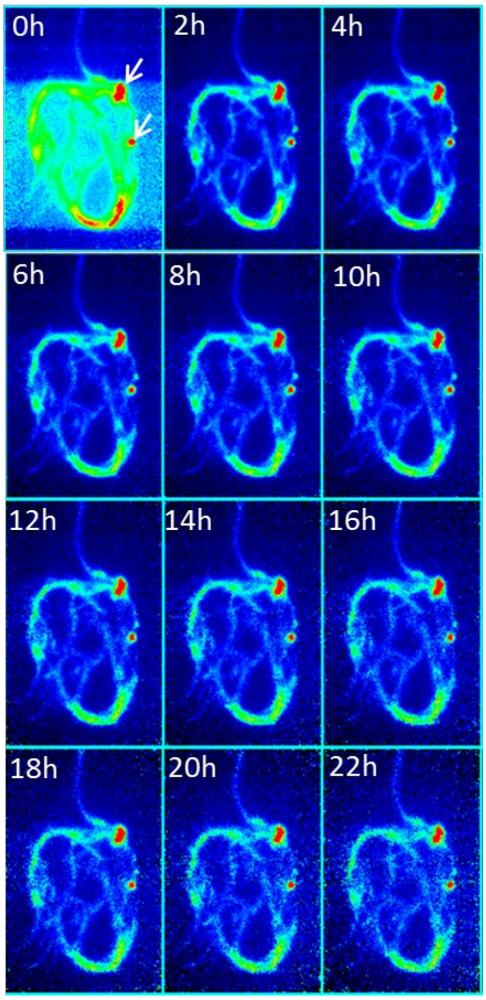

Fig. 1. Real-time imaging by PETIS on ^{127}Cs uptake in soybean roots and nodules (Chase experiment).
*White arrow indicates the position of nodules.

Reference

[1] M.Igura and T.Saito, “Elucidation of Cesium Transport Behavior in Soybean Root System”, QST Takasaki Annual Report 2018 **QST-M-23**, 95 (2019).

2 - 29

Estimation of Shifts of Therapeutic Carbon-Ion Beams Owing to Cavities in Target by Measuring Prompt X-rays

M. Yamaguchi[a], S. Yamamoto[b], M. Kitano[b], Y. Kubota[c], M. Sakai[c], T. Akagi[d],
Y. Nagao[a] and N. Kawachi[a]

[a]Department of Radiation-Applied Biology Research, TARRI, QST,
[b]Radiological and Medical Laboratory Sciences, Nagoya University Graduate School of Medicine,
[c]Gunma University Heavy Ion Medical Center, Graduate School of Medicine, Gunma University,
[d]Hyogo Ion Beam Medical Center

Particle-beam therapies have been established as radiation treatment with less damage to normal tissues because of its pinpoint-irradiation ability. However, if the irradiated beams shift due to anatomical changes in the patient's body, there is a risk of irradiating high doses to normal tissues. In order to detect such mis-irradiations, a new method based on measuring prompt X-rays, which mainly consist of secondary electron bremsstrahlung (SEB), was proposed [1-4]. In this work, we have evaluated an estimation ability of shifts of therapeutic carbon-ion beams owing to cavities in a polyethylene target using the method measuring prompt X-rays.

Beam irradiation experiments were performed at the Hyogo Ion Beam Medical Center (HIBMC). Figure 1 shows a diagram of the experimental setup. Carbon-12 beams having the energy of 241.5 MeV/u were irradiated on a polyethylene target consisting of high-density polyethylene plates (10.0 cm × 10.0 cm × 0.3 cm) stacked on a table. We prepared two types of plates: one was "perforated plate", which had a square-shaped (5.0 cm × 5.0 cm) central hole; and the other was "normal plate", which had no holes. The outer dimension of the target was 10.0 cm × 10.0 cm × 23.4 cm. The target had a square-prism-shaped cavity made by sandwiching a cavity layer. The cavity layer made of perforated plates between two layers made of normal plates. The thickness of the cavity layer was changed from 3.0 cm to 0.0 cm with 0.3-cm steps by exchanging perforated and normal plates. The number of the injected ions was 7.5×10^{10} for each setup of the cavity layers. Each irradiation time was 60 seconds.

An X-ray camera, named "YAP camera-S", was utilized to measure the SEB images. Details of the camera was explained in another paper [4]. The camera consists of a tungsten-alloy radiation shield and a Ce-doped $YAlO_3$ (YAP(Ce)) plate optically coupled to a high quantum efficiency cross-wire anode-type position sensitive photomultiplier tube (PS-PMT). The radiation shield had a wide-angle pinhole collimator on the front face of it. The camera was placed at the distance of approximately 44 cm apart from the beam axis.

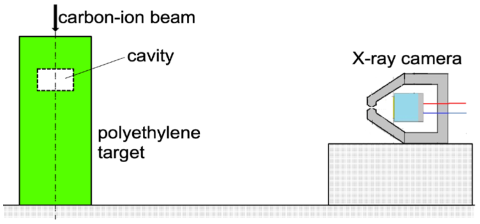

Fig. 1. A diagram of the experimental setup.

Acquired images are shown in Fig. 2(a)-(c). The beam trajectory and a gap on the trajectory in the targets clearly appeared for the image of 3-cm cavity. As the thickness of the cavity layer decreases, the end position of the trajectory seems to move up correctly and the gap on the trajectory seems to decrease correctly. Figure 2(d) shows correspondence between the cavity-layer thicknesses and the beam shifts estimated from the acquired images. The actual beam shifts well coincided with the estimated beam shifts and the maximum fluctuation of the estimated shifts was small, approximately 0.2 cm.

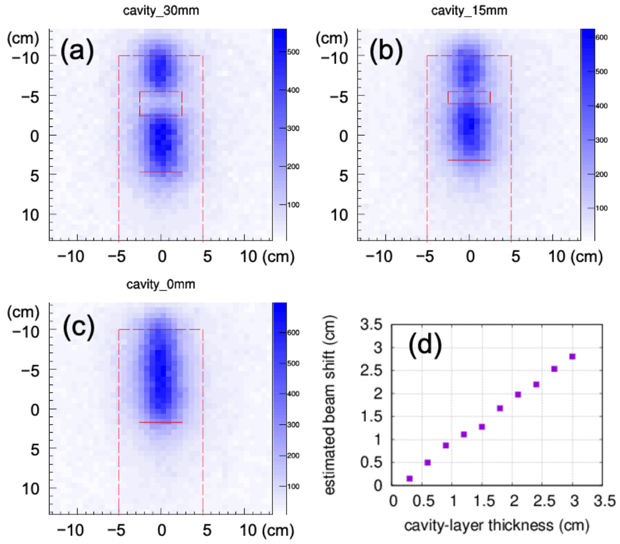

Fig. 2. Acquired prompt X-ray images for cavity thicknesses of (a) 3.0, (b) 1.5 and (c) 0.0 cm and (d) correspondence between the cavity-layer thickness and estimated beam shifts. The red dashed and solid lines in (a)-(c) represent the outlines of the targets and cavities and the Bragg-peak positions, respectively.

References

[1] M. Yamaguchi *et al.*, Nucl. Instrum. Meth. Phys. Res. A **833**, 199 (2016).
[2] K. Ando *et al.*, Phys. Med. Biol. **62**, 5006 (2017).
[3] M. Yamaguchi *et al.*, Phys. Med. Biol. **63**, 045016 (2018).
[4] S. Yamamoto *et al.*, Phys. Med. Biol. **65**, 105008 (2020).

2 - 30 Visualization of Photoassimilate Translocation in Oilseed Rape Plants by Using a Positron-Emitting Tracer Imaging System

S. Nakamura[a], N. Suzui[b], Y.-G. Yin[b], S. Ishii[b] and N. Kawachi[b]

[a]Faculty of Life sciences, Tokyo University of Agriculture,
[b]Department of Radiation-Applied Biology Research, TARRI, QST

Roots in higher plants play an important role in plant survival. In order to survive under various environmental conditions, plants secrete various substances from their roots to function in the rhizosphere. The source of these materials secreted from roots is the photosynthetic products transported to the roots via phloem. To elucidate the mechanisms of their transport via phloem and to control them will help to improve crop productivity. Recently, Yin et al. reported that C-11 was rapidly translocated to their roots and secreted into the rhizosphere in leguminous plants such as soybean and lupin plants [1]., In this study, we attempted to compare the behaviors of photosynthetic products in oilseed rape plants with that of leguminous plants using positron emitting tracer imaging system (PETIS).

We conducted noninvasive imaging experiment using oilseed rape plants (*Brassica napus*) as described previously [2] with small modification. $^{11}CO_2$ gas tracer was produced at TIARA and fed to the leaves of an oilseed rape plant. The dynamics of C-11 in the intact plant was monitored by PETIS every 10 s for 150 min.

Figure 1 shows serial images of C-11 distribution in the oilseed rape plant. Regions of interests (ROIs) were set in the stem (about halfway between the point where the petiole branches and the shoot base) (ROI-1) and the shoot base (ROI-2). Time course of ^{11}C-radioactivity (Time-Activity Curve: TAC) in each ROI was generated from the serial images (Fig. 2). There was a difference in the onset of signal accumulation between the stem and the shoot base. The intensities of the signals in both ROIs reached almost identical at 120 minutes after the start of $^{11}CO_2$ absorption into the leaves of oilseed rape plants. The result indicates that the rate of carbon translocation in oilseed rape plant was much slower than in leguminous plants. Future analysis of obtained imaging data will provide clues to elucidate the molecular mechanisms of material secretion in root.

References

[1] Y.G. Yin *et al.*, Sci. Rep. **10**, 8446 (2020).
[2] N. Kawachi *et al.*, Nucl. Instrum. Meth. Phys. Res. A **648**, S317 (2011).

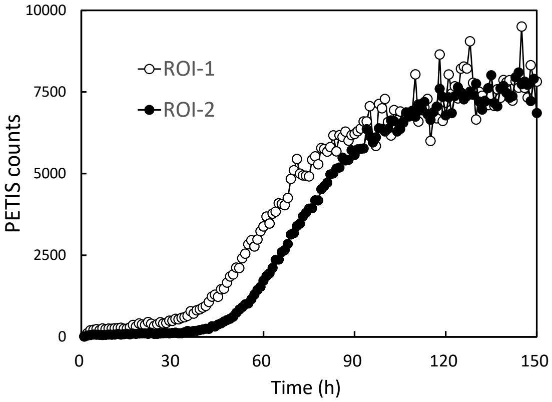

Fig. 2. Typical Time-Activity Curves in ROI-1 (the base of stem) and ROI-2 (the shoot base).

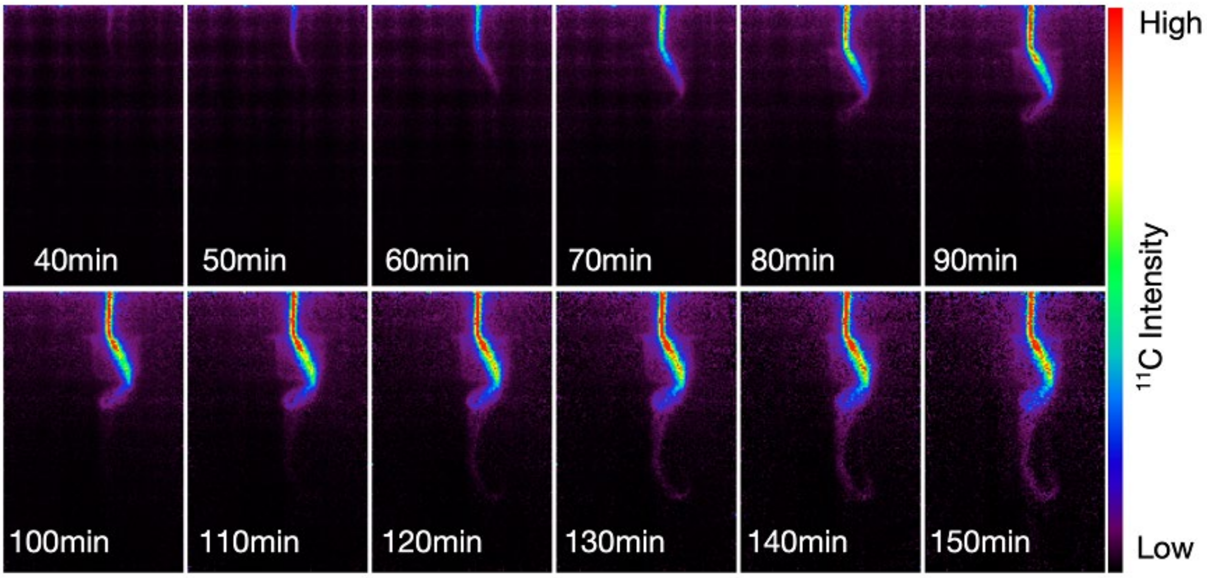

Fig. 1. Serial images of ^{11}C distribution in the root area of oilseed rape plant. Each image comes from the integration of 60 original images collected every 10 s.

2 - 31

Effects of Titanium Fluoride to Inhibition of Demineralization and Distribution of Elements

K. Okuyama[a], Y. Matsuda[b], H. Yamamoto[c], K. Naito[c], M. Sakurai[b], T. Saito[b],
M. Hayashi[c], Y. Tamaki[a], T. Satoh[d] and N. Yamada[d]

[a]Asahi University School of Dentistry,
[b]School of Dentistry, Health Sciences University of Hokkaido,
[c]Graduate School of Dentistry, Osaka University,
[d]Department of Advanced Radiation Technology, TARRI, QST

Introduction

The previous report said that lower pH of titanium fluoride (TiF_4) solution made distribute more fluorine (F) and titanium (Ti) into the tooth structure when the tooth was applied with various pH of TiF_4 and subjected pH cycling for 8 weeks [1]. The purpose of this study is to evaluate the distribution of fluorine and titanium, and lesion depth of the specimen after a long period of pH cycling.

Materials and methods

Extracted human teeth were sliced (300 μm thickness) longitudinally, coated with wax except for buccal dentin surface. Specimens were performed on pH cycling (pH 4.5 and 7.0, 6 cycles/day; simulate oral condition) for 20 weeks to prepare artificial carious dentin. During this cycle, specimens were soaked into 1% TiF_4 solution adjusted to pH 4(P4), 5(P5), 6 (P6), unadjusted solution (pH 1: P1), or 1.35% (same as fluoride concentration of 1% TiF_4) NaF for 5 min once a week. Control (Cont) involved no fluoride application during test periods. After cycling, calcium, F, and Ti distribution were analyzed by an in-air micro-PIXE/PIGE system with a 1.7-MeV $^1H^+$ microbeam at TIARA [1]. Then the cumulative concentration of F or cumulative contents of Ti in each specimen was calculated as an area of 100 μm from the defined surface [1]. Each specimen was observed with a polarizing microscope, and then the lesion depth of each specimen was measured. The obtained data ($n = 8$) were analyzed by a Kruskal–Wallis test and Steel–Dwass test ($\alpha = 0.05$).

Results

Figure 1 or 2 shows the distribution of F or Ti, respectively. P1 indicated the highest value of F or Ti among all groups. For F distribution, there was no significant difference between P4, P5, P6, and NaF. Cont had lowest F. For Ti distribution, P4 and P5 indicated higher value than P6. NaF showed a significantly lower value of Ti than all TiF_4 solutions, and no significant difference compared with Cont. Figure 3 shows the lesion depth of each group. P1 indicated lower depth than that on NaF, and Cont indicated higher depth than that on fluoride-treated groups.

Discussion

Low pH (P1) solution indicated higher F or Ti distribution than another pH of TiF_4 because dentin was more demineralized and then larger amounts of elements infiltrated into dentin. Higher F or Ti may contribute with lower lesion depth than NaF or Cont, however, P1 showed no significant F than NaF. Ti might have an ability to the prevention of demineralization. Among P4, P5, and P6, the distribution of Ti showed a significant difference, but there was no difference of F because of the difference of atomic size on Ti and F. It is suggested that the TiF_4 solution may be expected to caries inhibition compared with NaF.

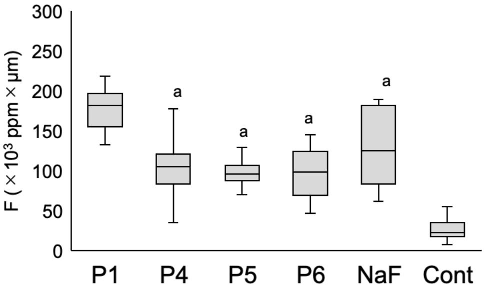

Fig. 1. Concentration of penetrated fluorine into dentin at 100 μm depth area from superficial surface (ppm × μm). Same letters no indicate significant differences ($p > 0.05$).

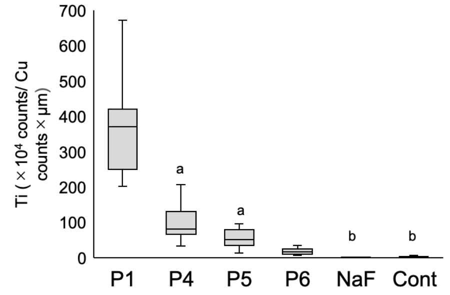

Fig. 2. Concentration of penetrated titanium into dentin at 100 μm depth area from superficial surface (10^4 counts/Cu counts×μm). Same letters no indicate significant differences (p>0.05).

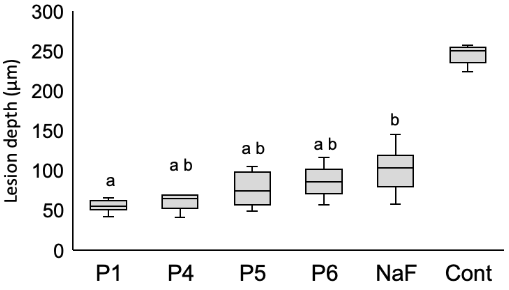

Fig. 3. Lesion depth of each specimen (μm). Same letters no indicate significant differences ($p > 0.05$).

Reference

[1] K. Okuyama *et al.*, QST Takasaki Annu. Rep. 2018, **QST-M-23**, 100 (2020).

2 - 32

Application of Micro-PIXE/PIGE Analysis for Two Biological Researches: Boron Analysis for Neutron Capture Therapy, and Targeted Anticancer Drug Delivery Directed by Radiation

S. Harada[a], K. Nakai[b], E. Sakurai[c] and T. Satoh[d]

[a] School of Medicine, Iwate Medical University,
[b] School of Medicine, University of Tsukuba,
[c] Faculty of Pharmacy, Iryo Sosei University,
[d] Department of Advanced Radiation Technology, TARRI, QST

We performed three studies to demonstrate useful applications of micro-particle-induced X/gamma-ray emission (micro-PIXE/PIGE) camera in biomedical research, aiming to improve cancer radiotherapy.

Study of the utility of micro-PIXE camera in boron neutron capture therapy (BNCT)

To investigate the utility of the micro-PIGE camera in BNCT, imaging of intra- and extracellular borocaptate sodium (BSH) in rat C6 and human U251 glioma cells was attempted in vitro. Micro-PIGE imaging was performed in TIARA by detecting the 2.124-MeV gamma-rays from $^{11}\mathrm{B}(p,p'\gamma)^{11}\mathrm{B}$. This time, the sensitivity of the micro-PIGE camera has been improved by changing the previous NaI(Tl) detector with a new HPGe detector providing high energy resolution. As a result, obtained superior images by detecting the 429-MeV gamma-rays from $^{10}\mathrm{B}(p,\alpha\gamma)^{7}\mathrm{Be}$ enable us assess the kinetics of B between intra- and extracellular in the U251 glioma cells (Fig. 1).

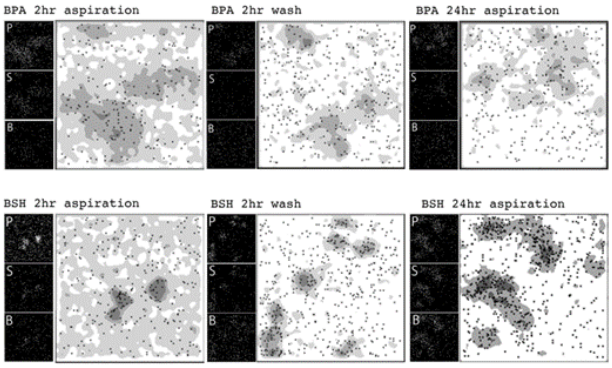

Fig. 1. Images of 10B in U251 glioma cells, obtained using a HPGe detector.

Study of targeted delivery of carboplatin using particles that release their contents upon radiation

To study the targeted delivery of carboplatin, the nanoparticles were prepared by spraying a mixture of hyaluronic acid and alginate; supplemented with carboplatin, into a solution of $CaCl_2$ and $FeCl_2$ through a 0.8 μm pore stainless mesh filter. The 1×10^{10} nanoparticles were injected intravenously into tumor model mice, which irradiated by 10 or 20 Gy of 100-keV soft X-ray when the nanoparticles were accumulated around the tumors with maximum 9 hours after injection. On subsequent irradiation, the accumulated nanoparticles (Fig. 2 A) released carboplatin (Fig. 2 B). The outer shells were gelatinized, prolonging the intratumoral localization of carboplatin and synergistically increasing the antitumor effect in combination with radiation (Fig. 3 A, B)[1].

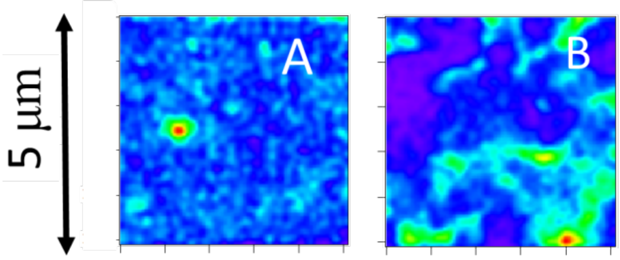

Fig. 2. Releasing of carboplatin from particles upon radiation.
A: Unirradiated particle.B: Irradiated particle

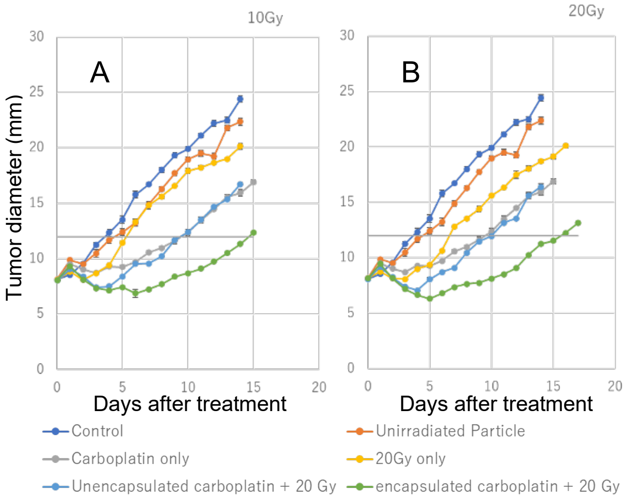

Fig. 3. Antitumor effect. A: 10 Gy, B: 20 Gy.

Reference

[1] T. Segawa *et al.*, Radiat. Res. **193**, 263 (2020).

2 - 33 Elemental Analysis of Collagen Vascular Disease-Associated Interstitial Lung Disease by In-Air Micro-PIXE

Y. Koga[a], T. Satoh[b], K. Kaira[c], M. Koka[b], N. Yamada[b], T. Hisada[d] and K. Dobashi[e]

[a] Department Respiratory Medicine, Gunma University,
[b] Department of Advanced Radiation Technology, TARRI, QST,
[c] Saitama Medical University International Medical Center,
[d] Gunma University Graduate School of Health Sciences,
[e] Jobu Hospital for Respiratory Diseases

Introduction

Collagen disease is a systemic disorder in which connective tissue abnormalities of systemic organs such as the skin, kidneys, lungs, and lymph nodes are caused by abnormal functions of the immune system. The cause of collagen disease has not been clarified yet, but it has been suggested that exposure to heavy metals and silica may be the cause of vasculitis and scleroderma. There is also a report that the concentration of silica in blood is high in patients with scleroderma. Therefore, we performed elemental analysis of surgically resected lung tissue complicated with collagen-vascular associated interstitial lung disease (CVD-ILD) by in-air micro particle induced X-ray emission (micro-PIXE) and compared the accumulated elements in the lungs between control and CVD-ILD lungs.

Materials and Methods

Video-assisted thoracic surgery (VATS) in 5 patients with CVD-ILD was performed at the Gunma University Hospital between 2008 and 2014 consecutively. Normal lung tissue sections resected from early-stage lung cancer patients (n=5) were analyzed as control lungs to compare the tissue elements in the CVD-ILD lungs. The surgically obtained paraffin-embedded lung tissue specimens were dissected and traced onto a polycarbonate membrane. The tissue section on a polycarbonate membrane was subjected to an in-air micro-PIXE analysis, as previously described [1]. Statistical analyses were performed using the GraphPad Prism. This study was conducted in accordance with the tenets of the Declaration of Helsinki and approved by the Gunma University Hospital Institutional Review Board (approval number: HS2020-049).

Results

In-air micro-PIXE detected various inorganic elements such as aluminum, magnesium, silicon, iron, and zinc. Relative ratio of these elements compared to sulphur was lower than those of calcium or phosphate (Fig. 1A). Interestingly, both silicon and zinc were significantly increased in the CVD-ILD lungs (Fig. 1B).

Discussion

Silicon and zinc were increased in the CVD-ILD lungs. Inhalation of inorganic elements may be partly involved with the pathogenesis of CVD-ILD.

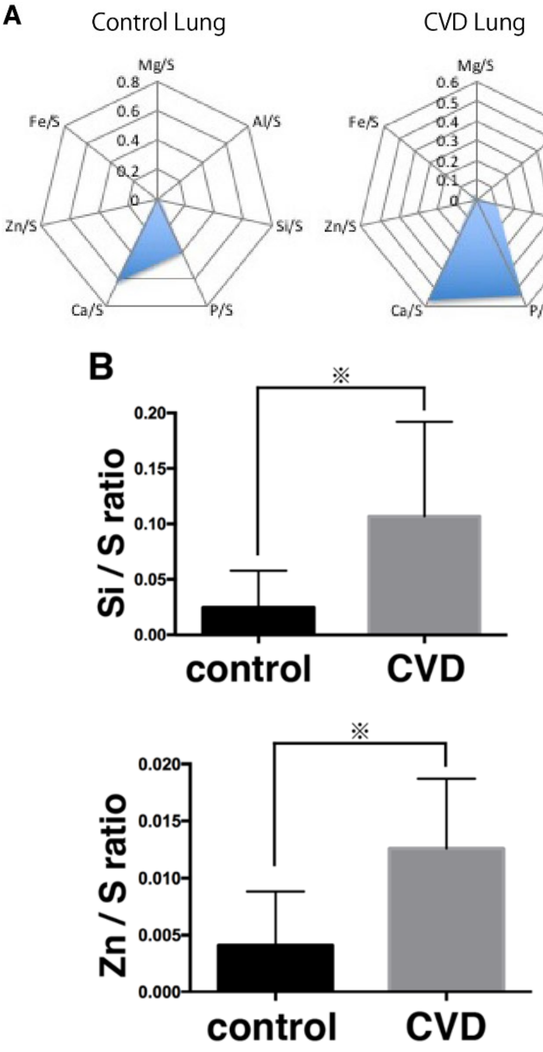

Fig. 1. Comparison of accumulated elements in the lungs between control (n=5) and collagen-vascular associated interstitial lung disease (CVD-ILD) (n=5) patients.
A: Rader chart of accumulated elements in the lungs of control (left) and CVD-ILD (right) patients.
B: Significant elevation of silicon (Si) and zinc (Zn) in the CVD-ILD lungs compared to the control lungs (※ $P<0.05$).

Reference

[1] Y. Koga *et al.*, Environl. Health. Prev. Med. **21**, 492 (2016).

2 - 34

Estimation of DNA Damage Localization of $^{40}Ar^{13+}$-irradiated DNA Using Fluorescence Anisotropy

K. Akamatsu, N. Shikazono and K. Satoh

Institute for Quantum Life Science, QST

Introduction

Ionizing radiation-induced DNA damage can cause mutation and carcinogenesis. In particular, “clustered damage”, that is a DNA region with two or more lesions within a few helical turns, is believed to be hardly repaired. This damage is considered to be induced around high-LET ionizing radiation tracks. However, detail of the damage is unknown. We have already developed a method for estimating localization of apurinic/apyrimidinic sites (APs) on DNA using fluorescence resonance energy transfer (FRET) occurring between different fluorescent dyes (Alexa350 and Alexa 488) (*hetero*-FRET). The FRET efficiency (E) was calculated from Alexa350 fluorescence intensities before/after enzymatic digestion of the labeled DNA with APs [1]. We succeeded in estimating qualities of clustered APs produced in $^{4}He^{2+}$-, $^{12}C^{5+}$-, and ^{60}Co γ-irradiated dry DNA film to study “direct” radiation effects using the method [2]. We also applied the method to aqueous DNA solution to study “indirect” radiation effects. However, there are some problems of the complex protocol and of the sensitivity due to the low extinction coefficient of Alexa350. We have, therefore, developed “*homo*-FRET” occurred between two or more Alexa488 molecules. We will obtain magnitude of FRET also from “fluorescence anisotropy” of *homo*-FRET between Alexa488 molecules [3]. The new protocol using *homo*-FRET enables us to estimate DNA damage localization without any enzymes and improves sensitivity to detect a clustered damage.

Experiments

●*Sample preparation and irradiation*

PUC19 digested by Sma I was used (linear formed) for DNA samples to be irradiated. The DNA was dissolved in 0.2 M Tris-HCl buffer (pH 7.5), which is a cell-mimetic condition, to be ~10 g/L. Eight microliters of the DNA solution was mounted on a 10 mmϕ glass plate (thickness: ~0.1 mm), and was irradiated with $^{40}Ar^{13+}$ (7.55 MeV/u, LET: ~1890 keV/μm, HY) at doses of 2, 5, 10kGy. Moreover, ^{60}Co γ-rays were also used as a standard radiation source at Kyoto University. In addition, as another reference, Fenton reagents-treated DNA was prepared.

●*Preparation of fluorophore-labeled irradiated DNA and FRET observation [3]*

The irradiated DNA (10 μL in water) and 10 μL of 100 mM Tris-HCl (pH 7.5) were mixed in a microtube. Two microliters of Alexa488/DMSO was added to the DNA solution and was incubated for 24 h at 35 °C. The fluorophore-labeled DNA was purified by ethanol-precipitation followed by ultrafiltration. The fluorescence anisotropy was measured at 525 nm (ex. 470 nm).

The anisotropy, $< r >$, is defined as follows:

$$< r > = (I_{VV} - G\cdot I_{VH}) / (I_{VV} + 2\cdot G\cdot I_{VH})$$

where I_{VV} is the fluorescence intensity when the excitation and emission polarizers are both vertically oriented. I_{VH} is one when the excitation/emission polarizers are vertically/horizontally oriented. G is the grating factor defined as I_{HV}/I_{HH}.

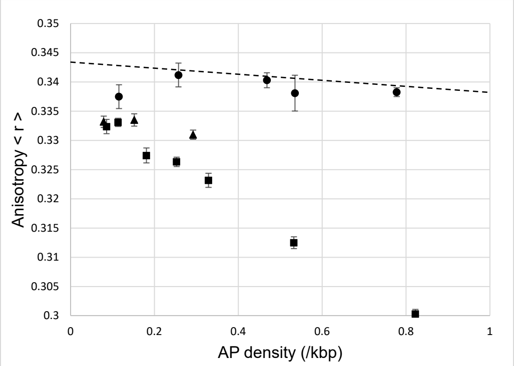

Fig.1. Fluorescence anisotropy of DNA irradiated with ^{60}Co γ-rays (●), $^{40}Ar^{13+}$ (▲), and of Fenton-treated DNA (■) as a function of averaged AP density. The broken line indicates a theoretical one when APs are randomly distributed on DNA.

Results and Discussion

Figure 1 shows relationships between averaged AP density and fluorescence anisotropy, <*r*>, for Ar ion, ^{60}Co γ-rays, and Fenton reagents- treated DNA. This indicates that <*r*> for Ar ion tends to form clustered AP lesions more than the γ-rays. <*r*> data of these two radiations seem to be almost constant within the range of AP density shown here. On the other hand, interestingly, Fenton-treated DNA is more likely to produce clustered lesions with increasing AP density in comparison to the others. However, these Fenton data imply that the cluster would not be formed at once (*e.g.*, by an OH radical) but sequentially.

Acknowledgments

We would like to gratefully thank Dr. Takeshi Saito of Institute for Integrated Radiation and Nuclear Science at Kyoto University for supporting ^{60}Co γ-ray irradiation.

References

[1] K. Akamatsu and N. Shikazono, Anal. Biochem. **433**, 171 (2013).
[2] K. Akamatsu *et al.*, Radiat. Res. **183**, 105 (2015).
[3] K. Akamatsu *et al.*, Anal. Biochem. **536**, 78 (2017).

2 - 35 Development of New Strains with Sporeless Mutation in Mushrooms Using Ion Beam Irradiation

M. Ishikawa[a], M. Takano[a], Y. Hase[b], S. Nozawa[c] and K. Ouchi[a]

[a]Mushroom Research Laboratory, Hokuto Corporation,
[b]Department of Radiation-Applied Biology Research, TARRI, QST,
[c]Department of Research Planning and Promotion, QuBS, QST

To develop novel strains of sporeless mutants, protoplasts derived from a commercial strain of *Pleurotus* sp. were irradiated with 50 MeV helium ion beam. As a result, two sporeless mutants were obtained with the dose of 50 Gy and 100 Gy. Frequency of sporeless mutation and other mutations suggested that 100 Gy was the proper dose to develop sporeless mutants with sufficient quality for commercial use.

きのこの胞子飛散は、商品の品質低下や栽培従事者の呼吸器疾患等の問題を起こす可能性がある。この問題を解決するため、イオンビーム照射により無胞子性品種を開発し、実用化を目指した。本研究では、ヒラタケ属品種「HOX 1 号」を供試体とし、無胞子性変異のスクリーニングおよび照射線量の検討を行った。

「HOX 1 号」子実体を酵素処理しプロトプラストを取得した。1.0×10^4 個/ml に調製したプロトプラストを寒天培地にのせ、軟寒天培地を加えて重層した。カプトンフィルムで密封した後、高崎量子応用研究所の AVF サイクロトロンにより発生させたイオンビーム（^{4}He^{2+}, 50 MeV）を 10 Gy-500 Gy の範囲で照射した。イオンビーム非照射培地における再生コロニー数に対する照射培地のコロニー数から生存率を算出した。再生コロニーを分離して子実体を発生させ、傘を黒紙上に置いて 20℃で一晩静置した後、胞子落下の有無を目視で確認した。「HOX 1 号」よりも胞子落下量が明らかに少ない菌株については栽培試験を反復して再現性を確認した上で、無胞子性変異体とした。また、無胞子性以外にも子実体の色や形態が「HOX 1 号」と明らかに異なる場合、その他変異体として変異率を算出した。本稿では、計 6 回の照射実験および栽培試験から得られた結果を報告する。

プロトプラスト生存率は、線量の増加に伴って低下した（Fig. 1）。各線量区から再生したコロニーを合計 11591 株分離し、現在までに 7457 株の栽培試験が終了している。その中で、2 株（No.81, 2074）の無胞子性変異体を取得した（Fig. 2）。これらの菌株は、「HOX 1 号」と比べて胞子落下量が顕著に少ない性質の再現性が確認できた。しかしながら、いずれの菌株とも栽培性や収量性には問題ないものの、背地性喪失を伴っていた。背地性喪失は、タモギタケ等の無胞子性変異体で報告のある形質であり、無胞子性形質と密接に連鎖していることも報告されている[1]。これにより、子実体の発生方向がばらつき、株の形状が元の品種である「HOX 1 号」とは異なり、販売する際の包装形態に合わないため、実用化には至らなかった（Fig. 2）。

栽培試験が終了した試験区について、生存率と変異体が得られた頻度との関係を示した（Table 1）。無胞子性変異体は生存率 41-60%の試験区のみで得られたが、子実体の色や形態に関するその他変異を併せた変異体取得率は生存率 31-40%で最も高かった。以上の結果より、無胞子性変異体を効率よく取得するためには、生存率 31-40%になるような線量すなわち 100Gy 付近で照射するのが良いと考えられた。今後は、栽培試験を継続し、背地性喪失を伴わない無胞子性変異体を取得し、実用化を目指したい。

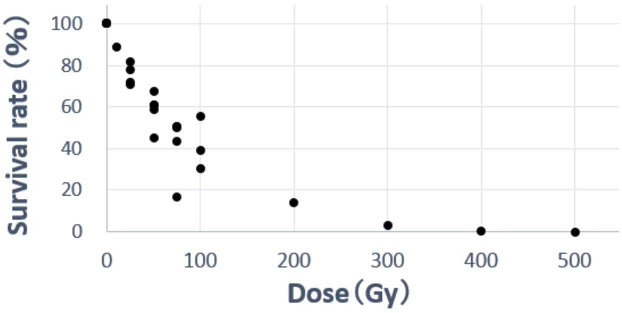

Fig. 1. Effects of ion beam irradiation on survival rate of protoplasts.

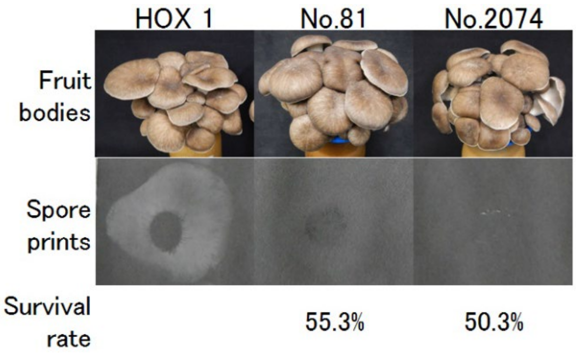

Fig. 2. Fruit bodies and spore prints on black paper of HOX 1 and sporeless mutants obtained by ion beam irradiation.

Table 1
Relationship between suvival rate and mutation frequency.

Survival rate (%)	Number of tested colonies	Number of mutants (Mutation frequency)		
		Sporeless	Other	Sporeless+Other
0-10	23			
11-20	471			
21-30	104			
31-40	413		3 (0.73%)	3 (0.73%)
41-50	2253	1 (0.04%)	11(0.49%)	12 (0.53%)
51-60	3065	1 (0.03%)	8 (0.26%)	9 (0.29%)
61-70	551			
71-80	200			
81-90	377			

Reference

[1] Gisusi *et al.*, Jpn. J. Mycol. **56**, 27 (2015).

Part Ⅱ

3. Advanced Quantum-Beam Technology

3 - 01

Characterization Study of Hollow Ion Beams Formed Through Nonlinear Focusing of Multipole Magnets

Y. Yuri[a], T. Yuyama[a], T. Ishizaka[a] and M. Fukuda[b]

[a]Department of Advanced Radiation Technology, TARRI, QST,
[b]Research Center for Nuclear Physics, Osaka University

Applying a nonlinear focusing force to a charged-particle beam properly, it is possible to generate different extraordinary beam intensity distributions that cannot be realized through common linear-focusing systems or that are difficult to achieve through beam scanning. We, therefore, study the beam profile manipulation based on nonlinear focusing force produced by multipole magnets so that the shape, size and distribution of a beam can be tailored for advanced, dedicated utilization especially in high-energy or high-power accelerators. In fact, we recently demonstrated that a hollow transverse beam profile with different cross-sectional shapes can be formed using octupole magnets [1]. The cross-sectional shape of the hollow beam can be changed through the gradient of the octupole magnets. We further experimentally investigated the characteristics of the hollow beams toward the utilization of such a unique beam [2].

The beam experiment was performed at the LB line of the TIARA cyclotron where two octupole and two sextupole magnets were installed together with several quadrupole magnets. 10-MeV proton and 190-MeV $^{12}C^{6+}$ ion beams were chosen for the study. We first confirmed that the hollow beam with almost equivalent characteristics (beam size and cross-sectional shape) can be formed through almost the same beam optics for both beams. This indicates that the nonlinear-focusing effect of multipole magnets does not strongly depend on the initial characteristics of the beam, i.e., beam emittance. Therefore, the dependence of the hollow beam profile on the beam emittance was investigated for the carbon ion beam. In order to obtain a higher-emittance beam, the beam extracted from the cyclotron was multiply-scattered using a thin aluminum foil (before nonlinear focusing). The emittance of the scattered beam is estimated to be increased several times. (The energy loss of the beam due to multiple Coulomb scattering is sufficiently small (~0.1%), according to an estimate with SRIM.) Then, the beam was transported and focused into a hollow profile through the same beam optics. The hollow-beam profiles are shown in Fig. 1. For an original lower-emittance beam (Fig. 1(a)), a steep peak is generated at the radial edge. The transverse size of the hollow beam is 72 mm in diameter. On the other hand, for a scattered higher-emittance beam, the peak height is reduced and the intensity of background particles is increased around the main part. However, the diameter and round shape of the primary hollow beam in Fig. 1(b) are almost unchanged despite the large difference in emittance. We confirmed that this experimental result is consistent with the results of theoretical analysis and particle tracking simulations.

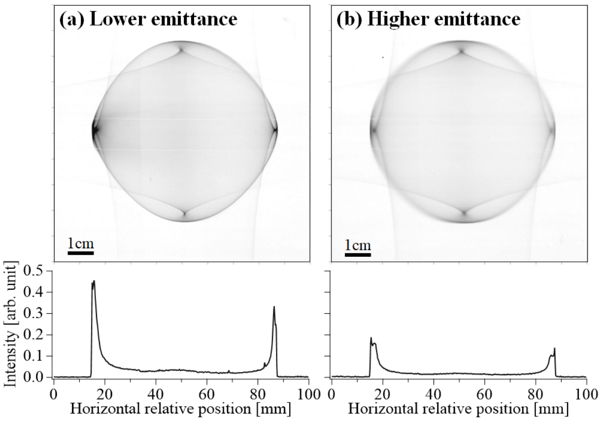

Fig. 1. Dependence of the hollow profile on beam emittance. A 190-MeV $^{12}C^{6+}$ ion beam was focused into an approximately round hollow profile using two octupole magnets. (a) Lower-emittance beam without multiple scattering. (b) Scattered higher-emittance beam. In both cases, the parameters of the beam optics are the same except for multiple scattering in (b). The 1D distributions along the horizontal axis are also plotted in the lower panels.

Another characteristic of the hollow beam was explored toward the utilization of the beam at the Research Center for Nuclear Physics, Osaka University [3]. As a possible application of the beam, high-energy hollow beam irradiation along the side surface of a cylindrical muon production target is studied to improve the yield of low-energy muons that are produced at the side surface of the target. Therefore, the effect of multiple scattering of a hollow beam (392-MeV proton) while passing through a long target material (20-cm-long graphite) was investigated by tracking simulations. We confirmed that the round cross-sectional shape and hollow profile are approximately maintained even at the rear side of the target.

In summary, we have revealed basic characteristics of the hollow beam, especially in terms of beam emittance and multiple scattering. The present result shows that, with a properly-designed beam optics, the hollow beam formed through nonlinear focusing can be applied to irradiation of a long target.

This work was supported in part by JSPS KAKENHI (JP18K11934) and JST OPERA (JPMJOP1721).

References

[1] Y. Yuri *et al.*, Prog. Theor. Exp. Phys. **2019**, 053G01 (2019).

[2] Y. Yuri *et al.*, Proc. 16th Annual Meeting of Particle Accelerator Society of Japan, 2019, pp. 112-115.

[3] Y. Yuri *et al.*, J. Phys.: Conf. Ser. **1350**, 012115 (2019).

3 - 02

Development of Pepper-pot Emittance Monitor in Low-Energy Beam Transport Line of the Cyclotron

N. Miyawaki, H. Kashiwagi and S. Kurashima

Department of Advanced Radiation Technology, TARRI, QST

A pepper-pot emittance monitor (PPEM) [1] has been developed to obtain the four-dimensional (4D) emittance data, which are required for the beam transport calculation to improve beam transport efficiency in the low-energy beam transport line of the TIARA AVF cyclotron. The transport efficiency from the HYPERNANOGAN electron cyclotron resonance (HECR) ion source to the cyclotron is less than 50%. The beam loss mainly occurs in the section between the beam diagnostic station (HS2) just after the analyzing magnet and the second diagnostic station (IS1). Since the existing emittance monitor (EM) is located downstream of IS1, it is difficult to study methods for improving the beam transport efficiency by beam transport calculation. Therefore, PPEM, which has a relatively small installation space and can obtain the 4D emittance data, was installed just after HS2.

The PPEM consists of a pepper-pot (PP) mask, a multichannel plate (MCP) with phosphor screen, a mirror, and a CMOS camera, as shown in Fig. 1. In order to measure various beams with different divergence angles, the distance between PP mask and MCP must be variable so that size of the beam image on the PP mask can be adjusted. Therefore, by placing each of MCP and the camera on the movable stage, the distance between PP mask and MCP can be changed while keeping the distance between the camera and MCP. The measurement method of beam emittance with PPEM is as follows: The ion beam from the HECR ion source is intercepted by PP mask which has a grid pattern of holes with diameters of 0.1 mm each and pitch of 2 mm. The beam transmitted by these holes are projected onto the phosphor screen of MCP located at downstream of PP mask. The beam image of the fluorescent screen in vacuum is deflected by the mirror and taken by the camera in the atmosphere through the window.

In order to evaluate emittance, it is necessary to determine the divergence angle of each pixel in each beam by correctly setting the distance per pixel and the position of each hole of PP mask in the image. The distance per pixel of the image obtained by the camera was calibrated from the marking points on the MCP holder before measurement. The position of PP mask hole on the camera image is determined by extrapolating the beam positions measured at each MCP position in the beam axis direction. The divergence angle is calculated by the distance between the pixel position in each beam and corresponding PP mask hole divided the distance between PP mask and MCP.

The emittance measurement test of PPEM was performed using a $^{4}He^{2+}$ ion beam extracted at 8.52 kV from a HECR ion source. As a result, the intensity distributions in the real space (*x*-*y*) and in the phase space (*x*-*x′*) and (*y*-*y′*) were obtained from the camera image, as shown in Fig. 2. In this case, the 80% emittance was 166 π mm mrad in the x direction and 189 π mm mrad in the y direction. It was also found that these measurements to analysis can be performed at a cycle of about 1 Hz.

The 4D emittance data can be obtained by another analysis program and will be used for the beam transport calculations to improve the beam transport efficiency.

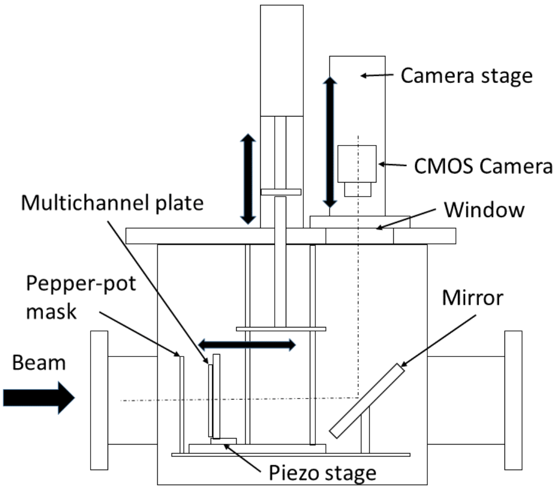

Fig. 1. Schematic view of PPEM.

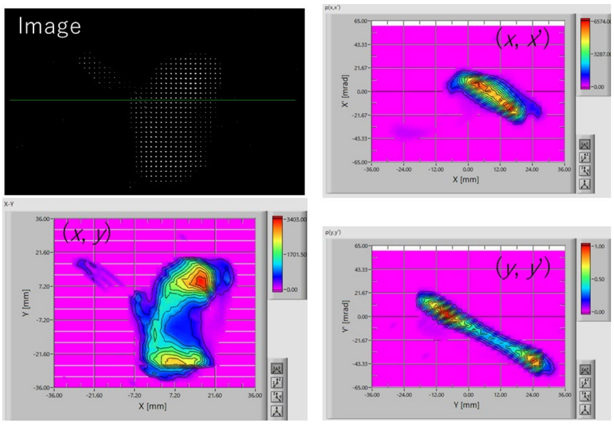

Fig. 2. Measured Image and particle distribution in the transversal plane of (X, Y), and the phase space of (X, X’) and (Y, Y’).

Reference

[1] H. R. Kremers *et al.*, Rev. Sci. Instrum. **84**, 025117 (2013).

3 - 03

Structural Analysis of Eu-DGA Complex Formed in Adsorbent

S. Watanabe[a], M. Okada[b], H. Matsuura[b], W. Kada[c], M. Koka[d], R. Yamagata[d],
N. Yamada[d], Y. Yuri[d], T. Satoh[d] and Y. Ishii[d]

[a]Nuclear Fuel Cycle Engineering Laboratories, JAEA,
[b]Atomic Energy Research Laboratory, Tokyo City University,
[c]Faculty of Engineering, Gunma University,
[d]Department of Advanced Radiation Technology, TARRI, QST

Trivalent minor actinides (MA(III): Am and Cm) are contained in high level liquid waste (HLLW) generated from reprocessing of spent nuclear fuel possess radiotoxicity. Partitioning and transmutation of those elements are important strategy for sustainable nuclear energy [1]. Japan Atomic Energy Agency has been developing an extraction chromatography technique for practical MA(III) recovery process [2]. We have desinged an appropriate flow-sheet for the MA(III) recovery consisting of a 2 step-column operation of MA(III)+lanthanides (Ln(III)) recovery and MA(III)/Ln(III) separation [3]. In the first column, Tetraoctyl diglycolamide (TODGA) emplyed as impreganated adsorbent (referred as TODGA/SiO_2-P), and MA(III)+Ln(III) recovery was successfully done from simulated HLLW containing tracer amount of MA(III). However, MA(III) recovery performance from genuine HLLW was poor due to strong MA(III)-TODGA complex formed in the adsorbent. Currently, we are focusing on Tetraethylhexyl diglycolamide (TEHDGA) extractant which has less affinity for MA(III) and Ln(III) than TODGA for better MA(III) recovery performance, and conducting series of fundamental studies for characterization of TEHDGA/SiO_2-P adsorbent. One of our interests is correlation between adsorption performance and strucure of complex formed in the adsorbents. In this study, the structural information of Eu-DGA complexes was investigated by Extended X-ray Absorption Fine Structure (EXAFS) analysis and Ion Beam Induced Luminescence (IBIL). Eu and MA(III) are considered to form similar complexes with the DGA.

Eu-L_{III} edge (keV) EXAFS measurements were carried out at the BL5S1 beamline of Aichi Synchrotron Radiation Facility, Japan. The adsorbent was put in a SUS flat washer with 1 mm thickness and 10 mm inner diameter, and then sealed by two Kapton films.

The IBIL measurements were performed using the ILUMIS system equipped in the light-ion microbeam line connected to a 3-MV single-ended accelerator in TIARA. A few tiny particles of the adsorbent were put on a Kapton film attached to a sample holder, and sealed by a Kapton film. The samples were irradiated by a 3 MeV proton beam with beam current of about 100 pA. The IBIL Spectra were observed by an UV-vis spectrometer (Solid Lambda CCD, Spectra CO., Ltd.).

Two adsorbents showed similar adsorption coefficient at high acidic condition, whereas the adsorption ratio onto TEHDGA/SiO_2-P was smaller than that onto TODGA/SiO_2-P at low acidic region. This feature is considered to be contribution of better elution performance.

The EAXFS analysis of Eu loaded in TODGA/SiO_2-P and TEHDGA/SiO_2-P revealed that the number of nearest oxygen around Eu in the TEHDGA/SiO_2-P system was smaller than that in the TODGA/SiO_2-P system at the low acidic region. The difference might correlate to the different adsorption behavior.

The IBIL spectra obtained for the adsorbents at low acidic condition are shown in Fig. 1. Characteristic peaks could be attributed to the transition of 4f electrons in Eu^{3+} ion. A distinct difference in the two systems was the shape of spectrum at λ = 620 - 630 nm which corresponds to ${}^0D_6 \rightarrow {}^7F_3$ transition. The profile of TODGA/SiO_2-P seems to have two peaks, while the peak of TEHDGA/SiO_2-P was single. This difference is considered to be the suggestion of a difference in the structure of the complex and the correspondence to the difference observed in the adsorption performance and EXAFS analysis. In order to evaluate the IBIL spectra quantitatively, numerical simulation on DGA complex and calculation of the luminescence is currently underway.

References

[1] IAEA, Technical Reports Series No. **435**, IAEA, Vienna (2004).
[2] H. Funasaka and M. Itoh, Proc. Global 2007, September 9-13, 2007, Boise, Idaho, USA (2007).
[3] Y. Koma *et al.*, Proc. 11th IEMPT, San Francisco, USA, November 1-4, 2010, IV-4, OECD/NEA (2010).

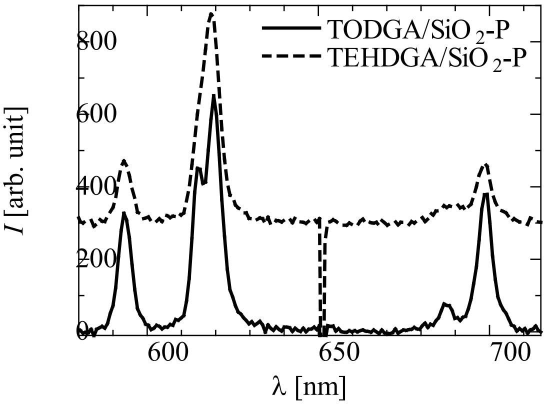

Fig. 1. IBIL spectra of Eu loaded in DGA adsorbents.

3 - 04

Microstructures of PVDF-TrFE Film Fabricated by Proton Beam Writing

Y. Nojiri [a], Y. Ishii [b] and H. Nishikawa [a]

[a] Department of Electrical Engineering, Shibaura Institute of Technology,
[b] Department of Advanced Radiation Technology, TARRI, QST

Polyvinylidene fluoride trifluoroethylene (PVDF-TrFE) is a piezoelectric fluorinated polymer and shows the highest open-circuit voltage among piezoelectric polymers. Compared to ceramic piezoelectric materials such as PZT, it is flexible and easy to manufacture for low crystallization temperature [1].

The purpose of this paper is a feasibility study of proton beam writing for micro-structuring of PVDF-TrFE for sensing applications. Utilizing the superior feature of PBW as a lithographic tool, we patterned the surface of PVDF-TrFE film with three-dimensional structures.

Powder of PVDF-TrFE (composition rate: 75:25, Kureha Co. Ltd.) are dissolved in N,N-Dimethylformamide with a weight ratio of 20 %. This solution is then spin-coated giving a thickness of about 80 μm on silicon. Two steps of heat treatment are then performed; first at 40 °C for 2 h, followed by a 140 °C for 1 h.

Sample of the PVDF-TrFE is patterned by irradiation with 3 MeV single-ended accelerator installed at National Institutes for Quantum and Radiological Science and Technology, Takasaki (beam energy: 1.7 MeV, beam size: 1.0 μm, fluence: 1.0 to 7.0 μC/mm^2). The proton beam was scanned in a grid pattern of 10 mm wide lines spaced 20 mm apart over a 130-mm squared area of the PVDF-TrFE surface.

After PBW, wet etching is performed: 9.0 mol/L potassium hydroxide (KOH) solution with 0.25 mol/L potassium permanganate ($KMnO_4$) added at 80 °C for 1 to 5 h. As evaluation methods, surface shapes were observed by a laser microscope (OLYMPUS, OLS4000), and three-dimensional structures were observed by a scanning electron microscope (SEM, JEOL, JSM-6010LV).

In Fig. 1, we show the SEM image for PVDF-TrFE with the fluence of 3.0 μC/mm^2 with the subsequent etching process for 3 h. Here, the remaining structure of the PVDF-TrFE represents 4×4 pillar arrays. For the etching time of 1 h, a shallower grid pattern appears than in Fig. 1, while for the etching time of 5 h, the pillar arrays have almost collapsed away (data not shown).

Figure 2 shows dependence of the patterned depth of the PVDF-TrFE on the fluence of 1.7 MeV proton beam. The depth of the grid pattern increases with etching time. With the fluence of 1.0 μC/mm^2, the depth does not reach to the penetration depth even at etching time of 5 h. At the fluence of 3.0 μC/mm^2, the depth of the grid pattern reached to around 40 μm for the etching time more than 3 h. The depth is very close to the penetration depth of 1.7 MeV protons [3].

At the fluence more than 5.0 μC/mm^2, the depth of the grid pattern exceeds the penetration depth of protons, because of excessive deposition of energy. However, the etching time of 5 h is too long, since the pillar structures collapsed away, as described above.

From these results, the 1.7 MeV proton fluence of 3.0 μC/mm^2 and etching time of 3 h are appropriate for micro-structuring of the PVDF-TrFE. The etching rate is estimated to be about 13 μm/h for this condition.

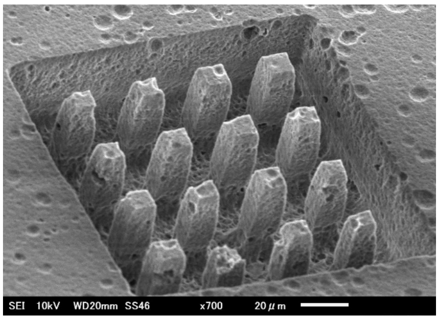

Fig. 1. SEM image PVDF-TrFE tilted at 45° after PBW at 1.7 MeV with fluence of 3.0 μC/mm^2 for etching time of 3 h.

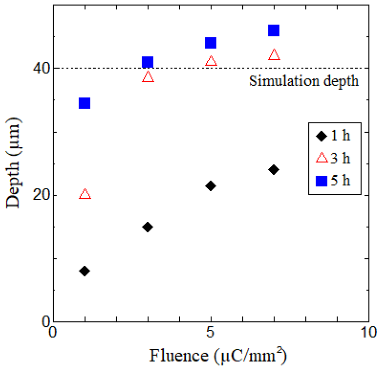

Fig. 2. Dependence of the pattern depth of PVDF-TrFE on the fluence of 1.7 MeV proton. The simulation depth was obtained by SRIM code [3].

References

[1] H. Jiang *et al.*, Energy Convers. Manage. **211**, 112771 (2020).
[2] Y. Nojiri *et al.*, 45th International Conference on Micro and Nano Engineering (MNE) 2019, Sep. 23-26. Paper No. PB46 (2019).
[3] J. F. Ziegler *et al.*, Nucl. Instrum. Meth. Phys. Res. B **268**, 1818 (2010).

3 - 05

Micro-meter-scaled Patterning on Radio-photoluminescence (RPL) Phosphate Glass Substrate by Focused Particle Beam Writing Technique

S. Kimura[a], S. Kawabata[a], K. Iiduka[a], Y. Akagami[a], S. Yokosawa[a], W. Kada[a],
K. Miura[a], T. Satoh[b], N. Yamada[b], Y. Ishii[b] and O. Hanaizumi[a]

[a]Faculty of Science and Technology, Gunma University,
[b]Department of Advanced Radiation Technology, TARRI, QST

Among various microfabrication technique, Proton/Particle Beam Writing (PBW) technology is recognized as one of the unique techniques which have high selectivity in processing target, from polymers to wide-bandgap semiconductors by accomplishing fabrication of optical communication devices [1,2] to defect engineering in diamond and SiC [3,4]. Before the micro-processing starts, it always requires prior evaluation of irradiation conditions using several amounts of target substrates. While there are individual variations in dose at each point, such radiation monitoring in microscopic regions must be carried out for successive micro-processing by PBW. Conventionally, CR-39, a type of solid-state nuclear track detector (SNTD), has been utilized for the purpose. Still, the chemical treatment required for observation is irreversible, and the results are strongly affected by the operator's skill level. As an alternative to SNTD, a fluorescent track detector (Fluorescent Nuclear Track Detector: FNTD) that can repeatedly readout using fluorescence is recently underway. Radio-photoluminescence (RPL) phosphate glass (PG) is one of the FNTD detector candidate materials that can be easily manufactured in house. RPL-PG FNTD does not require a post chemical process and can be utilized as a convenient micrometer-scale visualization tool of dose distribution by PBW. In this study, we have developed an RPL-PG based FNTD as a sensor for the PBW process. Convenient observation of an exposure area of protons was visualized RPL-PG with simplified steps.

The host chemical composition of RPL-PG consists of sodium metaphosphate ($NaPO_3$) and aluminum metaphosphate ($Al(PO_3)_3$). RPL response is accomplished by adding silver (Ag) and the other elements as active centers to a host chemical composition. The host substrate and silver activators were mixed and melted for 1 hour at 1000 ℃ in an alumina crucible. Then RPL-PG was cast on metal at room temperature using the rapid quenching method. Figure 1 illustrates the typical process of RPL-PG fabrication. It was shaped into an arbitrary shape using a manufactured glass diamond saw.

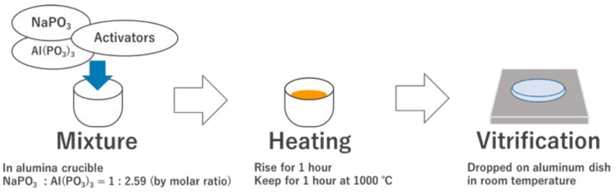

Fig. 1. Schematic illustration of RPL-PG fabrication process to be utilized in visualization of micro-patterns by PBW.

After obtaining the evaluation of the fundamental responsibility of the manufactured RPL-PG by X-ray irradiation, the sample was irradiated by protons at the microbeam line of 3MV single-ended accelerator at TARRI-QST. Examples of micropatterns are shown in Fig. 2, and a comparison of PL spectra obtained from the region of the intense and low dose irradiation is shown in Fig. 3. Localized dose distribution in the area of irradiation was illustrated as RPL distribution. Further research and development will enable us to integrate RPL-PG into the PBW process for detailed characterization of beam patterns without complicated post-process but high spatial accuracy.

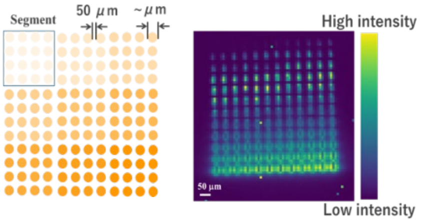

Fig. 2. Schematic illustration of PBW pattern on RPL-PG and its PL mapping image visualized in post process.

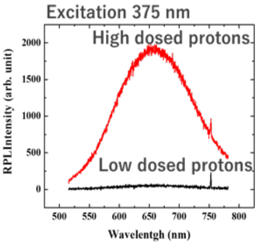

Fig. 3. Examples of RPL spectra from different irradiated

Acknowledgments

The authors sincerely thank Dr. S. Onoda of QST and Dr. T. Kurobori of Kanazawa university for the support and advice on photoluminescence measurement and evaluation of RPL glass dosimeters irradiated by PBW.

References

[1] W. Kada *et al.*, Nucl. Instrum. Meth. Phys. Res. B. **348**, 218 (2015).
[2] R. K. Parajuli *et al.*, Jpn. Appl. Phys. **55**, 06GD01 (2016).
[3] H. Kraus *et al.*, Nano Letters **17**(5), 2865 (2016).
[4] M. Haruyama *et al.*, Key Eng. Mater. **790**, 48 (2018).

3 - 06

Preliminary Study of Measurement of Ion Beam Energy Spreads Produced by a Penning Ionization Gauge-Type Ion Source Using Electromagnets for a Compact MeV Ion Microbeam System

Y. Ishii[a)], T. Ohkubo[a)] and Y. Miyake[b)]

[a)]Department of Radiation Advanced Radiation Technology, TARRI, QST,
[b)]Beam Seiko Instruments Inc.

An ion microbeam with an energy range of several MeV is a powerful tool for microfabrication using proton beam writing (PBW) and ion beam analysis using proton-induced X-ray emission (PIXE). To date, MeV ion microbeams have been produced by an ion microbeam system that comprises an accelerator, a long beam line, and a focusing lens system with quadrupole magnets. However, the typical size of the microbeam system is above 30 m, which represents a significant hurdle for the installation of a microbeam system in an experimental room with an average size of 4 × 5 × 3 m^3. A compact ion microbeam system, referred to hereafter as “CompactMB,” with beam energy up to 1 MeV has been developing to enable the installation.

In the development, a dedicated penning ionization gauge-type ion source with two electrostatic magnets (EM-PIG-IS) was designed and assembled to generate a gaseous ion beam with high brightness and narrow energy spread. General penning ionization gauge-type ion sources (PIG-IS) serve compact-sized ion sources with low electric power consumption and long-time interval without the need for maintenance. However, PIG-ISs typically produce gaseous ion beams with low brightness and wide energy spread; such an ion source cannot be directly used for CompactMB. Therefore, EM-PIG-IS was designed to generate a gaseous ion beam with high brightness and low energy spread, which was suitable for the CompactMG, by extracting the high-density plasma with a small volume using a strong magnetic field.

As the first experiment, the brightness of a hydrogen ion beam generated by EM-PIG-IS was measured because it was essential to obtain beam current at a focus point. In the experiment, the brightness of a hydrogen ion beam including H^+, H_2^+, and H_3^+ was measured using a geometrical configuration of extraction electrodes. The separation of the hydrogen ion beam was not necessary because the three-stage acceleration lens, constructed only by an electric field, focused the same energy ion beam at the same point, regardless of the ion mass. The measurement result showed that the brightness was approximately ten times that of the dedicated duoplasmatron ion source [1].

In the current study, beam energy spreads of hydrogen ion beams extracted from EM-PIG-IS with a high-density plasma of a small volume were measured using a parallel electrostatic analyzer without separating the ion species. The energy spreads of hydrogen ion beams generated were measured by changing the parameters of EM-PIG-IS. The energy spreads were measured on the basis of changing ion source parameters, such as gas presser, magnetic strength, anode voltage, and extraction voltage. A minimum beam energy spread width of approximately 5.0 ± 0.1 eV at 200 eV was obtained in the experiments as a function of extraction voltage, as shown in Fig. 1. The beam energies were also shown in Fig. 1, which changed according to the extraction energy. The characteristics of the ion beam generated EM-PIG-IS were evaluated from the results of the measured beam energy spread for installing EM-PIG-IS in CompactMB [2]. The width is acceptable to form microbeam of about 1 μm diameter using CompactMB from a numerical simulation.

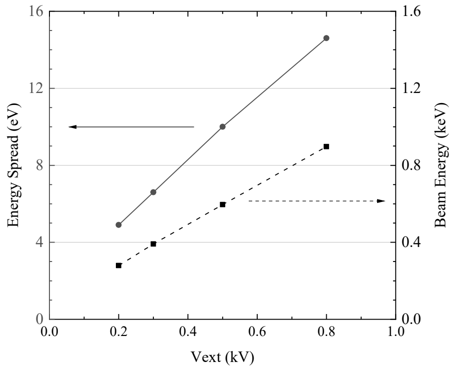

Fig. 1. Relationship between the beam energy spread and the beam energy as a function of extraction voltage. Vacuum degree = 0.283 Torr, anode voltage = 0.7 kV.

References

[1] Y. Ishii *et al.*, AIP Conference Proceedings **2011**, 080015 (2018).

[2] Y. Ishii *et al.*, Rev. Sci. Instrum. **91**, 043304 (2020).

3 - 07

Microscopic PIXE Imaging and Analysis on Atmospheric Particulate Matter (PM)s Hourly-collected from an Automatic Sampler Unit

K. Tozaka[a], T. Imayoshi[a], W. Kada[a], S. Nakatasu[a], T. Satoh[b], K. Kumagai[c],
H. Tago[c], N. Yamada[b], Y. Ishii[b] and T. Kamiya [a]

[a]Faculty of Science and Technology, Gunma University,
[b]Department of Advanced Radiation Technology, TARRI, QST,
[c]Gunma Prefectural Institute of Public Health and Environmental Sciences

Microscopic imaging and analysis utilizing a focused proton beam are a useful tool to characterize and visualize material compositions' details with a limited specimen volume. These features are desirable to the environmental research field, where limited numbers or amounts of specimens are available without duplication. One such sample is collected from the atmosphere, known as particulate matters (PM)s. PMs are often used as an indicator of air pollutions. However, they are dramatically affected by environment and meteorological conditions. Therefore, PM samples should be collected within a short time domain. However, it would limit PMs' concentration in collection volume, which is sometimes below the limit of detection for conventional elemental composition analysis. Particle-induced X-ray emission (PIXE) analysis can be recognized as a useful tool for such elemental composition analysis [1, 2]. This study investigated the applicability of micro-PIXE analysis for elemental composition analysis of PM collected in a short time domain.

Micro-PIXE analysis and imaging on an hourly-collected PM sample were demonstrated at a microbeam line of 3MV single-ended accelerator at TIARA. The PM sample was collected by an automatic sampling unit of AEROS (Atmospheric Environmental Regional Observation System), founded by Ministry of Environment, Japan. The AEROS system is distributed all over Japan to collect PM concentration with a high time resolution of an hour. In this trial, samples are collected from the one installed at Gunma Prefectural Institute of Public Health and Environmental Sciences. The sample was sandwiched with thin polyimide films, as illustrated in In Fig. 1. It allows us to avoid degradation of filter substrate and PM samples via desorption from the surface or gaseous decomposition.

With this configuration, micro-PIXE imaging and analysis were demonstrated on hourly collected PM filters. An external microbeam probe, with a typical beam energy of 3 MeV and a diameter of approximately 1 µm, was utilized for the analysis. We performed the PIXE analysis within a particular irradiation period, which was monitored by the integrated charge of the incident protons. We obtained PIXE images as a uniform elemental distribution for most PM samples [3]. However, there could be some inhomogeneous distribution of elemental compositions, as shown in Fig. 2. Inhomogeneities had variety in elemental composition, density, and total coverage over the whole analytical area. In the two examples shown in the figure, a single iron particle was observed in the sample collected on 17th March 2018, 13:00-13:59, while several calcium-rich particles are seen on the sample collected from 4:00 - 4:59 on 26th March 2018. These particulate matters will be averaged out if those particles are limited in numbers and volumes. However, in some cases, those might bring the minor misguides into the PM samples' source identification. This result suggested that conventional PIXE could over- or under-estimate PM's elemental composition, where uniform composition distribution is assumed. On the other hand, micro-PIXE imaging could be a useful tool to reveal such microscopic deterioration in samples.

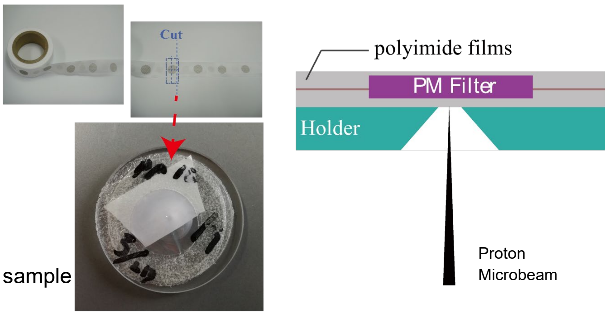

Fig. 1. (Left) Picture and (Right) schematic illustration of PM sample film and sample holder's analytical setup prepared for micro-PIXE analysis and imaging.

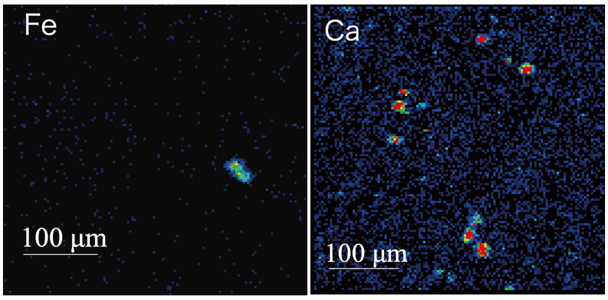

Fig. 2. Micro-PIXE visualized inhomogeneity in hourly-collected PM sample filters obtained in March 2018. Two examples indicate a single iron-rich particle and several calcium-rich particles in the analytical field of 400 × 400 µm^2.

References

[1] C.-J. Ma *et al.*, Atmos. Environ. **35**, 2707 (2001).
[2] K. Saitoh *et al.*, Int. J. PIXE **14**, 43 (2004).
[3] Kada *et al.*, Nucl. Instrum. Meth. B **477**, 133 (2020).

3 - 08

Lithium Distribution Analysis of All-solid-state Lithium Batteries Using Micro-PIXE and Micro-PIGE Techniques

Y. Yamada[a)], K. Suzuki[a)], T. Satoh[b)], M. Finsterbusch[c)], T. Kamiya[d)], A. Yamazaki[e)],
K. Fujita[f)], Y. Kato[f)] and K. Mima[f)]

[a)]Department of Chemical Science and Engineering, Tokyo Institute of Technology,
[b)]Department of Advanced Radiation Technology, TARRI, QST,
[c)]Institute of Energy and Climate Research, Forschungszentrum Jülich GmbH,
[d)]Graduate School of Science and Technology, Gunma University,
[e)]Faculty of Pure and Applied Sciences, University of Tsukuba,
[f)]The Graduate School for the Creation of New Photonics.

Introduction

Since the contact area between solids provides as a charge transfer reaction field in the all-solid-state Li batteries, it is necessary to analyze the correlation between the electrode microstructure and the variation in the charge carrier distribution to design the battery with the better performance. To analyze the Li concentration distribution in micrometer- or larger-scale areas that are typical particle sizes of the practical cells, we used microbeam analysis. The micro-PIXE and micro-PIGE analysis were adapted for the elemental mapping of the cross-section of the pellet-type battery. We carried out *ex situ* measurements at before and after-charged states in advance [1]. The *in situ* analysis was conducted to elucidate the kinetic behavior of the Li distribution during the charging process.

Experiment

Elemental distribution analysis was carried out using a 3.0-MeV proton ion beam in TIARA to obtain spatial Li distributions of the cross-section near anode layer by the gamma-ray from the ^{7}Li(p,p'γ)^{7}Li. The pellet-type cell was composed of a cathode ($LiNbO_3$-coated $LiCoO_2$ + solid electrolyte (SE) ($Li_{10}GeP_2S_{12}$)), SE and an anode (amorphous TiS_3), and assembled in a closed cell with a Kapton film window designed for *in situ* observation. The cell was charged by linear sweep voltammetry (scan rate at 0.1 mV/s) from OCV to 2.2 V (*vs.* TiS_3/Li_2TiS_3), then maintained at 2.2 V for 200 min. The elemental mapping data was collected by the integration of PIXE/PIGE signals for 5 min, and intensity profiles were visualized by accumulating the four data (total 20 min).

Results

Figure 1 shows the electrochemical performance of the battery in the charging process. The current value reached 0.45 mA at 2.2 V, and by keeping the voltage constantly, the capacity of 2.6 C was used for the charging process. This value is equivalent to the $Li_{0.36}TiS_2$ formation. The Li distribution mapping and profiles near the anode and electrolyte layer of the battery are shown in Fig. 2. Li gradually diffused from the boundary of the electrolyte layer to the anode region, depending on the charging time. However, the migration was observed only in a limited area near the interface compared to the *ex situ* analysis [1]. This result indicates that the charge transfer reaction on the observation surface was insufficient. To analyze the kinetic behavior of the charging process, it is necessary to improve the processing method for the cross-section surface to be observed.

The next attempt is to optimize the pellet-type cell processing method to ensure reaction on the observed surface and to analyze the Li concentration and its variation quantitatively.

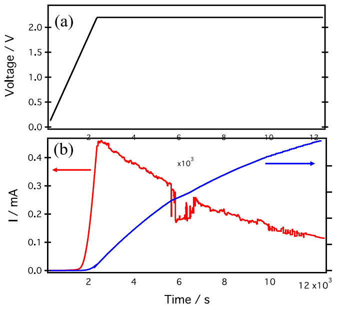

Fig. 1. Electrochemical performance of the $LiCoO_2$ + SE / SE / amorphous TiS_3 cell in the charging process. (a) Voltage, (b) Current [Red] and Electric quantity [Blue].

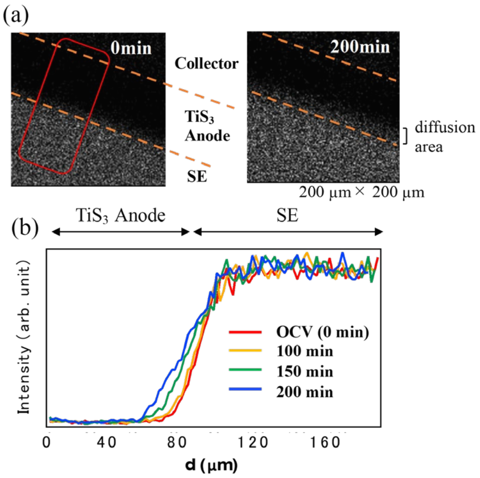

Fig. **2.** (a) Li distribution mapping of the anode side at OCV (0min) and 200 min later, (b) Li line profiles for the anode side during the charge process. It corresponds to the area indicated by the square frame in (a).

Acknowledgments

This project has been supported by the NEDO-BMBF Japan-German collaboration program.

Reference

[1] Y. Yamada *et al.*, Electrochemistry **88**, 45 (2020).

3 - 09 Measurements of Relative Angular Distribution of the n-p Elastic Scattering Reaction for 60 MeV Neutrons

T. Matsumoto[a], A. Masuda[a], H. Harano[a] and S. Kurashima[b]

[a]National Metrology Institute of Technology, AIST,
[b]Department of Advanced Radiation Technology, TARRI, QST

In many cases, recoil protons produced by the n-p elastic scattering reaction are used in neutron detectors and neutron dosimeters [1]. Especially, information on the angular distribution of n-p elastic scattering reaction is important for proton recoil telescopes (PRTs) that are used to determine the neutron fluence in neutron energy region above several MeV [2]. Energy dependent detection efficiency of a PRT is usually obtained using simulation codes with an evaluated data file such as LA150 and JENDL-HE files. However, the angular distribution of the n-p elastic scattering reaction has discrepancy between LA150 and JENDL-HE2007 in high energy region above 20 MeV. In our previous study, a PRT composed of a Si surface barrier detector and a liquid scintillation detector was developed to measure high energy neutrons above 20 MeV. The recoil angle of 10 degrees were used in the PRT. In this case, the detection efficiency for 45 MeV neutrons had 5% discrepancy between LA150 and JENDL-HE2007 [2]. We have experimentally verified the relative angular distribution of the n-p elastic scattering reaction for 45 MeV and 60 MeV neutrons at TIARA

In the present experiments, the relative angular distribution for 60-MeV neutrons is verified by changing the recoil angle from 10 to 25 degrees using the proton recoil telescope composed of a plastic scintillation detector (BC-400, 100 × 100 × 0.5 mm) and a liquid scintillation detector (BC501A, 7.62 cm diameter and 7.62 cm thick) and a high-density polyethylene plate (0.929 g/cm^3) as shown in Fig. 1. The plastic and liquid scintillation detectors are placed outside of the collimated neutron beam to reduce background signals. An aluminum aperture was put between the plastic scintillator and the liquid scintillator to make clear the sensitive area of the liquid scintillator. A high-density polyethylene plate (0.929 g/cm^3) was used as an n-p converter in the PRT and was located 1.5 m away from the collimator exit. A carbon plate (1.82 g/cm^3) was also used to subtract background due to Carbon included in Polyethylene. Neutrons were produced by the ^{7}Li(p,n) reaction in the LC0 beam line at TIARA. The neutrons reached the experimental room through a collimator with iron and concrete. Figure 2 shows two-dimensional plots for pulse height outputs from the plastic and liquid scintillation detectors. Recoil proton data are extracted from the two-dimensional plots. Proton pulse height spectra of the liquid scintillation detector were successfully observed for coincidence measurements with the plastic scintillation and liquid scintillation detectors in the PRT as shown in Fig. 3. The neutron fluences will be derived for each recoil angle, using detection efficiencies calculated with the MCNPX code. Finally, comparison between JENDL-HE2007 and LA150 files will be performed for the angular distribution of the n-p elastic scattering reaction.

Fig. 1. The proton recoil telescope composed of the plastic and liquid scintillation detectors and the high-purity polyethylene plate.

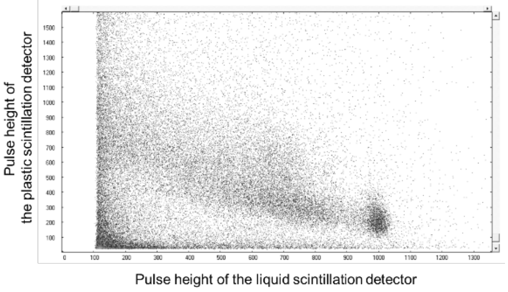

Fig. 2. Two-dimensional plots for pulse height outputs from the plastic and liquid scintillation detectors.

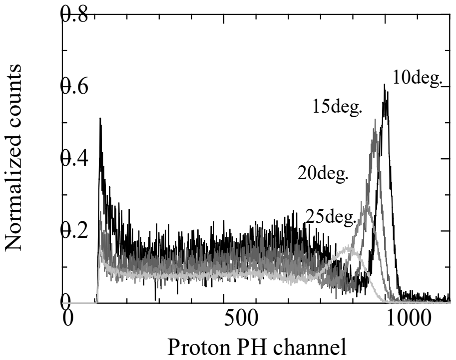

Fig. 3. Proton pulse height spectra of the liquid scintillation detector for each recoil angle.

References

[1] T. Matsumoto *et al.*, IEEE Trans. Nucl. Sci. **52**(6), 2923 (2005).

[2] T. Matsumoto *et al.*, J. Nucl. Sci. Technol. **54**(5), 529 (2017).

3 - 10

LET Effects on the Scintillation Properties of Organic–Inorganic Layered Perovskite-Type Compounds

M. Koshimizu[a], N. Kawano[b], A. Kimura[c], S. Kurashima[d], M. Taguchi[c],
Y. Fujimoto[a] and K. Asai[a]

[a]Department of Applied Chemistry, Tohoku University,
[b]Department of Materials Science, Akita University,
[c]Department of Advanced Functional Materials Research, TARRI, QST,
[d]Department of Advanced Radiation Technology, TARRI, QST

Irradiation effects of solids dependent on linear energy tranfer (LET) have been widely investigated. In the case of radiation detection, the LET dependence of detector response has long been identified as an issue. The LET dependence of the response of scintillators was phenomenologically formulated by Birks as early as 1964 [1]. This formula has long been used for compensating the LET-dependent scintillation light yield, although the formula has little physical basis and limited applicability. LET-dependent scintillation properties are caused by the interaction of excited states. Because excited states are mobile and their density decreases during diffusion, LET dependence and excited state interactions responsible for this dependence have to be analyzed from the viewpoint of the dynamics of scintillation, i.e., scintillation temporal profiles. Thus far, we have reported LET-dependent scintillation rise and decay for several scintillators having dopants as luminescent centers, e.g. Ce-doped Li-glass scintillator [2], and self-activated scintillators such as $Bi_4Ge_3O_{12}$ [3].

In this study, we focused on the LET dependence of the scintillation properties of a novel class of scintillators, i.e., organic–inorganic layered perovskite-type compounds. The basic concept of scintillator development based on these compounds was proposed by our group more than 16 years ago [4]. Recently, we have developed single crystalline scintillators based on compounds with a relatively high light yield and fast decay [5]. These compounds have a layered structure of alternating organic amine layers and inorganic lead halide layers. Owing to the significantly lower band-gap energy of the inorganic layers than that of the organic layers, the compounds have multiple quantum-well structures in their crystal structure. Fast and efficient scintillation has successfully been obtained from quantum-confined Wannier excitons in the inorganic layers. In this study, we analyzed the LET dependence of the scintillation properties of such compounds with a focus on the scintillation temporal profiles from the viewpoint of interactions of Wannier excitons at high LET.

The sample was a single crystal of the layered perovskite-type compound with phenethylamine in its organic layers. The chemical formula of the compound is $(C_6H_5C_2H_4NH_3)_2PbBr_4$. The compound was synthesized through the reaction of the amine and hydrobromic acid, and subsequent reaction of the reaction products with $PbBr_2$. Single crystals were grown using a poor solvent diffusion method [5]. The scintillation temporal profiles at different LETs were measured using a measurement system at TIARA, QST, Japan. The sample was irradiated with pulsed beams of 20 MeV H^+, 50 MeV He^{2+}, and 220 MeV C^{5+} from the AVF cyclotron. The overall time resolution of the measurement system was ~2 ns at half width at half maximum (HWHM).

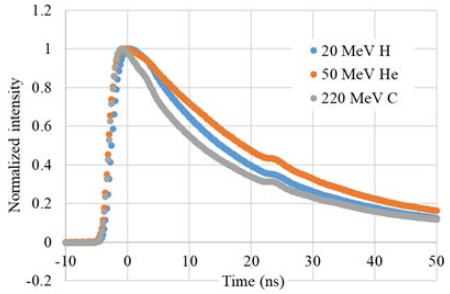

Fig. 1. Scintillation temporal profiles up to 50 ns of $(C_6H_5C_2H_4NH_3)_2PbBr_4$ under irradiation with 20 MeV H^+, 50 MeV He^{2+}, and 220 MeV C^{5+}.

Figure 1 shows the scintillation temporal profiles up to 50 ns. The LET dependence of the rise in scintillation temporal profile was negligible. The initial decay up to 50 ns exhibited a complicated LET dependence: the fastest and the slowest decay were observed for irradiations of 220 MeV C^{5+} and 50 MeV He^{2+}, respectively, i.e., the decay initially became slower and subsequently faster for higher LET in the LET range investigated in this study. As for the faster decay at higher LET, some processes can be proposed: one is the formation of bi-excitons, whose rate of radiative process is significantly higher than that of free excitons. Another possible cause of the faster decay at higher LET is the nonradiative Auger process, in which one exciton during its annihilation gives its energy to another exciton nearby, which is converted into a higher excited state.

References

[1] J. B. Birks, The Theory and Practice of Scintillation Counting, Pergamon, New York, 1964.
[2] M. Koshimizu *et al.*, J. Lumin. **169**, 678 (2016).
[3] M. Koshimizu *et al.*, Nucl. Instrum. Meth. Phys. Res. B **409**, 19 (2017).
[4] K. Shibuya *et al.*, Appl. Phys. Lett. **84**, 4370 (2004).
[5] N. Kawano *et al.*, Jpn. J. Appl. Phys. **55**, 110309 (2016).

3 - 11

Status Report on Technical Developments of Electrostatic Accelerators

Y. Hirano, A. Chiba, K. Yamada, A. Yokoyama, Y. Ishii and S. Kurashima

Department of Advanced Radiation Technology, TARRI, QST

Installation of a new ion source for the fullerene negative ion

The irradiation effects of the swift fullerene ion beams offer a highly sensitive analysis with secondary ion mass spectrometry. Especially, the effects are very suitable for an analysis of samples such as polymer materials and biomolecules which are hardly analyzed using monatomic ion beams. In order to further expand a study on the irradiation effects of the swift fullerene ion beams, we have increased the intensity of the MeV fullerene ion beams in the tandem accelerator at TIARA. The novel ionization technique has produced the μA-beam intensity that is 100,000 times greater than the conventional method (the Cs sputter) [1]. We have started to develop a molecular mapping system for a microscopic analysis using the MeV fullerene ion micro-beams. However, the fullerene ion beam intensity was still not enough to be formed the ion micro-beams because the ion beam intensity was decreased by the micro-slits that eliminate divergence of the ion beams to pass through a focusing lens. Therefore, in expectation of an increase in the ion beam intensity, we installed a new ion source at the location shown in Fig. 1 in order to improve the transmission efficiency from the ion source to the accelerator. The electrostatic deflector installed in the incident beam line deflects the ion beams without dependence on mass of ions so that the higher-energy ion beams can be transmitted with great transmission efficiency to enter the accelerator. Fig 2 shows the result of a trajectory simulation in which the ion beams were transmitted toward the existing Faraday cup via the deflector. The aperture electrodes before and behind the deflector have a role of focusing the ion beams. The position of the deflector equipped with a slide mechanism is switched corresponding to the incident direction of the ion beams (see Fig. 3).

In the next fiscal year, the transmission efficiency of the fullerene ion beams will be compared between the new ion source and the existing one.

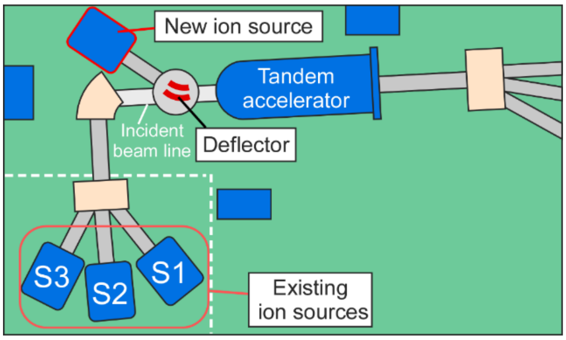

Fig. 1. Place of the new ion source.

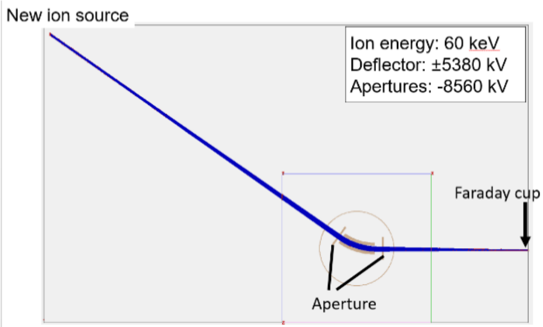

Fig. 2. The result of a trajectory simulation of the fullerene negative ion beams passing

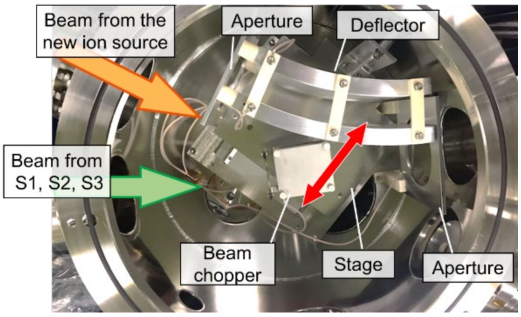

Fig. 3. Photo image of the electrostatic deflector in the chamber.

Development of a laser ion source for the Ion Implanter

A laser ion source (LIS) produces plasma directly from solid materials by focused irradiation with a high-intensity pulsed laser. Because a LIS can produce plasma of various species from any solid material, we are developing a LIS as an ion source for the Ion Implanter [2]. To conduct ion implantation experiments using the LIS that require high ion dose, it is necessary to operate the ion source in a high laser repetition rate. In this study, we investigated the particle number of ions per laser pulse for each charge state in the laser-produced carbon plasma using off-line LIS test bench to estimate the required laser repetition rate for the ion implantation experiments. In the experiment, the carbon plasma was produced from a graphite target using a Nd:YAG laser with a fundamental wavelength at laser energy below 40 mJ. The particle number of ions was highest for singly charged ions, with particle number on the order of 1010 per laser pulse. From this result, in the case of carbon ion, it was found that the laser repetition rate should be 1 kHz or higher to obtain the average ion beam intensity on the order of μA [3].

References

[1] A. Chiba *et al.*, Quantum Beam Sci. **4**(1), 13 (2020).
[2] H. Kashiwagi *et al.*, Nucl. Instrum. Meth. Phys. Res. B **406**, 256 (2017).
[3] K. Yamada *et al.*, Rev. Sci. Instrum. **91**, 013305 (2020).

3 - 12

Theoretical Study on Electron-loss and Excitation in Collision of Swift MeV/atom Carbon Cluster Ions with Gases and Solids

T. Kaneko[a)], Y. Saitoh[b)], A. Chiba[b)] and K. Narumi[b)]

[a)]Department of Applied Physics, Okayama University of Science,
[b)]Department of Advanced Radiation Technology, TARRI, QST

MeV/atom swift cluster ion beams have been employed to irradiate biological materials [1], since they have an advantage of obtaining SIMS signals of intact large molecular ions much more effectively than single-particle ion beams. In some cases, such SIMS signals are coincided with the projectile information on, *e.g.*, charges and alignment of fragmented ions. These aspects come from the feature of cluster beams which is never found in the single-ion beams. It is well-known that the so-called cluster effect has been found in several aspects, *e.g.*, reduction of average charge of constituent particles [2, 3], non-linear dependence of energy deposition [2, 4, 5], strong suppression of low-energy secondary electron production [6-8] and strong enhancement of convoy electron production [6].

This academic year we presented the research on the positive cluster-ion yield as a function of charge-changing gas pressure, and found the cluster effect in incorporated electron-loss cross sections. In addition, the energy-loss of carbon 60 cluster ion with a few MeV energies was estimated. First, on the basis of the rate equation we obtained an analytical expression for a fraction of the singly charged cluster ion at penetrating depth *x* in the charge-changing region as

$$\phi_1(x) = \frac{A}{\sigma_{1d} - \sigma_{-1}}\left(e^{-Nx\sigma_{-1}} - e^{-Nx\sigma_{1d}}\right) + \frac{B}{\sigma_{1d} - \sigma_0}\left(e^{-Nx\sigma_{1d}} - e^{-Nx\sigma_0}\right)$$

with $A = \sigma_{-11} + B$, $B = \sigma_{-10}\sigma_{01} / (\sigma_0 - \sigma_1)$, $\sigma_0 = \sigma_{01} + \sigma_{0d}$, $\sigma_{-1} = \sigma_{-10} + \sigma_{-11} + \sigma_{-1d}$. Here σ_{ij} is the cross section for changing charge from *i* to *j* of a cluster, σ_{id} is the destruction cross section for a cluster in charge state *i* in collision with a target gas, and *N* is the number density of a rare gas. We assumed carbon cluster ions C_n^+ ($n = 2 - 4$) composed of an isolated carbon ion/atom in a linear structure of equal spacing 1.27×10^{-10} m. Using the quantum mechanical treatment and the Independent Electron Model (IEM), 6 cross sections are estimated. If we denote the cross section for a C_n by $\sigma(n)$, it can be approximated as

$$\sigma(n) = \sigma(2)[1 + \beta(n-2)]$$

In case where Ne is used as the charge-changing gas, $\beta \simeq 0.16$ in σ_{01}, $\beta \simeq 0.07 - 0.08$ in σ_{-10}, σ_{-11} and $\beta \simeq 0.13 - 0.20$ in σ_{id} ($i = -1, 0, 1$) for the 1.2 MeV/atom C_n^+ ions. The values of β ranging $0 < \beta < 0.5$ mean that the corresponding cross sections indicate a sub-linear dependence on the number of atoms in a cluster, *i.e.*, the so-called cluster effect. On the basis of these 6 cross sections, we calculated the singly-charged fraction C_n^+ ($n = 2, 4$) with 2.5 MeV in collision with Ne gas as a function of gas pressure *Nx*. In order to compare with the experimental data [9], both data are normalized at the maximum value. As a result, both data are found to coincide with each other in both the maximum gas pressure and the profile with high accuracy [10].

Second, we calculated the energy loss of a few MeV carbon 60 (C_{60}^+) ions, travelling the electron gas. The basic formulation was made previously [11]. The spatial positions of constituent atoms form a fullerene structure where the radius of the sphere is 3.5×10^{-10} m. Each ion has the charge determined as a function of its speed and mutual spatial distance, based on our statistical average charge theory [2]. The energy loss is estimated in a dielectric function method making use of dielectric functions. Numerical result shows that for a few MeV carbon 60 ions, whose speed is less than the Bohr speed, the electronic stopping power of carbon (rs = 1.526) amounts to about 0.8 in magnitude, compared with 60 times the corresponding stopping power for a single carbon ion at equivalent speed. In future, this result will be utilized to estimation of the energy deposited to biological materials and the sputtering yield of bio-molecules.

References

[1] K. Nakajima *et al.*, Appl. Phys. Lett. **104**, 114103 (2014).
[2] T. Kaneko, Phys. Rev. A **66**, 052901 (2002).
[3] A. Chiba *et al.*, Phys. Rev. A **76**, 063201 (2007).
[4] S. Tomita *et al.*, Phys. Rev. A **82**, 044901 (2010).
[5] T. Kaneko, Phys. Rev. A **86**, 012901 (2012).
[6] H. Kudo *et al.*, Jpn. J. Appl. Phys. **45**, L565 (2006).
[7] S. Tomita *et al.*, Phys. Rev. A **73**, 060901(R) (2006).
[8] T. Kaneko *et al.*, J. Phys. Soc. Jpn. **75**, 034717 (2006).
[9] Y. Saitoh *et al.*, private communication.
[10] T. Kaneko *et al.*, Nucl. Instrum. Meth. Phys. Res. B, (accepted).
[11] T. Kaneko, Bull.Okayama Univ. Sci. **53A**, 1 (2017).

3 - 13 Molecular Imaging by Transmission Secondary Ion Mass Spectrometry Using 9-MeV C_{60} Ions

S. Kitamura[a], K. Morimoto[a], K. Nakajima[a], A. Chiba[b], K. Yamada[b], Y. Hirano[b],
K. Narumi[b] and Y. Saitoh[b]

[a]Department of Micro Engineering, Kyoto University,
[b]Department of Advanced Radiation Technology, TARRI, QST

Imaging mass spectrometry (IMS) allows us to visualize the spatial distribution of mass-resolved materials in a sample. It attracts a growing attention as a label-free imaging technique which can be applied to wide variety of samples including biological samples. Secondary ion mass spectrometry (SIMS) is a widely-used method for desorbing and ionizing analytes along with matrix-assisted laser desorption/ionization (MALDI). Although SIMS is superior to MALDI in lateral spatial resolution, it has a significant shortcoming in sensitivity to large organic molecules because the yield of high-mass ions, in particular intact molecular ions, is usually very low due to the serious fragmentation in the desorption/ionization process in SIMS. Recently, we have found that the yield of intact molecular ions is significantly enhanced when a thin film of an amino acid on a self-supporting silicon nitride (SiN) membrane is bombarded with 5-MeV C_{60}^{+} ions from the SiN side and the positive secondary ions emitted in the forward direction are detected [1]. This result indicates that transmission SIMS using MeV C_{60} primary ions is promising for SIMS imaging with higher sensitivity to biological molecules. Thus we have recently developed a transmission SIMS imaging system equipped with a modified photoelectron emission microscope (PEEM). The PEEM acquires the image of position of the secondary electron emission from the sample surface on the entrance side for each primary ion to specify the position where each secondary ion is ejected. In this study, imaging experiments were conducted with the system to examine the performance, in particular the lateral resolution.

A thin-film sample with a microscale 2D pattern of phenylalanine and gold was prepared in the following manner. First, gold film (thickness ~15 nm) was evaporated on one side (back side) of a self-supporting silicon nitride (SiN) membrane to prevent charging during the SIMS. Then, phenylalanine film (thickness ~40 nm) was evaporated on the other side (front side) of the membrane. Finally, gold (thickness ~20 nm) was deposited again on the phenylalanine film through the mask of a cupper grid mesh to form a microscale 2D grid pattern. Transmission SIMS of the sample was performed using 9-MeV C_{60}^{2+} primary ions from the 3-MV Tandem accelerator of TIARA. The ion beam collimated to the size of ~0.2 × 0.2 mm^2 was incident on the sample from the back side. The beam intensity was not higher than ~200 cps to reduce the occurrence of an accidental coincidence. The secondary electron microscope was operated with the extractor voltage of 10 kV and the field-of-view diameter of 125 µm.

Figure 1 shows an example of the mass spectrum of positive secondary ions. No peak corresponding to the protonated intact molecules is clearly recognizable at *m/z* 166, whereas there are peaks corresponding to relatively high-mass fragment ions originating from phenylalanine at *m/z* 77, 91, 103 and 120. Figure 2 shows the mass-resolved image showing the lateral position from which those fragment ions were ejected. The 2D pattern of phenylalanine and gold with a sharp boundary is observed. The width of the boundary is about 1.4 µm, which specifies the upper limit of the lateral resolution of the IMS system.

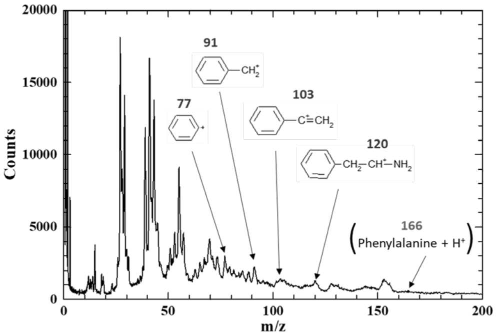

Fig. 1. Mass spectrum of positive secondary ions from the thin-film sample with a microscale 2D pattern of phenylalanine and gold.

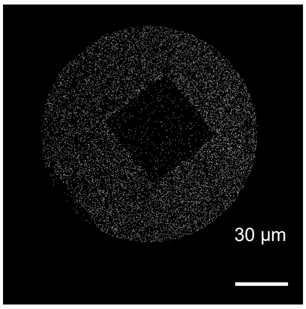

Fig. 2. Mass-resolved image of the thin-film sample with a microscale 2D pattern of phenylalanine and gold. The lateral positions where fragment ions originating from phenylalanine were ejected are shown with bright spots.

Reference

[1] K. Nakajima *et al.*, Appl. Phys. Lett. **104**, 114103 (2014).

3 - 14

Development of Micro Processing Technology by C_{60} Ion Beams

T. Kunibe [a], H. Takeuchi [a], H. Arai [a], H. Hashimoto [a], K. Narumi [b],
Y. Saitoh [b], A. Chiba [b], K. Yamada [b] and Y. Hirano [b]

[a] Engineering Department, Metal Technology Co. Ltd.,
[b] Department of Advanced Radiation Technology, TARRI, QST

Since diamond surfaces synthesized with a plasma CVD method usually have unevenness of about several μm [1], polishing of cutting tools is usually performed on a rotating disk with diamond abrasives (a scaife polishing method). However, it is not easy to apply synthesized diamonds to heat sinks, optical windows, and semiconductor substrates because it requires smoothing of a relatively large area; furthermore, abrasion of the polishing plate and scratches on the substrate sample are also problems. There are few applications other than cutting tools.

In the previous study [2], Si sputter rates by C_{60}-ion bombardment are up to about 600 per C_{60} ion compared to Ar ions, so high-speed processing of diamond can be expected. We have reported diamond sputter rates by C_{60}-ion bombardment vertical to the surface: The sputter rate by C_{60} ions is approximately 100 times higher than that by Ar ions; futhermore, the surface sputtered by the former is smoother than that by the latter. In this report, two tests are reported: One is angular dependence of diamond sputter rate by C_{60}-ion bombardment. The other is effect of co-irradiation with C_{60} ions and oxygen ions, which can induce chemical reactions on a diamond surface in addition to physical sputtering.

60-keV C_{60}-ion irradiation was carried out using a 400-kV ion implanter of TIARA. Single crystal diamond substrates (3 mm × 3 mm × thickness 1 mm, TMD-Ib type) manufactured by Tomei Dia Ltd. and single crystal silicon substrates were used as the irradiation samples. Co-irradiation with C_{60} and oxygen ions were performed as shown in Fig. 1, where a 1-keV oxygen-ion beam was extracted from an ECR ion source installed to the irradiation chamber. The etched depth of the irradiated sample was measured with New View 600s, manufactured by Zygo Co. This device can measure a three-dimensional shape of a surface within a range of several mm^2. It is possible to obtain the sputter rate from the etched volume even if the beam distribution is somewhat non-uniform.

The obtained results are summarized in Fig. 2. As shown in the figure, the sputter rates at irradiation angles of 45 and 60 degrees are approximately four times as high as those of the vertical irradiation. From the view point of smoothing a surface, such angular dependence of the sputter rate seems to be more advantageous than chemical etching, which has no angular dependence. Furthermore, the co-irradiation effect is observed: the sputter rate by simultaneous irradiation with C_{60} (1×10^{16} /cm^2) and oxygen (230 nA for 200 min.) ions is approximately two times as high as that only with C_{60} ions, while etching rate only by oxygen ions was 1/3 of the latter. It is speculated that the sputtering by C_{60} ions can be accelerated by the chemical-etching effect of oxygen ions.

It was found that both of the oblique irradiation with C_{60} ions and simultaneous irradiation with C_{60} and oxygen ions increase the sputter rate without roughing a surface of a single crystal diamond. In the future, we plan to verify an effect of C_{60}-ion irradiation on smoothing a surface.

References

[1] H. Tokura, J. Jpn. Soc. Precis. Eng. **78**, 215 (2012). (in Japanese)

[2] K. Narumi *et.al.*, JAEA-Review 2009-066, 55 (2010). (in Japanese)

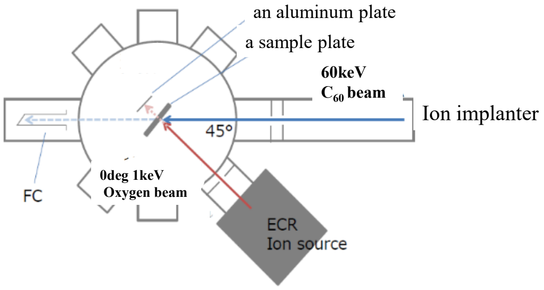

Fig. 1. Schematic of simultaneous irradiation with C_{60} ions (45° incidence) and oxygen ions.

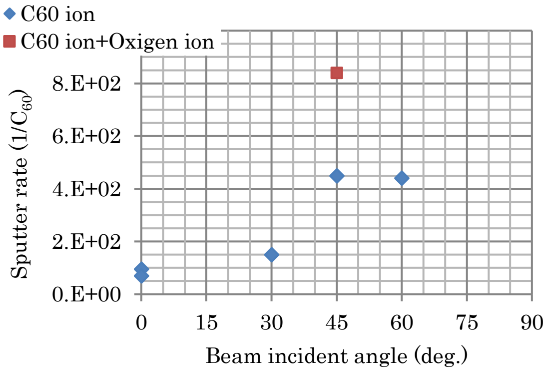

Fig. 2. Angular dependence of the sputter rate of C_{60} ions for single crystal diamond with energy of 60 keV.

3 - 15 Surface Structure of Si Irradiated by C_{60} Cluster Ion Beams with Different Irradiation Angles

Y. Murao[a], N. Nitta[a], H. Tsuchida[b], S. Tomita[c], K. Sasa[d], K. Hirata[e], H. Shibata[f],
Y. Hirano[g], K. Yamada[g], A. Chiba[g], Y. Saitoh[g], K. Narumi[g] and Y. Hoshino[h]

[a]School of Environmental Science and Engineering, Kochi University of Technology,
[b]Quantum Science and Engineering Center, Kyoto University,
[c]Institute of Applied Physics, University of Tsukuba,
[d]Tandem Accelerator Complex, University of Tsukuba,
[e]National Metrology Institute of Japan, AIST,
[f]The Institute of Scientific and Industrial Research, Osaka University,
[g]Department of Advanced Radiation Technology, TARRI, QST,
[h]Department of Mathematics and Physics, Kanagawa University

Si is the most common semiconductor material, and it is expected to be applied to electronic devices by fabricating fine structures on the surface. Photolithography has been used as a process for fabricating Si microstructures, however, multiple wet processes are required. As an alternative method, the microstructures structure can be fabricated in a dry process of ion beam irradiation. Cluster ion beam irradiation induces sputtering more efficiently than single atoms on the material surface. It has been reported that a ripple structure is formed on the surface of Si irradiated with a monatomic ion beam [1], [2]. In this study, the surface structures of Si after irradiation with C_{60} cluster ion beams at different angles were investigated by electron microscopy.

The mirror-polished Si(001) and Ge(001) single crystal substrates were irradiated with C_{60}^+ cluster ion beam using an ion implanter (NH40SR, Nissin Electric, QST) and a tandem Pelletron accelerator (9SDH-2, National Electronic Corporation, QST). A well-collimated C_{60}^+ projectile with incident energy of 6-MeV was incident at 0°, 30°, and 60° to the surface normal of samples. The fluence of the C_{60}^+ beams was set to 1×10^{14} and 5×10^{15} ions cm^{-2}. The irradiation temperature was room temperature. The evaluation of the surface was performed with a SEM (SU8020, Hitachi, KUT) and a TEM (2100F, Jeol, KUT) The TEM samples were prepared by micro-sampling using a FIB (Quanta 3D 200i, FEI, KUT).

Table 1 summarizes the types of surface structures of Si after irradiation of6-MeV C_{60}^+ beams with different irradiation angle and dose. In the case of small irradiation dose and small irradiation angle, the concave and convex structure was formed on the surface, and in the case of large irradiation dose, the string-like structure was formed.

Fig. 1 shows surface SEM images and cross-sectional TEM images of Si (irradiation angle: 0º, 60º) irradiated with 6-MeV C_{60}^+ beams at 5×10^{14} ions cm^{-2}. The observation angle of SEM images was 0º and TEM images were observed at (011) incidence. In the surface SEM image, there was no difference between the structures obtained at the irradiation angles of 0º and 60º, however in the cross-sectional TEM image, it was confirmed that the surface structure was tilted in the irradiation direction at the irradiation angle of 60º. The amorphous layer was observed both the irradiation angle of 0º and 60º. It was also confirmed that the size of string-like structure at the irradiation angle of 60º is larger than that obtained at the irradiation angle of 0º. It is thought that the effect of sputtering is greater due to the tilted irradiation angle.

References

[1] J. Erlebacher *et al.*, Phys. Rev. Lett. **82**, 2330 (1999).
[2] B. Ziberi *et al.*, Phys Rev. B **72**, 235310 (2005).

Table 1
Types of surface structures of Si after irradiation of 6-MeV C_{60}^+ beams.

Angle (°)	$1×10^{14}$	$5×10^{14}$ (cm^{-2})
0	concave and convex	string-like
30	concave and convex	string-like
60	string-like	string-like

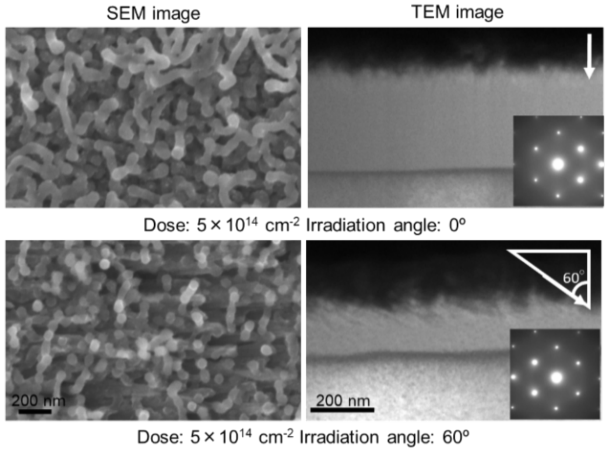

Fig. 1. Surface SEM images and cross-sectional TEM images of Si irradiated with 6-MeV C_{60}^+ beams.

3 - 16

Comparison of Total Yields of Negative Secondary Ions Emitted by C₆₀ Ion Impacts in Sub MeV to MeV Range for a Poly(methyl methacrylate) Target

K. Hirata[a)], K. Yamada[b)], A. Chiba[b)], Y. Hirano[b)], K. Narumi[b)] and Y. Saitoh[b)]

[a)]National Metrology Institute of Japan, AIST,
[b)]Department of Advanced Radiation Technology, TARRI, QST

When a primary ion impacts a solid target, secondary ions (SIs) are emitted from the target surface due to energy transfer from the primary ion to the target. Yields of the emitted SIs strongly depend on various parameters of the target and incident ions, and cluster ion impacts, where the constituent atoms of the cluster deposit their energy to a very small area of the target surface, provide higher SI emission yields. C_{60} ion is one of the most useful primary cluster ions to enhance SI emission yields due to its large cluster number and is promising candidates as primary ion species for highly sensitive SI mass spectrometry [1,2]. In this paper, we report total yields of negative SIs (N-SIs) emitted by energetic C_{60} ion impacts ($TY_{\text{N-SI}}$) in the sub-MeV to MeV energy range on a poly(methyl methacrylate) (PMMA) film target to study the effect of C_{60} impact energy on N-SI emission yield [3]. For $TY_{\text{N-SI}}$, it is difficult to obtain it by direct measurements of primary ion beam and N-SI electric currents (ECs) because the measured EC of negative secondary particles must be separated into ECs for N-SIs and for secondary electrons (SEs). We obtained it using a time-of-flight (TOF) spectrometer by counting only the N-SI number [3].

The experiments were performed using C_{60} ion beams with energies of 0.12 to 5.0 MeV at QST/Takasaki. A direct C_{60} ion beam with a current of several tens of fA was pulsed by electrostatic deflection plates triggered by a pulse generator and a series of collimators to obtain single impact per pulse condition. The pulsed C_{60} ion beam was incident on a PMMA target at an angle of 45° to the target surface. N-SIs produced by C_{60} ion impact, together with SEs, were detected by a microchannel plate (MCP) placed at the end of a TOF spectrometer. The N-SI and SE detection counts were separated by measuring and sorting the time difference between each counting signal and its corresponding start signal for primary ion beam pulsing, based on event-by-event measurements. We compared $TY_{\text{N-SI}}$ using the ratio $R_{\text{N-SI/D-event}}$ ($\equiv N_{\text{N-SI}}/N_{\text{D-event}}$), where $N_{\text{N-SI}}$ and $N_{\text{D-event}}$ are the total numbers of detected N-SIs and of their corresponding start signals, respectively, based on our previous model for event number analysis [4], as described below [3].

In the case of that N-SIs are emitted from a target with a fixed number n ($n \geq 1$) for one start signal, the probability that a number p of N-SIs is counted for one start signal by a detection system with an efficiency γ ($0 < \gamma < 1$) is given by ${}_nC_p(1-\gamma)^{n-p}\gamma^p$. As the N-SI detection events should be $p \geq 1$, the mean number of detected N-SIs for each N-SI detection event, *i.e.*, $R_{\text{N-SI/D-event}}$, is expressed by using the probability for $p \geq 1$ events $1-(1-\gamma)^n$ as

$$R_{N-SI/D-event} = \sum_{p=1}^{n} p \frac{{}_nC_p(1-\gamma)^{n-p}\gamma^p}{1-(1-\gamma)^n} = \frac{n\gamma}{1-(1-\gamma)^n} \quad (1).$$

When the N-SI number n has a probability distribution (PD) with a mean number μ, $P_n(\mu)$, $R_{\text{N-SI/D-event}}$ is expressed by

$$R_{N-SI/D-event} = \sum_{n=1}^{n_{max}} \frac{P_n(\mu)}{1-P_0(\mu)} \frac{n\gamma}{1-(1-\gamma)^n} \quad (2),$$

where $P_0(\mu)$ is the probability that an N-SI is not emitted even when the primary ion is incident on the target, and n_{max} is the maximum N-SI number for analysis. Equation (2) is expected to be asymptotic to $R_{\text{N-SI/D-event}} = \mu\gamma$ at large μ as $P_0(\mu)$ approaches 0 and the $\mu\gamma/[1-(1-\gamma)^n]$ term with large n, which is approximated to $\mu\gamma$ at large n, makes a large contribution to the sum in Eq. (2). Based on a recent study of the PDs of N-SI number for sub-MeV C_{60} ion impacts [5] and analysis of $R_{\text{N-SI/D-event}}$ values for the experiment, $TY_{\text{N-SI}}$ can be estimated by $TY_{\text{N-SI}} \approx R_{\text{N-SI/D-event}}/\gamma$ (γ should be constant within a series of measurements) [3]. Figure 1 shows the $TY_{\text{N-SI}}$ values for C_{60} impact energy of 0.12 to 5.0 MeV, where the values are displayed as the ratio R_{TY} of the $TY_{\text{N-SI}}$ value to that for 1.08-MeV C_{60}, to compare the values among the impacts. This gives information on the relative N-SI emission yield for C_{60} ion impact; the total N-SI emission yields increases with increasing C_{60} impact energy studied.

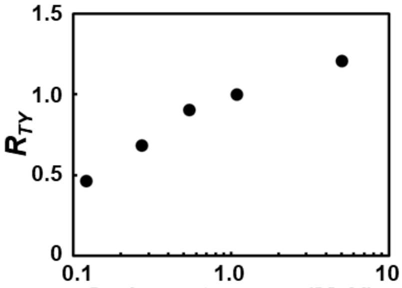

Fig. 1. Dependence of R_{TY} of N-SIs for a PMMA target on C_{60} ion impact energy.

References

[1] K. Hirata *et al.*, Nucl. Instrum. Meth. Phys. Res. B **266**, 2450 (2008).
[2] K. Hirata *et al.*, Rev. Sci. Instrum. **85**, 033107 (2014).
[3] K. Hirata *et al.*, J. Appl. Phys. **127**, 214302 (2020).
[4] K. Hirata *et al.*, J. Chem. Phys. **145**, 234311 (2016).
[5] K. Hirata *et al.*, Nucl. Instrum. Meth. Phys. Res. B **460**, 161 (2019).

3 - 17

Shape Elongation of Embedded Metal Nanoparticles Induced by C_{60} Cluster Ion Irradiation

H. Amekura[a], K. Narumi[b], A. Chiba[b], Y. Hirano[b], K. Yamada[b],
S. Yamamoto[c] and Y. Saitoh[b]

[a]Center for Green Research on Energy and Environmental Materials, NIMS,
[b]Department of Advanced Radiation Technology, TARRI, QST,
[c]Department of Advanced Functional Materials Research, TARRI, QST

Shape elongation of embedded nanoparticles (NPs) induced under swift heavy ion (SHI) irradiation has been extensively studied for this decade [1]. While the mechanism is still under debate, the majority agree with an assumption that large electronic energy deposition induced by SHIs plays an important role.

Primarily SHI is defined by its high velocity, i.e., large kinetic energy per nucleon, which is higher than ~0.1 MeV/u. An arising question is whether the shape elongation of NPs is induced under irradiation with slow ions but high electronic stopping power Se. We have irradiated Zn NPs with 6 MeV C_{60}^+ ions, which have a slow velocity of 0.008 MeV/u. The Se value of the C_{60} ions was estimated as the sum of independent sixty pieces of 6 MeV/60 = 0.1 MeV carbon monomer ions. The estimated value was 15.5 keV/nm in silica, which was comparable to Se of 200 MeV Xe SHIs.

However, contrary to SHIs, the cluster ions interact with NPs in shallow depth only. A C_{60} ion injected into a solid can be no longer stable, which is suffered by atomic collisions with constituent atoms in the solid. The interatomic distances increase with the depth and finally the C_{60} ion is no longer a cluster ion but 60 pieces of C monomer ions. While the ion range of 100 keV C-monomer ion is 315 nm in silica, the cluster effect can be active only much shallower than the ion range of 315 nm. We formed Zn NPs in the surface layer of silica (SiO_2) shallower than 70 nm [2] using 60 keV Zn^+ ion implantation to a fluence of 1×10^{17} Zn-ions/cm^2.

We have irradiated shallow Zn NPs in SiO_2 with C_{60}^+ ions of 1, 2, 4, and 6 MeV using a high-flux C_{60} negative ion source, which were recently developed in TARRI, QST [3]. While obvious optical anisotropy due to the shape elongation of Zn NPs was observed at the fluence of 1×10^{13} C_{60}/cm^2, TEM observation indicated only weakly elongated NPs only. If the fluence could increase to 5×10^{13} C_{60}/cm^2, clearer elongation would be induced. However, highly efficient sputtering destroyed the NPs and mostly removed them from the sample at 5×10^{13} C_{60}/cm^2.

While the mean sizes of our Zn NPs were ~10 nm, Rizza et al. reported that Au NPs of ~30 nm showed the highest elongation efficiency [4]. Then, we have applied a new synthesis method of NPs in SiO_2 [5]. First, Au thin film of 3 nm was deposited on SiO_2 wafers by e-beam evaporation. After then, rapid thermal annealing at 300°C for 10 minutes transformed the Au film to Au NPs on the SiO_2 surface. Finally, a SiO_2 layer of 100 nm thick was deposited in order to form embedded Au NPs in SiO_2. The NPs formed are in nearly oblate spheroid shapes as shown in Fig. 1(a). The mean major axis diameter was ~20 nm. The samples were irradiated with 4 MeV C_{60}^+ ions with an incident angle of 45°. The total fluence was 5×10^{13} C_{60}/cm^2. Obvious deformation, which is probably ascribed to the shape elongation of NPs, was observed [5].

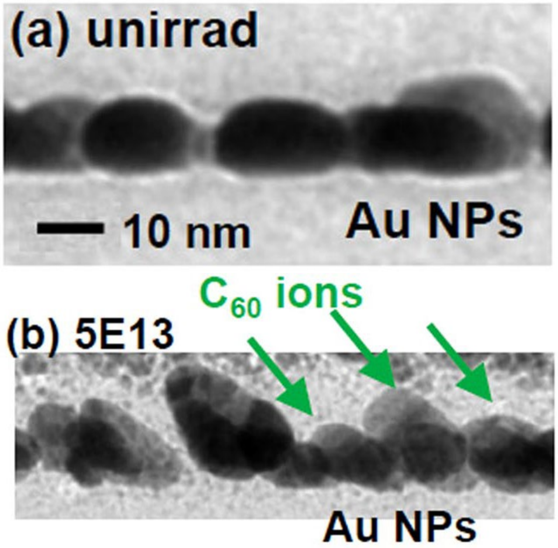

Fig. 1. Cross-sectional TEM images of Au oblate spheroids embedded in SiO_2, in unirradiated state (a) and after the irradiation to 5×10^{13} C_{60}/cm^2 (b). The incident angle of the 4 MeV C_{60}^+ beam was 45° [5].

References

[1] H. Amekura *et al.*, *Shape Elongation of Nanoparticles Induced by Swift Heavy Ion Irradiation,* in "Ion Irradiation of Dielectrics for Photonic Applications" (Springer Nature, Singapore, 2020), Chap. 5.

[2] H. Amekura *et al.*, in *"Lecture Notes in Nanoscale Science and Technology" Vol. 5*, ed. Z. Wang (Springer, New York, 2009), p. 1~75.

[3] A. Chiba *et al.*, Quantum Beam Science **4**, 13 (2020).

[4] G. Rizza *et al.*, Phys. Rev. B **86**, 035450 (2012).

[5] H. Amekura *et al.*, Sci. Rep. **9**, 14980 (2019).

3 - 18

Analysis of J-HBC Stripper Foil for the J-PARC RCS

M. Yoshimoto[a)], T. Nakanoya[a)], Y. Yamazaki[a)] P.K. Saha[a)], M. Kinsho[a)], S. Yamamoto[b)],
H. Okazaki[b)], T. Taguchi[c)], N. Yamada[d)] and R. Yamagata[d)]

[a)]Accelerator Division, J-PARC center, JAEA,
[b)]Department of Advanced Functional Materials Research, TARRI, QST,
[c)]Tokai Quantum Beam Science Center, TARRI, QST,
[d)]Department of Advanced Radiation Technology, TARRI, QST

The J-PARC RCS adopts the Hybrid type Boron-doped Carbon (HBC) stripper foil, which was developed in KEK to improve the lifetime [1]. Recently, the deposition apparatus for the HBC foils has been relocated from the KEK Tsukuba-site to the JAEA Tokai-site, where a new foil called J-HBC foil, has been fabricated since 2017 [2]. To investigate the factors for the very long lifetime of the HBC foil, the ion beam irradiation tests with a 400-keV ion implanter in TIARA were carried out and subsequent microstructure modifications in J-HBC foil were then studied by TEM observation.

Figure 1 shows typical TEM images and selected area electron diffraction (SAED) patterns of J-HBC foils for the cases with non-irradiation and after irradiation of Ar^+ beam. From the low-magnification TEM image, grains few hundred nm in size and derived from the B_4C powder in the cathode, were embedded into the amorphous carbon and boron matrix. From the high-resolution TEM images and SAED patterns, shell layers of graphite forming onion-like structure could be observed on the grain boundaries. These graphitic layers should be generated at foil deposition. In addition, the B_4C grains and the onion-like graphitic layers did not change significantly due to the beam irradiation in this experiment. Meanwhile, SAED patterns of the matrix area exhibited a drastic change from a bright and broad ring to several coaxial circles These results indicate that the amorphous carbon and boron were crystallized with beam irradiation. Indeed, the high-resolution TEM image after irradiation of J-HBC foil at matrix area reveals a mixture of amorphous and nano-sized crystalline structures as shown in Fig. 1 (b-3). The HBC foil density with 1.1 g/cm3 is rather significantly small, thus the beam irradiation easily induced the amorphous-to-crystalline transition. The beam-induced crystallization is an important issue to clarify the macro-scale specific phenomena of stripper foil.

Acknowledgments

The authors would like to thank O. Takeda, R. Saeki, and M. Mutoh of Nippon Advanced Technology Co., Ltd. for technical assistance with foil manufacturing.

References

[1] I. Sugai *et al.*, Nucl. Instrum. Meth. Phys. Res .A **561** 16 (2006).
[2] M. Yoshimoto *et al.*, EPJ Web conf. **229**, 01001(2020).

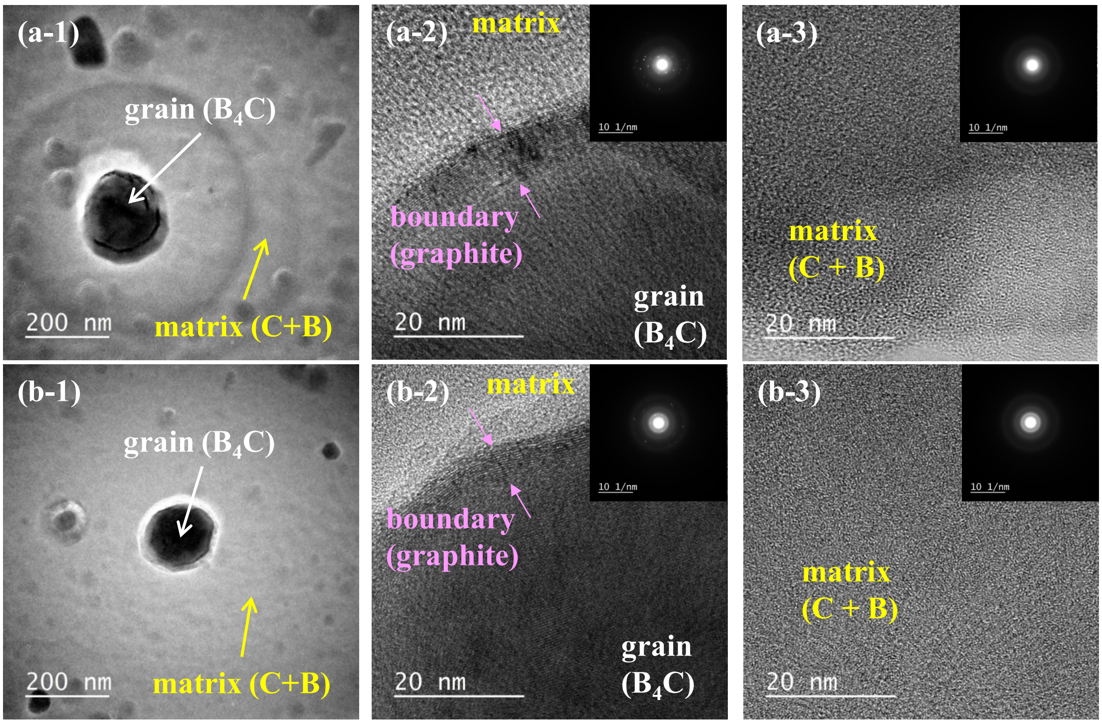

Fig. 1. Typical TEM images and SAED patterns of J-HBC foil for (a) non-irradiation and (b) after irradiation of Ar^+ beam with 200 nA for 15 min. —(-1): Low magnification TEM image, (-2): high-resolution of the grain area, and (-3): high resolution of the matrix area.

Part Ⅱ

4. Status of Quantum-Beam Facilities

4 - 01

Utilization Status at TIARA Facility

H. Hanaya[a)], I. Ishibori[a)], H. Takizawa[a)], S. Watanabe[a)],
H. Kaneko[b)], S. Kaneya[b)], M. Kawabata[b)], K. Saga[b)] and T. Shimizu[b)]

[a)]Department of Advanced Radiation Technology, TARRI, QST,
[b)]Takasaki Establishment, Radiation Application Development Association

Research & Industrial Use

Four kinds of accelerators, a cyclotron and three electrostatic accelerators (tandem accelerator, single-ended accelerator and an ion implanter), are used at the TIARA facility to meet various researchers' needs. The activities of research fields that the cyclotron was used for the past 5 fiscal years are shown in Fig. 1. Total utilization time amounted to about 2200 hours per year until FY 2015. However, after FY 2016, the total utilization time reduced due to the remodeling of a cooling system of the cyclotron facility and repair of the main coil of the cyclotron. The trend of each research field also changed after FY 2016. The utilization time of "Basic Technology of Quantum Beam" extremely decreased, as compared with the other three research fields.

On the other hand for the three electrostatic accelerators, as shown in Fig. 2, the utilization time of "Material Science" and "Basic Technology of Quantum Beam" accounted for more than about 60% of the total time. The utilization time of "Facility use program" increased since FY 2016, because JAEA users were categorized into "Facility use program", changing from "Internal use".

The trend of the number of users in the past 5 years is shown in Fig. 3. The total number of users decreased from FY 2015. The trend of the number of project category (Internal use, Joint research, Cooperation priority research, Funded research and Facility use program) for the past 5 years is shown in Fig. 4. The number of projects was in the range of 120 to 140 per year until FY 2015. However, the number had decreased since FY 2016, because projects of "Cooperation priority research", "Joint research" and "Internal use" were unified.

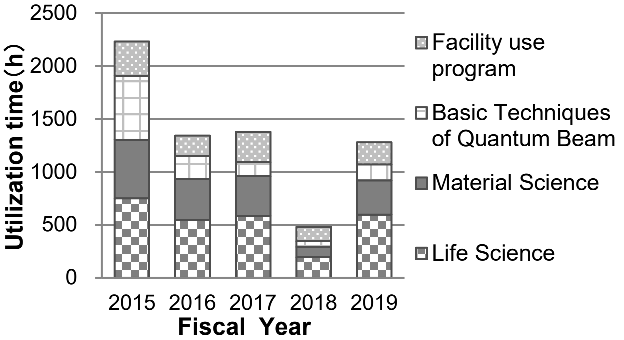

Fig. 1. Research activities for the cyclotron for the past 5 years.

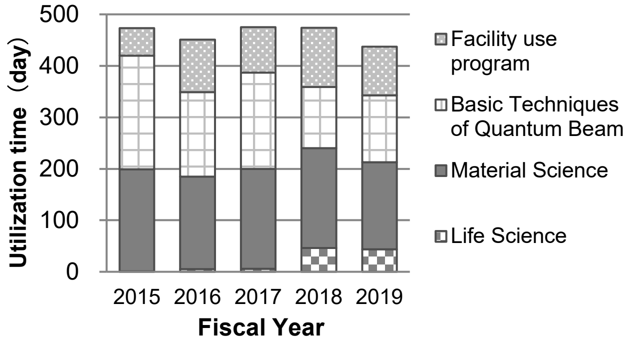

Fig. 2. Research activities for the three electrostatic accelerators for the past 5 years.

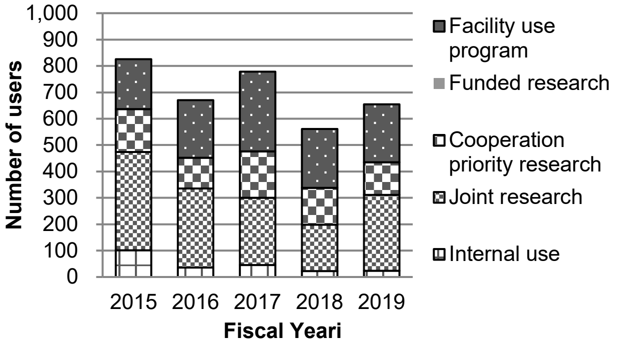

Fig. 3. The number of users for the past 5 years.

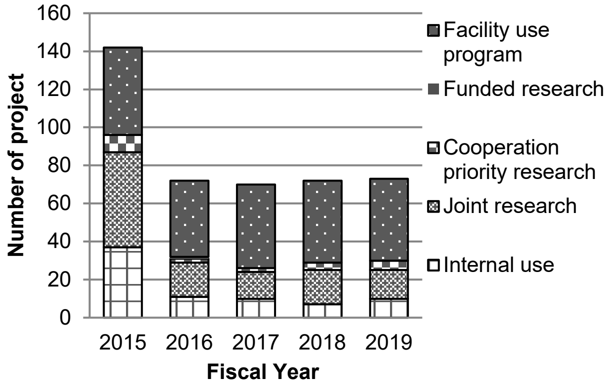

Fig. 4. The number of projects for the past 5 years.

Others

QST Takasaki science festa 2019 was held successfully in December 10 and 11, 2019 at Takasaki city gallery. The numbers of oral presentations and the poster sessions were 23 and 88, respectively. The number of participants were 563, and 27 decreased as compared with the last meeting.

The QST Takasaki annual report 2018 including 17 research projects and 88 individual research papers was published. About 700 books were mainly distributed to domestic related departments. In addition, 43 English letters to notify the URL for the download of an electric version of the annual report were sent to overseas related departments.

4 - 02

Operation of the AVF Cyclotron

K. Yoshida[a)], T. Yuyama[a)], T. Ishizaka[a)], S. Hosoya[a)], I. Ishibori[a)], N. Miyawaki[a)],
H. Kashiwagi[a)], Y. Yuri[a)], T. Nara[a)], S. Kurashima[a)], To. Yoshida[b)], S. Ishiro[b)],
Tu. Yoshida[b)], S. Kanou[b)], K. Takano[b)], H. Saitoh[b)] and T. Atobe[b)]

[a)]Department of Advanced Radiation Technology, TARRI, QST,
[b)]Beam Operation Co., Ltd.

Operation

In fiscal year of 2019, the AVF cyclotron was smoothly operated without serious trouble. The total operation time amounted to 2422 h, and monthly operation times are shown in Fig. 1. Almost all the beam tuning parameters were retuned in April after replacement of the cyclotron main coils completed in March, 2019 [1]. The scheduled maintenances were carried out from the middle of July to October and in March. Table 1 shows the statistics of the cyclotron operation of fiscal 2019, with the data of fiscal 2018 for comparison. The percentages of operation time of the year used for regular experiments, facility use program and promotion of shared use program, beam tuning, and beam development are 40.7%, 8.7%, 46.0%, and 4.6%, respectively. There was no cancellation of the experiments due to machine troubles. The accumulative operation time was 85544 h and the total number of experiments was 12296 from the first beam extraction in 1991 to March, 2020. Table 2 shows the operation time of each ion source. NANOGAN ion source is used to produce H, D, and He ions. For production of ions heavier than He, HYPERNANOGAN ion source is used. OCTOPUS ion source is mainly used for the cocktail beam of M/Q = 5. Fractional distribution of major ions used for experiments is shown in Fig. 2. The tendencies of the statistics are similar to those of the past years.

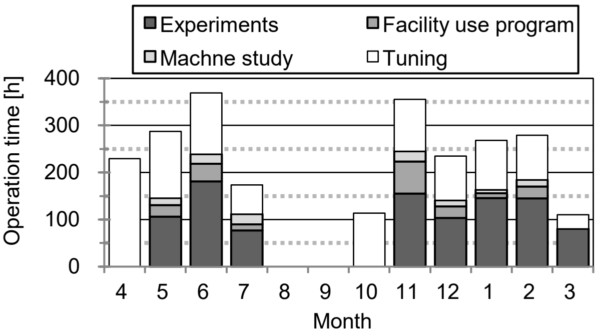

Fig. 1. Monthly operation times in fiscal 2019.

Table 1
Statistics for cyclotron operation.

Fiscal year	2018	2019
Beam service time (h)	473	1196
Beam tuning (h)	291	1113
Machine study (h)	22	113
Total operation time (h)	786	2422
Change of particle and/or energy	76 times	199 times
Change of beam course	74 times	179 times
Change of harmonic number	23 times	87 times
The number of experiments	105	246
Cancellation due to machine trouble	0	0

Table 2
Operation times of ion sources.

ECR Ion source	Operation time	Ratio
NANOGAN	819 h	29.6 %
OCTOPUS	532 h	19.2 %
HYPERNANOGAN	1419 h	51.2 %

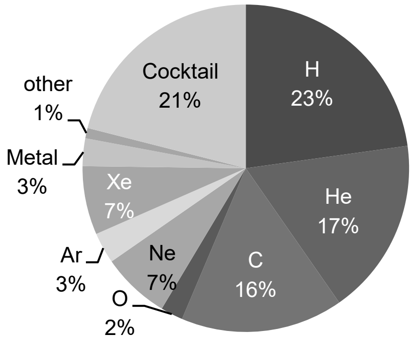

Fig. 2. Ion species used for experiments in fiscal 2019.

Machine trouble and maintenance

The number of the machine troubles of the year was 135. Twenty-seven out of those troubles needed repair.

The number of the maintenance of the year was 87. The rubber hoses of the main coils for cooling water were replaced, because the hoses considerably deteriorated due to the high temperature and radiation environment for more than 10 years. In order to avoid air leak into the vacuum chamber of the beam transport lines when the actuation valves were accidentally open with interruption of compressed air supply, the manual operation valves were installed into all the vacuum systems. The vacuum-tube of the preamplifier of the RF resonator was replaced by the last spare tube which was discontinued in 2018. Therefore, we planned to change the preamplifier system from the vacuum-tube type to the solid-state one in summer 2020.

The other major items of the maintenance were as follows: 1) Inspection of the power supplies and the main RF system 2) Change of lubricating oil for about 50 vacuum pumps. 3) Replacements of internal power supply and cooling fan in the control systems. 4) Improvement of the vacuum system in the No.4 heavy ion room. 5) Replacements of three klystrons of the microwave amplifier for the ion sources. 6) Repair of the deflector probe. 7) Periodic inspection of the gas detecting system.

References

[1] S. Kurashima *et al.*, QST Takasaki Annu. Rep. 2018, **QST-M-23**, 123 (2020).

4 - 03 Operation of Electrostatic Accelerators in TIARA

A. Chiba[a)], K. Yamada[a)], A. Yokoyama[a)], Y. Hirano[a)],
T. Takayama[b)], S. Kanai[b)], Y. Aoki[b)], M. Hashizume[b)],
Y. Takahashi[b)] and M. Hasegawa[b)]

[a)]Department of Advanced Radiation Technology, TARRI, QST,
[b)]Beam Operation Co., Ltd.

In FY2019, three electrostatic accelerators (the 3-MV tandem accelerator, the 3-MV single-ended accelerator and the 400-kV ion implanter) in TIARA have successfully completed operations for all ion irradiation experiments as planned prior to the beginning of the fiscal year. The total operating time of the single-ended accelerator, which started operation in 1991, reached 60,000 h in March 2020. The annual operating time of the tandem accelerator, the single-ended accelerator and the ion implanter were 1,752 h, 2,057 h and 1,686 h, respectively. The trends in annual operating time since the start of operation and the monthly operating time in FY2019 for each electrostatic accelerator are shown in Fig. 1 and Fig. 2, respectively. The annual operating times for three accelerators have been gradually decreasing in the last few years. In particular, the annual operating time of the single-ended accelerator in FY2019 decreased significantly, and it reduced by about 15% compared to the average operation time of the last five years, except for that in FY2015 when the accelerator stopped for several weeks due to a serious breakdown. The decreases in the annual operating times of the tandem accelerator and the ion-implanter were due to the fact that the planned outage period in August and December was about a week to 10 days longer than before. On the other hand, the annual operating time of the single-ended accelerator decreased due to the decrement of the number of applications in addition to the increase in the planned outage period. Furthermore, there was no use of electron beams with the single-ended accelerator.

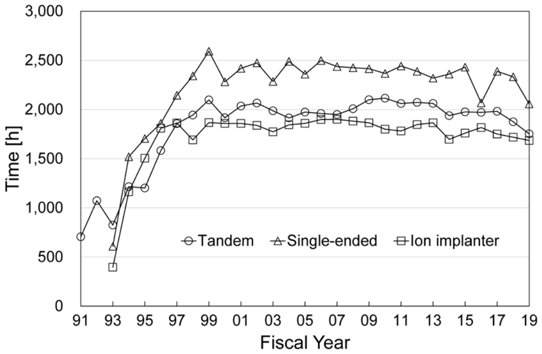

Fig. 1. Trends in annual operating times.

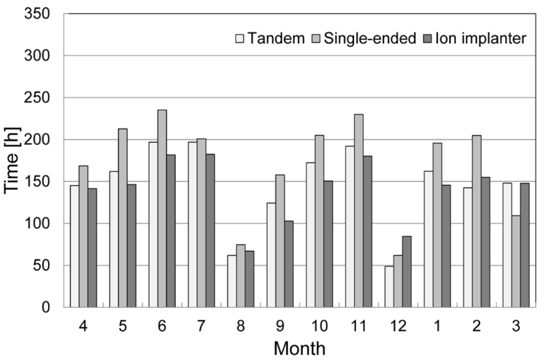

Fig. 2. Monthly operating times.

Figure 3 shows the utilization rates of ion species in each electrostatic accelerator. The C_{60} ion beams were most frequently used in the tandem accelerator and the ion implanter. One of the reasons behind this trend is the successful development of a high intensity C_{60} ion source [1]. It is the first time that H_2 ion beams have been provided using the single-ended accelerator. The H_2 beams were used for studies on the biological effects of cluster ions.

Table 1 shows the number of major troubles occurred in each accelerator in FY2019. There were no serious problems that had to stop the experiment. On the other hand, there were frequent problems that the accelerator could not be controlled due to communication errors in the control network or the terminal hangups.

Reference

[1] A. Chiba *et al.*, Quantum Beam Sci. **4**, 13 (2020).

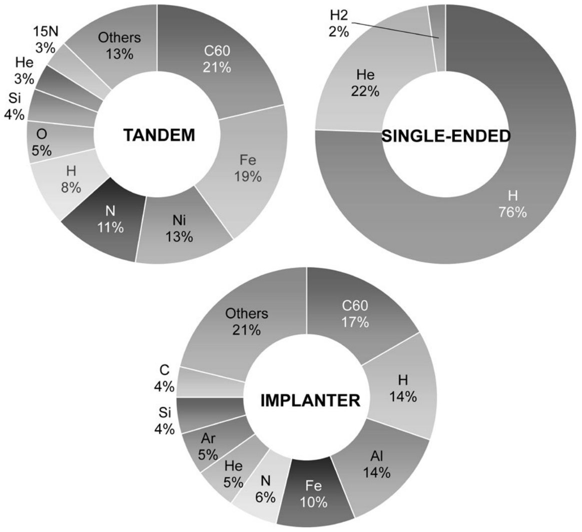

Fig. 3. Utilization rates of ion species.

Table 1
Number of troubles and maintenances in FY2019.

	Tandem	Single-ended	Ion implanter
Minor trouble	14	11	15
Serious trouble	5	2	0
Maintenance	26	20	12

4 - 04

Operation of the Electron Accelerator and the Gamma-ray Irradiation Facilities

S. Uno[a], H. Seito[a], Y. Nagao[a], S. Yamasaki[a],
Y. Haruyama[a], T. Agematsu[a], M. Hosono[a], N. Nagasawa[a],
N. Yagi[b], M. Takagi[b], K. Imai[b] and K. Akaiwa[b]

[a] Department of Advanced Radiation Technology, TARRI, QST,
[b] Takasaki Establishment, Radiation Application Development Association

Operation

The electron accelerator and the ^{60}Co gamma-ray irradiation facilities in TARRI were operated almost smoothly in Fiscal Year (FY) 2019.

The annual operation time of the electron accelerator in FY 2019 was 1,052 h, including 57 h of conditioning operation. The operation time in recent years is shown in Fig. 1. There was a lot of trouble in FY 2015. Although there was a trouble about the high frequency power supply unit of the accelerator for one month, the annual irradiation time in FY 2016 increased because long-time irradiation increased. The annual irradiation time in FY 2018 and 2019 increased because long-time irradiation increased.

The ^{60}Co gamma-ray irradiation facilities consisting of three buildings with eight irradiation rooms cover a wide dose-rate range from 2×10^{-1} Gy/h to 1.1×10^{4} Gy/h as of January 2020. The annual operation times of the first and the second cobalt irradiation facilities and the food irradiation facility were 17,064 h, 15,028 h and 10,423 h, respectively, as shown in Fig. 2. Based on the revision of the law on the regulation of radioisotopes etc., the regulations and implementation guidelines for the protection of specific radioisotopes at TARRI were formulated and became operational on September 1, 2019.

Maintenance

・*Electron accelerator*

The trouble of the horizontal beam line occurred at the beginning of December 2017, and generation of the horizontal beam came to a halt. We found that this trouble was due to trouble at the capacitor on the power supply circuit for the electron gun, not to trouble at the filament by the maintenance in 2018. This repair was performed during the maintenance inspection conducted in October 2019 and we confirmed that the electron beams were generated from the horizontal beamline.

・*Gamma-ray irradiation facilities*

The periodical maintenance check mainly on mechanical systems for radiation source transportation is performed every year on one of the three gamma-ray irradiation facilities in turn. The maintenance check of the food irradiation facility was done in July 2019 with suspension of operation for 19 days.

The purifier system of the water pools for the three gamma-ray irradiation facilities was damaged by long-time use. The activated carbon filter units were renewed in February 2020. Besides, damaged electrical equipment on the field control panel was replaced and the water storage tank circulation system and its piping were installed.

The total amount of ^{60}Co sources of all the facilities in TARRI has decreased by isotope decay. New ^{60}Co sources were installed to the second ^{60}Co gamma-ray irradiation facility in December 2019. Therefore, the maximum dose rate has increased in an irradiation room of the second irradiation facility. In addition, the data logger systems in the cobalt facilities were updated in January 2020 due to the end of support for the OS in the systems.

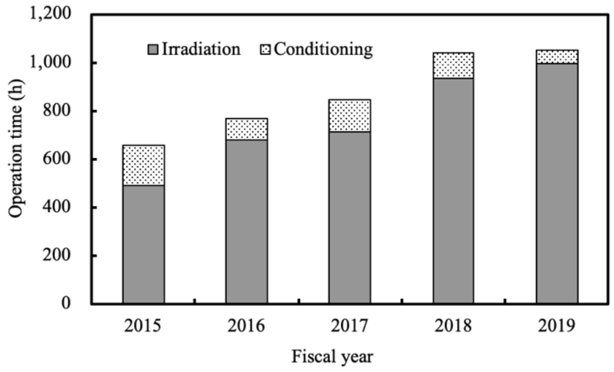

Fig. 1. Annual operation time of the electron accelerator.

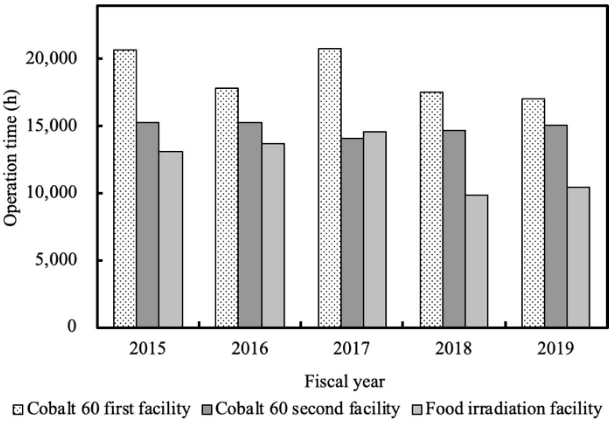

Fig. 2. Annual operation times of the ^{60}Co gamma-ray irradiation facilities.

4 - 05

Utilization Status of the Electron Accelerator and the Gamma-ray Irradiation Facilities

S. Uno[a)], H. Seito[a)], Y. Nagao[a)], S. Yamasaki[a)],
Y. Haruyama[a)], T. Agematsu[a)], M. Hosono[a)], N. Nagasawa[a)],
N. Yagi[b)], M. Takagi[b)], K. Imai[b)] and K. Akaiwa[b)]

[a)]Department of Advanced Radiation Technology, TARRI, QST,
[b)]Takasaki Establishment, Radiation Application Development Association

The electron accelerator and the three gamma-ray irradiation facilities were operated for various research subjects according to the operation plans of fiscal year (FY) 2019. Their research fields were classified to 'Materials science', 'Life science', and 'Quantum beam science'. Figure 1 shows the number of irradiation experiments in each research field in FYs 2015-2019. The accelerator was mainly used for NV-center process in diamonds, novel catalyst materials, graft-polymerization for new absorbent material and so on. The first cobalt gamma- irradiation facility was mainly employed for long-term-radiation-resistant tests, such as polymeric materials used for accelerators, cables used in nuclear power plants and nuclear reactor facilities. The second cobalt gamma-irradiation facility, including the irradiation room No.6 operated on hourly schedule, was mainly used for development of new functional materials, such as biocompatible protein hydrogels and fuel cell separator membrane, and other research subjects. The food irradiation facility of a lower-dose-rate field was used for radiation-resistant tests at wide dose-rate ranges and radiation effects of organisms such as microorganisms and plants.

Figure 2 shows the irradiation time of experiments in each research field in FYs 2015-2019. At the electron accelerator, the irradiation time increased in FYs 2017 to 2019 due to smoother operation than in FY 2015 and in FY 2016. The reasons of the time shortages in FY 2015 and 2016 are that we had troubles with high-voltage transformers and current control systems in those years, respectively. The irradiation time in FYs 2018 and 2019 increased, because of increase in long-term irradiation for research in material science, such as developing techniques of NV-center process in diamonds and novel catalyst. The classification of users in JAEA was changed from "internal users" to "external users" in FY 2016, when we transferred and integrated from JAEA to QST. Therefore, the irradiation time of internal users decreased, and that of 'Facility use program' using by external users increased. Especially in the cobalt gamma-irradiation facilities, because of the influence of procedure for transfer from JAEA to QST and decrease in long-term irradiation, the irradiation time decreased in FYs 2016 to 2018 compared to FY 2015. Irradiation-resistant experiments of various devices used in the accident of the Fukushima Daiichi Nuclear Power Station of Tokyo Electric Power Company were carried out mainly in 'Facility use program'.

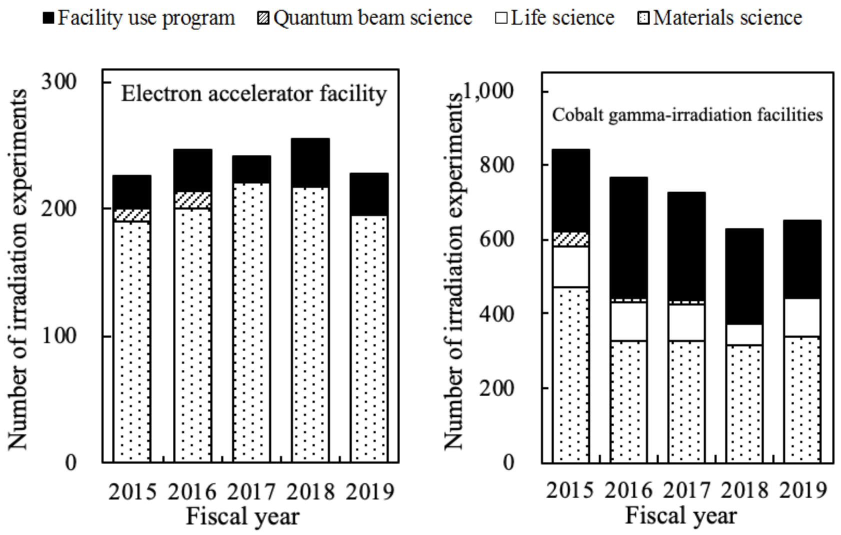

Fig. 1. The number of irradiation experiments (FY 2015-2019).

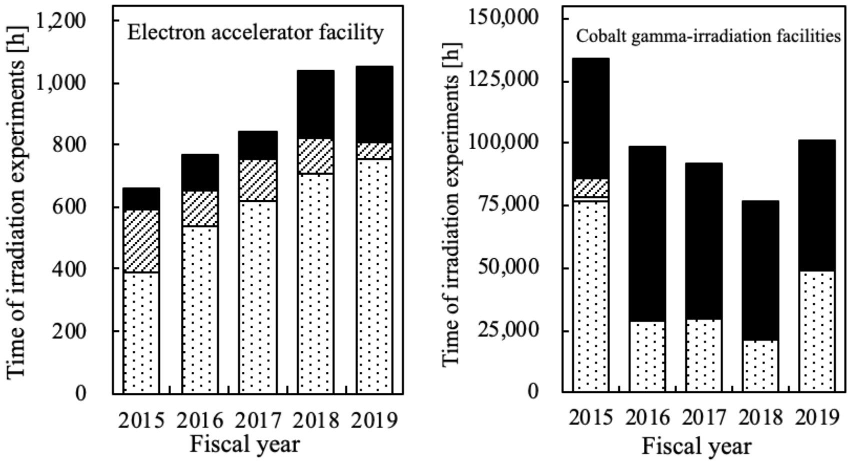

Fig. 2. The time of irradiation experiments (FY 2015-2019).

4 - 06

Radiation Monitoring in TIARA

Safety Management Section

Department of Administrative Services, TARRI, QST

Individual monitoring

(1) Individual monitoring for the radiation workers

Table 1 shows a distribution of effective dose of the radiation workers in FY 2019. The effective dose values of almost all radiation workers were below the detection limit of 0.1 mSv.

The maximum dose of the radiation worker was 0.3 mSv/y by desorption work of positron source.

Table 1
Distributions of the effective dose of the radiation workers in FY 2019.

Items		Number of persons in each periods				
		1st quarter	2nd quarter	3rd quarter	4th quarter	Annual
Distribution range of effective dose HE:Effective dose[*1] (mSv)	HE < 0.1	473	585	627	682	882
	0.1 ≦ HE ≦ 1.0	1	3	1	1	6
	1.0 < HE ≦ 5.0	0	0	0	0	0
	5.0 < HE ≦ 15.0	0	0	0	0	0
	15.0 < HE	0	0	0	0	0
Total number of persons (A)		474	588	628	683	888
Exposure above 1mSv	Number of persons (B)	0	0	0	0	0
	(B)/(A)×100(%)	0	0	0	0	0
Mass effective dose (Person･mSv)		0.1	0.4	0.3	0.1	0.9
Mean dose (mSv)		0.00	0.00	0.00	0.00	0.00
Maximum dose (mSv)		0.1	0.2	0.3	0.1	0.3

*1 The dose by the internal exposure was not detected.

(2) Individual monitoring for the visitors and others

Table 2 shows the number of people who temporarily entered the radiation controlled areas. The effective doses of all people were less than 0.1 mSv.

Table 2
The number of people who temporarily entered the radiation controlled areas in FY 2019.

Periods	1st quarter	2nd quarter	3rd quarter	4th quarter	Total
Number of persons	400	447	503	355	1,705

Monitoring of radioactive gases and dusts

Table 3 shows the maximum radioactive concentrations and total activities for radioactive gases released from the stack of TIARA, during each quarter of FY 2019.

Small amounts of ^{41}Ar, ^{11}C, ^{18}N, ^{18}F and ^{77}Br were detected occasionally during the operation of the cyclotron or experiments, but the particulate substances (^{65}Zn, etc.) were not detected.

Table 3
Monitoring results of released radioactive gases and dust in FY 2019.

Nuclide	Periods / Items	1st quarter	2nd quarter	3rd quarter	4th quarter	Total
^{41}Ar	Maximum concentration	$<1.3\times10^{-4}$	$<1.3\times10^{-4}$	$<1.3\times10^{-4}$	$<1.2\times10^{-4}$	
	Activity	2.8×10^{7}	0	0	1.5×10^{8}	1.8×10^{8}
^{11}C	Maximum concentration	2.7×10^{-4}	$<1.3\times10^{-4}$	$<1.3\times10^{-4}$	$<1.2\times10^{-4}$	
	Activity	6.9×10^{8}	2.9×10^{7}	4.4×10^{7}	1.8×10^{8}	9.4×10^{8}
^{18}N	Maximum concentration	—	—	—	$<1.2\times10^{-4}$	
	Activity	—	—	—	2.8×10^{7}	2.8×10^{7}
^{18}F	Maximum concentration	—	—	$<1.3\times10^{-4}$	—	
	Activity	—	—	2.3×10^{6}	—	2.3×10^{6}
^{77}Br	Maximum concentration	—	—	—	5.8×10^{-9}	
	Activity	—	—	—	1.8×10^{5}	1.8×10^{5}
^{65}Zn	Maximum concentration	$<6.9\times10^{-10}$	$<1.3\times10^{-9}$	$<7.1\times10^{-10}$	$<7.7\times10^{-10}$	
	Activity	0	0	0	0	0

Unit : Bq/cm^3 for Maximum concentration, Bq for Activity.

Monitoring for external radiation and surface contamination

The monitoring for external radiation and surface contamination was routinely performed in/around the radiation controlled areas. Neither anomalous value of dose equivalent rate nor surface contamination was detected.

Figure 1 shows a typical example of distribution of the dose equivalent rate in the radiation controlled area of the cyclotron building.

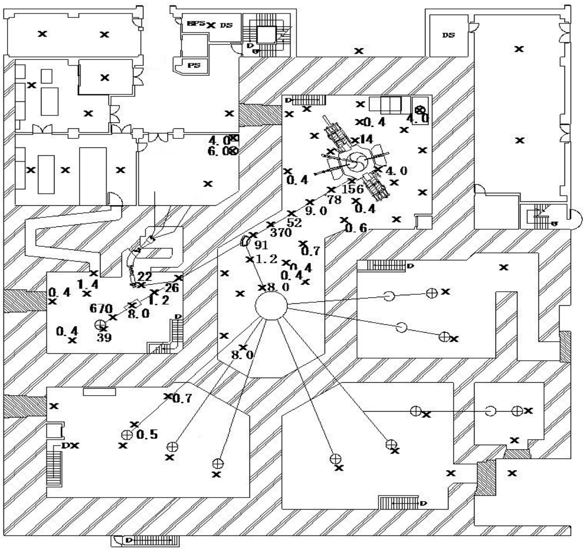

Fig. 1. Dose equivalent rate distribution in the radiation controlled area of the cyclotron building.
Measurement date : 12th, 24th and 25th March 2020,
Measuring position : Indicated with × (1 m above floor),
Unit : μSv/h.
(The values are not indicated if less than 0.2 μSv/h.)

4 - 07

Radioactive Waste Management in TIARA

N. Higuchi

Department of Administrative Services, TARRI, QST

Radioactive waste management

The radioactive waste generated in TIARA is managed by Utilities and Maintenance Section. The main radioactive waste is the solid waste generated from research experiments and the maintenance of the cyclotron. Other radioactive waste is the liquid waste such as inorganic waste fluids generated from research experiments and the air-conditioning machines in the radiation controlled area. These wastes are managed according to their properties. Radioactive waste is stored in a storage facility and handed over to the Japan Radioisotope Association for disposal.

Solid radioactive waste

Table 1 shows that the amounts of various types of solid waste were generated in each quarter of FY 2019. Combustible waste consists of papers and clothes, and so on. Flame-retardant waste consists of rubber gloves, plastic articles, and polyethylene articles. Incombustible waste consists of metal pieces, the glasses, and contaminated parts. Solid waste emitting α, β, and γ is classified according to the properties.

Liquid radioactive waste

Table 2 shows that the amounts of liquid waste were generated in each quarter of FY 2019. Most of liquid waste was inorganic waste water generated from chemical experiments and others were condensed water going out of the air-conditioner installed in the radiation controlled area. The largest amount of waste water in summer season (2nd quarter) was the condensed water. After the treatment of evaporation of the waste water, inorganic water is reused in the radiation controlled area. Only small amounts of concentrated liquid were generated by the treatment.

Table 1
Radioactive solid waste generated in FY 2019.

Amounts / Items	Amounts of generation in each period (m^3)					Number of package /drum
	1st quarter	2nd quarter	3rd quarter	4th quarter	Total	
Category β , γ*	0	0	0.14	0.30	0.44	22
Combustible	0	0	0.04	0.08	0.12	6
Flame-retardant	0	0	0.04	0.12	0.16	8
Incombustible(Compressible)	0	0	0	0.06	0.12	6
〃 (Incompressible)	0	0	0	0	0	0
Laboratory animal	0	0	0	0	0	2
Filters	0	0	0	0	0	0
Category α*	0	0	0	0.20	0.42	21
Combustible	0	0	0	0	0.02	1
Flame-retardant	0	0	0	0.16	0.26	13
Incombustible(Compressible)	0	0	0	0	0	1
〃 (Incompressible)	0	0	0	0	0	0
Laboratory animal	0	0	0	0.04	0.12	6
Filters	0	0	0	0	0	0

* defined by amount in Bq (β, γ): < 2 GBq , (α) : < 37 MBq,
** 50-liter drum.

Table 2
Radioactive liquid waste generated in FY 2019.

Amounts / Items	Amounts of generation in each period (m^3)					Number of package /drum
	1st quarter	2nd quarter	3rd quarter	4th quarter	Total	
Category β , γ*	10.84	13.40	7.99	5.93	38.16	-
1)Inorganic	10.84	13.40	7.99	5.93	38.16	-
Inorganic	10.84	13.40	7.81	5.93	37.98	treatment
Sludge, Evaporation residue	0.00	0.00	0.18	0.00	0.18	12**
2)Organic	0.00	0.00	0.00	0.00	0.00	0
Organic	0.00	0.00	0.00	0.00	0.00	0
Oil	0.00	0.00	0.00	0.00	0.00	0
Category α*	0.00	0.00	0.00	0.00	0.00	0

* defined by concentrations in Bq/mL (β, γ Inorganic) : < 200 kBq, (Organic) : < 2 kBq, (α) : ≤ 1.85 kBq,
** 50-liter container.

4 - 08

Facility Use Program in Takasaki Advanced Radiation Research Institute (TARRI)

S. Nozawa, H. Hanaya and M. Seki

Department of Research Planning and Promotion, QuBS, QST

Introduction

The use of the facilities in TARRI is widely allowed for many users in universities, public institutes, research-and-development's (R&D's) divisions of private companies, and so on (hereafter 'external users') under Facility Use Program. Under this program in TARRI, external users can use gamma-rays, electron beams, and ion beams that have been provided from the facilities of Co-60 gamma-ray, electron accelerator, TIARA's four ion accelerators, and off-line analytical instruments. When using these facilities, external users have to pay the operating charge of the equipment for irradiation.

Charging system of Facility Use Program in FY2019

Charging system of Facility Use Program is classified based on the purpose of irradiation and disclosure/non-disclosure experimental results, as shown in Table 1. On the charging system, the cost of irradiation have been calculated from the total amount of service charge, irradiation charge, and additional consumable goods and human support.

Especially, R&D's users, who disclose the experimental results by publication, are partially discounted for the costs of irradiation. To receive the discount, users are required to hand in research proposals to Research Planning and Promotion Office in TARRI. The proposals were reviewed by the expert committee members in terms of the effectiveness of experimental plans. The approved proposals have been carried out under Facility Use Program with the partially discounted cost. The users, who are categorized as Non-R&D's, such as commercial irradiation, are charged the additional depreciation cost of the irradiation facilities.

Table 1
Charging system for Facility Use Program in FY2019.

	R&D's for public disclosure	Non-disclosure R&D's	Others
Purpose	Research and Development		Non-R&D's
Belonging of Results	Non-proprietary	Proprietary	
Duty for publishing	Yes	No need to public disclosure	
Charging fees*	A	B	C

*A = handling fees + expendables fee (other charges are exempted)
B = Charging fee "A" + irradiation fee + radioactive waste disposal expenses
C = Charging fee "B" + depreciation cost for irradiation facilities

Number of irradiation experiments in FY2019

The number of irradiation experiments for each facility in FY2019 were shown in Table 2.

The main users of the four accelerators in TIARA belonged to universities and public institutes. On the other hand, many users of Co-60 gamma-ray irradiation facilities and electron accelerator belonged to private companies.

Table 2
Number of irradiation experiments at each facility under the Facility Use Program in FY2019.

Facility \ User's affiliation		University	Public Institute	Private Company	Total
TIARA	AVF cyclotron	17	5	10	32
	3 MV tandem accelerator	17	13	2	32
	3 MV single-ended accelerator	1	4	1	6
	400 kV ion implanter	12	9	3	24
Co-60 gamma-ray irradiation facilities		43	45	121	209
Electron accelerator		5	10	17	32
Total		95	86	154	335

Some outside users were inexpert for irradiation experiments. Therefore, they needed detailed information about the irradiation facilities and the related techniques of irradiation experiment. For the convenience of outside users, Research Planning and Promotion Office in TARRI provided the information for experiments at our facilities, such as preparation of request for issuance of entry permission, procedure of payment, contact person of each irradiation equipment, and so on.

The additional information about this program is available on the QST website as follows:
https://www.qst.go.jp/site/qubs/1954.html

Appendices

Appendix 1 Publication List

Items in gray show the works in collaboration with other projects of QST.
Bold letters and **numbers** at the last of each item mean as follows.
Letter : Accelerators or irradiation facilities used for the work.
C : Cyclotron, **T** : Tandem accelerator, **S** : Single-ended accelerator, **I** : Ion implanter,
E : Electron accelerator, **G** : Gamma-ray irradiation facilities, **N** : Not used.
Number that contains hyphen: Serial number of the related paper in Part II.

P1-1 Project “Functional Polymer ”

Papers

1) Y. Zhao, K. Yoshimura, H. Takamatsu, A. Hiroki, Y. Kishiyama, H. Shishitani, S. Yamaguchi, H. Tanaka, S. Koizumi, A. Radulescu, M. Appavou and Y. Maekawa, “Imidazolium-based anion exchange membranes for alkaline anion fuel cells: Interplay between morphology and anion transport behavior”, Journal of The Electrochemical Society, **166**, F472-F478 (2019). **G, 1-01, 1-02**

2) L. Bai, Y. He, J. Zhou, Y. Lim, V-C. Mai, Y. Chen, S. Hou, Y. Zhao, J. Zhang and H. Duan, “Responsive amorphous photonic structures of spherical/polyhedral colloidal metal–organic frameworks”, Advanced Optical Materials, **7**, 1900522 (2019). **N**

3) S. Koizumi, Y. Zhao and A. Patra, “Hierarchical structure of microbial cellulose and marvelous water uptake, investigated by combining neutron scattering instruments at research reactor JRR-3, Tokai”, Polymer **176**, 244-255 (2019). **N**

4) T.D. Tap, L.L. Nguyen, Y. Zhao, S. Hasegawa, S. Sawada, N.Q. Hung, L.A. Tuyen and Y. Maekawa, “SAXS investigation on morphological change in lamellar structures during propagation steps of graft-type polymer electrolyte membranes for fuel cell applications”, Macromolecular Chemistry and Physics **221**, 1900325 (2020). **G, 1-01, 1-02**

5) S. Hasegawa, A. Hiroki, Y. Ohta, N. Iimura, A. Fukaya and Y. Maekawa, “Thermally stable graft-type polymer electrolyte membranes consisting based on poly (ether ether ketone) and crosslinked graft-polymers for fuel cell applications”, Radiat. Phys. Chem., **171**, 108647 (2020). **G, 1-01, 1-02**

6) 廣木 章博, 田口 光正, “放射線架橋ゲルを母材とするポリマーゲル線量計の LET 効果”, RADIOISOTOPES, **68**, 277-283 (2019). **E, G**

7) A. Kitamura, T. Yamaki, Y. Yuri, H. Koshikawa, S. Sawada, T. Yuyama, A. Usui and A. Chiba, “Control of the size of etchable ion tracks in PVDF - Irradiation in an oxygen atmosphere and with fullerene C60”, Nucl. Instrum. Meth. Phys. Res. B **460**, 254-258 (2019). **C**

8) Y. Inagaki, N. Sakaba, N. Tanaka, M. Nomura, S. Sawada and T. Yamaki, “膜技術と水素社会 ー膜分離新 IS プロセス技術の開発ー”, 日本海水学会誌, **73**, 194-202 (2019). **G**

9) S. Sawada, M. Yasukawa, H. Koshikawa, A. Kitamura, M. Higa and T. Yamaki, “高エネルギー重イオンビームによる海水濃縮用カチオン、アニオン交換膜の開発”, 日本海水学会誌, **73**, 208-216 (2019). **G**

10) S. Sawada, H. Koshikawa, A. Kitamura, M. Higa and T. Yamaki, “Ion and water transport properties of cation exchange membranes prepared by heavy-ion-track grafting technique”, Separation Science and Technology **55**, 2211-2216 (2020). **G**

11) O. Myagmarjav, N. Tanaka, S. Kubo, M. Nomura, T. Yamaki, S. Sawada, J. Iwatsuki, H. Noguchi, Y. Kamiji, I. Ioka, T. Tsuru, M. Kanezashi, X. Yu, M. Machida, T. Ishihara, H. Abekawa, M. Mizuno, T. Taguchi, Y. Hosono, Y. Kuriki, M. Inomata, K. Miyajima, Y. Inagaki and N Sakaba, “Research and development on membrane IS process for hydrogen production using solar heat”, International Journal of Hydrogen Energy, **44**, 19141-19152 (2019). **G**

Proceedings

1) A. M. A. Mahmoud, K. Yoshimura, A. Hiroki and Y. Maekawa, “The First Durable Imidazolium-based Radiation Grafted Anion Exchange Membranes for Alkaline Fuel cells: The Impact of Water Management”, 236th ESC meeting, [Atlanta, USA] Abstracts, I01B-1487 (2019/10). **G**

2) Y. Zhao, “Small-angle Scattering Study for Developing Alkaline Durable Imidazolium-Based Grafted Anion Exchange Membranes for Pt-Free Fuel Cells”, 32nd European Crystallographic Meeting, [Atlanta, USA] Abstracts, MS20-05 (2019/10). **G**

3) K. Yoshimura, Y. Zhao, A. Mahmoud, A. Hiroki, H. Shishitani, S. Yamaguchi, H. Tanaka and Y. Maekawa, “Structural Designs of Alkaline Durable Imidazolium-Containing Anion Conducting Membranes Prepared by Radiation-Induced Grafting for Pt-Free Fuel Cells”, 2019 MRS Fall Meeting, [Boston, USA] Abstracts, EN04.01.05 (2019/10). **G**

4) A. Hiroki, S. Okushima, K. Yoshimura, Y. Zhao, H. Shishitani, S. Yamaguchi and Y. Maekawa, “Crosslinking Effects of Anion-conducting Polymer Electrolyte Membranes on their Properties”, 10th International Membrane Science & Technology Conference, [Sydney, Australia] Abstracts, 115 (2020/2). **G**

5) 吉村 公男, H. Yu, ザオ ユエ, 廣木 章博, 猪谷 秀幸, 岸山 佳央, 山口 進, 田中 裕久, 前川 康成, “イミダゾリウム基を有する放射線グラフト型アニオン伝導膜の電解質膜特性と階層構造の関係”, 第 62 回放射線化学討論会, [福井大学, 敦賀] 要旨集, 1-0 07 (2019/9). **G**

6) 柴田 康瑛, 長谷川 伸, 廣木 章博, 木下 基, 前川 康成, “放射線グラフト重合による高分子電解質膜の合成～基材膜の結晶モルフォロジーと重合性･機能性との関係～”, 日本化学会関東支部群馬地区研究交流発表会, [群馬大学, 桐生] 要旨集, P-36 (2019/12). **G**

7) 柴田 康瑛, 長谷川 伸, 廣木 章博, 前川 康成, “放射線グラフト重合法によるポリフェニレンスルフィドを基材とした高分子電解質膜の合成”, 第9回 CSJ 化学フェスタ 2019, [タワーホール船堀, 東京] 要旨集, P5-091 (2019/10).

G

8) 澤田 真一, 田中 健一, 船津 公人, 前川 康成, “高分子電解質膜のイオン伝導性を機械学習で予測する”, 第9回 CSJ 化学フェスタ 2019, [タワーホール船堀, 東京] 要旨集, I2-03 (2019/10). **G**

9) 澤田 真一, “機械学習に基づくグラフト型電解質膜の電気化学特性評価”, 第 68 回高分子討論会, [福井大学, 福井] 要旨集, 2G16 (2019/9). **G**

10) 奥島 駿, 前川 康成, 川勝 年洋, “粗視化分子動力学法とクラスター解析を組み合わせた電解質膜イオンチャネル構造の解析”, 第 68 回高分子討論会, [福井大学, 福井] 要旨集, 1G12 (2019/9). **G**

11) 澤田 真一, 田中 健一, 船津 公人, 前川 康成, “機械学習による放射線グラフト電解質膜のプロトン導電率予測”, 第 56 回アイソトープ・放射線研究発表会, [東京大学, 東京] 要旨集, 1p-III-0 (2019/7). **G**

12) S. Sawada, T. Kimura, H. Nishijima. N. Tanaka, S. Kubo. S. Imabayashi. M. Nomura and T. Yamaki, “Development of low-overvoltage membrane Bunsen reaction technology for thermochemical IS process”, World Hydrogen Technologies Convention 2019, [東京国際フォーラム, 東京] 要旨集, O2-1 (2019/6). **G**

13) 奥島 駿, “粗視化分子動力学法を用いた高分子電解質膜のイオンチャンネル構造の解析”, 第 68 回高分子学会年次大会, [大阪府立国際会議場, 大阪] 要旨集, 1Pa037 (2019/5). **G**

Patent

1) 袖子田 竜也、高橋 克巳、高橋 浩、前川 康成、陳 進華、長谷川 伸, “電解質膜および電解質膜の製造方法” 特許第 6522394 号 (2019.05.10). **G**

P1-2 Project “Advanced Catalyst”

Papers

1) S. Yamamoto, H. Koshikawa, T. Taguchi and T. Yamaki, ”Precipitation of Pt Nanoparticles inside Ion-Track-Etched Capillaries”, Quantum Beam Science **4**(1), (2020). **C, E**

2) A. Idesaki, S. Yamamoto, M. Sugimoto, T. Yamaki and Y. Maekawa, “Formation of Fe Nanoparticles by Ion Implantation Technique for Catalytic Graphitization of a Phenolic Resin”, Quantum Beam Science **4**(1), (2020), **I**

3) H. Okazaki, K. Kakitani, T. Kimata, A. Idesaki, H. Koshikawa, D. Matsumura, S. Yamamoto and T. Yamaki, “Change in electronic structure of carbon supports for Pt catalysts induced by vacancy formation due to Ar^+ irradiation”, J. Chem. Phys. **152**, 124708 (2020), **I**

4) T. Kimata, K. Kakitani, S. Yamamoto, T. Yamaki, T. Terai and K.G. Nakamura, “Platinum nanoparticles on HOPG surface modified by 380 keV Ar^+ irradiation: TEM and Raman studies”, Radiat. Eff. Defects Solids **175**, 433-439 (2020), **I**

5) R. Li, K. Narumi, A. Chiba, Y. Hirano, D. Tsuta, S. Yamamoto, Y. Saitoh, N. Okubo, N. Ishikawa, C. Pang, F. Chen and H. Amekura, “Matrix-material dependence on the elongation of embedded gold nanoparticles induced by 4 MeV C_{60} and 200 MeV Xe ion irradiation”, Nanotechnology **31**(26), (2020). **T**

6) S. Sakaguchi, T. Sakurai, A. Idesaki, H. Koshikawa, M. Sugimoto and S. Seki, “Highly Efficient Solid-State Intra-Track Polymerization of Ethynyl-Substituted Spirobifluorenes Triggered by Swift Heavy Ion Irradiations”, J. Photopolym. Sci. Technol. **33**, 91-96 (2020). **C**

7) H. Okazaki, K. Terashima, D. Billington, K. Iwata, T. Wakita, M. Tanaka, Y. Takano, Y. Muraoka and T. Yokoya, “Change in the electronic structure of the bismuth chalcogenide superconductor CsBi4−xPbxTe6 by dissociation of the bismuth dimers”, J. Phys. Condens. Matter **32**, 145501 (2020). **T, I**

8) H. Amekura, K. Narumi, A. Chiba, Y. Hirano, K. Yamada, D. Tsuya, S. Yamamoto, N. Ohkubo, N. Ishikawa and Y. Saitoh, “C_{60} ions of 1 MeV are slow but elongate nanoparticles like swift heavy ions of hundreds MeV”, Sci. Rep. **9**, 14980-1 (2019). **C**

9) A. Idesaki, Y. Kanuma, S. Yamamoto, M. Sugimoto, Y. Maekawa, T. Yamaki, “Fabrication of a nitrogen-doped carbon catalyst from a precursor polymer using the electron beam irradiation technique”, Jpn. J. Appl. Phys. **58**, SDDF03 (2019). **I**

10) A. Kitamura, N. Ishikawa, K. Kondo, S. Yamamoto, T. Yamaki, “FE-SEM observation of chains of nanohillocks in SrTiO3 and Nb-doped $SrTiO_3$ surfaces irradiated with swift heavy ions”, Nucl. Instrum. Meth. Phys. Res. B **460**, 175-179 (2019). **I, S**

11) A. Kitamura, T. Yamaki, Y. Yuri, H. Koshikawa, S. Sawada, T. Yuyama, A. Usui and A. Chiba, “Control of the size of etchable ion tracks in PVDF - Irradiation in an oxygen atmosphere and with fullerene C_{60}”, Nucl. Instrum. Meth. Phys. Res. B **460**, 254-258 (2019). **C, T**

12) S. Ito, T. Mori, A. Suzuki, H Okubo, S. Yamamoto, T. Sato and F. Ye, “Design of active site at heterointerface between brownmillerite type oxide promoter and fluorite cubic ZrO_2 in anode of intermediate temperature SOFCs”, ACS Appl. Energy Mater. **2**, 7, 5183-5197 (2019). **I, S**

13) N. Tanaka, T. Yamaki, M. Asano and T. Terai, “Effect of HIx solution concentration on ion-exchange membrane performance in electro-electrodialysis”, J. Membr. Sci. **587**, 117171 (2019). **C, G**

14) 稲垣 嘉之, 坂場 成昭, 田中 伸幸, 野村 幹弘, 澤田 真一, 八巻 徹也, “膜技術と水素社会 ー膜分離新ISプロセス技術の開発ー”, 日本海水学会誌, **73**, 194–202 (2019). **C, G**

15) 八巻 徹也, “荷電膜と「量子ビーム」との出会い 〜新たな研究開発プラットフォームへの期待〜”, 日本海水学会誌, **73**, 181 (2019). **C, G**

16) 澤田 真一, 安川 政宏, 越川 博, 喜多村 茜, 比嘉 充, 八巻 徹也, “高エネルギー重イオンビームによる海水濃縮用カチオン、アニオン交換膜の開発”, 日本海水学会誌, **73**, 208–216 (2019). **C, G**

17) S. Sawada, H. Koshikawa, A. Kitamura, M. Higa and T. Yamaki, "Ion and water transport properties of cation exchange membranes prepared by heavy-ion-track grafting technique", Sep. Sci. Technol. **55**, 2211-2216 (2020). **C, G**

18) O. Myagmarjav, J. Iwatsuki, N. Tanaka, H. Noguchi, Y. Kamiji, I. Ioka, S. Kubo, M. Nomura, T. Yamaki, S. Sawada, T. Tsuru, M. Kanezashi, X. Yu, M. Machida, T. Ishihara, H. Abekawa, M. Mizuno, T. Taguchi, Y. Hosono, Y. Kuriki, M. Inomata, K. Miyajima, Y. Inagaki and N. Sakaba, "Research and development on membrane IS process for hydrogen production using solar heat", Int. J. Hydrog. Energy **44**, 19141–19152 (2019). **C, G**

19) A. Kitamura, N. Ishikawa, K. Kondo, Y. Fujimura, S. Yamamoto and T. Yamaki, "FE-SEM observations of multiple nanohillocks on SrTiO3 irradiated with swift heavy ions", Trans. Mat. Res. Soc. Jpn. **44**, 85–88 (2019). **I, S**

20) T. Taguchi, S. Yamamoto and H. Ohba, "Synthesis of novel hybrid carbon nanomaterials inside silicon carbide nanotubes by ion irradiation", Acta Materialia **173**, 153–162 (2019). **I, S**

21) K. Amemiya, H. Koshikawa, M. Imbe, T. Yamaki and H. Shitomi, "Perfect blackbody sheets from nano-precision microtextured elastomers for light and thermal radiation management", J. Mater. Chem. C **7**, 5418–5425 (2019). **C**

22) T. Kimata, K. Kakitani, S. Yamamoto, T. Yamaki, T. Terai and K. G. Nakamura, "Raman spectroscopy of Ar^+-irradiated graphite surfaces supporting platinum nanoparticles", Nucl. Instr. Meth. Phys. Res. B **444**, 6–9 (2019). **I**

23) H. Ishitobi, S. Sugawara, K. Oba , T. Hirano, H. Doki, Y. Handa, Y. Sato, S. Yamamoto and N. Nakagawa, "Highly Active Electrode With Efficiently Added Surface Oxygen Groups for a Vanadium Redox Flow Battery", Journal of Electrochemical Energy Conversion and Storage, **17**(3), 031001 , (2019). **E**

24) N. Nakagawa, H. Ishitobi, S. Abe, M. Kakinuma, H. Koshikawa, S. Yamamoto and T. Yamaki, "A novel method to enhance the catalytic activity of PtRu on the support using CeO_2 by high-energy ion-beam irradiation", Catalysis Today, (2019). **I**

25) 小川 達彦, 佐藤 達彦, 八巻 徹也, "飛跡構造計算に基づく無機シンチレータ発光強度の予測", 放射線化学, **108**, 11-17 (2019). **N**

Proceedings

1) 雨宮 邦招, 清水 雄平, 越川 博, 井邊 真俊, 八巻 徹也, 蕨 洋司, "「光吸収率 99.5%以上」と「高い耐久性」を両立した「暗黒シート」開発への挑戦"【招待講演】, ものづくりパートナーフォーラム東京 2019, [東京都港区], (2019/11). **C**

2) 雨宮 邦招, 清水 雄平, 井邊 真俊, 蕨 洋司, 越川 博, 八巻 徹也, "全ての光を吸収する究極の暗黒シート 高い耐久性も両立、遮光・乱反射防止・迷光除去に"【招待講演】, 産総研テクノブリッジフェア 2019 in つくば, [つくば市], (2019/10). **C**

3) T. Ozaki, S. Semboshi, T. Sueyoshi, H. Okazaki, H. Koshikawa, S. Yamamoto, T. Yamaki and H. Sakane, "Vortex dynamics of REBCO films irradiated with low-energy ion irradiations",【Invited talk】, Materials Research Meeting 2019, [Yokohama], (2019/12). **T, I**

4) S. Yamamoto, T. Taguchi, A. Idesaki, H. Okazaki, H. Koshikawa, T. Yamaki and T. Mori, "Electron-Beam-Induced Formation of Pt Nanoparticles on Oxide Films",【Invited talk】, 20th International Union of Materials Research Societies International Conference in Asia, International Union of Materials Research Societies, [Perth, Australia], (2019/9). **E**

5) T. Ozaki, S. Semboshi, T. Sueyoshi, H. Okazaki, H. Koshikawa, S. Yamamoto, T. Yamaki and H. Sakane, "Vortex pinning landscape by ion irradiation for REBCO thin films",【Invited talk】, Cryogenic Engineering Conference and International Cryogenic Materials Conference 2019 (CEC-ICMC 2019), [Hartford], (2019/7). **T, I**

6) 宮下 太志, 野村 幹弘, 澤田 真一, 八巻 徹也, "重イオンビームによる高性能イオン交換膜の開発", 第 22 回化学工学会学生発表会, [東京都文京区], C01 (2020/3). **C, G**

7) 小幡 隆亮, 土岐 帆乃佳, 石飛 宏和, 山本 春也, 岡崎 宏之, 中川 紳好, "バナジウムレドックスフロー電池に用いるカーボン電極に電子線照射が与える影響", 化学工学会, [大阪府吹田市], (2020/03). **E**

8) 雨宮 邦招, 清水 雄平, 越川 博, 井邊 真俊, 八巻 徹也, 蕨 洋司, "マイクロ空洞加工による面状黒体(暗黒シート)の開発と大面積化の検討", 日本光学会年次学術講演会, [大阪大学コンベンションセンター], (2019/12). **C**

9) 宮下 太志, 野村 幹弘, 澤田 真一, 八巻 徹也, "熱化学水素製造 IS プロセス用新規イオン交換膜の開発", 第 39 回水素エネルギー協会大会, [船堀], P17 (2019/12). **C, G**

10) 丸橋 司, 萱沼 洋輔, 松本 啓, 木全 哲也, 鹿野 豊, 山本 春也, "イオン照射 GaAs 単結晶における電子フォノン結合系の量子コヒーレンス計測", 第 30 回光物性研究会, [宇治市], (2019/12). **I**

11) 出崎 亮, 山本 春也, 杉本 雅樹, 八巻 徹, "金属イオン注入したカーボン前駆体高分子のグラファイト構造形成挙動", 第 46 回炭素材料学会年会, [岡山大学],(2019/11). **I**

12) A. Idesaki, S. Yamamoto, M. Sugimoto and T. Yamaki, "Formation of Fe Nanoparticles for Catalytic Graphitization of a Phenolic Resin Utilizing Ion Implantation Technique", 29th Annual Meeting of MRS-J, [Yokohama], (2019/11). **I**

13) S. Yamamoto, H. Koshikawa, T. Taguchi, A. Idesaki, H. Okazaki and T. Yamaki, "Formation of Noble Metal Nanoparticles inside Ion-Track-Etched Capillaries", 29th Annual Meeting of MRS-J, [Yokohama], (2019/11). **E, C**

14) H. Okazaki, A. Idesaki, H. Koshikawa, D. Matsumura, S. Yamamoto, Y. Maekawa and T. Yamaki, "The change of electronic structure at the interface between Pt nanoparticles and the carbon support by the ion irradiation", 29th Annual Meeting of MRS-J, [Yokohama], (2019/11). **I**

15) H. Okazaki, A. Idesaki, H. Koshikawa, S. Yamamoto, Y. Maekawa and T. Yamaki, "The improvement of corrosion resistance of carbon by the ion irradiation", 29th Annual Meeting of MRS-J, [Yokohama], (2019/11). **I**

16) 本間 海斗, 伊藤 滋啓, 森 利之, 鈴木 彰, 山本 春也, ジャン ユージャン, "PEFC カソード用窒素ドープカーボン

合成における表面欠陥制御による活性サイト形成と親水性抑制効果”, 第29回日本 MRS 年次大会, [横浜], (2019/11). **E**

17) N. Nakagawa, H. Ishitobi, S. Abe, M. Kakinuma, H. Koshikawa, S. Yamamoto and T. Yamaki, “Improved catalytic activity of PtRu/CECNF by the ion-beam irradiation to the CECNF support”, Innovative Materials and Processes in Energy Systems (IMPRES2019), [Kanazawa], (2019/10). **C**

18) H. Ishitobi, S. Yamamoto, T. Ishii, K. Oba, H. Doki, N. Nakagawa, “Enhancement of electrochemical activity of vanadium redox flow battery by electron-beam irradiation”, Innovative Materials and Processes in Energy Systems (IMPRES2019), [Kanazawa], (2019/10/21). **E**

19) A. Idesaki, S. Yamamoto, M. Sugimoto, T. Yamaki, “Synthesis of Graphitic Nanostructure from Metal-ion Implanted Precursor Polymer”, The 13th Pacific Rim Conference of Ceramic Societies (PACRIM13), [Okinawa], (2019/10). **I**

20) 宮下 太志, 野村 幹弘, 澤田 真一, 八巻 徹也, “イオンビーム照射によるカチオン交換膜開発”, 第9回 CSJ 化学フェスタ2019, [船堀] P1-102 (2019/10). **C, G**

21) H. Doki, H. Ishitobi, S. Yamamoto, K. Oba and N. Nakagawa, “Activation of carbon electrode for vanadium redox flow battery by electron beam-irradiation”, 18th Asian Pacific Confederation of Chemical Engineering, [Sapporo] (2019/9). **E**

22) K. Honma, S. Ito, T. Sato, T. Mori, A. Suzuki and S. Yamamoto, “Electron beam irradiation synthesis of non-platinum nitrogen doped carbon without high temperature for cathode of PEFC”, 20th International Union of Materials Research Societies International Conference in Asia, [Perth, Australia] (2019/9). **E**

23) N. Nakagawa, H. Ishitobi, S. Abe, M. Kakinuma, H. Koshikawa, S. Yamamoto and T. Yamaki, “Ion-beam irradiation to the CECNF support of the anode catalyst for DMFC”, 18th Asian Pacific Confederation of Chemical Engineering, [Sapporo], (2019/9). **C**

24) K. Amemiya, Y. Shimizu, H. Koshikawa, M. Imbe, T. Yamaki and H. Shitomi, “Large-Area Perfect Blackbody Sheets from Nano-Precision Microtextured Elastomers”, Proc. OSA Frontiers in Optics + Laser Science (FiO/LS 2019), [Washington, District of Columbia, USA] (2019/9). **C**

25) T. Kimata, K. Kakitani, S. Yamamoto, T. Yamaki, T. Terai and K.G. Nakamura, “Ar-ion-irradiated graphite with platinum nanoparticles studied by Raman spectroscopy”, 30th International Conference on Diamond and Carbon Materials, [Seville, Spain], (2019/9). **I**

26) 櫻井 庸明, 坂口 周悟, 香山 一登, 神谷 昂志, 堀尾 明史, 竹下 友輝, 出崎 亮, 越川 博, 杉本 雅樹, 八巻 徹也, 関 修平, “低分子化合物の粒子線誘発固相重合による有機ナノワイヤの形成とその配向制御”, 第62回放射線化学討論会, [敦賀], (2019/9). **C**

27) 尾崎 壽紀, 柏原 卓弥, 久保 友幸, 千星 聡, 末吉 哲郎, 岡崎 宏之, 越川 博, 山本 春也, 八巻 徹也, 坂根 仁, “Au イオン照射した YBa_2Cu_3Oy 薄膜の磁束ピンニング特性”, 2019年第80回応用物理学会秋季学術講演会, [札幌], (2019/9). **T, I**

28) 岡崎 宏之, 出崎 亮, 越川 博, 松村 大樹, 山本 春也, 前川 康成, 八巻 徹也, “イオンビーム照射した炭素担体上の Pt ナノ粒子触媒の界面電子構造”, 日本物理学会2019年秋季大会, [岐阜市], 10aK21-4 (2019/9). **I**

29) 越川 博, 山本 春也, 杉本 雅樹, 澤田 真一, 八巻 徹也, “イオン穿孔膜を用いた金属酸化物ナノコーンの形成”, 2019年電気化学秋季大会, [甲府市], 1F07 (2019/9). **C**

30) 石飛 宏和, 柿沼 政貴, 長島 健, 山本 春也, 岡崎 宏之, 越川 博, 中川 紳好, “有機ハイドライドから加圧水素を取り出すための電気化学水素ポンプ”, 2019年電気化学秋季大会, (2019/09/05). **S**

31) 山本 春也, 田口 富嗣, 越川 博, 岡崎 宏之, 出崎 亮, 八巻 徹也, “電子線還元法による円柱状ナノ空間内への貴金属ナノ粒子形成”, 2019年電気化学秋季大会, [甲府市], 1F05 (2019/9). **C, E**

32) A. Idesaki, S. Yamamoto, M. Sugimoto and T. Yamaki, “Study of graphitization behavior of metal-ion implanted precursor polymer”, Carbon 2019, [Lexington, U.S.A.], (2019/7). **I**

33) M. Kakinuma, H. Ishitobi, N. Nakagawa, H. Koshikawa, S. Yamamoto and T. Yamaki, “Development of an MCH-based electrochemical pump for hydrogen transport and storage”, 18th Asian Pacific Confederation of Chemical Engineering, [Sapporo], (2019/9). **S**

34) H. Koshikawa, S. Yamamoto, M. Sugimoto, S. Sawada and T. Yamaki, “Fabrication of TiO_2 Nanocones Using Ion-Tracks of Polymer Membranes”, 10th International Conference on Molecular Electronics and Bioelectronics (M&BE10), [Nara], AP2-14 (2019/6). **C**

35) S. Sawada, T. Kimura, H. Nishijima, N. Tanaka, S. Kubo, S. Imabayashi, M. Nomura and T. Yamaki, “Development of low-overvoltage membrane Bunsen reaction technology for thermochemical IS process”, World Hydrogen Technologies Convention 2019, [東京都千代田区], (2019/6). **C, G**

36) 宮下 太志, 木村 壮宏, 野村 幹弘, 今林 慎一郎, 澤田 真一, 八巻 徹也, 田中 伸幸, 久保 真治, “熱化学水素製造 IS プロセス用膜型反応器の過電圧解析”, 日本膜学会第41年会, [早稲田], P-14S (2019/5). **G**

37) 上野 蓮, 竹内 健太郎, 斉藤 剛, 八巻 徹也, 越川 博, 澤田 真一, 垣花 百合子, 安川 政宏, 比嘉 充, “イオン飛跡グラフト重合法によるモザイク荷電膜の作製及び膜の性能評価”, 2019年度日本海水学会第70年会, [徳島市], O-07, P-06S (2019/6). **C**

38) R. Ueno, K. Takeuchi, T. Yamaki, S. Sawada, H. Koshikawa, Y. Kakihana, M. Yasukawa, M. Higa, “Evaluation of Charge Mosaic Membrane Prepared by Ion-track Irradiation Graft Polymerization”, The 12th Conference of the Aseanian Membrane Society, [Jeju, Korea], P2-131 (2019/7). **C**

Book

1) 澤田 真一, 田中 伸幸, 八巻 徹也, 久保 真治, 野村 幹弘, “水素製造・貯蔵”, 技術情報協会, (2019). **C, G**

Press・TV

1) 雨宮 邦招, 越川 博, 井邊 真俊, 八巻 徹也, 蔀 洋司, “全ての光を吸収する究極の暗黒シート －世界初！高い光吸収率と耐久性を併せ持つ黒色素材－”, 2019/4/24 プレス発表: 新聞23紙（読売新聞, 化学工業日報, 日経産業新聞, ゴム化学新聞, 科学新聞, 電波新聞, ぐんま経済新聞, 日刊工業新聞, 日本経済新聞, 読売新聞（大阪）,

朝日新聞，朝日新聞（大阪），中国新聞，北海道新聞，熊本日日新聞，佐賀新聞，河北新報，静岡新聞，神戸新聞，朝日小学生新聞，中部経済新聞，日本経済新聞，京都新聞）に掲載．雑誌 5 誌（子供の科学 2019 年 7 月号，Newton2019 年 8 月号，科博情報誌 milsil70 号，日経ものづくり 2019 年 9 月号，月刊 OPTRONICS 2020 年 3 月号）に掲載．テレビ等 3 件（テレビ東京 ワールドビジネスサテライト，TBS ラジオ 森本毅郎スタンバイ！ 現場にアタック，TBS テレビ Nスタ 3 コマニュース）で放送．ネットニュース等 8 件（Yahoo!ニューストピックス，時事ドットコム，朝日新聞デジタル，ITmedia NEWS，日経 XTECH，FNN PRIME online，マイナビニュース，さがせ、おもしろ研究！ブルーバックス探検隊が行く）に掲載． **C**

P1-3 Project “Positron Nanoscience”

Papers

1) M. Maekawa, S. Sakai, S. Hagiwara, A. Miyashita, K. Wada, A. Kawasuso, A. Yabuuchi and S. Hasegawa, “Magnetic Doppler Broadening Measurement on Gadolinium-doped GaN”, AIP Conf. Proc. **2182**, 050007-1-4 (2019). **I, O, 1-17**

2) M. Maekawa, K. Wada, A. Miyashita and A. Kawasuso, “Construction of a Spin-Polarized Positronium Time-of-Flight Measurement Apparatus”, Acta Physica Polonica A **137**, 105-108 (2020). **N**

3) A. Miyashita , S. Li , S. Sakai , M. Maekawa and A. Kawasuso, “Spin polarization of graphene on $Co_2FeGe_{0.5}Ga_{0.5}$(001) observed by spin-polarized surface positronium spectroscopy”, Phys. Rev. B **102**, 045425 (2020). **N**

4) M. Maekawa , A. Miyashita , S. Sakai and A. Kawasuso, “Gadolinium-implanted GaN studied by spin-polarized positron annihilation spectroscopy”, Phys. Rev. B **102**, 054427 (2020). **N**

5) K. Wada, M. Maekawa, I. Mochizuki, T. Shidara, A. Kawasuso, M. Kimura, T. Hyodo, “A pulse stretcher for a LINAC-based pulsed slow-positron beam providing a quasi-continuous beam with an energy of 5.2 keV”, Nucl. Instrum. Meth. Phys. Res. A **975**, 164161 (2020). **N**

6) T. Yamada, A. Takano, K. Sugita, A. Iwase, M. Maekawa, A. Kawasuso, “Effect of dual implantation with Ag and Ni ions on the optical absorption of silica glass”, Transactions of the Materials Research Society of Japan **45**, 138 (2020). **N**

7) M. Maekawa, S. Sakai, A. Miyashita and A. Kawasuso, "Spin-Polarized Positron Annihilation Measurement on Ga Vacancies in p-type GaN", e-J. Surf. Sci. Nanotech. **16**, 347-350 (2018). **I, 1-17**

8) A. Iwase and F. Hori,“Modification of lattice structures and mechanical properties of metallic materials by energetic ion irradiation and subsequent thermal treatments”, Quantum Beams Sci. 4, 17 (2020). **T, 1-18**

Proceedings

1) I. Mochizuki, K. Wada, Y. Fukaya, T. Shirasawa, Y. Endo, A. Takayama, S. Hasegawa, A. Ichimiya, Y. Nagashima, M. Maekawa, A. Kawasuso, A. Ishida, N. Toge, K. Furukawa, Y. Nagai, T. Hyodo, ”Present Status of the Slow Positron Facility of Institute of Materials Structure Science, KEK”,15th International Workshop on Slow Positron Beam Techniques & Applications (SLOPOS-15) , September2-6, 2019, Prague, Czech. **N**

2) M. Maekawa, K. Wada, S. Hagiwara, A. Miyashita, a. Kawasuso, “Construction of a spin-polarized positronium time-of-flight measurement apparatus”, 15th International Workshop on Slow Positron Beam Techniques & Applications (SLOPOS-15), September2-6, 2019, Prague, Czech. **N**

3) K. Wada, T. Shirasawa, I. Mochizuki, M. Fujinami, T. Takahashi, M. Maekawa, A. Kawasuso and T. Hyodo, “A low-energy positron diffraction (LEPD) experiment station for a linac-based slow-positron beam” ,【Invited talk】, 15th International Workshop on Slow Positron Beam Techniques & Applications (SLOPOS-15) , September2-6, 2019, Prague, Czech. **N**

4) A. Kawasuso, S. Hagiwara, K. Wada, M. Maekawa, A. Miyashita, S. Li, S. Entani, S. Sakai, S. Iida, T. Kaiwa, H. Iwamori and Y. Nagashima, “Positronium Formation at Metal, Semiconductor and Graphene Surfaces”,【Invited talk】, 15th International Workshop on Slow Positron Beam Techniques & Applications (SLOPOS-15) , September2-6, 2019, Prague, Czech. **N**

5) K. Wada, T. Shirasawa, I. Mochizuki, M. Fujinami, T. Takahashi, M. Masaki, A. Kawasuso and T. Hyodo, “Improvement of a detection system for observing low-energy positron diffraction using a linac-based slow-positron beam”,【Invited talk】, 4th Japan-China Joint Workshop on Positron Science, October 28- November 2, 2019, Nara, Japan. **N**

6) 前川雅樹、和田健、宮下敦巳、萩原聡、河裾厚男、“スピン偏極ポジトロニウム飛行時間測定装置の開発” 、日本アイソトープ協会第 56 回アイソトープ・放射線研究発表会 令和元年 7 月 4 日． **N**

7) 河裾 厚男、和田 健、宮下 敦巳、前川 雅樹、萩原 聡、岩森 大直、長嶋 泰之、“六方晶 SiC 単結晶表面におけるポジトロニウム生成”、日本アイソトープ協会第 56 回アイソトープ・放射線研究発表会 令和元年 7 月 4 日． **N**

8) 和田 健、白澤 徹朗、望月 出海、藤浪 真紀、前川 雅樹、河裾 厚男、高橋 敏男、兵頭 俊夫、“Ge(001)-2x1 表面からの低速陽電子回折図形の観測 II Ge(001)-2x1 表面からの低速陽電子回折図形の観測 II”、日本アイソトープ協会第 56 回アイソトープ・放射線研究発表会 令和元年 7 月 4 日． **N**

9) 和田 健、白澤 徹朗、望月 出海、藤浪 真紀、前川 雅樹、河裾 厚男、高橋 敏男、兵頭 俊夫、“低速陽電子回折装置の開発”、真空展「大学・公的機関における真空科学・技術・応用の最先端研究紹介」令和元年9月4～6日． **N**

10) 前川 雅樹、境 誠司、和田 健、宮下 敦巳、河裾 厚男、“スピン偏極陽電子ビームを用いた磁性元素添加半導体材料の空孔誘起磁性評価”、日本物理学会 2019 年秋季大会 令和元年 9 月日． **N**

11) 和田健、白澤徹朗、望月出海、藤浪真紀、前川雅樹、河裾厚男、高橋敏男、兵頭俊夫、“低速陽電子回折(LEPD)の特徴と装置開発”、2019 年日本表面真空学会学術講演会 令和元年 10 月 30 日． **N**

12) 和田健、白澤徹朗、望月出海、藤浪真紀、前川雅樹、河裾厚男、高橋敏男、兵頭俊夫、“Observation of low-energy positron diffraction patterns with a linac-based slow-positron beam"【招待講演】、2019年日本表面真空学会学術講演会令和元年10月30日. **N**

13) 河裾 厚男、和田 健、前川 雅樹、宮下 敦巳、岩森 大直、長嶋 泰之、"4H-SiC表面におけるポジトロニウム生成"、令和元年年度京都大学複合原子力科学研究所専門研究会「陽電子科学とその理工学への応用」令和元年12月5日. **N**

14) 前川 雅樹、和田 健、宮下 敦巳、萩原 聡、河裾 厚男、"スピン偏極ポジトロニウム飛行時間測定装置の開発"、令和元年年度京都大学複合原子力科学研究所専門研究会「陽電子科学とその理工学への応用」令和元年12月5日. **N**

15) 和田健、白澤徹朗、望月出海、藤浪真紀、前川雅樹、河裾厚男、高橋敏男、兵頭俊夫、"低速陽電子回折装置への六角型遅延アノード検出器の導入"、令和元年年度京都大学複合原子力科学研究所専門研究会「陽電子科学とその理工学への応用」令和元年12月5日. **N**

16) 河裾 厚男、"スピン偏極陽電子を用いたスピントロニクス関連物質の評価"【招待講演】、公益社団法人日本磁気学会第75回スピントロニクス専門研究 令和2年7月22日. **N**

P1-4 Project "Semiconductor Radiation Effects"

Papers

1) T. Makino, S. Onoda, T. Ohshima, D. Kobayashi, H. Ikeda and K. Hirose, "A Methodology for reconstructing DSET pulses from heavy-ion broad-beam measurements", Quantum Beam Sci., **4**, 15-1-9 (2020). **C**

2) D. Kobayashi, K. Hirose, K. Sakamoto, S. Okamoto, S. Baba, H. Shindo, O. Kawasaki, T. Makino, T. Ohshima, Y. Mori, D. Matsuura, M. Kusano and T. Narita, "Data-retention-voltage-based analysis of systematic variations in SRAM SEU hardness: A Possible Solution to Synergistic Effects of TID", IEEE Trans. Nucl. Sci., **67**, 1, 328-335 (2020). **C, G**

3) A. Rifai, N. Tran, P. Reineck, A. Elbourne, E. Mayes, A. Sarker, C. Dekiwadia, E. P. Ivanova, R. J. Crawford, T. Ohshima, B. C. Gibson, A. D. Greentree, E. Pirogova and K. Fox, "Engineering the interface: nanodiamond coating on 3D-printed titanium promotes mammalian cell growth and inhibits staphylococcus aureus colonization", ACS Appl. Mater. Interfaces **11**, 24588-24596 (2019). **E**

4) K. C. Miao, A. Bourassa, C. P. Anderson, S. J. Whiteley, A. L. Crook, S. L. Bayliss, G. Wolfowicz, G. Thiering, P. Udvarhelyi, V. Ivády, H. Abe, T. Ohshima, Á. Gali, D. D. Awschalom, "Electrically driven optical interferometry with spins in silicon carbide", Sci. Adv. **5**, eaay0527-1-7 (2019). **E**

5) M. Widmann, M. Niethammer, D. Y. Fedyanin, I. A. Khramtsov, T. Rendler, I. D. Booker, J. U Hassan, N. Morioka, Y.-C. Chen, I. G. Ivanov, N. T. Son, T. Ohshima, M. Bockstedte, A. Gali, C. Bonato, S.-Y. Lee, J. Wrachtrup, "Electrical charge state manipulation of single silicon vacancies in a silicon carbide quantum optoelectronic device", Nano Lett. **19**, 7173-7180 (2019). **E**

6) C. P. Anderson, A. Bourassa, K. C. Miao, G. Wolfowicz, P. J. Mintun, A. L. Crook, H. Abe, J. U. Hassan, N. T. Son, T. Ohshima, D. D. Awschalom, "Electrical and optical control of single spins integrated in scalable semiconductor devices", Science **366**, 1225-1230 (2019). **E**

7) A. Takeyama, T. Makino, S. Okubo, Y. Tanaka, T. Yoshie, Y. Hijikata and T. Ohshima, "Radiation response of negative gate biased SiC MOSFETs", Materials, **12**, 2741-1-10 (2019). **G**

8) M. Pfender, P. Wang, H. Sumiya, S. Onoda, W. Yang, D. B. R. Dasari, P. Neumann, X-Y. Pan, J. Isoya, R-B. Liu and J. Wrachtrup, "High-resolution spectroscopy of single nuclear spins via sequential weak measurements", Nat. Commun. **10**, 594-1~8 (2019). **E**

9) N. Oi, T. Kudo, M. Inaba, S. Okubo, S. Onoda, A. Hiraiwa and H. Kawarada, "Normally-OFF two-dimensional hole gas diamond MOSFETs through nitrogen-ion implantation", IEEE Ele. Dev. Lett. **40**, 933-936 (2019). **I**

10) D. Terada, T. F. Segawa, A. I. Shames, S. Onoda, T. Ohshima, E. Osawa, R. Igarashi and M. Shirakawa, "Monodisperse five-nanometer-sized detonation nanodiamonds enriched in nitrogen-vacancy centers", ACS Nano **13**, 6461-6468 (2019). **E**

11) M. Haruyama, S. Onoda, T. Higuchi, W. Kada, A. Chiba, Y. Hirano, T. Teraji, R. Igarashi, S. Kawai, H. Kawarada, Y. Ishii, R. Fukuda, T. Tanii, J. Isoya, T. Ohshima and O. Hanaizumi, "Triple nitrogen-vacancy centre fabrication by $C_5N_4H_n$ ion implantation", Nat. Commun. **10**, 2664-1-9 (2019). **T**

12) J. Michl, J. Steiner, A. Denisnko, A. Bulau, A. Zimmermann, K. Nakamura, H. Sumiya, S. Onoda, P. Neumann, J. Isoya and J. Wrachtrup, "Robust and accurate electric field sensing with solid state spin ensembles", Nano Lett. **19**, 4904-4910 (2019). **E**

13) T. Fujisaku, R. Tanabe, S. Onoda, R. Kubota, T. F. Segawa, F. T.-K. So, T. Ohshima, I. Hamachi, M. Shirakawa and R. Igarashi, "pH nanosensor using electronic spins in diamond", ACS Nano **13**, 11726-11732 (2019). **E**

14) M. Niethammer, M. Widmann, T. Rendler, N. Morioka, Y-C. Chen, R. Stohr, J. U. Hassan, S. Onoda, T. Ohshima, S-Y. Lee., A. Mukherjee, J. Isoya, N. T. Son and J. Wrachtrup, "Coherent electrical readout of defect spins in silicon carbide by photo-ionization at ambient conditions", Nat. Commun. **10**, 5569-1-8 (2019). **E**

15) S. Castelletto, A. S. A. Atem, F. A. Inam, H. J. von Bardeleben, S. Hameau, A. F. Almutairi, G. Guillot, S.-I. Sato, A. Boretti and J. M. Bluet, "Deterministic placement of ultra-bright near-infrared color centers in arrays of silicon carbide micropillars,", Beilstein J. Nanotechnol. **10**, 2383-2395 (2019). **N**

16) S.-I. Sato, T. Narahara, Y. Abe, Y. Hijikata, T. Umeda and T. Ohshima, "Formation of nitrogen-vacancy centers in 4H-SiC and their near infrared photoluminescence properties", J. Appl. Phys. **126**, 083105-1-10 (2019). **T, I**

17) Y. Chiba, Y. Yamazaki, T. Makino, S.-I. Sato, N. Yamada, T. Satoh, K. Kojima, S.-Y. Lee, Y. Hijikata and T. Ohshima, "Creation of color centers in SiC PN diodes using proton beam writing", Mater. Sci. Forum **963**, 709-713 (2019). **S, I**

18) T. Ishii, S.-I. Kuroki, H. Sezaki, S. Ishikawa, T. Maeda, T. Makino, T. Ohshima, M. Östling and C.-M. Zetterling, "Suppression of short-channel effects in 4H-SiC trench MOSFETs", Mater. Sci.

Forum **963**, 613-616 (2019). **N**

19) A. Csore, B. Magnusson, N. T. Son, A. Gallstrom, T. Ohshima, I. G. Ivanov and A. Gali1, “First-principles study on photoluminescence quenching of divacancy in 4H SiC”, Mater. Sci. Forum **963**, 714-717 (2019). **E**

20) F. Hasebe, T. Meguro, T. Makino, T. Ohshima, Y. Tanaka and S.-I. Kuroki, “Direct Bonding of 4H-SiC and SOI Wafers for Radiation-Hardened Image Sensors”, Mater. Sci. Forum **963**, 726-729 (2019). **G**

21) J. Inoue, S.-I. Kuroki, S. Ishikawa, T. Maeda, H. Sezaki, T. Makino, T. Ohshima, M. Östling and C.-M. Zetterling, “4H-SiC Trench pMOSFETs for High-Frequency CMOS Inverters”, Mater. Sci. Forum **963**, 837-840 (2019). **G**

22) I. Capan, Y. Yamazaki, Y. Oki, T. Brodar, T. Makino and T. Ohshima, “Minority carrier trap in n-type 4H–SiC schottky barrier diodes”, Crystals **9**, 328 (2019). **N**

23) S.-I. Sato, M. Deki, T. Nakamura, T. Nishimura, D. Stavrevski, A. D. Greentree, B. C. Gibson and T. Ohshima, “Photoluminescence properties of praseodymium ions implanted into submicron regions in gallium nitride”, Jpn. J. Appl. Phys. **58**, 051011-1-6 (2019). **I**

24) K. Muraoka, H. Sezaki, S. Ishikawa, T. Maeda, T. Makino, A. Takeyama, T. Ohshima and S.-I. Kuroki, “Gamma-ray irradiation-induced mobility enhancement of 4H-SiC NMOSFETs with a Ba-silicate interface layer”, Jpn. J. Appl. Phys. **58**, 081007-1-7 (2019). **G**

25) H. Zheng, J. Xu, G. Z. Iwata, T. Lenz, J. Michl, B. Yavkin, K. Nakamura, H. Sumiya, T. Ohshima, J. Isoya, J. Wrachtrup, A. Wickenbrock and D. Budker, “Zero-field magnetometry based on nitrogen-vacancy ensembles in diamond”, Phys. Rev. Applied **11**, 064068-1-7 (2019). **E**

26) M. U. Khan, D. Chen, S. Jafari, T. Ohshima, H. Abe, Z. Hameiri, C. M. Chong and M. Abbott, “Degradation and regeneration of radiation-induced defects in silicon: A study of vacancy-hydrogen interactions”, Solar Energy Materials and Solar Cells **200**, 109990-1-8 (2019). **E**

27) N. T. Son, P. Stenberg, V. Jokubavicius, H. Abe, T. Ohshima, J. U. Hassan and I. G. Ivanov, “Energy levels and charge state control of the carbon antisite-vacancy defect in 4H-SiC”, Appl. Phys. Lett. **114**, 212105-1-5 (2019). **E**

28) F. Dong, S. J. Meschter, S. Nozaki, T. Ohshima, T. Makino and J. Cho, “Effect of coating adhesion and degradation on tin whisker mitigation of polyurethane-based conformal coatings”, Polymer Degradation and Stability **166**, 219-229 (2019). **E**

29) T. Makino and T. Ohshima, “Radiation hardness testing for electronics against high energy ions”, Radioisotopes **68**, 423-431 (2019). **C**

30) R. Nagy, M. Niethammer, M. Widmann, Y. -C. Chen, P. Udvarhelyi, C. Bonato, J. U. Hassan, R. Karhu, I. G. Ivanov, N. T. Son, J. R. Maze, T. Ohshima, Ö. O. Soykal, Á. Gali, S.-Y. Lee, F. Kaiser and J. Wrachtrup, “High-fidelity spin and optical control of single silicon-vacancy centres in silicon carbide”, Nature Communications **10**, 1954-1-8 (2019). **E**

31) K. Takeuchi, T. Sakamoto, M. Tada, A. Takeyama, T. Ohshima, S. Kuboyama and H. Shindo, “Single-Event Effects Induced on Atom Switch-based Field-Programmable Gate Array”, IEEE Trans. Nucl. Sci. **66**, 1355-1360 (2019). **C, 1-20**

Proceedings

1) S. Abo, K. Tani, F. Wakaya, S. Onoda, Y. Miyato, H. Yamashita, and M. Abe, “Measurement of the Lateral Charge Distribution in Silicon Generated by High-Energy Ion Incidence”, Proc. 22nd International Conference on Ion Implantation Technology (IIT), [Wurzburg, Germany] (2019/09). IEEE. **T**

2) Y. Nakada, S. Kuboyama, E. Mizuta, A. Takeyama, T. Ohshima and H. Shindou, “Behavior of Damaged Sites Introduced by SEGR in Silicon Carbide Power MOSFETs”, Proc. 2019 20th European Conference on Radiation and Its Effects on Components and Systems (RADECS), [Montpellier, France] (2019/09). **C, 1-20**

3) K. Takeuchi, T. Kato, K. Sakamoto, K. Yukumatsu, K. Watanabe, Y. Tsuchiya, H. Matsuyama, A. Takeyama, T. Ohshima, S. Kuboyama and H. Shindo, “Characteristic Charge Collection Mechanism Observed in FinFET SRAM cells,” Proc. 2020 21th European Conference on Radiation and Its Effects on Components and Systems (RADECS), [Vannes, France] (2020). **C, 1-20**

4) M. Imaizumi, T. Takamoto, H. Sugimoto, T. Ohshima and S. Kawakita, “Preliminary Study on Super Radiation-Resistant Mechanical-Stack Triple-Junction Space Solar Cell: PHOENIX”, Proc. of 46th IEEE Photovoltaic Specialists Conference, 1495 (2019). **C, T, I, 1-21**

5) 武山 昭憲, 牧野 高紘, 山崎 雄一, 大島 武, 清水 奎吾, 田中 保宣, 西垣内 健汰, 長谷部 史明, 目黒 達也, 黒木 伸一郎, “炭化ケイ素半導体を用いた耐放射線性イメージセンサの開発”, 電気学会 電子デバイス研究会資料, [栃木,日本] (2020/03). **G**

P1-5 Project “Environmental Polymer”

Papers

1) Y. Ueki and N. Seko, “Synthesis of Fibrous Metal Adsorbent with a Piperazinyl-Dithiocarbamate Group by Radiation-Induced Grafting and Its Performance”, ACS Omega **5**, 2947–2956 (2020). **E, 1-24, 1-27**

2) N. A. F. Othman, S. Selambakkannu, T. T. Ming, N. H. Mohamed, T. Yamanobe and N Seko, “Application of Response Surface Modelling to Economically Maximize Thorium (IV) Adsorption”, Desalin. Water Treat. **179**, 172–182 (2020). **E, 1-24, 1-27**

3) N. A. F. Othman, S. Selambakkannu, T. Yamanobe, H. Hoshina, N. Seko and T. A. T. Abdullah, “Radiation grafting of DMAEMA and DEAEMA-based adsorbents for thorium adsorption”, J. Radioanal. Nucl. Chem. **324**, 429–440 (2020). **E, 1-24, 1-27**

4) N. A. F. Othman, S. Selambakkannu, H. Azian, C. T. Ratnam, T. Yamanobe, H. Hoshina and N. Seko, “Synthesis of surface ion-imprinted polymer for specific detection of thorium under acidic conditions”,Polym. Bull., Open Access (2020). **E, 1-24, 1-26, 1-27**

5) N. H. Zabaruddin, N. H. Mohamed, L. C. Abdullah, M. Tamada, Y. Ueki, N. Seko, T. Shean and Y. Choong, “Palm oil-based biodiesel synthesis by radiation-induced kenaf catalyst packed in a continuous flow system", Ind. Crops and Prod. **36**, 102–109 (2019). **E, 1-24, 1-26, 1-27**

6) M. Omichi, Y. Ueki, N. Seko and Y. Maekawa, "Development of a Simplified Radiation-Induced Emulsion Graft Polymerization Method and Its Application to the Fabrication of a Heavy Metal Adsorbent", Polymers **11**, 1373:1–11 (2019). **E, G, 1-24, 1-27**

7) M. Omichi, S. Yamashita, Y. Okura, R. Ikutomo, Y. Ueki, N. Seko and R. Kakuchi, "Surface Engineering of Fluoropolymer Films via the Attachment of Crown Ether Derivatives Based on the Combination of Radiation-Induced Graft Polymerization and the Kabachnik-Fields Reaction", Polymers **11**, 1337:1–11 (2019). **E, G, 1-25**

8) S. Watanabe, H. Ogi, Y. Arai, H. Aihara, Y. Takahatake, A. Shibata, K. Nomura, Y. Kamiya, N. Asanuma, H. Matsuura, T. Kubota, N. Seko and T. Arai, T. Moriguchi, "STRAD project for systematic treatments of radioactive liquid wastes generated in nuclear facilities", Prog. Nucl. Energy **117**, 103090:1–8 (2019). **E, 1-25**

9) J. Chen and N. Seko, "Cleavage of the Graft Bonds in PVDF-g-St Films by Boiling Xylene Extraction and the Determination of the Molecular Weight of the Graft Chains", Polymers, **11**, 1098:1–17 (2019). **G, 1-24, 1-27**

10) N. A. F. Othman, S. Selambakkannu, T. A. T. Abdullah, H. Hoshina, S. Sattayaporn and N. Seko, "Selectivity of Copper by Amine-Based Ion Recognition Polymer Adsorbent with Different Aliphatic Amines", Polymers **11**, 1994:1–21 (2019). **E, 1-24, 1-26, 1-27**

11) 瀬古 典明, "電子線加工技術による高分子吸着材の開発と応用", Rad Tech News Letter **114**, 2–5 (2019). **E**

12) 瀬古 典明, "高分子産業における放射線利用 グラフト重合", 放射線と産業 **147**, 17–20 (2019). **E, G**

13) 植木 悠二, "放射線グラフト重合技術による汎用プラスチックへの機能付与", プラスチックス **70**(11), 54–58 (2019). **E**

Proceedings

1) 大野 真平, 荒井 陽一, 渡部 創, 瀬古 典明, 笠井 昇, 保科 宏行, 柴田 淳広, 野村 和則, "劣化溶媒処理のための機能性グラフト重合吸着材の創出", 平成 31 年度第 9 回日本原子力学会北関東支部若手研究者発表会, 日本原子力学会, [東海村産業 情報プラザ・茨城] (2019/04/19). **E, 1-24, 1-26, 1-27**

2) R. Kakuchi, S. Yamashita, Y. Okura, T. Hamada, M. Omichi, Y. Ueki and N. Seko, "Multicomponent post-polymerization modification reactions on biomass-sourced organic hybrids", 第 68 回高分子学会年次大会, 高分子学会, [大阪府立国際会議場・大阪] (2019/05/29). **E, G, 1-25**

3) 荒井 陽一, 渡部 創, 大野 真平, 野村 和則, 中村 文也, 新井 剛, 瀬古 典明, 保科 宏行, 久保田 俊夫, "使用済み燃料再処理プロセスから発生する廃溶媒処理技術の開発", 日本原子力学会 2019 年秋の大会, 日本原子力学会, [富山大・富山] (2019/09/11). **E, 1-25**

4) 山下 修平, 大道 正明, 大倉 大和, 生友 隆太, 植木 悠二, 網井 秀樹, 瀬古 典明, 覚知亮平, "ETFE 膜表面へのクラウンエーテルの導入と色素吸着能の評価", 第 9 回フッ素化学若手の会, 日本フッ素化学会, [あわら温泉 清風荘・福井] (2019/09/12). **E, G, 1-25**

5) 大道 正明, 瀬古 典明, 前川 康成, "アルコール添加が及ぼす放射線エマルショングラフト重合への影響", 第 68 回高分子討論会, 高分子学会, [福井大・福井] (2019/09/25). **G, 1-24, 1-27**

6) 山下 修平, 大道 正明, 植木 悠二, 瀬古 典明, 覚知 亮平, "バイオマス由来材料のみを出発原料とした放射線グラフト重合及び 多成分連結反応による機能性ハイブリッド材料の合成", 第 68 回高分子討論会, 高分子学会, [福井大・福井] (2019/09/26). **E, G, 1-25**

7) 大道 正明, 植木 悠二, 瀬古 典明, 前川 康成, "機械学習で放射線グラフト重合は予測できるのか？", 第 9 回 CSJ 化学フェスタ 2019, 日本化学会, [タワーホール船堀・東京] (2019/10/16). **E, 1-33**

8) N. Seko, "Current Status of Quantum Beams Applications for Polymer Processing",【Invited talk】, Innovation in Polymer Science and Technology (IPST) 2019, Indonesian Institute of Sciences, Indonesian Polymer Association, [The Stones Hotel-Legian Bali, Indonesia] (2019/10/17). **E, G, 1-24, 1-27**

9) H. Hoshina and N. Seko, "Performance of Metal Adsorbent Synthesized by Radiation Graft Polymerization", OKINAWA COLLOIDS 2019, The Chemical Society of Japan, [Bankoku Shinryokan, Okinawa] (2019/11/06). **E, 1-24, 1-26, 1-27**

10) 大場 弘則, 瀬古 典明, 佐伯 盛久, 中西 隆造, 若井田 育夫, "環境水への LIBS 分析適用について", 第 6 回先端計測技術の応用展開に関するシンポジウム, LIBS 研究会, [京都大・京都] (2019/12/14). **E, 1-24, 1-26, 1-27**

11) N. Seko, H. Amada, H. Hoshina, Y. Ueki, S. Saiki, M. Omichi, J. Chen and M. Nakano, "Adsorption Performance of Fibrous Adsorbents by Radiation Emulsion Graft Polymerization", The 10th International Membrane Science and Technology Conference (IMSTEC2020), Membrane Society Australasia, [University of Technology Sydney Aerial Convention Centre, Australia] (2020/02/03). **E, 1-24, 1-26, 1-27**

12) H. Hoshina, N. Seko and H. Amada, "Development of Adsorbent for Rare Earth Recovery Synthesized by Radiation Graft Polymerization", The 10th International Membrane Science and Technology Conference (IMSTEC2020), Membrane Society Australasia, [University of Technology Sydney Aerial Convention Centre, Australia] (2020/02/03). **E, 1-24, 1-26, 1-27**

Book

1) 瀬古 典明, 植木 悠二, "電子線・放射線による加工・改質", 2020 版 薄膜作製応用ハンドブック, 660–665 (2020). **E**

Patent

1) 瀬古 典明, 保科 宏行, 笠井 昇, "溶解物除去装置及びこれに用いられるろ過助剤並びに溶解物除去方法", 特許第 6695542 号 (2020/04/24). **E**

Press・TV

1) 群馬大学・量研, "完全バイオマス由来の有機ハイブリッド材料の合成", 2019.05.22. プレス発表： 化学工業日報, ぐんま経済新聞に掲載. **E, G**

P1-6 Project “Biocompatible Materials”

Papers

1) M. Koshimizu, S. Kurashima, A. Kimura, M. Taguchi, T. Yanagida, H. Yagi, T. Yanagitani, Y. Fujimoto and K. Asai, “Effect of linear energy transfer on the scintillation Properties of $Ce:Gd_3Al_2Ga_3O_{12}$”, Nucl. Intr. Meth. B, **460**, 74-79 (2019). **C**

2) S. Ishii, K. Oyama, T. Arai, H. Itoh, S. A. Shintani, M. Suzuki, F. Kobirumaki-Shimozawa, T. Terui, N. Fukuda and S. Ishiwata, “Microscopic heat pulses activate cardiac thin filaments”, Journal of General Physiology, **151**(6) 860-869 (2019). **N**

3) Y.-G. Yin, S. Ishii, N. Suzui, M. Igura, K. Kurita, Y. Miyoshi, N. Nagasawa, M. Taguchi and N. Kawachi, “On-line rapid purification of [13N]N_2 gas for visualization of nitrogen fixation and translocation in nodulated soybean”, Applied Radiation and Isotopes **151**, 7-12 (2019). **C**

4) A. Kimura, N. Nagasawa and M. Taguchi, “Synthesis of polysaccharide hybrid gel in ionic liquids via radiation-induced crosslinking”, Polymer Degradation and Stability **159**, 133-138 (2019). **G**

5) Y. Hosaka, T. Oyama, H. Yamamoto, M. Ishino, T. Dinh, M. Nishikino and Y. Maekawa, “Sensitivity enhancement of poly(methyl methacrylate) upon exposure to picosecond-pulsed extreme ultraviolet”, Applied Physics Letters **115**(7), 073109 (2019). **N**

6) J. McGrady, S. Yamashita, A. Kimura, S. Kano, H. Yang, Z. Duan, T. Saito and H. Abe, “γ-radiation effects on metal oxide particles and their wetted surfaces”, J. Nucl. Sci. Tech. **57**, 463-471 (2020). **G**

7) L. S. Relleve, C. T. Aranilla, B. J. Barba, A. K. R. Gallardo, V. R.C. Cruz, C. R. M. Ledesma, N. Nagasawa and L. V. Abad, “Radiation-synthesized polysaccharides/polyacrylate super water absorbents and their biodegradabilities”, Radiation Physics and Chemistry, **170**, 108618 (2020). **G**

8) T.G. Oyama, A. Kimura, N. Nagasawa, K. Oyama and M. Taguchi, “Development of advanced biodevices using quantum beam microfabrication technology”, Quantum Beam Sci. **4**(1), 14 (2020).

9) F. Kobirumaki-Shimozawa, T. Nakanishi, T. Shimozawa, T. Terui, K. Oyama, J. Li, W. Louch, S. Ishiwata and N.Fukuda, “Real-time in vivo imaging of mouse left ventricle reveals fluctuating movements of the intercalated discs”, Nanomaterials **10**, 532 (2020). **N**

10) 廣木 章博, 田口 光正, “放射線架橋ゲルを母材とするポリマーゲル線量計の LET 効果”, Radioisotopes **68** 277-283 (2019).

11) 青木 祐太郎, 田口 光正, 長澤 尚胤, 砂川 武義, “新規メカニズムによる医療用高感度ゲル線量計の開発”, 放射線と産業 **146**, 43-47 (2019).

12) 大山 智子, “量子ビームでつくる、細胞を操る培養基材”, PETROTECH **42**(11), 834 - 838 (2019).

13) 保坂 勇志, 大山 智子, “電子線を用いた EUV レジスト感度予測法の研究”, 放射線化学 **107**, 3-8 (2019).

Patents

1) 田口 光正, 大山 智子, 木村 敦, 大山 廣太郎, 石原 弘, 下川 卓志, “細胞培養用ハイドロゲル、ゲルキット、細胞培養物の製造方法、及び細胞培養用ハイドロゲルの製造方法”, 国際出願 PCT/JP2019/025916 (2019. 6.28).

2) 田口 光正, 木村 敦, 宮本 久生, 今西 彩花, 吉井 文男, “臓器モデルおよびその製造方法並びに焼灼治療トレーニング用キット”, 特願 2019-117559 (2019. 6. 25).

3) 田口 光正, 大山 智子, 木村 敦, 大山 廣太郎, 石原 弘,下川 卓志, “細胞培養用ハイドロゲル、ゲルキット、細胞培養物の製造方法、及び細胞培養用ハイドロゲルの製造方法”, 台湾に出願, 108123011(2019. 6.28).

4) 長澤 尚嗣, 鈴木 淳史, 望月 亮弥, “摩擦特性向上デュアル架橋ハイブリッドゲル”, 出願 191226, 特願 2019-236517（19.12.26）. **E, G**

5) 大山 智子, 田口 光正, Barba Bin Jeremiah Duenas（バーバ ビン ジェレマイア デュナス）, 木下 忍, 井出 崇, “試験用基材、及び試験用基材の製造方法”, 国際出願（米国）16/620,400 (2019.12.24).

6) 大山 智子, 田口 光正, 小沢 幸雄, 小谷 卓司, 山田 高史, “接合体とその接合方法及びマイクロ流体デバイスとその製造方法”, 国際出願 PCT/JP2020/006436 (2020.02.25).

7) 大山 智子, 田口 光正, Barba Bin Jeremiah Duenas（バーバ ビン ジェレマイア デュナス）, 木下 忍, 井出 崇, “試験用基材、及び試験用基材の製造方法”, 特許第 6524563 号 (2019.5.17).

Press･TV

1) “体温において心臓が効率良く拍動するメカニズムの一端を解明”, 2019/4/23 プレス発表: 日経新聞電子版, 茨城新聞電子版, 共同通信 PR ワイヤー, J-CAST トレンド, 紀伊報 AGARA, CNET Japan, 福島友新聞社 みんゆう Net, 日経新聞に掲載. **N**

2) “診断や創薬における微量検体の分析性能が数 10 倍に！—マイクロ流路チップの一括積層技術を開発—”, 2019.6.25 プレス発表: 日刊工業新聞, 化学工業日報, 日経産業新聞, 科学新聞に掲載. **E,G**

P1-7 Project “Spintronics in Two-dimensional Materials”

Papers

1) S. Li, K. V. Larionov, Z. I. Popov, T. Watanabe, K. Amemiya, S. Entani, P. V. Avramov, Y. Sakuraba, H. Naramoto, P. B. Sorokin and S. Sakai, “Graphene/half-metallic Heusler alloy: a novel heterostructure toward high-performance graphene spintronic devices”, Adv. Mater. **32**, 1905734 (2020). **N**

2) S. Entani, K. V. Larionov, Z. I. Popov, M. Takizawa, M. Mizuguchi, H. Watanabe, S. Li, H. Naramoto, P. B. Sorokin, S. Sakai, ”Non-chemical fluorination of hexagonal boron nitride by high-energy ion irradiation” Nanotechnology **31**, 125705 (2020). **N**

3) D. G. Kvashnin, A. G. Kvashnin, E. Kano, A. Hashimoto, M. Takeguchi, H. Naramoto, S. Sakai and P. B. Sorokin, “Two-Dimensional CuO Inside the Supportive Bilayer Graphene Matrix”, J. Phys. Chem. C **123**, 17459-17465 (2019). **N**

4) S. Entani, M. Takizawa, S. Li, H. Naramoto, S. Sakai, “Growth of graphene on SiO$_2$ with hexagonal boron nitride buffer layer”, Appl. Surf. Sci. **475**, 6-11 (2019). **N**

Proceedings

1) M. Maekawa, S. Sakai, S. Hagiwara, A. Miyashita, K. Wada, A. Kawasuso, A. Yabuuchi and S. Hasegawa, “Magnetic Doppler broadening measurement on Gadolinium-doped GaN”, AIP Conf. Proc. **2182**, 050007 (2019). **I, O, 1-17**

P1-8 Project “EUV Ultra-fine Fabrication”

Papers

1) Y. Hosaka, T. G. Oyama, H. Yamamoto, M. Ishino, T.-H. Dinh, M. Nishikino and Y. Maekawa “Sensitivity enhancement of poly(methyl methacrylate) upon exposure to picosecond-pulsed extreme ultraviolet”, Appl. Phys. Lett. **115**, 073109-1-5 (2019). **N**

2) A. Sasaki, M. Ishino and M. Nishikino, “An estimation of line width roughness of photoresists due to photon shot noise for extreme ultraviolet lithography using the percolation model”, Jpn. J. Appl. Phys. **58**, 055002 (2019). **N**

3) N. Nishimori, R. Nagai, R. Hajima, M. Yamamoto, Y. Honda, T. Miyajima and T. Uchiyama, “Operational experience of a 500 kV photoemission gun”, Phys. Rev. Accel. Beams **22**, 053402 (2019). **N**

4) H. Kudo, M. Fukunaga, T. Yamada, T. Watanabe, H. Yamamoto, K. Okamoto and Takahiro Kozawa, “Synthesis and Property of Tellurium-Containing Molecular Resist Materials for Extreme Ultraviolet Lithography System”, J. Photopolym. Sci. Technol., **6,** 805-810 (2019). **N**

5) H. Yamamoto, G. Dawson, T. Kozawa, and A. P.G. Robinson, “Lamellar orientation of a block copolymer via an electron-beam induced polarity switch in a nitrophenyl self-assembled monolayer”, Quantum. Beam Sci. **4**, 12-1-10 (2020). **N**

6) M. Ishino , T. Dinh , Y. Hosaka , N. Hasegawa , K. Yoshimura , H. Yamamoto , T. Hatano , T. Higashiguchi , K. Sakaue , S. Ichimaru , M. Hatayama , A. Sasaki , M. Washio , M. Nishikino and Y. Maekawa, “Soft x-ray laser beamline for surface processing and damage studies”, Applied Optics **59**, 3692-3698 (2020). **N**

Proceedings

1) A. Sasaki. “Simulation of statistical effects in exposure and development of EUV photoresists using the percolation and diffusion limited aggregation mode”, Proc. SPIE **10957**, Advances in Patterning and Processes XXXV, 109571Q (2019). **N**

2) T. Obina, D.A. Arakawa, M. Egi, T. Furuya, K. Haga, K. Harada, T. Honda, Y. Honda, T. Honma, E. Kako, R. Kato, H. Kawata, Y. Kobayashi, Y. Kojima, T. Konomi, H. Matsumura, T. Miura, T. Miyajima, S. Nagahashi, H. Nakai, N. Nakamura, K. Nakanishi, K.N. Nigorikawa, T. Nogami, F. Qiu, H. Sagehashi, H. Sakai, S. Sakanaka, M. Shimada, M. Tadano, T. Takahashi, R. Takai, O.A. Tanaka, Y. Tanimoto, T. Uchiyama, K. Umemori, M. Yamamoto, R. Hajima, R. Nagai, M. Sawamura and N. Nishimori, “1 mA Stable Energy Recovery Beam Operation with Small Beam Emittance”, Proceedings of the 10th International Particle Accelerator Conference (IPAC-2019), pp.1482-1485, 19-24 May, 2019, Melbourne, Australia.

P1-9 Project "Element Separation and Analysis"

Papers

1) Y. Kurosaki, R. Nakanishi, M. Saeki and H. Ohba, “Ab initio MRCI study on potential energy curves for a single Cl loss from the palladium tetrachloride anion $PdCl_4^{2-}$”, Chemical Physics Letters, **746**, 137288 (2020). **N**

2) 大場 弘則, 佐伯 盛久, 中西 隆造, “廃液にレーザーを照射して希少金属を回収する”, ケミカルエンジニヤリング, **65**(6), 347-352 (2020). **N**

3) 田村 浩司, 遠山 伸一, “レーザー法による原子炉厚板鋼材切断技術の開発”, 日本原子力学会誌, **62**(5), 268-271 (2020). **N**

4) 大場 弘則, 若井田 育夫, 平等 拓範, “過酷環境下での遠隔レーザー分析技術”, 日本原子力学会誌, **62**(5), 263-267 (2020). **G**

5) R. Nakanishi, M. Saeki, T. Taguchi and H. Ohba, “Photoinduced gold recovery mediated by isopolymolybdate in strongly acidic HCl/NaCl solutions”, Journal of Photochemistry and Photobiology A: Chemistry, 383, 111994 (2019). **N**

6) Y. Kurosaki and K. Yokoyama, “Quantum optimal control of rovibrational excitations of a diatomic alkali halide: one-photon vs. two-photon processes”, Universe 5, 109-1 - 109-15 (2019). **N**

7) T. Taguchi, S. Yamamoto and H. Ohba, “Synthesis of novel hybrid carbon nanomaterials inside silicon carbide nanotubes by ion irradiation”, Acta materialia, **173**, 153 – 162(2019). **N**

8) A. Matsumoto, H. Ohba, M. Toshimitsu, K. Akaoka, A. Ruas, Ikuo Wakaida, T. Sakka and S. Yae, “Enhancement of molecular formation in fiber-optic laser ablation with a long nanosecond pulsed laser”, Spectrochimica Acta Part B, **155**, 56-60(2019). **G**

9) N. Okubo, Y. Okuno, A. Kitamura and T. Taguchi, “Influence of gamma-ray irradiation on mechanical property of YSZ for oxygen sensors in ADS”, Nucl.Instrum. Meth. Phys. Res. B **435**, 198-202(2018). **N**

10) C. Shibazaki, S. Arai, R. Shimizu, M. Saeki, Y. Kinoshita, Andreas Ostermann, Tobias E. Schrader, Y. Kurosaki, T. Sunami, R. Kuroki and M. Adachi, “Hydration structures of the human protein kinase CK2α clarified by joint neutron and X-ray crystallography”, Journal of Molecular Biology **430**(24), 5094-5104(2018). **N**

11) N. Igawa, K. Kodama, T. Taguchi, Y. Yoshida, T. Matsukawa, A. Hoshikawa and T. Ishigaki, “Local Disorder in Proton Conductor BaSn0.5In0.5O2.75 Analyzed by Neutron Diffraction/ Atomic Pair Distribution Function”, Transactions of the Materials Research Society of Japan **43**(6), 329-332(2018). **N**

12) M. Saeki, D. Matsumura, T. Yomogida, T. Taguchi, T. Tsuji, H. Saito and H. Ohba, “In Situ Time-Resolved XAFS Studies on Laser-Induced Particle Formation of Palladium Metal in an Aqueous / EtOH Solution”, Journal of Physical Chemistry C, **123**(1), 817-824(2019). **N**

13) Y. Sasaki, M. Saeki and K. Yoshizuka, “Extractions and spectroscopic studies of various metals with Diglycolamide-Type Tridentate Ligands”, Solvent Extraction Research and Development, Japan, **26**(1), 21-34(2019). **N**

14) T. Nozawa, K. Ozawa, C. Park, J. Park, A. Kohyama, A. Hasegawa, S. Nogami, T. Hinoki, S. Kondo, T. Yano, T. Shibayama, B. Tsuchiya, T. Shikama, S. Nagata, T. Tanaa, H. Iwakiri, Y. Yamamoto, S. Konishi, R. Kasada, M. Kondo, T. Kunugi, T. Yokomine, Y. Ueki, N. Okubo, T. Taguchi and H. Tanigawa, “Japanese activities of the R&D on silicon carbide composites in the broader approach period and beyond”, Journal of Nuclear Materials **511**, 582 -590(2018). **N**

15) K. Kakitani, T. Kimata, T. Yamaki, S. Yamamoto, D. Matsumura, T. Taguchi, T. Terai, “X-ray Absorption Study of Platinum Nanoparticles on an Ion-Irradiated Carbon Support”, Radiation Physics and Chemistry **153**, 152-155(2018). **I**

16) K. Kakitani, T. Kimata, T. Yamaki, S. Yamamoto, T. Taguchi, T. Kobayashi, W. Mao, T. Terai, “The interface between platinum nanoparticle catalysts and an Ar+-irradiated carbon support”, Surface and Coating Technology, **355**(2018). **I**

17) S. Asai, M. Ohata, T. Yomogida, M. Saeki, H. Ohba, Y. Hanzawa, T. Horita and Y. Kitatsuji, “Determination of 107Pd in Pd purified by selective precipitation from spent nuclear fuel by laser ablation ICP-MS”, Analytical and Bioanalytical Chemistry, **411**(5), 973-983(2018). **N**

18) 田村 浩司, 遠山 伸一, “厚板鋼材のレーザー切断技術-廃炉の時代の先端技術開発－”, 日本原子力学会誌, **61**(5), 413 – 415(2019). **N**

19) 若井田 育夫, 大場 弘則, 宮部 昌文, 赤岡 克昭, 大場 正規, 田村 浩司, 佐伯 盛久, “核燃料サイクルおよび福島第一原子力発電所廃炉への適用を念頭としたレーザー誘起ブレークダウン分光と関連分光技術”, 光学（日本光学会機関誌）, **48**(1), 13 – 20(2019). **N**

20) T. Taguchi, S. Yamamoto and H. Ohba, “Ion irradiation-induced novel microstructural change in silicon carbide nanotubes”, Acta Materialia, **154**, 90-9 (2018). **I**

21) A. Matsumoto, H. Ohba, M. Toshimitsu, K. Akaoka, A. Ruas and T. Sakka, “Fiber-optic laser-induced breakdown spectroscopy of zirconium metal in the air: The special feature of the plasma produced by the long-pulse laser”, Spectrochimica Acta Part B: Atomic Spectroscopy, **142**, 37-49 (2018). **N**

22) 佐伯 盛久, 浅井 志保, 大場 弘則, “レーザー微粒子化反応を利用した放射性廃液からの白金族元素分離法の開発”, ぶんせき, (4), 138−43 (2018). **N**

Patent

1) 大場 弘則, 佐伯 盛久, 田口 富嗣, 中西 隆造, “回収装置、回収システム、及び回収方法”, 特願 2019-097119. **N**

Press・TV

1) “廃液からパラジウムや金、銀”,プレス発表： 日経サイエンス（2020 年 2 月号）に掲載. **N**

2) “廃液中の金属、レーザーで回収～量研、連続処理装置開発めざす～”, 2019/9/18 プレス発表： 日経産業新聞に掲載. **N**

P1-10 Advanced Functional Polymer Materials Research Group

Papers

1) M. Omichi, Y. Ueki, N. Seko and Y. Maekawa, “Development of a Simplified Radiation-Induced Emulsion Graft Polymerization Method and Its Application to the Fabrication of a Heavy Metal Adsorbent”, Polymers, **11**, 1373:1–11 (2019). **E, G**

2) Y. Zhao, K. Yoshimura, H. Takamatsu, A. Hiroki, Y. Kishiyama, H. Shishitani, S. Yamaguchi, H. Tanaka, S. Koizumi, A. Radulescu, M. Appavou and Y. Maekawa, “Imidazolium-based anion exchange membranes for alkaline anion fuel cells: Interplay between morphology and anion transport behavior”, Journal of The Electrochemical Society, **166**, F472-F478 (2019). **G**

3) L. Bai, Y. He, J. Zhou, Y. Lim, V-C. Mai, Y. Chen, S. Hou, Y. Zhao, J. Zhang, H. Duan, “Responsive amorphous photonic structures of spherical/polyhedral colloidal metal–organic frameworks”, Advanced Optical Materials, **7**, 1900522 (2019). **N**

4) S. Koizumi, Y. Zhao and A. Patra, “Hierarchical structure of microbial cellulose and marvelous water uptake, investigated by combining neutron scattering instruments at research reactor JRR-3, Tokai”, Polymer, **176**, 244-255 (2019). **N**

5) T.D. Tap, L.L. Nguyen, Y. Zhao, S. Hasegawa, S. Sawada, N.Q. Hung, L.A. Tuyen and Y. Maekawa, “SAXS investigation on morphological change in lamellar structures during propagation steps of graft-type polymer electrolyte membranes for fuel cell applications”, Macromolecular Chemistry and Physics, **221**, 1900325 (2020). **G**

6) S. Hasegawa, A. Hiroki, Y. Ohta, N. Iimura, A. Fukaya and Y. Maekawa, “Thermally stable graft-type polymer electrolyte membranes consisting based on poly (ether ether ketone) and crosslinked graft-polymers for fuel cell applications”, Radiat. Phys. Chem., **171**, 108647 (2020). **G**

7) 廣木章博, 田口光正, “放射線架橋ゲルを母材とするポリマーゲル線量計の LET 効果”, RADIOISOTOPES, **68**, 277-283 (2019). **E, G**

8) A. Kitamura, T. Yamaki, Y. Yuri, H. Koshikawa, S. Sawada, T. Yuyama, A. Usui and A. Chiba, “Control of the size of etchable ion tracks in PVDF - Irradiation in an oxygen atmosphere and with fullerene C60”, Nucl. Instrum. Meth. Phys. Res. B, **460**, 254-258 (2019). **C**

9) Y. Inagaki, N. Sakaba, N. Tanaka, M. Nomura, S. Sawada and

T. Yamaki, “膜技術と水素社会　ー膜分離新 IS プロセス技術の開発ー”, 日本海水学会誌, **73**, 194-202 (2019). **G**

10) S. Sawada, M. Yasukawa, H. Koshikawa, A. Kitamura, M. Higa and T. Yamaki, “高エネルギー重イオンビームによる海水濃縮用カチオン、アニオン交換膜の開発”, 日本海水学会誌, **73**, 208-216 (2019). **G**

11) S. Sawada, H. Koshikawa, A. Kitamura, M. Higa and T. Yamaki, “Ion and water transport properties of cation exchange membranes prepared by heavy-ion-track grafting technique”, Separation Science and Technology, **55**, 2211-2216 (2020). **G**

12) O. Myagmarjav, N. Tanaka, S. Kubo, M. Nomura, T. Yamaki, S. Sawada, J. Iwatsuki, H. Noguchi, Y. Kamiji, I. Ioka, T. Tsuru, M. Kanezashi, X. Yu, M. Machida, T. Ishihara, H. Abekawa, M. Mizuno, T. Taguchi, Y. Hosono, Y. Kuriki, M. Inomata, K. Miyajima, Y. Inagaki and N Sakaba, “Research and development on membrane IS process for hydrogen production using solar heat”, International Journal of Hydrogen Energy, **44**, 19141-19152 (2019). **G**

13) Y. Ueki and N. Seko, “Synthesis of Fibrous Metal Adsorbent with a Piperazinyl-Dithiocarbamate Group by Radiation-Induced Grafting and Its Performance”, ACS Omega, **5**, 2947–2956 (2020). **E**

14) N. A. F. Othman, S. Selambakkannu, T. T. Ming, N. H. Mohamed, T. Yamanobe and N. Seko, “Application of Response Surface Modelling to Economically Maximize Thorium (IV) Adsorption”, Desalin. water Treat., **179**, 172–182 (2020). **E**

15) N. A. F. Othman, S. Selambakkannu, T. Yamanobe, H. Hoshina, N. Seko and T. A. T. Abdullah, “Radiation grafting of DMAEMA and DEAEMA-based adsorbents for thorium adsorption”, J. Radioanal. Nucl. Chem., **324**, 429–440 (2020). **E**

16) N. A. F. Othman, S. Selambakkannu, H. Azian, C. T. Ratnam, T. Yamanobe, H. Hoshina and N. Seko, “Synthesis of surface ion-imprinted polymer for specific detection of thorium under acidic conditions”, Polym. Bull., Open Access (2020). **E**

17) N. H. Zabaruddin, N. H. Mohamed, L. C. Abdullah, M. Tamada, Y. Ueki, N. Seko, T. Shean and Y. Choong, “Palm oil-based biodiesel synthesis by radiation-induced kenaf catalyst packed in a continuous flow system”, Ind. Crops and Prod., **36**, 102–109 (2019). **E**

18) M. Omichi, S. Yamashita, Y. Okura, R. Ikutomo, Y. Ueki, N. Seko and R. Kakuchi, “Surface Engineering of Fluoropolymer Films via the Attachment of Crown Ether Derivatives Based on the Combination of Radiation-Induced Graft Polymerization and the Kabachnik-Fields Reaction”, Polymers, **11**, 1337:1–11 (2019). **E, G**

19) S. Watanabe, H. Ogi, Y. Arai, H. Aihara, Y. Takahatake, A. Shibata, K. Nomura, Y. Kamiya, N. Asanuma, H. Matsuura, T. Kubota, N. Seko, T. Arai and T. Moriguchi, “STRAD project for systematic treatments of radioactive liquid wastes generated in nuclear facilities”, Prog. Nucl. Energy, **117**, 103090:1–8 (2019). **E**

20) J. Chen and N. Seko, “Cleavage of the Graft Bonds in PVDF-g-St Films by Boiling Xylene Extraction and the Determination of the Molecular Weight of the Graft Chains”, Polymers, **11**, 1098:1–17 (2019). **G**

21) N. A. F. Othman, S. Selambakkannu, T. A. T. Abdullah, H. Hoshina, S. Sattayaporn and N. Seko, “Selectivity of Copper by Amine-Based Ion Recognition Polymer Adsorbent with Different Aliphatic Amines”, Polymers, **11**, 1994:1–21 (2019). **E**

22) 瀬古　典明, “電子線加工技術による高分子吸着材の開発と応用”, Rad Tech News Letter **114**, 2–5 (2019). **E**

23) 瀬古　典明, “高分子産業における放射線利用　グラフト重合”, 放射線と産業, **147**, 17–20 (2019). **E, G**

24) 植木　悠二, “放射線グラフト重合技術による汎用プラスチックへの機能付与”, プラスチックス **70**(11), 54–58 (2019). **E**

Proceedings

1) A. M. A. Mahmoud, K. Yoshimura, A. Hiroki and Y. Maekawa, “The First Durable Imidazolium-based Radiation Grafted Anion Exchange Membranes for Alkaline Fuel cells: The Impact of Water Management”, 236th ESC meeting, [Atlanta, USA] Abstracts, I01B-1487 (2019/10 月). **G**

2) Y. Zhao, “Small-angle Scattering Study for Developing Alkaline Durable Imidazolium-Based Grafted Anion Exchange Membranes for Pt-Free Fuel Cells”, 32nd European Crystallographic Meeting, [Atlanta, USA], Abstracts, MS20-05 (2019/10). **G**

3) K. Yoshimura, Y. Zhao, A. Mahmoud, A. Hiroki, H. Shishitani, S. Yamaguchi, H. Tanaka and Y. Maekawa, “Structural Designs of Alkaline Durable Imidazolium-Containing Anion Conducting Membranes Prepared by Radiation-Induced Grafting for Pt-Free Fuel Cells”, 2019 MRS Fall Meeting, [Boston, USA] Abstracts, EN04.01.05 (2019/10). **G**

4) A. Hiroki, S. Okushima, K. Yoshimura, Y. Zhao, H. Shishitani, S. Yamaguchi and Y. Maekawa, “Crosslinking Effects of Anion-conducting Polymer Electrolyte Membranes on their Properties”, 10th International Membrane Science & Technology Conference, [Sydney, Australia] Abstracts, 115 (2020/2). **G**

5) 吉村　公男, H. Yu, ザオ　ユエ, 廣木　章博, 猪谷　秀幸, 岸山　佳央, 山口　進, 田中　裕久, 前川　康成, “イミダゾリウム基を有する放射線グラフト型アニオン伝導膜の電解質膜特性と階層構造の関係”, 第 62 回放射線化学討論会, [福井大学, 敦賀] 要旨集, 1-0 07 (2019/9)　. **G**

6) 柴田　康瑛, 長谷川　伸, 廣木　章博, 木下　基, 前川　康成, “放射線グラフト重合による高分子電解質膜の合成　～基材膜の結晶モルフォロジーと重合性・機能性との関係～”, 日本化学会関東支部群馬地区研究交流発表会, [群馬大学, 桐生] 要旨集, P-36 (2019/12). **G**

7) 柴田　康瑛, 長谷川　伸, 廣木　章博, 前川　康成, “放射線グラフト重合法によるポリフェニレンスルフィドを基材とした高分子電解質膜の合成”, 第9回 CSJ 化学フェスタ 2019, [タワーホール船堀, 東京] 要旨集, P5-091 (2019/10). **G**

8) 澤田　真一, 田中　健一, 船津　公人, 前川　康成, “高分子電解質膜のイオン伝導性を機械学習で予測する”, 第9回 CSJ 化学フェスタ 2019, [タワーホール船堀, 東京] 要旨集, I2-03 (2019/10). **G**

9) 澤田　真一, “機械学習に基づくグラフト型電解質膜の電気化学特性評価”, 第 68 回高分子討論会, [福井大学, 福井] 要旨集, 2G16 (2019/9). **G**

10) 奥島　駿, 前川　康成, 川勝　年洋, “粗視化分子動力学法とクラスター解析を組み合わせた電解質膜イオンチャネル構造の解析”, 第 68 回高分子討論会, [福井大学, 福井]

要旨集, 1G12 (2019/9). **G**

11) 澤田 真一, 田中 健一, 船津 公人, 前川 康成, “機械学習による放射線グラフト電解質膜のプロトン導電率予測”, 第56回アイソトープ・放射線研究発表会, [東京大学, 東京] 要旨集, 1p-III-0 (2019/7). **G**

12) S. Sawada, T. Kimura, H. Nishijima. N. Tanaka, S. Kubo. S. Imabayashi. M. Nomura and T. Yamaki, “Development of low-overvoltage membrane Bunsen reaction technology for thermochemical IS process”, World Hydrogen Technologies Convention 2019, [東京国際フォーラム, 東京] 要旨集, O2-1 (2019/6). **G**

13) 奥島 駿, “粗視化分子動力学法を用いた高分子電解質膜のイオンチャンネル構造の解析”, 第68回高分子学会年次大会, [大阪府立国際会議場, 大阪] 要旨集, 1Pa037 (2019/5). **G**

14) 大野 真平, 荒井 陽一, 渡部 創, 瀬古 典明, 笠井 昇, 保科 宏行, 柴田 淳広, 野村 和則, “劣化溶媒処理のための機能性グラフト重合吸着材の創出”, 平成 31 年度第 9 回日本原子力学会北関東支部若手研究者発表会, 日本原子力学会, [東海村産業 情報プラザ・茨城] (2019/04/19). **E**

15) R. Kakuchi, S. Yamashita, Y. Okura, T. Hamada, M. Omichi, Y. Ueki and N. Seko, “Multicomponent post-polymerization modification reactions on biomass-sourced organic hybrids”, 第 68 回高分子学会年次大会, 高分子学会, [大阪府立国際会議場・大阪] (2019/05/29). **E, G**

16) 荒井 陽一, 渡部 創, 大野 真平, 野村 和則, 中村 文也, 新井 剛, 瀬古 典明, 保科 宏行, 久保田 俊夫, “使用済み燃料再処理プロセスから発生する廃溶媒処理技術の開発”,日本原子力学会 2019 年秋の大会, 日本原子力学会, [富山大・富山] (2019/09/11). **E**

17) 山下 修平, 大道 正明, 大倉 大和, 生友 隆太, 植木 悠二, 網井 秀樹, 瀬古 典明, 覚知亮平, “ETFE 膜表面へのクラウンエーテルの導入と色素吸着能の評価”, 第 9 回フッ素化学若手の会, 日本フッ素化学会, [あわら温泉 清風荘・福井] (2019/09/12). **E, G**

18) 大道 正明, 瀬古 典明, 前川 康成, “アルコール添加が及ぼす放射線エマルショングラフト重合への影響”, 第 68 回高分子討論会, 高分子学会, [福井大・福井] (2019/09/25). **G**

19) 山下 修平, 大道 正明, 植木 悠二, 瀬古 典明, 覚知 亮平, “バイオマス由来材料のみを出発原料とした放射線グラフト重合及び 多成分連結反応による機能性ハイブリッド材料の合成”, 第 68 回高分子討論会, 高分子学会, [福井大・福井] (2019/09/26). **E, G**

20) 大道 正明, 植木 悠二, 瀬古 典明, 前川 康成, “機械学習で放射線グラフト重合は予測できるのか？”, 第 9 回 CSJ 化学フェスタ 2019, 日本化学会, [タワーホール船堀・東京] (2019/10/16). **E**

21) N. Seko, “Current Status of Quantum Beams Applications for Polymer Processing”,【Invited talk】, Innovation in Polymer Science and Technology (IPST) 2019, Indonesian Institute of Sciences, Indonesian Polymer Association, [The Stones Hotel-Legian Bali, Indonesia] (2019/10/17). **E, G**

22) H. Hoshina and N. Seko, “Performance of Metal Adsorbent Synthesized by Radiation Graft Polymerization”, OKINAWA COLLOIDS 2019, The Chemical Society of Japan, [Bankoku Shinryokan, Okinawa] (2019/11/06) **E**

23) 大場 弘則, 瀬古 典明, 佐伯 盛久, 中西 隆造, 若井田 育夫, “環境水への LIBS 分析適用について”, 第 6 回先端計測技術の応用展開に関するシンポジウム, LIBS 研究会, [京都大・京都] (2019/12/14). **E**

24) N. Seko, H. Amada, H. Hoshina, Y. Ueki, S. Saiki, M. Omichi, J. Chen and M. Nakano, “Adsorption Performance of Fibrous Adsorbents by Radiation Emulsion Graft Polymerization”, The 10th International Membrane Science and Technology Conference (IMSTEC2020), Membrane Society Australasia, [University of Technology Sydney Aerial Convention Centre, Australia] (2020/02/03). **E**

25) H. Hoshina, N. Seko nd H. Amada, “Development of Adsorbent for Rare Earth Recovery Synthesized by Radiation Graft Polymerization”, The 10th International Membrane Science and Technology Conference (IMSTEC2020), Membrane Society Australasia, [University of Technology Sydney Aerial Convention Centre, Australia] (2020/02/03). **E**

Book

1) 瀬古 典明, 植木 悠二, “電子線・放射線による加工・改質” 2020 版 薄膜作製応用ハンドブック, 660–665 (2020). **E**

Patent

1) 袖子田竜也、高橋克巳、高橋浩、前川康成、陳進華、長谷川伸, “電解質膜および電解質膜の製造方法”, 特許第 6522394 号 (2019.05.10). **G**

P1-11 Quantum Sensing and Information Materials Research Group

Papers

1) A. Rifai, N. Tran, P. Reineck, A. Elbourne, E. Mayes, A. Sarker, C. Dekiwadia, E. P. Ivanova, R. J. Crawford, T. Ohshima, B. C. Gibson, A. D. Greentree, E. Pirogova and K. Fox, “Engineering the interface: nanodiamond coating on 3D-printed titanium promotes mammalian cell growth and inhibits staphylococcus aureus colonization”, ACS Appl. Mater. Interfaces 11, 24588-24596 (2019). **E**

2) K. C. Miao, A. Bourassa, C. P. Anderson, S. J. Whiteley, A. L. Crook, S. L. Bayliss, G. Wolfowicz, G. Thiering, P. Udvarhelyi, V. Ivády, H. Abe, T. Ohshima, Á. Gali and D. D. Awschalom, ”Electrically driven optical interferometry with spins in silicon carbide”, Sci. Adv. 5, eaay0527-1-7 (2019). **E**

3) M. Widmann, M. Niethammer, D. Y. Fedyanin, I. A. Khramtsov, T. Rendler, I. D. Booker, J. U Hassan, N. Morioka, Y.-C. Chen, I. G. Ivanov, N. T. Son, T. Ohshima, M. Bockstedte, A. Gali, C. Bonato, S.-Y. Lee and J. Wrachtrup, “Electrical charge state manipulation of single silicon vacancies in a silicon carbide quantum optoelectronic device”, Nano Lett. 19, 7173-7180 (2019). **E**

4) C. P. Anderson, A. Bourassa, K. C. Miao, G. Wolfowicz, P. J. Mintun, A. L. Crook, H. Abe, J. U. Hassan, N. T. Son, T. Ohshima and D. D. Awschalom, “Electrical and optical control of single spins integrated in scalable semiconductor devices”, Science 366, 1225-1230 (2019). **E**

5) M. Pfender, P. Wang, H. Sumiya, S. Onoda, W. Yang, D. B. R. Dasari, P. Neumann, X-Y. Pan, J. Isoya, R-B. Liu and J. Wrachtrup, “High-resolution spectroscopy of single nuclear spins via sequential weak measurements”, Nat. Commun., 10, 594-1~8 (2019). **E**

6) D. Terada, T. F. Segawa, A. I. Shames, S. Onoda, T. Ohshima, E. Osawa, R. Igarashi and M. Shirakawa, “Monodisperse five-nanometer-sized detonation nanodiamonds enriched in nitrogen-vacancy centers”, ACS Nano, 13, 6461-6468 (2019). **E**

7) M. Haruyama, S. Onoda, T. Higuchi, W. Kada, A. Chiba, Y. Hirano, T. Teraji, R. Igarashi, S. Kawai, H. Kawarada, Y. Ishii, R. Fukuda, T. Tanii, J. Isoya, T. Ohshima and O. Hanaizumi, “Triple nitrogen-vacancy centre fabrication by $C_5N_4H_n$ ion implantation”, Nat. Commun., 10, 2664-1-9 (2019). **T**

8) J. Michl, J. Steiner, A. Denisnko, A. Bulau, A. Zimmermann, K. Nakamura, H. Sumiya, S. Onoda, P. Neumann, J. Isoya and J. Wrachtrup, “Robust and accurate electric field sensing with solid state spin ensembles”, Nano Lett., 19, 4904-4910 (2019). **E**

9) T. Fujisaku, R. Tanabe, S. Onoda, R. Kubota, T. F. Segawa, F. T.-K. So, T. Ohshima, I. Hamachi, M. Shirakawa and R. Igarashi, “pH nanosensor using electronic spins in diamond”, ACS Nano, 13, 11726-11732 (2019). **E**

10) M. Niethammer, M. Widmann, T. Rendler, N. Morioka, Y-C. Chen, R. Stohr, J. U. Hassan, S. Onoda, T. Ohshima, S-Y. Lee., A. Mukherjee, J. Isoya, N. T. Son and J. Wrachtrup, “Coherent electrical readout of defect spins in silicon carbide by photo-ionization at ambient conditions”, Nat. Commun. **10**, 5569-1-8 (2019). **E**

11) S. Castelletto, A. S. A. Atem, F. A. Inam, H. J. von Bardeleben, S. Hameau, A. F. Almutairi, G. Guillot, S.-I. Sato, A. Boretti and J. M. Bluet, “Deterministic placement of ultra-bright near-infrared color centers in arrays of silicon carbide micropillars,” Beilstein J. Nanotechnol. **10**, 2383-2395 (2019). **N**

12) S.-I. Sato, T. Narahara, Y. Abe, Y. Hijikata, T. Umeda and T. Ohshima, “Formation of nitrogen-vacancy centers in 4H-SiC and their near infrared photoluminescence properties”, J. Appl. Phys. **126**, 083105-1-10 (2019). **T, I**

13) Y. Chiba, Y. Yamazaki, T. Makino, S.-I. Sato, N. Yamada, T. Satoh, K. Kojima, S.-Y. Lee, Y. Hijikata and T. Ohshima, “Creation of color centers in SiC PN diodes using proton beam writing”, Mater. Sci. Forum **963**, 709-713 (2019). **S, I**

14) A. Csore, B. Magnusson, N. T. Son, A. Gallstrom, T. Ohshima, I. G. Ivanov and A. Gali1, “First-principles study on photoluminescence quenching of divacancy in 4H SiC”, Mater. Sci. Forum **963**, 714-717 (2019). **E**

15) S.-I. Sato, M. Deki, T. Nakamura, T. Nishimura, D. Stavrevski, A. D. Greentree, B. C. Gibson, and T. Ohshima, “Photoluminescence properties of praseodymium ions implanted into submicron regions in gallium nitride”, Jpn. J. Appl. Phys. **58**, 051011-1-6 (2019). **I**

16) H. Zheng, J. Xu, G. Z. Iwata, T. Lenz, J. Michl, B. Yavkin, K. Nakamura, H. Sumiya, T. Ohshima, J. Isoya, J. Wrachtrup, A. Wickenbrock and D. Budker, “Zero-field magnetometry based on nitrogen-vacancy ensembles in diamond”, Phys. Rev. Applied **11**, 064068-1-7 (2019). **E**

17) N. T. Son, P. Stenberg, V. Jokubavicius, H. Abe, T. Ohshima, J. U. Hassan and I. G. Ivanov, “Energy levels and charge state control of the carbon antisite-vacancy defect in 4H-SiC”, Appl. Phys. Lett. **114**, 212105-1-5 (2019). **E**

18) R. Nagy, M. Niethammer, M. Widmann, Y. -C. Chen, P. Udvarhelyi, C. Bonato, J. U. Hassan, R. Karhu, I. G. Ivanov, N. T. Son, J. R. Maze, T. Ohshima, Ö. O. Soykal, Á. Gali, S.-Y. Lee, F. Kaiser and J. Wrachtrup, “High-fidelity spin and optical control of single silicon-vacancy centres in silicon carbide”, Nature Communications **10**, 1954-1-8 (2019). **E**

P2-1 Project “Microbeam Radiation Biology”

Papers

1) T. Funayama, “Heavy-Ion Microbeams for Biological Science: Development of System and Utilization for Biological Experiments in QST-Takasaki”, Quantum Beam Sci. **3**, 13 (2019). **C**

2) T. Funayama, T. Sakashita, M. Suzuki, Y. Yokota, N. Miyawaki, H. Kashiwagi, T. Satoh and S. Kurashima, “An irradiation device for biological targets using focused microbeams of cyclotron-accelerated heavy ions”. Nucl. Instrum. Meth. Phys. Res. B **465**, 101-109 (2020). **C**

3) Y. Yokota, Y. Wada and T. Funayama, “Distinct modes of death in human neural stem and glioblastoma cells irradiated with carbon-ion and gamma-rays”, Int. J. Radiat. Biol. **96**, 172-178 (2020). **C, G**

Patent

1) 鈴木 芳代, 坂下 哲哉, 舟山 知夫, 平塚 哉, “生物試料用マイクロチップ, カバー、生物試料封入キットおよび方法”, 国際出願 PCT/JP2019/020219(2019.05.22), 公開番号 WO/2019/225633（2019.11.28）. **C**

P2-2 Project “Ion Beam Mutagenesis”

Papers

1) Y. Oono, H. Ichida, R. Morita, S. Nozawa, K. Satoh, A. Shimizu, T. Abe, H. Kato and Y. Hase, "Genome sequencing of ion-beam-induced mutants facilitates detection of candidate genes responsible for phenotypes of mutants in rice", Mutat. Res. - Fundam. Mol. Mech. Mutagen. **821**, 111691 (2020). **C**

2) Y. Hase, K. Satoh, H. Seito and Y. Oono, "Genetic consequences of acute/chronic gamma and carbon ion irradiation of *Arabidopsis thaliana*", Front. Plant Sci. **11**, 336 (2020). **C, G**

3) J. Zhang, M. Xu, M. S. Dwiyanti, S. Watanabe, T. Yamada,

Y. Hase, A. Kanazawa, T. Sayama, M. Ishimoto, B. Liu and J. Abe, "A soybean deletion mutant that moderates the repression of flowering by cool temperatures", Front. Plant Sci. **11,** 429 (2020). **G**

4) S. Fujinami, K. Satoh, I. Narumi and M. Ito, "Draft genome sequence of calcium-dependent *Novosphingobium* sp. strain TCA1, isolated from a hot spring containing a high concentration of calcium ions", Microbiol. Resour. Announc. **9**, e00145-20 (2020). **N**

5) K. Satoh and Y. Oono, "Studies on application of ion beam breeding to industrial microorganisms at TIARA", Quantum Beam Sci. **3**, 11 (2019). **C**

6) Y. Hase, K. Satoh, A. Chiba, Y. Hirano, S. Tomita, Y. Saito and K. Narumi, "Experimental study on the biological effect of cluster ion beams in bacillus subtilis spores", Quantum Beam Sci. **3**, 8 (2019). **T**

7) A.N. Sakamoto, "Translesion synthesis in plants: ultraviolet resistance and beyond", Front. Plant Sci, **10**, 1208 (2019). **C, G**

8) A. Shibai, K. Satoh, M. Kawada, H. Kotani, I. Narumi and C. Furusawa, "Complete genome sequence of a radioresistant bacterial strain, *Deinococcus grandis* ATCC 43672", Microbiol. Resour. Announc. **8**(45), e01226-19 (2019). **N**

9) 横田 裕一郎, “生物の放射線耐性研究の意味するところ」, 放射線と産業, **146**, 38–42 (2019). **C, G**

10) 長谷 純宏, 佐藤 勝也, 千葉 敦也, 平野 貴美, 斎藤 勇一, 鳴海 一雅, “クラスターイオンの生物効果に関する研究」, 平成 30 年度原子力機構施設利用共同研究連携重点研究 成果報告書, 3–4, (2019). **T**

11) 渡部 貴志, 佐藤 勝也, 林 秀謙, 増渕 隆, “輸出用に適した群馬清酒酵母の育種に関する研究（第3報）」, 群馬県立産業技術センター研究報告（2018）, 1–4, (2019). **N**

Proceedings

1) 三善 英彦, 佐藤 勝也, 大野 豊, 鳴海 一成, “放射線抵抗性細菌デイノコッカス･ラジオデュランスのDNA修復機構の正確性に関する比較ゲノム解析」, 日本農芸化学会2020年度大会, ［九州大学, 福岡］, 大会講演要旨集, 2A09a10, (2020) **G**

2) 小山 智己, 加藤 悠一, 佐藤 勝也, 大野 豊, 蓮沼 誠久, 近藤 昭彦, “窒素源存在下で油脂を高蓄積する海洋性クラミドモナス変異株の選択的育種」, 第 71 回日本生物工学会大会, 日本生物工学会, ［岡山大学, 岡山］, 大会講演要旨集, 1Bp01, (2019) **C**

3) 加藤 悠一, 小山 智己, 佐藤 勝也, 大野 豊, 張 嘉修, 蓮沼 誠久, 近藤 昭彦, “海洋性クラミドモナス油脂高蓄積変異株における油脂･カロテノイド増産メカニズムの解明”, 第 71 回日本生物工学会大会, 日本生物工学会, ［岡山大学, 岡山］, 大会講演要旨集, 1Bp02/トピックス集 pp. 37–38, (2019). **C**

4) 副島 敬佑, 岩田 康嗣, 長谷 純宏, 大野 豊, 鈴木 石根, 新家 弘也, “ハプト藻におけるオイル分解抑制変異体の解析”, 2019 年度関東学院大学理工／建築･環境学会研究発表講演会論文集, ［関東学院大学, 神奈川］, pp. 18-19 (2019) **C**

5) 吉田雅貴, 岩田康嗣, 長谷純宏, 大野豊, 鈴木石根, 新家弘也, “アルケノン高産生変異株における CO_2影響”, 2019 年度関東学院大学理工／建築･環境学会研究発表講演会論文集, ［関東学院大学, 神奈川］, pp. 110 (2019). **C**

6) Y. Yokota, and A. N. Sakamoto, “Contribution of the homologous recombination pathway in DNA double-strand break repair of the haploid model plant *Physcomitrella patens*”, 日本放射線影響学会第62回大会要旨集, ［京都大学, 京都］, P76 (2019). **C, G**

7) 横田 裕一郎, 「植物のイオンビーム育種と放射線耐性研究について」**【招待講演】**, 2019 年東京 RBC 夏のラボ合宿要旨集, [高エネルギー加速器研究機構, つくば] (2019). **C, G**

Patents

1) 山口 絵梨香, 長谷 純宏, 野澤 樹, 大野 豊, “はまごろも 6 号”, 品種登録 34284 (2019.10.31).

2) 山口 絵梨香, 長谷 純宏, 野澤 樹, 大野 豊, “はまごろも 7 号”, 品種登録 34285 (2019.10.31).

3) 蓮沼 誠久, 加藤 悠一, 小山 智己, 近藤 昭彦, 佐藤 勝也, 大野 豊, “窒素源存在条件下オイル高蓄積藻類株の育種方法、窒素源存在条件下オイル高蓄積藻類株及びそれを用いた油脂製造方法”, 特願 2019-145222 (2019.8.7).

4) 蓮沼 誠久, 加藤 悠一, 近藤 昭彦, 佐藤 勝也, 大野 豊, “オイル高蓄積有用藻類株の育種方法、藻類のオイル高蓄積変異株及びそれを用いた油脂製造方法”, 特願 2019-104643 (2019.6.4).

Press･TV

1) “群馬県オリジナルの輸出用清酒酵母ができました！～県産清酒の輸出拡大を目指します～”, 2019/11/27 プレス発表：読売新聞, 上毛新聞に掲載. **C**

2) “植物は、弱いガンマ線でも積極的に反応して変異の発生を抑制し、DNAを守る―モデル植物シロイヌナズナへの長期間照射試験で発見！―”, 2020/3/10 プレス発表. **C, G**

P2-3 Project “Medical Radioisotope Application”

Papers

1) A. Yamaguchi, A. Achmad, H. Hanaoka, Y. D. Heryanto, A. Bhattarai, Ratianto, E. Khongorzul, R. Shintawati, A. A. P. Kartamihardja, A. Kanai, Y. Sugo, N. S. Ishioka, T. Higuchi and Y. Tsushima, “Immuno-PET imaging for non-invasive assessment of cetuximab accumulation in non-small cell lung cancer” BMC Cancer, **19**, 1000 (2019). **C, 2-23**

2) T. Sakashita, T. Sato, N. Hamada, “A biologically based mathematical model for spontaneous and ionizing radiation cataractogenesis” PLoS ONE, **14**, e0221579 (2019). **C**

3) 大島 康宏, “α 線放出 ^{211}At を利用した悪性褐色細胞腫に対する標的アイソトープ治療薬の開発”, JSMI Report, **13**, 3-10 (2020/01). **C**

Proceedings

1) 坂下 哲哉, 大島 康宏, 河野 暢明, 横田 裕一郎, 渡辺 茂樹, 佐々木 一郎, 石岡 典子, 荒川 和晴, “Anti-tumor effects of [At-211]-MABG treatment in PC12 pheochromocytoma cells and cell death via p53-p21 signaling pathway”, 日本放射線影響学会第 62 回大会, 要旨集 Oral session 8, [京都大吉田キャンパス･京都] (2019/11).

2) 坂下 哲哉, 佐藤 達彦, 篠原 彩花, 石岡 典子, 花岡 宏史, “標的アイソトープ治療における 3D 培養スフェロイド研究への 3D 線量評価シミュレーションの適用”, 第 3 回がん三次元培養研究会, 要旨集 P3, [国立がん研究センター・東京](2019/11). **N**

3) 花岡 宏史、大島 康宏、鈴木 博元、佐々木 一郎、渡辺 茂樹、羽場 宏光、荒野 泰、石岡 典子、対馬 義人, “At-211 標識 α メチル-フェニルアラニンを用いた内用放射線療法”, 第 59 回日本核医学会学術総会, 要旨集 M2VB1, [松山・愛媛] (2019/11). **C**

4) 大平 慎一, 宮地 凌摩, 丸山 洋平, 須郷 由美, 石岡 典子, 森 勝伸, 戸田 敬, “電気透析による放射性金属イオンの抽出とカウンターイオンの置換”, 第 38 回溶媒抽出討論会, 要旨集 A-16, [佐賀大・佐賀] (2019/11). **C**

5) 森 勝伸, 須郷 由美, 大平 慎一, 丸山 洋平, 宮地 凌摩, 戸田 敬, 石岡 典子, “カラム型フロー電解セルを用いた放射性同位体銅の分離”, 第 56 回フローインジェクション分析講演会, 要旨集, [愛知工業大・名古屋] (2019/10). **C**

6) 丸山洋平, 須郷 由美, 大平 慎一, 山崎 直亨, 宮地 凌摩, 戸田 敬, 石岡 典子, 渡辺 茂樹, 森 勝伸, “カラム型フロー電解セルを用いた医療用放射性銅の分離”, 日本分析化学会第 68 年会, 要旨集 Y1043, [千葉大・千葉] (2019/9). **C**

7) 宮地 凌摩, 丸山 洋平, 須郷 由美, 石岡 典子, 森 勝伸, 大平 慎一, 戸田 敬, “PET 検査薬剤合成のための放射性同位体金属イオンのハンドリング”, 日本分析化学会第 68 年会, 要旨集 Y2027, [千葉大・千葉] (2019/9). **C**

8) 貝塚 祐太, 鈴木 博元, 龍田 真帆, 田中 浩士, 上原 知也, 白神 宜史, 大江 一弘, 渡辺 茂樹, 豊嶋 厚史, 渡部 直史, 石岡 典子, 畑澤 順, 荒野 泰, “Radiotheranostics に有用な放射性ヨウ素/アスタチン-211 標識母体としてのネオペンチル誘導体の評価”, 第 17 回次世代を担う若手のためのフィジカル・ファーマフォーラム (PPF2019), [アヤハレークサイドホテル・滋賀](2019/9).

9) 石岡 典子, 渡辺 茂樹, 近藤 浩夫, 高井 俊秀, 古川 智弘, “がん治療用アスタチン 211 の連続製造を可能にする液体ビスマス標的の開発(1) プロジェクトの概要”, 日本原子力学会 2019 年秋の大会, 要旨集 1M16, [富山大五福キャンパス・富山] (2019/09). **C**

10) 渡辺 茂樹, 近藤 浩夫, 江夏 昌志, 高井 俊秀, 古川 智弘, 石岡 典子, “がん治療用アスタチン 211 の連続製造を可能にする液体ビスマス標的の開発(2) 液体ビスマス標的の照射試験”, 日本原子力学会 2019 年秋の大会, 要旨集 1M17, [富山大五福キャンパス・富山] (2019/09). **C**

11) 古川 智弘, 高井 俊秀, 近藤 浩夫, 渡辺 茂樹, 石岡 典子, “がん治療用アスタチン 211 の連続製造を可能にする液体ビスマス標的の開発(3) 標的窓候補材の高温液体ビスマスとの共存性”, 日本原子力学会 2019 年秋の大会, 要旨集 1M18, [富山大五福キャンパス・富山] (2019/09). **C**

12) 渡辺 茂樹, “核医学治療への応用を目指したアルファ線放出核種の分離・標識法の研究”【招待講演】, PET サマーセミナー2019 in 福島, 要旨集 セッション 12-2, [コラッセ福島・福島] (2019/08). **C**

13) 森 勝伸, 山崎 直亨, 須郷 由美, 大平 慎一, 宮地 凌摩, 戸田 敬, 石岡 典子, 渡辺 茂樹, “電気化学的手法を用いた医療用放射性銅の分離精製”, 第 79 回 分析化学討論会, 要旨集 B2001R, [北九州国際会議場＆AIM・北九州] (2019/5). **C**

14) 宮地 凌摩, 山崎 直亨, 須郷 由美, 石岡 典子, 森 勝伸, 大平 慎一, 戸田 敬, “超微量放射性金属のインラインカウンターイオン置換”, 第 79 回 分析化学討論会, 要旨集 Y1047, [北九州国際会議場＆AIM・北九州] (2019/5). **C**

15) S.Watanabe, M. Anwar-Ul Azim, I. Nishinaka, I. Sasaki, Y. Ohshima, K. Yamada, N.S. Ishioka, “Synthesis of 4-[^{211}At]astato-L-phenylalanine via electrophilic demetallation from a silyl precursor”, 11th International Symposium on Targeted Alpha Therapy (TAT11), Poster #21 [Ottawa, Canada] (2019/04). **C**

16) Y. Ohshima, N. Kono, Y. Yokota, S. Watanabe, I. Sasaki, N. S. Ishioka, T. Sakashita and K. Arakawa, “RNA-seq Reveals Tumor Radiation Response and Novel Molecular Targets on α-emitting Meta-^{211}At-astato-benzylguanidine Therapy for Malignant Pheochromocytoma”, 11th International Symposium on Targeted Alpha Therapy (TAT11), Poster #2 [Ottawa, Canada] (2019/04). **C**

17) H. Suzuki, H. Tanaka, N. Washiya, M. Tatsuta, Y. Sato, Y. Kaizuka1, S. Watanabe3, T. Uehara1, N.S. Ishioka, N. Shirakami, T. Watabe, J. Hatazawa and Y. Arano, “Radiohalogenated neopentyl derivatives: A novel scaffold for radioiodinated and astatinated compounds of high stability against in vivo dehalogenation”, 11th International Symposium on Targeted Alpha Therapy (TAT11), 要旨集 14 [Ottawa, Canada] (2019/04). **C**

Patent

1) 石岡 典子, 近藤 浩夫, 渡 辺茂樹, “放射性同位体の製造方法, 製造装置”, 放射性標識化合物及び放射性同位体製造装置”, 特願 2019-068102 (2019.3.29). **C**

P2-4 Project "Radiotracer Imaging"

Papers

1) S. Yamamoto, M. Yamaguchi, T. Akagi, M. Kitano and N. Kawachi, “Sensitivity improvement of YAP(Ce) cameras for imaging of secondary electron bremsstrahlung X-rays emitted during carbon-ion irradiation: problem and solution”, Phys. Med. Biol. **65**: 105008, (2020). **N**

2) A. Yoneda, D. Yasutake, K. Hidaka, N. I. Muztahidin, Y. Miyoshi, M. Kitano and T. Okayasu, “Effects of supplemental lighting during the period of rapid fruit development on the growth, yield, and energy use efficiency in strawberry plant production”, International Agrophysics A **34**, 233-239 (2020). **N**

3) K. Kurita, Y. Miyoshi, Y. Nagao, M. Yamaguchi, N. Suzui, Y.-G. Yin, S. Ishii, N. Kawachi, K. Hidaka, E. Yoshida, S. Takyu, H. Tashima and T. Yamaya, “Fruit PET: 3-D imaging of carbon distribution in fruit using OpenPET”, Nucl. Instrum. Methods. Phys. Res. B **954**, 161843 (2020). **C, 2-25, 2-30**

4) S. Nakamura, N. Suzui, Y.-G. Yin, S. Ishii, S. Fujimaki, N. Kawachi, H. Rai, T. Matsumoto, K. Izawa-Sato, N. Ohkama-Ohtsu, “Effects of enhancing endogenous and exogenous glutathione in roots on cadmium movement in *Arabidopsis thaliana*”, Plant

Science **290**, 110304 (2020). **C, 2-25, 2-30**

5) 鈴井 伸郎, 河地 有木, 古川 純, 田野井 慶太朗, “植物科学における放射線イメージング”, RADIOISOTOPES **68**, 643-657 (2019). **C, 2-25, 2-30**

6) K. Yoshino, Y. Numajiri, S. Teramoto, N. Kawachi, T. Tanabata, T. Tanaka, T. Hayashi, T. Kawakatsu, Y. Uga, “Towards a deeper integrated multi-omics approach in the root system to develop climate-resilient rice”, Molecular Breeding **39**, 165 (2019). **C**

7) N. Suzui, K. Tanoi, J. Furukawa, N. Kawachi, “Recent Advances in Radioisotope Imaging Technology for Plant Science Research in Japan”, Quantum Beam Science **3**, 18 (2019). **C, 2-25, 2-30**

8) M. Yamaguchi, Y. Nagao and N. Kawachi, “A simulation study on reduction of the background component using veto counters for imaging of therapeutic proton beams by measuring secondary electron bremsstrahlung using a parallel-hole collimator”, Jpn. J. Appl. Phys. **58**, 021005 (2019). **N**

9) T. Nakano, M. Sakai, K. Torikai, Y. Suzuki, S. Noda, M. Yamaguchi, S. Takeda, Y. Nagao, M. Kikuchi, H. Odaka, T. Kamiya, N. Kawachi, S. Watanabe, K. Arakawa and T. Takahashi, “Imaging of ^{99m}Tc-DMSA and ^{18}F-FDG in humans using a Si/CdTe Compton camera”, Phys. Med. Biol. **65**, 05LT01 (2020). **N**

10) S. Yamamoto, M. Yamaguchi, T. Akagi, M. Sasano and N. Kawachi, “Development of a YAP(Ce) camera for the imaging of secondary electron bremsstrahlung x-ray emitted during carbon-ion irradiation toward the use of clinical conditions”, Phys. Med. Biol., **64**, 135019 (2019). **N**

11) T. Yoshihara, K. Kurita, H. Matsumura, V. Yoschenko, N. Kawachi, S. Hashida, A. Konoplev and H. Yoshida, “Assessment of gamma radiation from a limited area of forest floor using a cumulative personal dosimeter”, J. Environ. Radioact, **204**, 95-103 (2019). **N**

12) Y.-G. Yin, S. Ishii, N. Suzui, M. Igura, K. Kurita, Y. Miyoshi, N. Nagasawa, M. Taguchi and N. Kawachi, “On-line rapid purification of [^{13}N]N$_2$ gas for visualization of nitrogen fixation and translocation in nodulated soybean”, Appl. Radiat. Isot. **151**, 7-12 (2019). **C**

13) A. Wongkaew, S. Nakamura, N. Suzui, Y.-G. Yin, S. Ishii, N. Kawachi, K. Kojima, H. Sekimoto, T. Yokoyama and N. Ohkama-Ohtsu, “Elevated glutathione synthesis in leaves contributes to zinc transport from roots to shoots in Arabidopsis”, Plant Science **283**, 416-423 (2019). **C**

14) 三好 悠太, 日高 功太, “ポジトロンイメージング技術(PETIS)を用いたイチゴ果実への光合成産物転流動態の評価”, アグリバイオ, **3**, 761-764 (2019). **C**

15) M. Yamaguchi, Y. Nagao and N. Kawachi. “A simulation study on estimation of Bragg-peak shifts via machine learning using proton-beam images obtained by measurement of secondary electron bremsstrahlung”, IEEE Trans. Radiat. Plasma Med. Sci. **4**, 253-261 (2020). **N**

Proceedings

1) S. Sakurai, K. Kurita, H. Yoshida, N. Kawachi, K. Uchiyama and T. Yoshihara, “Development of a simple and easy method for measuring radioactivity of bark using cumulative personal dosimeters”, Proceedings of the 20th Workshop on Environmental Radioactivity, 242-247 [Tsukuba, Japan] (2019). **N**

2) Y.-G. Yin, “Visualizing and evaluating long-distance phloem transport of photoassimilates by the PETIS and 11CO2 tracer” 【Invited talk】, 第 61 回日本植物生理学会年会シンポジウム “植物における長距離情報伝達の分子基盤”, S03-6 [大阪大学・大阪](2020/03). **C, 2-25,2-30**

3) Y. Nagao, M. Yamaguchi, S. Watanabe, N. S. Ishioka, N. Kawachi and H. Watabe, “Optimization of Coincidence Time Window on Compton Imaging of Astatine-211 for Targeted α-Particle Radiotherapy”, 2019 IEEE NSS/MIC, Prgm. M-01-361, [Manchester, UK] (2019/10). **N**

4) M. Yamaguchi, Y. Nagao and N. Kawachi, “A Simulation Study on Estimation of Bragg-Peak Shifts via Machine Learning Using Proton-Beam Images Obtained by Measurement of Secondary Electron Bremsstrahlung”, 2019 IEEE NSS/MIC, Prgm. M-13-345, [Manchester, UK] (2019/10).

5) S. Yamamoto, M. Yamaguchi, T. Akagi, M. Sasano and N. Kawachi, “Imaging of secondary electron bremsstrahlung X-ray emitted during carbon-ion irradiation near clinical conditions”, 2019 IEEE NSS/MIC, Prgm. M-06-347, [Manchester, UK] (2019/10). **N**

6) 山本 誠一, 山口 充孝, 河地 有木, 赤城 卓, 鎌田 圭, 吉川 彰, “粒子線治療中ビーム飛跡画像化のための YAP(Ce) X 線カメラの改良：問題と解決策”, 第 67 回応用物理学会春季学術講演会, 講演番号 12p-D209-11 [上智大・東京都千代田区] (2020/03). **N**

7) 山口 充孝, 長尾 悠人, 後藤 紳一, 河地 有木, “ファインピッチ CdTe イメージャを使用した即発 X 線の測定による治療用イオンビーム可視化システムのシミュレーションによる性能評価”, 第 67 回応用物理学会春季学術講演会, 講演番号 15a-D209-4 [上智大・東京都千代田区] (2020/03). **N**

8) 山本 誠一 ,山口 充孝 ,赤城 卓 ,山下 智弘 ,笹野 理 ,河地 有木, “炭素線照射により発生する 2 次電子制動 X 線実時間画像化のための YAP カメラの開発”, 第 117 回日本医学物理学会学術大会, 講演番号 0-172 [パシフィコ横浜・横浜市] (2019/04). **N**

9) 鈴井 伸郎, “植物体内のセシウム動態を可視化するポジトロン放出核種 127Cs トレーサの開発”【招待講演】, 第 67 回応用物理学会春季学術講演会シンポジウム「植物 RI イメージング技術と応用~農業応用の最前線~」, 13p-A501-3 [上智大学・東京] (2020/03). **C, 2-25,2-30**

Press・TV

1) “新たな高性能画像診断機器である「医療用コンプトンカメラ」を開発し，世界で初めての臨床試験に成功―PET 薬剤と SPECT 薬剤の同時計測・画像化に成功―”, 2019/7/24, プレス発表：読売新聞，日本経済新聞に掲載，時事ドットコムニュースに掲載，Yahoo Japan ニュースに転載. **N**

2) “腫瘍の正しい位置に放射線照射ができているかリアルタイムで確認 ～粒子線がん治療の現場での応用に期待～”, 2019/8/8, プレス発表：MONOist 医療技術ニュースに掲載，Yahoo Japan ニュースに転載. **N**

3) “「イチゴ果実内部に運ばれる糖」が最優秀賞を受賞 - 第 2 回「科学の美」インスタ写真コンテスト –”, 2020/1/27, プレス発表：群馬テレビ（ニュース JUST6，ニュース eye8）で放映，朝日新聞，読売新聞，農業共済新聞，全国農業新聞に掲載. **C**

P2-5 Project "Generation of Radioisotopes with Accelerator Neutrons"

Papers

1) K. Tsukada, Y. Nagai, S. Hashimoto, F. Minato, M. Kawabata, Y. Hatsukawa, K. Hashimoto, S. Watanabe, H. Saeki and S. Motoishi, “Anomalous Radioisotope Production for ^{68}ZnO Using Polyethylene by Accelerator Neutrons”, J.Phys.Soc.Jpn. **89**, 034201-1~7 (2020). **C**

2) I. Nishinaka, K. Hashimotoand H. Suzuki, “Speciation of astatine reacted with oxidizing and reducing reagents by thin layer chromatography: formation of volatile astatine”, J. Radioanal. Nucl. Chem. **322**, 2003-2009 (2019). **N**

3) E. Maeda, A. Yokoyama, T. Taniguchi, K. Washiyama and I. Nishinaka “Measurements of excitation functions of radon and astatine isotopes from ^{7}Li-induced reactions with 209Bi for development of a ^{211}Rn-^{211}At generator”, J. Radioanal. Nucl. Chem. **323**, 921-926 (2019). **N**

Proceedings

1) 西中 一朗, 橋本 和幸, 鈴木 博元, “溶存・揮発性アスタチン化学種の同定”, 第 3 回日本核医学会分科会放射性薬品科学研究会／第 19 回放射性医薬品・画像診断薬研究会（2019）［岡山］要旨集, P9 B-1 (2019). **N**

2) 瀬川 麻里子, 西中 一朗, 前田 亮, 藤暢 輔, “^{211}At の生成量及び化学形同時分析技術”, 第 3 回日本核医学会分科会放射性薬品科学研究会／第 19 回放射性医薬品・画像診断薬研究会(2019)［岡山］要旨集, P9 B-2 (2019). **N**

3) 西中 一朗, 橋本 和幸, 鈴木 博元, 渡辺 茂樹, Azim Mohammad Anwar-Ul,石岡 典子, “医療用 α 放射性 At-211 利用のための基礎研究－溶存 At 化学種の同定－”, 第 56 回アイソトープ・放射線研究発表会（2019）［東京］要旨集 P18 1p-I-08 (2019). **C**

4) 太田 朗生, 川端 方子, 本村 新, 本石 章司, 佐伯 秀也, 橋本 和幸, 塚田 和明, 初川 雄一, 永井 泰樹, “Zn-Cu 熱分離法を用いた医療用放射性 Cu-64, 67 の製造開発”, 日本放射化学会第 63 回討論会（2019）［いわき］要旨集 3A03 (2018). **N**

5) 西中 一朗, 橋本 和幸, 鈴木 博元, “溶存アスタチン化学種と揮発性化学種－酸化・還元剤濃度依存性－”, 日本放射化学会第 63 回討論会（2019）［いわき］要旨集, 3A01 (2019). **N**

6) 川﨑 康平, 新 裕喜, 青井 景都, 東 美里, 鷲山 幸信, 西中 一朗, 横山 明彦, “ラドンガスの気相回収法とイオン液体抽出による Rn-At ジェネレーターシステムの開発”, 日本放射化学会第 63 回討論会（2019）［いわき］要旨集, 13 (2019). **N**

7) 青井 景都, 新 裕喜, 川﨑 康平, 東 美里, 鷲山 幸信, 西中一朗, 羽場宏光, 森 大輝, Yan Wang, 横山明彦, 上杉正樹, “^{211}Rn/^{211}At ジェネレーターシステムに必要な ^{207}Po の除去法の検討”, 日本放射化学会第 63 回討論会（2019）［いわき］要旨集, 11 (2019). **N**

Patent

1) 瀬川 麻里子, 藤暢 輔, 前田 亮, 西中 一朗, “α 線放出核種の分析方法及び分析装置”, 特願 2019-136227 (2019.7.24). **N**

P3-1 Project "Laser Compton Scattering (LCS) Gamma-ray Research"

Papers

1) T. Maruyama, T. Hayakawa and T. Kajino, “Compton Scattering of Gamma-Ray Vortex with Laguerre Gaussian Wave Function”, Scientific Reports 9, Article number: 51 (2019). **N**

2) H. Sakai, E. Cenni, K. Enami, T. Furuya, M. Sawamura, K. Shinoe and K. Umemori, “Field emission studies in vertical test and during cryomodule operation using precise x-ray mapping system”, Phys. Rev. Accel. Beams **22**, 022002 (2019). **N**

3) H. Zen, H. Ohgaki, Y. Taira, T. Hayakawa, T. Shizuma, I. Daito, J. Yamazaki, T. Kii, H. Toyokawa and M. Katoh, “Demonstration of tomographic imaging of isotope distribution by nuclear resonance fluorescence”, AIP Advances **9**, 035101 (2019). **N**

4) N. Nishimori, R. Nagai, R. Hajima, M. Yamamoto, Y. Honda, T. Miyajima and T. Uchiyama, “Operational experience of a 500 kV photoemission gun”, Phys. Rev. Accel. Beams **22**, 053402 (2019). **N**

5) T. Maruyama, T. Hayakawa and T. Kajino, “Compton Scattering of Hermite Gaussian Wave γ Ray”, Scientific Reports, volume **9**, Article number: 7998 (2019). **N**

6) T. Shizuma, M. Omer, R. Hajima, N. Shimizu, and Y. Utsuno, “Spin and parity determination of the 3.004-MeV level in 27Al: Its low-lying multiplet structure”, Phys. Rev. C **100**, 014307 (2019). **N**

7) M. Omer and R. Hajima, “Validating polarization effects in γ-rays elastic scattering by Monte Carlo simulation”, New Journal of Physics **21**, 113006 (2019). **N**

8) 羽島 良一, “自由電子レーザーによる位相安定化パルス光の発生”, パリティ **34**, No.1, pp.12-14 (2019). **N**

9) 早川 岳人, 梶野 敏貴, “反電子ニュートリノ反応で 98Tc を生成”, Isotope News, No.**762**, pp.26-29 (2019) **N**

10) 静間 俊行, “原子核のハサミ状振動を探る（最近の研究から）”, 日本物理学会誌 **74**, No.5, pp.325-329 (2019). **N**

Proceedings

1) T. Obina, D.A. Arakawa, M. Egi, T. Furuya, K. Haga, K. Harada, T. Honda, Y. Honda, T. Honma, E. Kako, R. Kato, H. Kawata, Y. Kobayashi, Y. Kojima, T. Konomi, H. Matsumura, T. Miura, T. Miyajima, S. Nagahashi, H. Nakai, N. Nakamura, K. Nakanishi, K.N. Nigorikawa, T. Nogami, F. Qiu, H. Sagehashi, H. Sakai, S. Sakanaka, M. Shimada, M. Tadano, T. Takahashi, R. Takai, O.A. Tanaka, Y. Tanimoto, T. Uchiyama, K. Umemori, M. Yamamoto, R. Hajima, R. Nagai, M. Sawamura and N. Nishimori, “1 mA Stable Energy Recovery Beam Operation with Small Beam Emittance”, Proceedings of the 10th International Particle Accelerator Conference (IPAC-2019), [Melbourne, Australia], 1482-1485 (2019). **N**

2) Y. Sumitomo, Y. Hayakawa, T. Sakai and R. Hajima, “Simulation of Short-Pulse Generation from a Dynamically Detuned IR-FEL Oscillator and Pulse Stacking at an External

Cavity", Proceedings of the 10th International Particle Accelerator Conference (IPAC-2019), [Melbourne, Australia], 1778-1781 (2019). **N**

3) S. Matsuba, M. Katoh, K.S. Shimada, K. Harada and K. Kawase, "Design Study of an Electron Storage Ring for the Future Plan of Hiroshima Synchrotron Radiation Center", Proceedings of the 10th International Particle Accelerator Conference (IPAC-2019), [Melbourne, Australia], 200-202 (2019). **N**

4) S. Matsuba, M. Fujimoto, M. Katoh, M. Hosaka, K. Kawase, T. Konomi, N. Yamamoto, A. Miyamoto and S. Sasaki, "Experimental Demonstration of Vector Beam Generation With Tandem Helical Undulators", Proceedings of the 10th International Particle Accelerator Conference (IPAC-2019), [Melbourne, Australia] 1766-1768 (2019/5). **N**

5) R. Hajima, K. Kawase, R. Nagai, Y. Hayakawa, T. Sakai, Y. Sumitomo, T. Miyajima, M. Shimada, H. Ohgaki and H. Zen, "Application of Infrared FEL Oscillators for Producing Isolated Attosecond X-Ray Pulses via High-Harmonic Generation in Rare Gases"【Invited talk】, Proc. FEL-2019, 272-275 (2019). **N**

6) 沢村 勝, 羽島 良一, 阪井 寛志, 梅森 健成, 許斐 太郎, 古屋 貴章, "C 形導波管型 HOM カップラー製作の現状", Proceedings of the 16th Annual Meeting of Particle Accelerator Society of Japan, July 31 - August 3, 2019, 706 (2019). **N**

7) 沢村 勝, 羽島 良一, 佐伯 学行, 岩下 芳久, 頓宮 拓, 中村 哲朗, 渡邉 直久, "超伝導スポーク空洞の電子ビーム溶接試験", Proceedings of the 16th Annual Meeting of Particle Accelerator Society of Japan, J [Kyoto, Japan], .709 (2019/7-8). **N**

8) 羽島 良一, 川瀬 啓悟, 永井 良治, 大垣 英明, 全 炳俊, 早川 恭史, 境 武志, 住友 洋介, 島田 美帆, 宮島 司, "自由電子レーザーで駆動する高繰り返しアト秒 X 線光源の開発", Proceedings of the 16th Annual Meeting of Particle Accelerator Society of Japan, [Kyoto, Japan], 742 (2019/7-8). **N**

9) 坂本 文人, 加藤 龍好, 羽島 良一, "Genesisを用いたcERLによる中赤外自由電子レーザー光の数値解析", Proceedings of the 16th Annual Meeting of Particle Accelerator Society of Japan, [Kyoto, Japan], 754 (2019/7-8) . **N**

10) 川瀬 啓悟, 羽島 良一, 永井 良治, "キャリアエンベロープ位相安定中赤外光源の検討", Proceedings of the 16th Annual Meeting of Particle Accelerator Society of Japan, [Kyoto, Japan], 780 (2019/7-8). **N**

11) 住友 洋介, 川瀬 啓悟, 羽島 良一, 黒澤 歩夢, 早川 恭史, 境 武志, "共振器型 IR-FEL パルス蓄積のための外部増幅共振器の開発と試験蓄積", Proceedings of the 16th Annual Meeting of Particle Accelerator Society of Japan, [Kyoto, Japan], 783 (2019/7-8). **N**

12) 阪井 寛志, 梅森 健成, 加古 永治, 許斐 太郎, 古屋 貴章, Feng Qiu, 三浦 孝子, 中西 功太, 本間 輝也, 小島 裕二, 沢村 勝, 石原 将治, 今田 信一, 泰中 俊介, 沼田 直人, 山田 浩気, "Compact ERL における長期ビーム運転下での主加速器部超伝導空洞性能の推移", Proceedings of the 16th Annual Meeting of Particle Accelerator Society of Japan, [Kyoto, Japan], 478 (2019/7-8). **N**

13) 川瀬 啓悟, 誉田 義英, 磯山 悟朗, "産研 THz-FEL における EO 計測の周波数解析", Proceedings of the 16th Annual Meeting of Particle Accelerator Society of Japan, [Kyoto, Japan], 1070 (2019/7-8). **N**

14) Ryoichi Hajima, "High-Repetition-Rate High-Harmonic Generation Driven by Infrared Free-Electron Lasers"【Invited talk】, Published in: 2019 IEEE Photonics Conference (IPC), 29 Sept.-3 Oct. 2019, San Antonio, USA. **N**

P3-2 Beam Engineering Section

Papers

1) Y. Yamada, K. Suzuki, K. Yoshino, S. Taminato, T. Satoh, M. Finsterbuch, T. Kamiya, A. Yamazaki, Y. Kato, K. Fujita, K. Mima, S. Hori, M. Hirayama, R.i Kanno, "Ex-situ Analysis of Lithium Distribution in a Sulfide-based All-solid-state Lithium Battery by Particle-induced X-ray and Gamma-ray Emission Measurements", Electrochemistry **88**(1), 45-49 (2020). **S, 3-08**

2) H. Kashiwagi, K. Yamada, "Investigation of the time interval of plasma generation for a high repetition rate laser ion source" Review of scientific instruments, 91(3), 033305-1 - 033305-5, (2020). **N**

3) K. Yamada, H. Kashiwagi, "Low-charge-state ion production by a laser ion source for the TIARA ion implanter", Review of scientific instruments, **91**(1), 013305-1 - 013305-4, (2020). **N**

4) Y. Yuri, M. Fukuda, T. Yuyama, "Transverse profile shaping of a charged-particle beam using multipole magnets - Formation of hollow beams –", Journal of Physics: Conference Series, **1350**, 012115, (2019). **C, 3-01**

5) A. Kitamura**,** T. Yamaki, Y. Yuri, H. Koshikawa, S. Sawada, T. Yuyama, A. Usui, A. Chiba, "Control of the size of etchable ion tracks in PVDF - Irradiation in an oxygen atmosphere and with fullerene C60", Nucl. Instrum. Meth. Phys. Res. B **460**, 254-258 (2019). **C, T, 3-01**

6) Y. Kaneko, H. Hayashi, Y. Ishii, W. Kada, H. Nishikawa, "Refractive index change and thermo-optic effect in polydimethylsiloxane nanocomposites with oxide nanoparticles induced by proton beam writing", Nucl.Instrum. Meth. Phys. Res. B **459**, 94-97 (2019) **S, 3-04**

7) T. Shibuya, S. Uchida, Y. Ishii, H. Nishikawa, "Assembling gold nanoparticles by dielectrophoresis with pit arrays on PMMA fabricated by proton beam writing", Nucl. Instrum. Meth. Phys. Res. B, **456**, 60-63 (2019). **S, 3-04**

8) K. Okuyama, Y. Matsuda, H. Yamamoto, Y. Tamaki, K. Saito, M. Hayashi, Y. Yoshida, K. Sano, T. Satoh, M. Koka, "Fluorine distribution from fluoride-releasing luting materials into human dentin", Nucl. Instrum. Meth. Phys. Res. B **456**, 16-20 (2019). **S, 2-31, 2-33**

9) Y. Matsuda, K. Okuyama, H. Yamamoto, M. Fujita, S. Abe, T. Satoh, N. Yamada, M. Koka, H. Sano, M. Hayashi, S. K. Sidhu, T. Saito, "Antibacterial effect of a fluoride-containing ZnO/CuO nanocomposite", Nucl. Instrum. Meth. Phys. Res. B **458**, 184-188 (2019). **S, 2-31, 2-33**

10) S. Watanabe, Y. Katai, H. Matsuura, W. Kada, M. Koka, T. Satoh, S. Arai, "Ion beam induced luminescence of complexes formed in adsorbent for MA recovery process", Nucl. Instrum.

Meth. Phys. Res. B **450**, 61-65, (2019). **N**

11) Y. Yuri, M. Fukuda, T. Yuyama, “Formation of hollow ion beams of various shapes using multipole magnets”, Progress of Theoretical and Experimental Physics, **2019**(5), 053G01, (2019). **C, 3-01**

12) Y. Ishii, T. Ohkubo, Y. Miyake, “Prototype of a penning ionization gauge type ion source with a permanent magnet for a MeV compact ion microbeam system”, AIP Conference Proseedings, 2160, 030003-1 - 030003-5, (2019). **N**

13) W. Kada, I. Sudić, N. Skukan, S. Kawabata, T. Satoh, J. Suzaki, S. Yamada, T. Sakine, R. Kumar Parajuli, M. Sakai, K. Miura, M. Koka, T. Kamiya, M. Jakšić, M. Hanaizumi, N. Yamada.”Evaluation of scintillation properties of α- and β-SiAlON phosphors under focused microbeam irradiation using ion-beam-induced luminescence analysis”, Nucl. Instrum. Meth. Phys. Res. B **450**, 157-162 (2019). **N**

14) Hidetaka Hayashi, Wataru Furukawa, Hiroyuki Nishikawa, Electronic circuit formation on flexible polymer surface processed by 1 MV accelerated hydrogen molecular ions, Nucl. Instrum. Meth. Phys. Res. B **459**, 76-80 (2019). **S, 3-04**

15) T. Segawa, S. Harada, T. Sato and S. Ehara, “Delivery and Effectiveness of Carboplatin via Targeted Delivery Compared to Passive Accumulation of Intravenously Injected Particles Releasing Carboplatin upon Irradiation”, Radiat. Res. 193, 263–273 (2020). **S, 2-32**

16) W. Kada, T. Satoh, S. Yamada, M. Koka, N. Yamada, K. Miura and O. Hanaizumi, “Micro-ion beam-induced luminescence spectroscopy for evaluating SiAlON scintillators”, Nucl. Instrum. Meth. B **193**, 66–72 (2020). **S, 3-07**

17) H. Amekura, K. Narumi, A. Chiba, Y. Hirano, K. Yamada, D. Tsuya, S. Yamamoto, N. Okubo, N. Ishikawa, and Y. Saitoh, “C_{60} ions of 1 MeV are slow but elongate nanoparticles like swift heavy ions of hundreds MeV”, Scientific Reports **9,** 14980-1~10 (2019). **T**

18) 百合 庸介, “高エネルギーイオンビームの Roll-to-Roll 均一照射技術の開発”, 日本海水学会誌, **73**(4), 203-207 (2019). **C, 3-01**

19) Y. Hase, K. Satoh, H. Seito and Y. Oono, "Genetic consequences of acute/chronic gamma and carbon ion irradiation of *Arabidopsis thaliana*", Front. Plant Sci., **11**, 336 (2020). **C, G**

20) L.S. Relleve, C.T. Aranilla, B.J.Barba, A.K.R. Gallardo, V.R.C. Cruz, C.R.M. Ledesma, N. Nagasawa and L. V. Abad, “Radiation-synthesized polysaccharides/polyacrylate super water absorbents and their biodegradabilities.” Radiation Physics and Chemistry, **170**, 108618 (2020). **G**

21) 青木 祐太郎, 田口 光正, 長澤 尚胤, 砂川 武義, “新規メカニズムによる医療用高感度ゲル線量計の開発”, 放射線と産業, **146**, 43-47 (2019). **G**

Proceedings

1) 宮脇 信正, 倉島 俊, “マイクロビーム形成･利用を実現したAVF サイクロトロンにおけるビーム位相制御技術の開発”, Proceedings of the 16th Annual Meeting of Particle Accelerator Society of Japan 175 – 178 (2019). **N**

2) 宮脇 信正, 柏木 啓次, 石岡 典子, “TIARA AVF サイクロトロンのペッパーポット型エミッタンス測定装置の開発”, Proceedings of the 16th Annual Meeting of Particle Accelerator Society of Japan, 810-813 (2019). **N**

3) 明午 伸一郎, 武井 早憲, 松田 洋樹, 百合 庸介, 湯山 貴裕, “大強度陽子加速器のための標的上のプロファイルモニタの開発”, Proceedings of the 16th Annual Meeting of Particle Accelerator Society of Japan, 515-519 (2019). **C**

4) 百合 庸介, 福田 光宏, 湯山 貴裕, “多重極電磁石を用いたビーム強度分布中空化の実証”, Proceedings of the 16th Annual Meeting of Particle Accelerator Society of Japan, 112–115 (2019). **C, 3-01**

5) Y. Yuri, M. Fukuda and T. Yuyama, “Transverse profile shaping of a charged-particle beam using multipole magnets – Formation of hollow beams –“, Proceedings of the 10th International Particle Accelerator Conference, 184-186 (2019). **N**

6) Y. Nojiri, Y. Koike, Y. Ishii and H. Nishikawa, “Surface modification and microfabrication of piezoelectric fluorinated polymers by proton beam writing“, 45th International Conference on Micro and Nano Engineering (MNE) 2019, Sep. 23-26, 2019, Paper No. PB46. **S, 3-04**

7) 野尻 佳孝, 西川 宏之, 林 秀臣, “陽子線描画における高分子圧電材料(PVDF-TrFE)への照射効果”, 令和元年電気学会基礎･材料･共通部門大会 No.3-P-28 (2019/9/3). **S, 3-04**

8) 野尻 佳孝, 西川 宏之, 林 秀臣, 石井 保行, “陽子線描画を用いた PVDF-TrFE マイクロピラーの作製”, 令和元年放電学会 年次大会, 講演番号4-4 (2019). **S, 3-04**

9) 野原 悠暉, 林 秀臣, 西 川宏之, “エポキシ系導電性コンポジットの陽子線描画によるパターニング”, 令和 2 年電気学会全国大会講演予稿集 p.96, 講演番号 2-081 (2020/3/11). **S, 3-04**

10) 野尻 佳孝, 林 秀臣, 石井 保行, 西川 宏之, “陽子線描画による圧電性を有するフッ素系高分子材料の 3 次元構造体の形成”, 令和 2 年電気学会全国大会講演予稿集, p.38-39, 講演番号 2-034 (2020/3/11). **S, 3-04**

11) 河嶋 涼介, 内田 諭, 西川 宏之, “ピット型誘電泳動デバイス内での粒子輸送における界面動電効果の影響”, 令和 2 年電気学会全国大会講演予稿集, p.218, 講演番号 3-154 (2020/3/11～13). **S, 3-04**

12) N. Miyawaki, H. Kashiwagi and N. S Ishioka,” Development of a pepper-pot emittance monitor system for the TIARA AVF cyclotron” Proceedings of the 16th Annual Meeting of Particle Accelerator Society of Japan (2019) 175-178. **C, 3-02**

13) N. Miyawaki and S. Kurashima, “ Development of beam phase control technology of AVF cyclotron for realization of microbeam formation and its application”, Proceedings of the 15th Annual Meeting of Particle Accelerator Society of Japan, 810-813 (2019). **C**

14) A. Chiba, A. Usui, Y. Hirano, K. Yamada, K. Narumi and Y. Saitoh, “Novel approaches for intensifying negative C_{60} ion beams using conventional ion sources installed on a tandem accelerator”, Quantum Beam Sci. **4**, 13 (2020). **T**

15) 平野 貴美, 千葉 敦也, 山田 圭介, 横山 彰人, 高山 輝充, 金井 信二, 青木 勇希, 橋爪 将司, 高橋 悠人, 長谷川 雅人, 佐藤 隆博, 大久 保猛, 鳴海 一雅, 斎藤 勇一, 倉島 俊, “TIARA 静電加速器の現状”, 第 31 回｢タンデム加速器及びその周辺技術の研究会 [東京] 報告集 112-115 (2019). **T, S, I**

16) S. Hosoya, S. Kurashima, A. Chiba, K. Yoshida, K. Yamada, T.

Yuyama, T. Ishizaka, A. Yokoyama, Y. Hirano, N. Miyawaki, H. Kashiwagi, Y. Yuri, T. Satoh, I. Ishibori, S. Okumura, T. Nara, “Present status of TIARA at QST”, Proc, 16th Annu. Meet. Part. Accel. Soc. Jpn. 1285-1288 (2019) **C**

17) H. Amekura, “Shape Elongation of Embedded Nanoparticles Induced by MeV C_{60} Ion Irradiation”【Invited talk】, Proc. of International Workshop on Radiation Effects of Materials and Devices (REMD-2020), [Harbin,China] (2020). **T**

18) 雨倉 宏, “高速重イオンの代替ビームとしての MeV C_{60} クラスターイオンビーム”【招待講演】, 荷電粒子ビームの工業への応用第 132 委員会（独立行政法人日本学術振興会）, 第 238 回研究会[東京](2019), 資料集 p.14-21. **T**

Patent

1) 長澤 尚嗣, 鈴木 淳史, 望月 亮弥, “摩擦特性向上デュアル架橋ハイブリッドゲル”, 出願 191226, 特願 2019-236517 (19.12.26). **E, G**

External Research Groups Except for Takasaki Advanced Radiation Research Institute

Journals

1) Y. Matsuya, T. Nakano, T. Kai, N. Shikazono, K. Akamatsu, Y. Yoshii, T. Sato, “A simplified cluster analysis of electron track structure for estimating complex DNA damage yields”, Int. J. Mol. Sci. **21,** 1701(2020). **N, 2-34**

2) M. Koshimizu, S. Kurashima, A. Kimura, M. Taguchi, T. Yanagida, H. Yagi, T. Yanagitani, Y. Fujimoto and K. Asai, “Effect of linear energy transfer on the scintillation properties of $Ce:Gd_3Al_2Ga_3O_{12}$”, Nucl. Instrtrum. Meth. Phys. Res. B **460**, 74 (2019). **C, 3-10**

3) M. Zhao, “Deuterium permeation behavior in Fe ion damaged tungsten studied by gas-driven permeation method”, Fusion Science and Technology **76**, 246-251 (2020). **N**

4) M. Nakata, K. Azuma, A. Togari, Q. Zhou, M. Zhao, T. Toyama, Y. Hatano, N. Yoshida, H. Watanabe, M. Shimada, D. Buchenauer and Y. Oya, “Dynamics evaluation of hydrogen isotope behavior in tungsten simulating damage distribution”, Fusion Engineering and Design **146** 2096-2099 (2019). **N**

5) M. Yoshimoto, Y. Yamazaki, T. Nakanoya, P. K. Saha, and M. Kinsho, “Progress status in fabrication of HBC stripper foil for 3-GeV RCS at J-PARC in Tokai site”, EPJ Web of Conferences 229, 01001 (2020). **S, I, 3-18**

Proceedings

1) M. Ando, H. Tanigawa, H. Kurotaki, T. Nozawa, Y. Katoh, “The μ-tensile deformation behavior of single block structure of F82H irradiated at 573K”, Proceedings of The 19th International Conference on Fusion Reactor Materials (ICFRM-19), Oct. 28, 2019, La Jolla, California, U.S.A. **T, 1-36**

2) 片岡 頌治, 高野 雅人, 佐藤 史紀, 齋藤 恭央, “東海再処理施設における低放射性廃液の処理技術開発（22）ガンマ線照射によるセメント固化体の水素生成評価”, 日本原子力学会 2019 年秋の大会, 予稿集 3I02 (2019). **G, 1-41**

3) T. Nakanoya, M. Yoshimoto, Y. Yamazaki, O. Takeda, R. Saeki, M. Mutoh, “Fabrication status of charge stripper foil for 3GeV synchrotron of J-PARC”, Proc. 16th Annual Meeting of Particle Accelerator Society of Japan, [Kyoto, Japan] (2019/08). PASJ2019 WEPI036. **S, I, 3-18**

Appendix 2　Type of Research Collaboration and Facilities Used for Research

Paper No.	Type of Research Collaboration*1					Irradiation Facilities*2					
	Joint Res.	Entr. Res.	Coop. Res.	Inter. Use	Ext. Use	C	T	S	I	E	G
1-01	●										◎
1-02	●N										
1-03				●		◎					◎
1-04	●								◎		
1-05	●								◎		
1-06	●					◎				◎	
1-07	●									◎	
1-08	●					◎					
1-09				●							◎
1-10	●					◎					
1-11	●					◎					
1-12	●						◎				
1-13	●					◎					
1-14	●								◎		
1-15	●					◎					
1-16				●							◎
1-17				●					◎		
1-18	●								◎		
1-19	●						◎		◎		
1-20	●					◎					
1-21	●									◎	
1-22				●				◎	◎		
1-23	●								◎		
1-24				●						◎	
1-25	●									◎	◎
1-26				●				◎		◎	
1-27				●							◎
1-28	●										◎
1-29	●										◎
1-30	●									◎	◎
1-31				●							◎
1-32				●			◎		◎		
1-33	●										◎
1-34	●										◎
1-35				●							◎
1-36				●			◎	◎	◎		
1-37	●						◎				
1-38				●			◎	◎	◎		
1-39				●							◎
1-40					●	◎					
1-41					●						◎
1-42					●						◎
1-43					●						◎
1-44					●						◎
1-45					●		◎	◎			
1-46					●				◎		
1-47					●				◎		
1-48					●						◎
1-49					●						◎
2-01	●					◎					
2-02	●					◎					
2-03	●					◎					
2-04	●					◎					
2-05	●					◎					
2-06	●					◎					
2-07	●					◎					◎
2-08	●					◎					
2-09	●										◎
2-10	●					◎					
2-11	●										◎
2-12	●										◎
2-13			●					◎			
2-14	●					◎					
2-15	●										◎
2-16	●										◎
2-17	●					◎					
2-18	●					◎					
2-19	●					◎					
2-20	●					◎					
2-21	●					◎					
2-22				●							◎
2-23	●					◎					
2-24	●					◎					
2-25	●					◎					
2-26			●					◎			
2-27			●					◎			
2-28					●	◎		◎			
2-29	●N										
2-30	●					◎					
2-31			●					◎			
2-32			●					◎			

Paper No.	Type of Research Collaboration*1					Irradiation Facilities*2					
	Joint Res.	Entr. Res.	Coop. Res.	Inter. Use	Ext. Use	C	T	S	I	E	G
2-33			●					◎			
2-34				●		◎					
2-35					●	◎					
3-01				●		◎					
3-02				●		◎					
3-03	●							◎			
3-04	●							◎			
3-05	●							◎			
3-06	●N										
3-07			●					◎			
3-08	●							◎			
3-09	●					◎					
3-10					●	◎					
3-11				●			◎		◎		
3-12			●N								
3-13			●				◎				
3-14			●						◎		
3-15			●				◎		◎		
3-16			●				◎		◎		
3-17			●				◎				
3-18					●			◎	◎		
4-01						○	○	○	○		
4-02						○					
4-03							○	○	○		
4-04										○	○
4-05										○	○
4-06						○	○	○	○		
4-07						○	○	○	○		
4-08						○	○	○	○	○	○
Total	56	0	13	19	14	35	12	18	18	7	27

*1 Type of Research Collaboration

Joint Res. : Joint research with external users

Entr. Res. : Research entrusted to QST

Coop. Res. : Cooperative research with plural universities through The University of Tokyo

Inter. Use : Internal use

Ext. Use : Common use based on two programs of "QST-facility-use" and "Creation of Research Platforms and Sharing of Advanced Research Infrastructure" supported from MEXT

*2 Utilization of Irradiation Facilities

C : AVF Cyclotron

T : 3 MV Tandem Electrostatic Accelerator

S : 3 MV Single-ended Electrostatic Accelerator

I : 400 kV Ion Implanter

E : 2 MV Electron Accelerator

G : Co-60 Gamma-ray Irradiation Facilities

◎ : Study use of irradiation facilities at TARRI

○ : Management of irradiation facilities at TARRI

N : Non-use of irradiation facilities at TARRI

Appendix 3　Abbreviation Name for National Organizations

【National Institutes for Quantum and Radiological Science and Technology: **QST**】
（量子科学技術研究開発機構）

◆Directorate and Institutes of QST appearing in this report

QuBS 量子ビーム科学部門 : Quantum Beam Science Research Directorate
TARRI 高崎量子応用研究所 : Takasaki Advanced Radiation Research Institute
KPSI 関西光科学研究所 : Kansai Photon Science Institute
NFI 那珂核融合研究所 : Naka Fusion Institute
RFI 六ヶ所核融合研究所 : Rokkasho Fusion Institute
NIRS 放射線医学総合研究所 : National Institute of Radiological Sciences

◆Examples of Department and Center of QST

・量子ビーム科学部門、研究企画部
Department of Research Planning and Promotion, QuBS, QST

・量子ビーム科学部門、高崎量子応用研究所、先端機能材料研究部
Department of Advanced Functional Materials Research, TARRI, QST

・量子ビーム科学部門、高崎量子応用研究所、放射線生物応用研究部
Department of Radiation-Applied Biology Research, TARRI, QST

・量子ビーム科学部門、高崎量子応用研究所、放射線高度利用施設部
Department of Advanced Radiation Technology, TARRI, QST

・量子ビーム科学部門、高崎量子応用研究所、東海量子ビーム応用研究センター
Tokai Quantum Beam Science Center, TARRI, QST

・量子ビーム科学部門、高崎量子応用研究所、管理部
Department of Administrative Services, TARRI, QST

・量子ビーム科学部門、関西光科学研究所、光量子科学研究部
Department of Advanced Photon Research, KPSI, QST

・量子ビーム科学部門、関西光科学研究所、放射光科学研究センター
Synchrotron Radiation Research Center, KPSI, QST

・核融合エネルギー部門、那珂核融合研究所、ITERプロジェクト部
Department of ITER Project, NFI, QST

・核融合エネルギー部門、六ヶ所核融合研究所、核融合炉材料研究開発部
Department of Fusion Reactor Materials Research, RFI, QST

・量子医学・医療部門、放射線医学総合研究所、放射線障害治療研究部
Department of Basic Medical Sciences for Radiation Damages, NIRS, QST

・量子医学・医療部門、放射線医学総合研究所、重粒子線治療研究部
Department of Charged Particle Therapy Research, NIRS, QST

・量子医学・医療部門、放射線医学総合研究所、物理工学部
Department of Accelerator and Medical Physics, NIRS, QST

・量子生命科学領域
Institute for Quantum Life Science, QST

【Other National Organizations appearing in this report】

AIST	産業技術総合研究所	: National Institute of Advanced Industrial Science and Technology
JAEA	日本原子力研究開発機構	: Japan Atomic Energy Agency
JAXA	宇宙航空研究開発機構	: Japan Aerospace Exploration Agency
KEK	高エネルギー加速器研究機構	: High Energy Accelerator Research Organization
NARO	農業・食品産業技術総合研究機構	: National Agriculture and Food Research Organization
NIMS	物質・材料研究機構	: National Institute for Materials Science
NINS	自然科学研究機構	: National Institutes of Natural Sciences

QST Takasaki Annual Report 2019

(Ed) Hiroyuki YAMAMOTO

Date of Publishing : March 2021

Editorial committee : Hiroyuki YAMAMOTO, Yasunari MAEKAWA, Takeshi OHSHIMA,
Noriko ISHIOKA, Yuichi SAITOH, Kazumasa NARUMI, Ryoji NAGAI,
Yutaka OONO and Ryoichi HAJIMA

Publication : Takasaki Advanced Radiation Research Institute
National Institutes for Quantum and Radiological Science and Technology
1233 Watanuki, Takasaki, Gunma 370-1292, Japan

Tel : +81-27-346-9232

E-mail : taka-annualrep@qst.go.jp

Homepage : https://www.qst.go.jp/site/taka/

Printed in Japan

QST-M-29

http://www.qst.go.jp